Interplay in 3D between faults and water flow paths in crystalline bedrock (Grimsel, Switzerland)

Inauguraldissertation
der Philosophisch-naturwissenschaftlichen Fakultät
der Universität Bern

vorgelegt von
Raphael Benedict Schneeberger
von Basel-Stadt

Leiter der Arbeit:
Prof. Dr. M. Herwegh
PD Dr. U.K. Mäder
Institut für Geologie der Universität Bern

Interplay in 3D between faults and water flow paths in crystalline bedrock (Grimsel, Switzerland)

Inauguraldissertation
der Philosophisch-naturwissenschaftlichen Fakultät
der Universität Bern

vorgelegt von
Raphael Benedict Schneeberger
von Basel-Stadt

Leiter der Arbeit:
Prof. Dr. M. Herwegh
PD Dr. U.K. Mäder
Institut für Geologie der Universität Bern

Von der Philosophisch-naturwissenschaftlichen Fakultät angenommen.

Bern, 10.10.2017

Der Dekan:
Prof. Dr. G. Colangelo

Abstract

Granitic rocks are widespread and, in the upper crust, are generally fractured in complex networks across scales (kilometres down to submillimetres). In these rocks, physical parameters, like diffusivity or permeability, are controlled by the fracture networks and thus are anisotropic. Hence fault and fracture patterns govern water percolation, which is of fundamental importance for applied projects such as the disposal of radioactive waste. Therefore, knowledge about the geometry, aperture, spacing and mineralogical composition of fault rocks is key for the safe planning of such long-term projects.

In order to study the interplay between faults and water percolation in granitic host rock we examined in detail the underground rock laboratory at the Grimsel Test Site (GTS, operated by Nagra) in the Central Swiss Alps. The site was chosen for both its continuous rock exposure along the tunnel walls and the pristine outcrop conditions. Our study implemented a complementary interdisciplinary workflow to capture insights into the pertinent water-rock interactions of granitic rocks in rugged crystalline environments: this consisted of detailed surface and underground mapping across scales, in which we characterized both the petrology and structures of the site geology (chapter 2); investigations of the site discharge water which allowed for the hydrochemical analysis and modelling of the recent groundwater (chapter 3); 3D structural modelling that included uncertainty estimations of the data (chapter 4); and finally, we link our observations of the 3D geometry of faults and the groundwater flow in a conceptual water pathway model (chapter 5).

The bedrock surrounding the GTS is mainly composed of two granitoid rocks, the Grimsel granodiorite (GrGr) and the Central Aar granite (CAGr). Deformation related to the Alpine orogeny led to the formation of a pervasive foliation and of numerous zones of highly localized strain. High-strain zones are primarily of ductile origin and strike NE-SW, E-W as well as NW-SE, and are mostly steeply southwards dipping. During cooling and on-going exhumation, these mechanical discontinuities were reactivated in a heterogeneous brittle manner resulting in brittle faults, which consist of cataclasites and fault gouges. Dilation in these tectonites led to an increase in pore space, which ultimately became connected, culminating in an increased permeability.

Analysis of H and O isotopes of the sampled groundwater of GTS suggests a meteoric origin. Except for two samples, no Tritium was measured, indicating water infiltration before the 1950s, and therefore a minimum percolation time of >60 years. Two different groups of water (CAGr and GrGr water) could be distinguished based on isotopic composition, pH, and concentration in Na, Ca, Li and Cl ions. The observed differences do not derive from variations of the major water-rock interactions (dissolution of plagioclase and fluorite; precipitation of quartz and kaolinite) but rather result from longer residence times due to differences in overburden.

Faults in the GrGr and the CAGr are ubiquitous. Most brittle faults occur along a former ductile high-strain zone, therefore special emphasize was laid on the ductile zones as they are km to 100m-scale continuous planar structures. Structural 3D modelling allowed for extrapolation of the surface data to the GTS. Three different extrapolation algorithms were employed and compared based on a statistical interpolation. This comparison showed the importance of fieldwork for both acquiring data and validating modelling results. The obtained 3D structural model visualises several faults and fault intersections that crosscut the entire rock mass above GTS and link the major faults observed at GTS to today's surface topography. These km-scale faults are linked by secondary relay faults with length of couple of tens to few hundred meters. From surface information alone the exact occurrence of such relay structures cannot be accurately predicted underground, given their finite nature with small lateral extensions. Here, only probabilistic approaches could provide some additional information, however, these methods are subject to a substantial degree of uncertainty.

For the subsurface water flow, a combination of faults with enhanced slip tendency and fault intersections reveals that 90% of the mapped water discharge points at GTS occur along aforementioned structural features. The remaining 10% are also fault-bound discharge points, however along faults with low-slip tendency. Comparison of measured water fluxes in the GTS with domains with a specific water-conducting element predominating revealed that domains with high fault intersection density correlate with domains of high water fluxes. Domains with a high density of high-slip tendency faults correspond to domains with intermediate water fluxes. Domains of a high density of low-slip tendency fault show low water fluxes. Thereby, we infer that fault intersections with high-slip tendency faults act as major water flow paths in granitoid host rocks. Therefore a sequence of stepped importance between the different elements can be inferred, where fault intersections are the predominating water-conducting features followed by high-slip tendency faults.

In summary, a combination of groundwater sampling and structural analysis was found as a rather suitable approach to gain a fundamental understanding of water flow in fractured subsurface granitic bedrock. Such knowledge provides prerequisite information for a thorough site characterisation for radioactive waste disposal programs situated in granitoid host rocks.

Acknowledgments

This thesis results from research carried out from March 2014 to August 2017 at the Institute for Geological Sciences at the University of Bern and in the Grimsel Test Site (GTS). It benefitted from the support of diverse persons at the institute and from Nagra.

I would like to express my gratitude to everyone who supported me during this journey.

I want to deeply thank my doctoral advisor Marco Herwegh for his continuous support and enthusiasm. I greatly appreciated the fast and easy communication and the new ideas born in discussion.

Thanks to Urs K. Mäder, Alfons Berger and H. Niklaus Waber for co-advising my thesis and for all supportive discussions, remarks and ideas. Daniel Egli helped with numerous reviews of diverse manuscripts and fruitful discussions - thank you!

The Nagra is thanked for financing the project and for their very supportive manner. Special thanks go to Florian Kober, who managed the project (LASMO) in a very sensitive and pleasant way. Further the staff at GTS, Hans, Toni, Ann-Sofi, and René is thanked for diverse support during mapping and the funny lunchtimes.

Further, I would like to express my gratitude to Samuel Mock, Lukas Nibourel, Christoph Wanner and James Gilgannon for stimulating discussions at the institute.

Special thanks go to Zoe Shipton, who kindly agreed to evaluate this thesis as an external referee.

Finally, I would like to express my deepest thanks to Mirjam, my family and friends for their support during the last years.

Contents

List of Tables

List of Figures

Introduction

1.1. General introduction

Granitoid basement rocks are common, and are widely used for underground projects such as tunnelling, disposal of radioactive waste, or enhanced geothermal energy projects. It is the case that projects, like those listed, are a large infrastructural investment, and it is desired that they have a long and safe life span. Therefore it is important to understand the long-term stability of the properties of the granitoid rocks that host such projects. The properties of interest vary between projects but in general are related to the material properties of the granitoid material, the geological structures hosted in the rock and the characteristics of any fluid present. These different features are not independent and change with time, and it is the interaction of these features that determines the long-term stability of a project.

Permeability, which is the capability of a medium to allow fluids to circulate, is anisotropic in most granitoid basement rocks as it is fault-bound (Snow, 1969). Here the term fault comprises different features related to brittle deformation; such as fractures, joints, faults, fault zones, cataclasites and non-cohesive fault gouges. Water that percolates along a fault, interacts with its surroundings, and by this interaction the water changes its composition (e.g. Iwatsuki and Yoshida, 1999; Nordstrom et al., 1989). Interactions can involve processes such as dissolution of primary minerals, precipitation of secondary minerals or exchange with rock matrix pore water (e.g. Gascoyne, 2004). All of these named processes alter the water composition. Thus careful sampling and analysis of groundwater potentially sheds light on processes responsible for the present groundwater chemistry. Any knowledge of the groundwater evolution might help when interpreting the processes effecting the interaction of groundwater at a potential underground facility.

Faults, which form water pathways, are three-dimensional sub planar to planar features. They are formed in a rock mass when the applied stresses exceeds the rocks elastic yield strength (Mandl, 2000). Larger faults are known to occur on a kilometre scale, and thus could potentially link the Earth's surface with an underground facility. Therefore, the study of faults in 3D on a mountainside scale (km-scale) is of paramount importance when performing a site characterization for a future larger underground project.

Increased available computer power in the last decade, meanwhile enables 3D structural modelling to be performed on a standard desktop computer. Therefore, structural models are widely used to constrain the fault pattern in 3D (e.g. Caumon et al., 2009). In 3D structural models, known information is often extrapolated to unknown space. This extrapolation is uncertain and the model often cannot be validated for deep-seated continuation.

1.2. Research question

The present thesis is part of a larger project (LASMO) of Nagra (Swiss Cooperative for Disposal of Radioactive Waste), RWM (Radioactive Waste Management, United Kingdom) and SURAO (Czech Radioactive Waste Repository Authority, Czech Republic). LASMO stands for Large-Scale Monitoring. The project is dedicated to the long-term monitoring of processes potentially influencing the safe disposal of radioactive waste in any underground construction that will one day act as a long-term storage facility. The present thesis adds to a site characterization by contribution of a 3D structural model, by baseline monitoring of the groundwater discharging within Grimsel Test Site (GTS), and by linking the structural 3D model with mapped water discharge points in a conceptual water flow path model.

1.3. Objectives and methods

The following objectives were set for this thesis: (i) baseline monitoring and characterization of the groundwater occurring around the GTS, (ii) constraining the 3D geometry of faults around the GTS on the decametre scale and on a kilometre scale, and (iii) exploring their role in water conduction.

In order to achieve the aforementioned objectives, water samples were taken during 2 years from different pre-existing boreholes in the GTS and compared with literature data. In the first year, four sampling campaigns were carried out, whereas in the second year only two samplings were performed. Sampled groundwater was subsequently analysed for chemical composition and stable water isotopic composition. During the last sampling campaign additional samples were taken for tritium measurements.

In parallel to groundwater sampling, the GTS and the surface above were mapped with a focus on fault geometry and kinematics. The resulting maps served as a base for the 3D model of the study site and its validation.

Finally, mapped water discharge points in the GTS were compared with the analysed groundwater and with mapped structures in order to unravel potential links.

1.4. Hydro-geological setting

The GTS is situated in the upper Haslital, located in the canton of Bern in the Central Swiss Alps (Fig. 1.1). Geologically, it is located within the Aar massif, which belongs to the external crystalline massifs of the Alps (Mercolli and Oberhänsli, 1988; von Raumer et al., 2009, 1993). The Aar massif represents the inverted former European continental margin (Pfiffner, 1993).

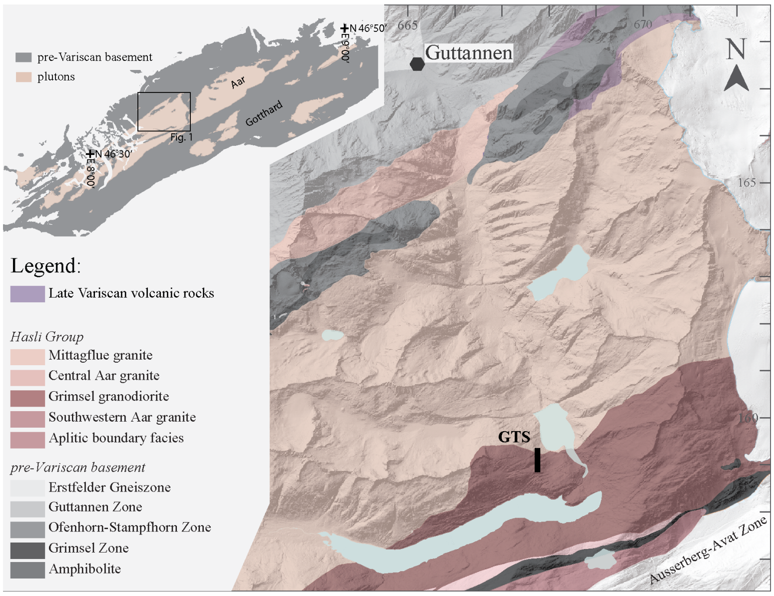

Figure 1.1. Geological map of the upper Haslital (modified after Berger et al., 2017a).

The bedrock of the upper Haslital can be subdivided into (i) pre-Variscan basement rocks, (ii) post- to Late Variscan intrusives, (iii) Late Variscan volcanics (Berger et al., 2017a). The pre-Variscan basement is also called "Altkristallin" (Abrecht, 1994; Labhart, 1977). It is composed of polymetamorphic gneisses. The post-to Late-Variscan intrusives (Hasli Group) form a calc-alkaline differentiation series (Berger et al., 2017a; Schaltegger, 1994).

In the surroundings of the GTS four different host rocks occur: (i) Grimsel granodiorite (GrGr), (ii) Central Aar granite (CAGr), (iii) aplitic dykes, and (iv) metabasic dykes (e.g. Keusen et al., 1989; Stalder, 1964). The GrGr, the CAGr and the aplitic dykes are part of a calc-alkaline differentiation series, where the GrGr is the most primitive member (Berger et al., 2017a; Keusen et al., 1989; Schaltegger, 1994). The origin of the metabasic dykes, formerly called "lamprophyres", is ambiguous as elaborated in chapter 2 (Oberhänsli, 1986).

Metamorphism, related to the Alpine orogeny, overprinted the aforementioned rocks with peak conditions around 450 ± 30 °C and 6 ± 1 kbar, which was reached around 22 - 20 Ma (Challandes et al., 2008; Rolland et al., 2009).

The solid-state deformation in the vicinity of the GTS has been described previously (e.g. Challandes et al., 2008; Choukroune and Gapais, 1983; Goncalves et al., 2012; Herwegh et al., 2017; Marquer, 1990; Marquer et al., 1985; Rolland et al., 2009; Steck, 1968; Wehrens et al., 2017, 2016). Single phase, and multistage kinematic models have been proposed. Generally, a southward increase in deformation intensity and metamorphic grade is inferred (e.g. Bambauer et al., 2009; Choukroune and Gapais, 1983; Niggli and Niggli, 1965; Rolland et al., 2009; Wehrens et al., 2017).

Ductile deformation is expressed by two dominant features: (i) a pervasive foliation and (ii) localized high strain zones, ductile shear zones (e.g. Rolland et al., 2009; Wehrens et al., 2017). Ductile structures form anisotropies that are often reactivated by subsequent retrograde brittle deformation resulting from cooling due to exhumation (e.g. Belgrano et al., 2016; Kralik et al., 1992; Wehrens et al., 2017, 2016). Typical brittle structures are: fractures, faults, fault zones, cataclasites, and fault breccias or gouges.

Glaciation and glacial retreat contributed to the latest landscape evolution of the area (e.g. Florineth and Schlüchter, 1998; Wirsig et al., 2016). In response to deglaciations, several generations of exfoliation joints formed (Ziegler et al., 2013).

Exfoliation joints are likely to influence the infiltration pattern of recent meteoric water as they form an interconnected network of fractures. Towards greater depth faults form the major water-conducting features, as they are characterized by higher porosity (ca. 10-30 vol%) than the rock matrix (open porosity: 0.8 - 1.5 vol%; Bossart and Mazurek, 1991). Diverse experiments run at the GTS measured transmissivity in test intervals with faults as well as rock matrix (e.g. Hoehn et al., 1990). Borehole test intervals containing faults typically have a transmissivity around 2×10^{-6} m^2/s, whereas borehole test intervals sampling the rock matrix are characterized by 9 order of magnitude smaller transmissivity values. This difference in porosity and transmissivity highlights the importance of faults for advective water flow.

1.5. Organisation of the thesis

The thesis consists of four main chapters, which are briefly introduced in the following.

Chapter 2 characterizes in detail the petrography and structural framework for both the Grimsel Test Site (GTS) as well as for the surface above. It is published in form of a Nagra Arbeitsbericht NAB 16-27.

> Schneeberger, R., Berger, A., Herwegh, M., Eugster, A., Kober, F., Spillmann, T., Blechschmidt, I., 2016. GTS Phase VI - LASMO: Geology and structures of the GTS and Grimsel region. Nagra Arbeitsbericht NAB 16-27, Wettingen, Switzerland.

Chapter 3 describes the groundwater sampled within the GTS and its evolution. Special focus was payed on the hydrochemistry (dissolved elements and stable isotopic water composition) and its link to the flow paths. It forms a paper in preparation.

> Schneeberger, R., Mäder, U.K., Waber, H.N., Berger, A., Kober, F., & Herwegh, M. (in preparation). Long-term chemical composition and evolution of groundwater in crystalline bedrock: A case study (Grimsel, Switzerland).

In chapter 4, we present a 3D structural model of the GTS and the surface, and discuss uncertainties related to the 3D structural modelling. The 3D structural model is based on the underground and the surface mapping, and describes the 3D geometry of faults. Chapter 4 is accepted for publication in Solid Earth:

> Schneeberger, R., De la Varga, M., Egli, D., Berger, A., Kober, F., Wellmann, F., and Herwegh, M. (2017). Methods and uncertainty-estimations of 3D structural modelling in crystalline rocks: A case study, Solid Earth Discussions, doi:10.5194/se-2017-47, in review.

In chapter 5, we link both the groundwater chemistry and the 3D fault pattern in order to develop a conceptual flow model of the groundwater flow around GTS. The chapter is submitted to Tectonophysics.

> Schneeberger, R., Egli, D., Lanyon, G.W., Mäder, U.K., Berger, A., Kober, F., & Herwegh, M. (in preparation). Structural permeability favourability in crystalline rocks: Implications for groundwater flow paths, a case study (Aar massif, Central Switzerland).

Conclusions and an outlook are presented in chapter 6.

Chapter 2

Nagra Arbeitsbericht - NAB 16-27

GTS Phase VI – LASMO: Geology and structures of the GTS and Grimsel region

Raphael Schneeberger[1], Alfons Berger[1], Marco Herwegh[1], Amadeo Eugster[1], Florian Kober[2], Thomas Spillmann[2], Ingo Blechschmidt[2]

[1]) University of Bern, Institute of Geological Sciences

2) Nagra, Hardstrasse 73, 5430 Wettingen

2.1. Introduction

2.1.1. The GTS and the LASMO project

The Grimsel Test Site (GTS) is an underground rock laboratory (www.grimsel.com) owned and operated by Nagra, the Swiss National Cooperative for the Disposal of Radioactive Waste, since 1984. It is located in the upper Hasli valley in Canton Bern, Switzerland (Fig. 2.1).

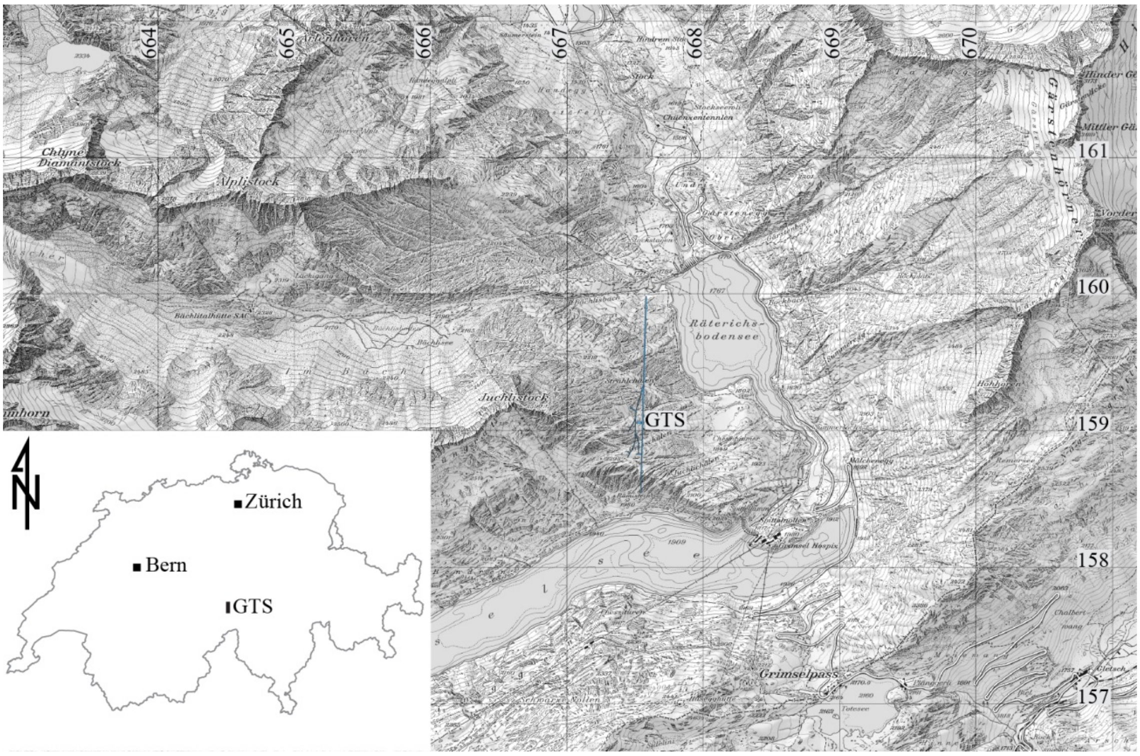

Figure 2.1. Geographic map of the Grimsel area (swisstopo).
The coordinates are given relative to the swiss coordinate system (CH1903 / LV 03).

Since the beginning, the GTS has been used for a wide range of experiments related to the deep geological disposal of radioactive waste. Overviews of the numerous experiments may be found in Blechschmidt et al. (2007), Kickmaier et al. (2005), McCombie et al. (1995) or Vomvoris et al. (2015, 2013).

This report is part of the project Large Scale Monitoring (LASMO) which is co-funded by RWM (Radioactive Waste Management, United Kingdom), SURAO (Czech Radioactive Waste Repository Authority, Czech Republic) and Nagra (Switzerland). The LASMO project is conducted in the framework of Phase VI of the GTS research programme, which runs from 2003 to 2018. LASMO started in 2013 and is scheduled until 2018. The overall goals of LASMO are to test monitoring systems, technologies or methods, and to study the associated data for the purpose of baseline versus incident discrimination during repository monitoring. In detail, LASMO intends (i) to establish and test a multi-parameter monitoring system for collecting data on groundwater pressures and chemistry, seismic signals, displacements, stress and deformation, (ii) to update existing or develop new 3D structural, hydrogeological, and / or

-chemical models, (iii) to investigate fluctuations in water pressure and chemistry as well as triggered or induced nano-seismic signals, (iv) to develop a stress model, monitor stress changes and mechanical strain on geological disturbances, and (v) to manage data flow into regular model updates and synthesize the results with a view to an integrated model (http://grimsel.com/gts-phase-vi/lasmo/lasmo-introduction).

The LASMO project depends, to a certain extent, on the thorough understanding of the geological setting in which its various experiments and observations are situated. The previously established understanding has been synthesized and enhanced with new thesis work by graduate students of the Institute of Geological Sciences at the University of Bern. The main author of this report is PhD candidate Raphael Schneeberger. Amadeo Eugster has contributed results from his master thesis. Instructors at the Institute and Nagra project partners have contributed to this report with general guidance and expertise.

2.1.2. Objectives and report outline

Keusen et al. (1989) were the first to present a geological overview of the GTS and the surface above (Juchlistock). Since then, several studies, e.g. Bossart & Mazurek (1991), Frick et al. (1992), Mäder & Ekberg (2006), Möri & Blechschmidt (2006), Möri et al. (2005), have enhanced the site-specific knowledge and general concepts of the structural geology in which the GTS evolved. Also, observations from new boreholes and galleries enlarged the information base. A borehole database compiles information from about 530 boreholes, with 279 boreholes being longer than 3 m. The available site-specific and regional geological models and the apparent simplicity of the geological context make the GTS an ideal place to test the 3D visualization of deformation patterns in crystalline bedrock. It is the report's aim to present updated versions of both the GTS map and the surface map as well as geological descriptions of the mapped features, as a base for 3D visualization studies. The new maps are attached to this report as Enclosures 1 to 5.

The report starts with an introduction to the regional geological context based on key literature and summarizes the site-specific knowledge at the time of reporting (Chapter 2.2). Then follow brief discussions of the analytical and mapping methods applied in the current study (Chapter 2.3). Chapters 2.4.1 and 2.4.2 are dedicated to petrographic and geochemical descriptions, respectively. The deformation structures observed within the crystalline bedrock are described and interpreted in a regional framework in Chapter 2.5. The first attempts of a 3D geometrical visualization are presented in Chapter 2.6. Recent water-conducting features are presented in Chapter 2.7. The report ends with a summary of the major findings (Chapter 2.8).

2.2. Geological setting

The GTS is situated within the Hasli valley in Canton Bern. Geologically speaking, the Hasli valley is part of the Aar massif, an external crystalline massif in the Central Swiss Alps. Regional geological understanding of the general Grimsel area has been gained in numerous studies (Baumberger, 2015; Choukroune and Gapais, 1983; Marquer et al., 1985; Michalski and Soom, 1990; Niggli and Niggli, 1965; Oberhänsli et al., 1988; Pfiffner, 2009; Schaltegger, 1994, 1990, 1989; Stalder, 1964; Steck, 1968; Wehrens, 2015).

The rock types and deformation structures in the Aar massif are described below on the basis of key literature (e.g. Abrecht, 1994, 1975; Keusen et al., 1989; Labhart, 1977; Oberhänsli, 1986; Schaltegger, 1990, 1989).

2.2.1. Petrography

Paleogeographically, the Aar massif belongs to the basement of the former European passive continental margin, which became tectonically inverted when the European plate collided with the Adriatic plate at the time of the Alpine orogeny (Mercolli and Oberhänsli, 1988). A general geological map and a cross section are presented in Fig. 2.2 based on Berger et al. (2017b) and Baumberger (2015), respectively.

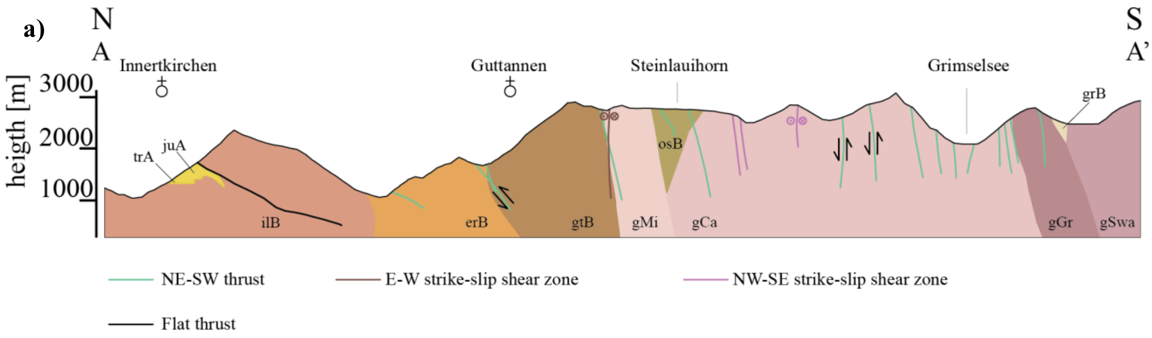

b)

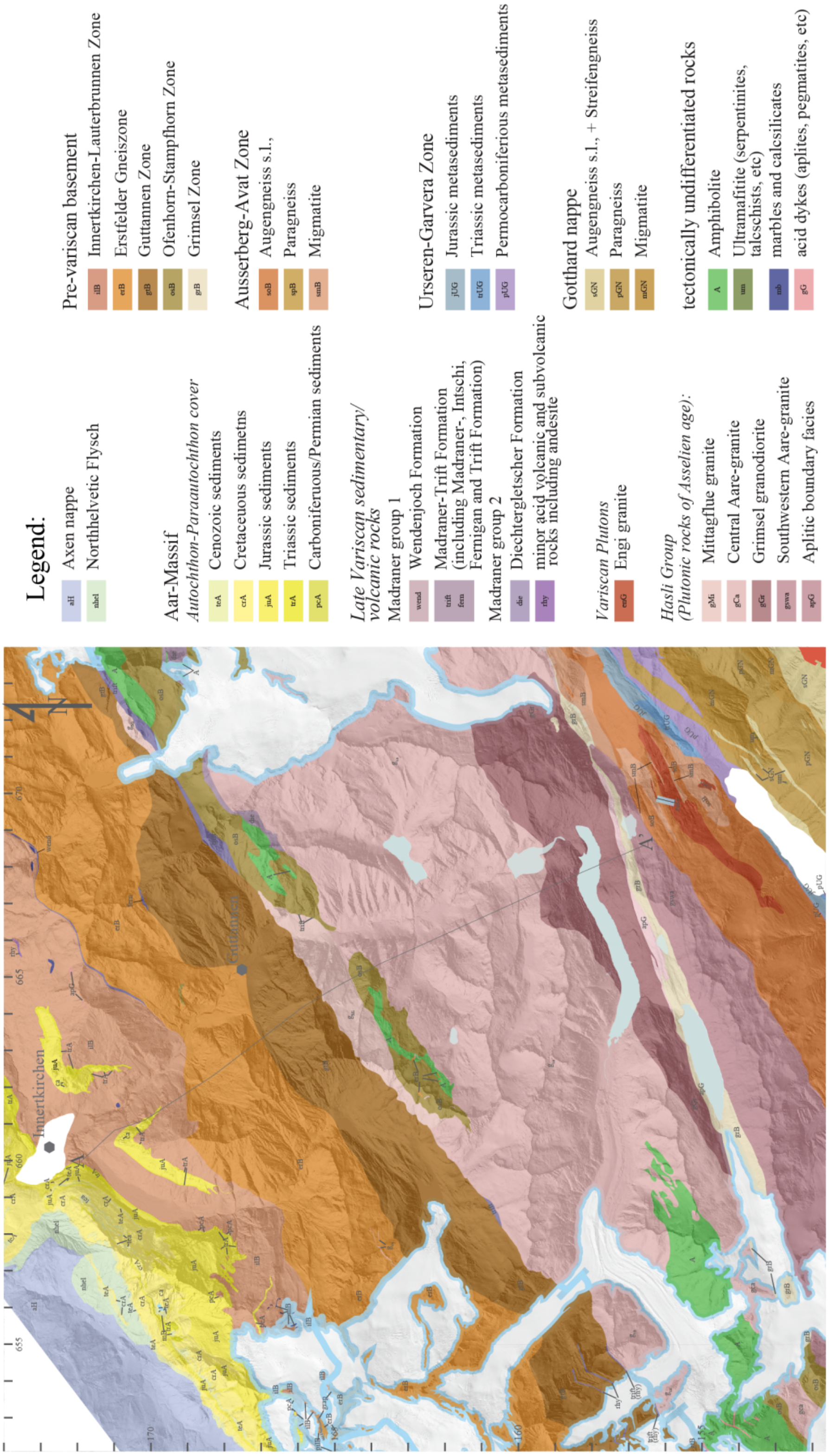

Figure 2.2. a) Cross-section along the western side of the Hasli valley. b) Geological regional map of the Hasli valley.

Map is modified after Berger et al. (2017). Cross-section is drawn using data by Baumberger (2015).

The Aar massif is composed of pre-Variscan rocks that are intruded by Late to post-Variscan plutonites (Fig. 2.2). Along the Hasli valley, the pre-Variscan basement is subdivided from north to south into Innertkirchen-Lauterbrunnen Zone, Erstfeld Zone, Ferden-Hüfi Zone (represented by the Guttannen Gneiss Complex) and Sustenhorn Zone (represented by the Ofenhorn-Stampfhorn Gneiss Complex) (Abrecht, 1994; Berger et al., 2017a; Labhart, 1977; Oberhänsli et al., 1988). The Innertkirchen-Lauterbrunnen Zone forms the northernmost tectonic unit of the Aar massif (Abrecht, 1994). The Innertkirchen-Lauterbrunnen Zone is composed of a series of polymetamorphic, partly migmatized metasediments, mainly sandstones and arkoses (Abrecht, 1994). The Erstfeld Zone is part of the so called "Altkristallin", which is an undifferentiated polymetamorphic pre-Variscan basement (Labhart, 1977) and has in parts typical migmatic appearance and is composed of metasediments. For further details the reader is referred to Abrecht (1994). The Guttannen Gneiss Complex is composed of biotite-plagioclase gneisses (Abrecht, 1994). The Ofenhorn-Stampfhorn Gneiss Complex outcrops south of the Mittagfluh, which is a prominent mountain flank on the eastern side of the Grimsel Pass road. The Ofenhorn-Stampfhorn Gneiss Complex is defined as a variable series of high-grade to anatectic biotite-plagioclase gneisses (Abrecht, 1994; Labhart, 1977). The migmatites juxtapose amphibolite lenses and dykes.

All aforementioned rocks form the Variscan basement into which the Late to post-Variscan plutonites intruded. The (post-)Variscan plutonites of the Haslital group can be subdivided into five different types: (i) Grimsel Granodiorite (GrGr), (ii) Southwestern Aar Granite, (iii) Central Aar Granite (CAGr), (iv) Mittagsfluh granite (MiGr) and (v) aplitic dykes and micrograrnites (Berger et al., 2017a; Stalder, 1964). All plutonites are of Early Permian Age (Schaltegger, 1994, 1990; Schaltegger and Corfu, 1992) with U/Pb isotope ages of 298±2 Ma for the CAGr and 299±2 Ma for the GrGr (Schaltegger, 1994). Combined they form a calc-alkaline differentiation series (Schaltegger, 1990), where the GrGr is the least differentiated member and the aplitic dykes mark the best differentiated part. As shown in the QAP diagram, the composition of the GrGr varies strongly from quartzmonzodioritic via granodioritic to granitic composition (Fig. 2.3).

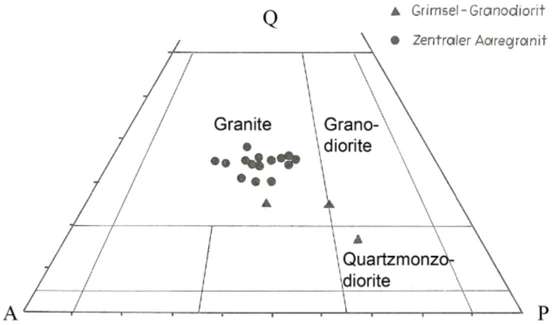

Figure 2.3. QAP-diagram for the plutonites in the GTS.

Modified after Labhart (1977).

The contact between GrGr and CAGr displays numerous “schlieren”, which is evidence for a coeval emplacement in a viscous magmatic state. The composition of the different rocks mainly varies in the modal composition, particularly in biotite as the major representative of mafic minerals in this plutonic series (Tab. 2.1). The GrGr contains ca. 11 vol % of biotite, whereas the CAGr is composed of ca. 5 vol % and the MiGr of ca. 3 vol % biotite (Keusen et al., 1989; Schaltegger, 1989). In addition to the variable amounts of biotite, also the amounts of quartz, K-feldspar and plagioclase vary slightly among the different members of the Haslital group (Keusen et al., 1989).

Table 2.1. Composition of various lithological units.

Indicated are the most important minerals in vol %. Note the distinct variation in sheet silicate content. Keusen et al. (1989), Schaltegger (1989), Wehrens (2015). MiGr: Mittagsfluh granite, GrGr: Grimsel Granodiorite, CAGr: Central Aar Granite, Qtz: quartz, K-fsp: K-feldspar, Plg: plagioclase, Bt: biotite, Wm: white mica, Chl: chlorite, Epi: epidote.

[vol %]	Qtz	K-fsp	Plg	Bt	Wm	Chl	Epi	Author	Method
MiGr	35	35	27	3				Schaltegger	Estimated
CAGr	35	27-31	30	4-8				Schaltegger	Estimated
	32	34.1	20.9	5.5	1.6	1	2.3	Keusen	Point counted
GrGr	30	25	30	15				Schaltegger	Estimated
	20.3	24.4	29.1	10.9	3.4	0.5	2	Keusen	Point counted
Aplitic dyke	40	32	26	2				Schaltegger	Estimated
	43.4	16	30.5	0.1		1.2		Keusen	Point counted
Metabasic dyke	8-15	0-6	0.5-20	66-85*				Wehrens	Point counted
		5-10	10-60	20-70	minor	minor	10-20	Keusen	Point counted

*** biotite vol % contains also minor wm and chl**

The available geochemical data preclude a purely crustal origin of the CAGr (Schaltegger, 1990), and thus for the whole differentiation series, require an enriched subcontinental mantle as source of the melt (Schaltegger and Corfu, 1992). The magmatic evolution is related to typical AFC (Assimilation and Fractional Crystallization) processes (Schaltegger, 1990). All members of the calc-alkaline suite lack evidence for Variscan deformation or metamorphism and are, therefore, considered post-tectonic intrusives (Schaltegger, 1990). The emplacement of the calc-alkaline suite occurred during (post)-Variscan extensional tectonics (Schaltegger, 1994).

The GrGr outcrops between Lake Rätrichsboden and Lake Oberaar (Fig. 2.2). At the surface it covers a 30 to 40 km^2 elongated area (Labhart, 1977). The transition between GrGr and CAGr is drawn as a straight line, but in the field the transition is gradual because of the aforementioned coeval magma emplacement and associated mingling phenomena. The CAGr outcrops north of the GrGr (Fig. 2.2). It is the largest magmatic body in the area and covers an area of 550 km^2 (Labhart, 1977). The MiGr represents a small-sized magmatic body of strongly elongate shape, situated to the north of the CAGr (Fig. 2.2). It is more leucocratic in composition than the CAGr. As a last member of the Haslital group, an aplitic dyke intruded the other members of the Haslital group.

The Haslital granitoids mentioned above are often cut by metabasic dykes, commonly referred to as lamprophyres (Keusen et al., 1989; Oberhänsli, 1986). However, the term lamprophyre refers to a rock with characteristic phenocrysts (Best, 2013; Wimmenauer, 1973). As no phenocrysts were observed under the optical microscope owing to metasomatism and Alpine overprint, we prefer the more general term metabasic dyke. The metabasic dykes are distributed throughout the entire Aar massif and adjacent units (Oberhänsli, 1986). They are mainly composed of biotite and plagioclase (Keusen et al., 1989; Oberhänsli, 1986) Wehrens (2015) reports from the Grimsel region a metabasic dyke cut by an aplitic dyke, which implies that the metabasic dyke is older than the aplitic dyke. The occurrence of the metabasic dykes in form of swarms provides evidence for intrusion during extensional tectonics (Esperanza and Holloway, 1987). According to Schaltegger (1990), the metabasic dykes are not part of the calc-alkaline differentiation suite of the major plutonites of the study area. Oberhänsli (1986) synthesizes the following points: (i) Trace element distribution indicates a high mantle component in the magma. (ii) MgO content suggests a small contribution of partial melting. (iii) Formation conditions of 20 to 30 kbar and at 950 to 1150°C were inferred from magmatic relicts of meta-lamprophyres in the Central Swiss Alps by Oberhänsli (1986). Those observations led to the following formation model (Oberhänsli, 1986): "*Variable percentages of melting of this earlier metasomatized mantle (metasomatized above the down going slab by fluids due to the dehydration of the slab) produce partial mantle melts of varying compositions. Mixing of the two melts and the possibility that potassium enriched calc-alkalic melts could stagnate at the bottom of the continental lithosphere provides a clue to the diversity of lamprophyres e.g. minettes, vogesites, spessartites and kersantites*."

2.2.2. Metamorphism and tectonic deformation

In this section, the deformation and the metamorphism of the rock mass are described based on literature data.

The metamorphism in the pre-Variscan basement units is polycyclic, whereas the granitoids of the Haslital group underwent Alpine metamorphism only. Alpine metamorphic overprint in the Hasli valley increases southwards (Challandes et al., 2008; Niggli and Niggli, 1965). The metamorphic peak underwent greenschist facies conditions and reached 450°C and 6.5 kbar (Challandes et al., 2008; Goncalves et al., 2012) at the Grimsel Pass around 20 Ma ago (Dempster, 1986; Rolland et al., 2009).

Some of the minerals in the studied area show mineral transformations both in deformed and undeformed parts. Therefore, these modifications evolved most likely prior to the Alpine deformation, in the Deuteric stage in Keusen et al. (1989). These transformations include the following alterations: (i) Plagioclase was replaced by albite, sericite and epidote by a process known as saussuritization. (ii) The K-feldspars show perthitic lamellae and sericite as alteration products. The exact age of the alterations is not known, but due to the homogeneous distribution in both Alpine deformed and undeformed parts it occurred most likely prior to the Alpine orogeny either during Mesozoic rifting or Permian times.

Deformation during the Alpine collision is expressed by both ductile and brittle deformation structures (Challandes et al., 2008; Choukroune and Gapais, 1983; Rolland et al., 2009; Steck, 1968; Wehrens, 2015). As for the Alpine metamorphism, southward increasing strain intensity is documented for the Hasli valley (Bambauer et al., 2009; Choukroune and Gapais, 1983; Wehrens, 2015). Background strain is manifested as steep southeast dipping pervasive foliations, whereas localized deformation is expressed by steep mainly southwards dipping shear zones. Both express ductile deformation. In terms of background strain (Wehrens, 2015) show a direct correlation with the biotite content of the granitoids, resulting in a more intense and pervasive foliation in the biotite-rich GrGr compared to the weakly foliated CAGr. Because of the pervasive foliation, the magmatic terms are not appropriate, requiring the pre-position 'meta' (e.g. meta-granite). However, for the sake of continuity and consensus with previous literature, the established terminology is kept in the current report.

The ductile shear zones differ from their host rock by symmetric or asymmetric strain gradients expressed by an increase in foliation intensity, a substantial grain size reduction (cm to tens of μm) and strong elongation of ductile deformed quartz aggregates. Ductile deformation started at a depth of approximately 20 km (6 kbar) and 450°C with a σ_1 of around 300 MPa (Diamond and Tarantola, 2015).

The observed deformation structures may be grouped into kinematic phases based on overprinting relationships and the overall stress field inferred for the different deformation structures. Since Steck (1968), several structural studies have been performed in the Grimsel area (Table 2.2, Choukroune and Gapais, 1983; Rolland et al., 2009; Wehrens, 2015). The structural description by Steck (1968) was not used because the approach is purely descriptive without considering large-scale dynamics. The work by Keusen et al. (1989) is updated, because their structural geological descriptions are purely for brittle deformation and solely based on measured structures' orientations. Rolland et al. (2009) proposed three stages of shear zone formation during the Alpine orogeny. Stage 1 deformation (approx. 20 - 22 Ma) yielded broad, biotite-rich, ductile shear zones. Stage 2 (13.8 - 12.2 Ma) produced relatively narrow, phengite-rich and predominantly ductile shear zones. Early biotite-rich cataclastic rocks are possibly also formed at this stage. During Stage 3 (< 10 Ma) brittle faults crosscutting the earlier structures were formed.

Most recently, Wehrens (2015) proposed two main kinematic phases, the Handeggphase and the Oberaarphase. They are differentiated based on three geometric orientations and relative movements observed along a deformation structure. The kinematic model by Wehrens (2015) is preferred over the model by Rolland et al. (2009) because the Oberaarphase of Wehrens (2015) is more differentiated than Stage 2 by Rolland et al. (2009).

The Alpine deformation evolution of the rock body surrounding the GTS is summarized in Fig. 2.4.

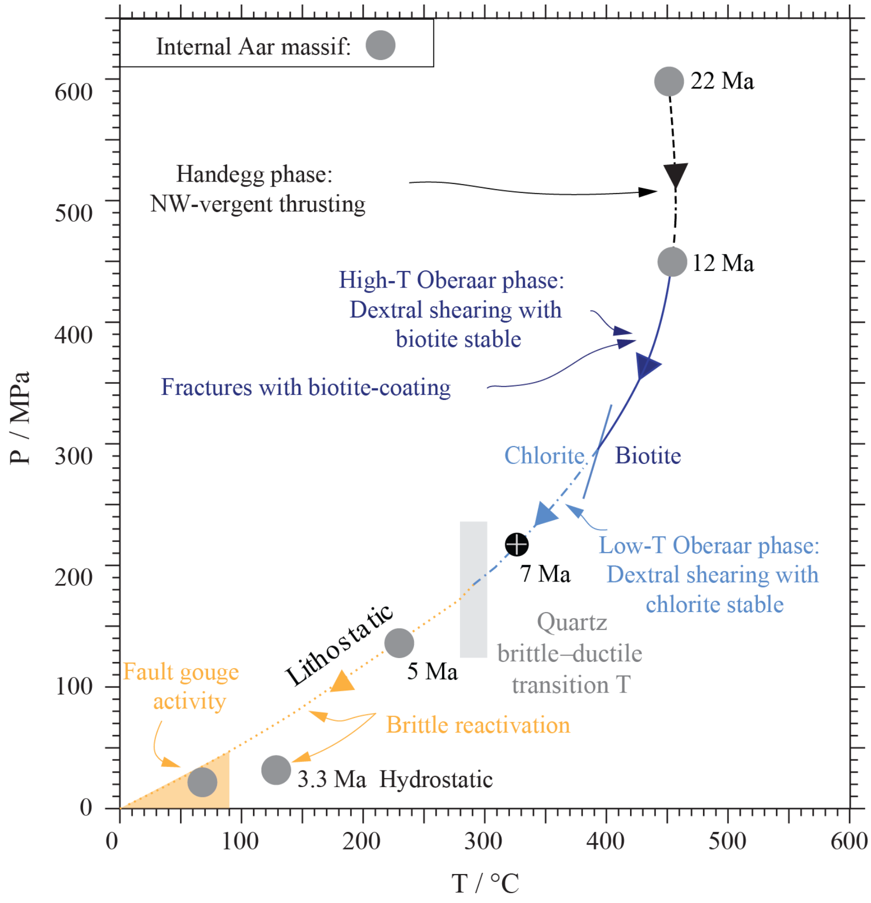

Figure 2.4. Alpine P-T-t evolution modified after Diamond & Tarantola (2015) and Wehrens (2015).

In the following, the two kinematic phases (Handegg and Oberaar) are described in greater detail.

Table 2.2. Comparison of deformation phase terminology from different studies in the Hasli valley.

Wehrens (2015) / this study	Rolland et al. (2009)	Steck (1968) / Keusen et al. (1989)
Handeggphase	Stage 1	S_1 / S_2
Oberaarphase a	Stage 2	S_3
Oberaarphase b	Stage 2	K_1 / K_2
Oberaarphase c	Stage 2	S_4 / K_4
Fault gouges	Stage 3	
Alpine clefts		ZK

Handeggphase

The Handeggphase is characterized by steep SE dipping shear zones (Figs. 2.5a and 2.6a) with nearly vertical lineation, i.e. vertical transport direction (Fig. 2.5a). The shear zones show crystallization of biotite and thus the deformation took place above 400°C (Spear 1995). The quartz is deformed in a ductile manner. The grain size is reduced via subgrain rotation recrystallization from cm-sized quartz in undeformed granite to µm-sized quartz in the mylonitic matrix. The quartz aggregates show a shape-preferred orientation (SPO) parallel to the foliation. Local static annealing overprinted the quartz microstructures after dynamic recrystallization (Peters, 2011). Annealing tends to erase the SPO. The K-feldspars porphyroclasts are broken, which is evidence for brittle behaviour. In the pressure shadow of the feldspar grains, micas and quartz are formed.

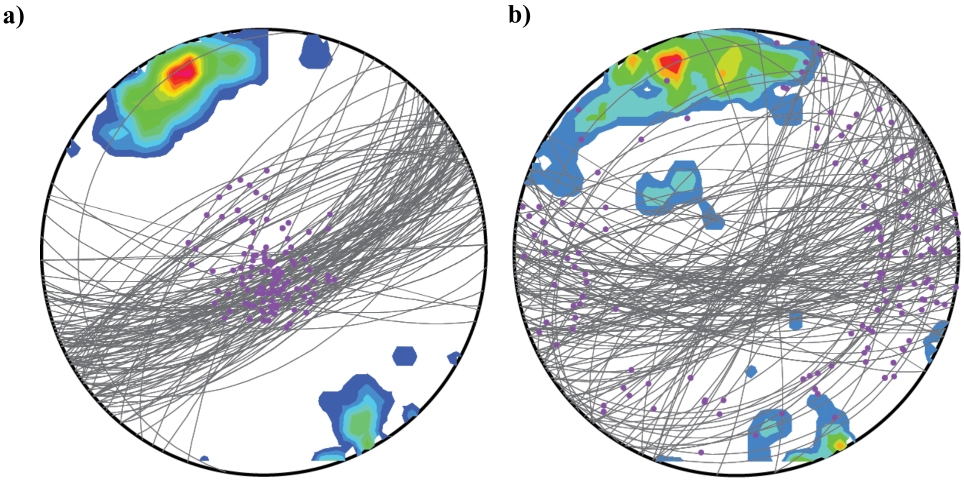

Figure 2.5. Stereoplots for kinematic phases, Handeggphase (a) and Oberaarphase (b).

Ductile shear zones are displayed as great circles and contoured for the poles with 1% density lines. According to the planes, the lineations are displayed as purple dots.

Oberaarphase

The Oberaarphase is characterized by strike-slip to oblique slip (Fig. 2.5b). This kinematic phase yields three different geometric orientations of ductile shear zones, E-W, NW-SE and NNE-SSW. The structures related to the Oberaarphase have orientations that evoke the orientation of brittle Riedel-shears (Tchalenko, 1970). This would point to a brittle precursor of the NW-SE and NNE-SSW oriented shear zones of the Oberaarphase. The main structures are E-W and dextral (Oberaarphase a). Numerous shear zones have an orientation that would correspond to the orientation of synthetic Riedel shears (Oberaarphase b). Only minor shear zones were found indicating a sinistral sense of shear (Oberaarphase c). They are orientated NNE-SSW and represent, in the brittle analogue, the antithetic Riedel shears. The orientations of the Oberaarphase are summarized in a block diagram in Fig. 2.6.

The transition from a vertical movement to a strike-slip movement might be due to over-thickening of the crust, by continuous material transport northwards and thus steepening of the shear zones and subsequent lateral material escape, as the steep S dipping shear zones hinder northward material transport (Schubert, 2013). In a first phase of the Oberaarphase biotite is stable in the shear zones; hence the temperature is still above 400°C. With ongoing uplift the temperature decreases and thus biotite is transformed to chlorite. Then, white mica shear zones are formed in absence of newly formed biotite. This is coherent with the Stage 2 shear zones defined by Rolland et al. (2009). During the entire deformation phase quartz shows a ductile behaviour and is first dynamically recrystallized via subgrain rotation and later statically via annealing at the shear zone rims and the host rocks, while bulging recrystallization occurs at the shear zone centres still active at that time (Peters, 2011). K-feldspar is deformed in a brittle manner and occurs as porphyroclasts in a fine-grained matrix.

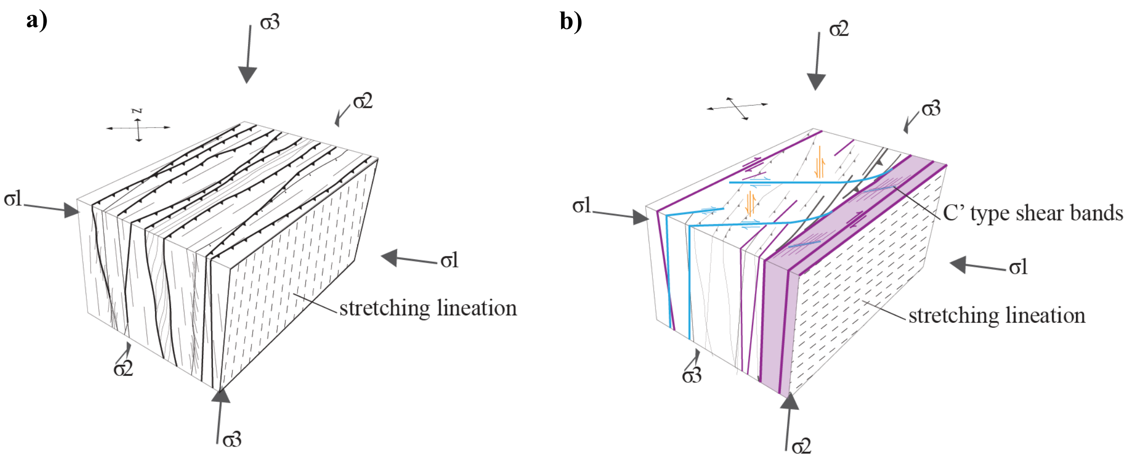

Figure 2.6. Block diagrams (modified after Wehrens 2015) showing the final orientation of the kinematic phases Handegg (a) and Oberaar (b).

Note that block diagram (b) is slightly rotated with respect to North for illustration purposes.

2.2.3. Exhumation and recent water inflow

Exhumation of the bedrock resulted in the formation of exfoliation joints (Ziegler et al., 2013). These exfoliation joints are formed parallel to the erosion surface. As the latter varies over time, different formation times of the exfoliation joints can be inferred. The exfoliation joints' density decreases rapidly with depth and they reach maximum depths of 200 m below surface (Ziegler et al., 2013).

Exhumation has been studied in the Aar massif since the early 1990s (Glotzbach et al., 2010; Michalski and Soom, 1990; Reinecker et al., 2008; Weisenberger et al., 2012). The local geothermal gradient is approx. 25°C / km (Vernon et al., 2008). Using this geothermal gradient, a constant exhumation rate of 0.5 mm / a for the last 14 Ma with an accelerated exhumation rate of 0.7 mm / a for the period between 10 to 7 Ma is reported (Glotzbach et al., 2010; Reinecker et al., 2008). Moreover, Reinecker et al. (2008) report an accelerated exhumation rate for the southern Aar massif since 3.5 Ma ago, which caused a northward tilting of the Aar massif. Furthermore, Weisenberger et al. (2012) describe higher long-term exhumation rates of 0.64 mm / a using metamorphic conditions peaking at 25 Ma. The early exhumation rates being higher due to homogeneous shortening and isostatic uplift of the Aar and Gotthard massifs.

Today's valley shape was strongly influenced in the late stage by glacial overprints. The glacial history of the Hasli valley was summarized by Wirsig et al. (2016).

The most recent deformation history, related to the latest exhumation, induced the formation of exfoliation joints and brittle structures. Those structures are prone to increase the rock permeability and thus affect the infiltration pattern of modern rain-water. Keusen et al. (1989) studied in detail the inflow of water into the GTS and found that water-inflow is restricted to brittle structures. Two different types of structures can be discriminated based on the inflow flux. Type 1 is characterized by low variation in the fluxes and high overburden, i.e., the climatic influence is negligible. Type 2 shows large variation during measurement campaigns (1983 - 1987) and low overburden, i.e., today's topography imposes strong climatic effects on the water fluxes. Moreover, Keusen et al. (1989) report that the GTS generally is dry. The only exception is the BK cavern, where the largest fluxes are observed (1.4 l / min). Water-conducting zones with climatic influence on the water flux are located S of the GTS, where the overburden is less.

2.3. Methods

With the emphasis on new structural concepts, GTS was remapped at a scale of 1:500. Mainly, a distinction between brittle and ductile deformation was introduced. Mapped features were consistently projected along dip and dip azimuth to the floor of the GTS. In this way, any feature has a specific geographic position, which is referenced with respect to the GTS tunnel meters in the different galleries (Fig. 2.8). During mapping the following characteristics were recorded: structural type, petrography, structure's thickness, dip azimuth, dip, lineation, and sense of movement. Feature' thickness is grouped in three classes, which are represented on the map by different width of stroke. Dip azimuth and dip angle are displayed on the maps in the appendix and were measured for the mapped features using a standard geological compass and the clinometer system of Apple ® IPhone 5. Where lineation was observable, it was measured with the clinometer system of Apple ® IPhone 5 and is shown as plunge azimuth / plunge.

Some of the mapped rock types were sampled for geochemical analyses to obtain locality-specific rock compositions. Rock-samples were collected in the GTS by drilling. The cores were crushed and milled using a tungstencarbid mill. Bulk rock aliquots for members of the Haslital group were analysed commercially at Acmelabs ®, Canada, whereas bulk rock samples for the metabasic dykes were analysed in Fribourg. Major elements (SiO_2, TiO_2, Al_2O_3, Fe_2O_3, MnO, MgO, CaO, Na_2O, K_2O, P_2O_5) were analysed by XRF technique and trace elements (Ba, Co, Cs, Ga; Hf, Nb, Rb, Sn, Sr, Ta, Th, U, Zr, Y, La, Ce, Pr, Nd, Sm, Eu, Gd, Tb, Dy, Ho, Er, Tm, Yb, Lu) by ICP-MS.

On two key samples chemical composition of minerals was analysed. Analyses were performed on a JEOL Superprobe JXA8600 at the University of Bern. Measuring conditions were 15kV and 10 – 20 nA. Synthetic and natural standards were used.

The petrography, ductile and brittle fabrics, and water inflows in the tunnel system represent the major features mapped according to a classification of rocks and structures defined below. The deformation structures can be subdivided into brittle fabrics and ductile fabrics resulting in characteristic tectonites (Fig. 2.7). This subdivision is made on a macroscopic scale and refers to the deformation processes responsible for the observed fabric. All different mapped tectonites with their deformation structures are graphically summarized in Fig. 2.7.

In the following, the structures as entitled in summary Fig. 2.7 are defined. Separation structures disrupt the host rock without altering it. Separation structures can either be open, indicating the existence of interconnected porosity (brittle faults) or closed by secondary mineral precipitation (veins or coatings). Brittle fault rocks are zones in which the host rock was disintegrated by brittle deformation resulting in cataclasites, ultracataclasites or even fault gouges.

Particularly in the latter, major grain size refinement by grinding happened with almost no neo-formation of clay (Bossart and Mazurek, 1991; Wehrens, 2015).

We consider background strain as the least observed strain within a specific rock type. Weakly schistous is defined as a discontinuous mica alignment whereas moderately schistous is represented by a continuous cleavage with >1 cm spacing. The observed strain is expressed by foliation. The more intense foliation in the case of the GrGr compared to the CAGr indicates a lower background strain in the latter (Wehrens, 2015). Localized deformation is used to express that any further ductile deformation is localized and not pervasive on a whole rock scale. Protomylonite and mylonite are defined according to Passchier & Trouw (2005). A protomylonite is a rock with 10 - 50 % fine-grained matrix, whereas a mylonite is defined as a rock with 50 - 90% fined grained matrix.

After mapping of all available galleries, the mapped structures and lithological contacts were interpolated between the galleries, using the measured orientation in the gallery, the specific regional trend of the observed feature and the available borehole information. Exposed parts were drawn solid on the maps, whereas the interpolated parts are given as dashed lines, enabling a clear distinction between mapped information and interpolated information with their high and reduced degrees of certainty. The interpolation had to fulfil following assumptions: (i) shear zones are planar regular features at the scale of GTS and (ii) their extent is larger than a few meters. These assumptions are justified for the GTS region as documented by different field studies performed recently in the upper Hasli valley (Baumberger, 2015; Schubert, 2013; Vouillomaz, 2009; Wehrens, 2015; Wicki, 2011).

Besides mapping inside the GTS, also the surface above GTS was mapped (Appendix 2.4). Lake Grimsel, the pass road, the end of Lake Räterichsboden and the Juchlistock defined the mapping perimeter (Fig. 2.1). Additionally to the field investigations conducted in this study, existing maps were compiled (Baumberger, 2015; Keusen et al., 1989; Vouillomaz, 2009; Wehrens, 2015; Wicki, 2011). In the resulting surface map, the structural resolution is less compared to the map of the GTS due to the variable outcrop conditions (e.g. vegetation, gravel filled gullies) and restricted accessibility, particularly in the case of steep mountainous terrain. The mapping at the surface focused on both ductile and brittle deformation features as well as on the location of metabasic dykes. Aforementioned limitations prevented a detailed petrographic mapping as performed in the GTS. Surface mapping was complemented by remote sensing data using aerial photographs and the SwissAlti3D (swisstopo) in ArcGIS 9.3. Mostly in order to connect different outcrop observation.

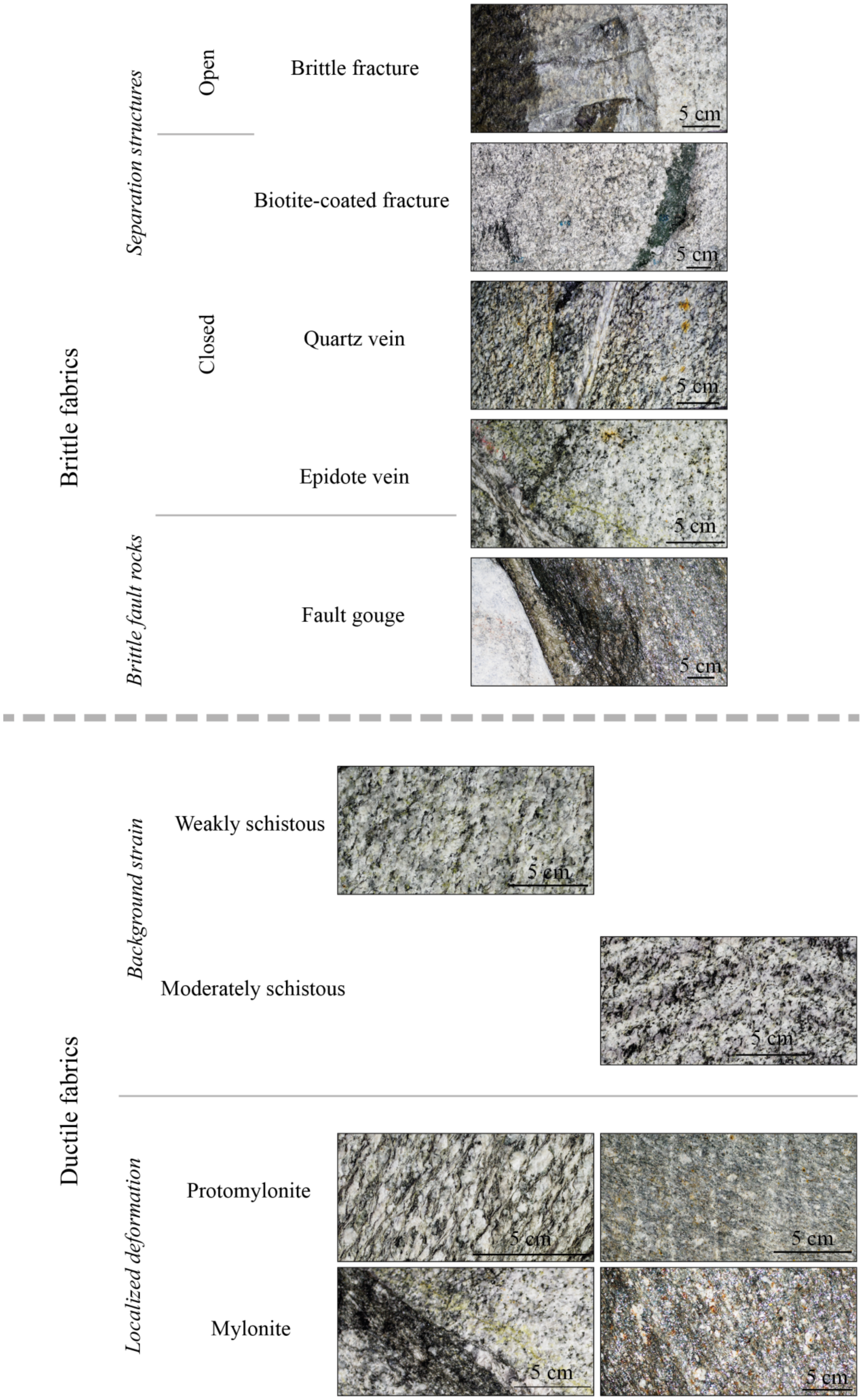

Figure 2.7. Summary of mapped deformation features.

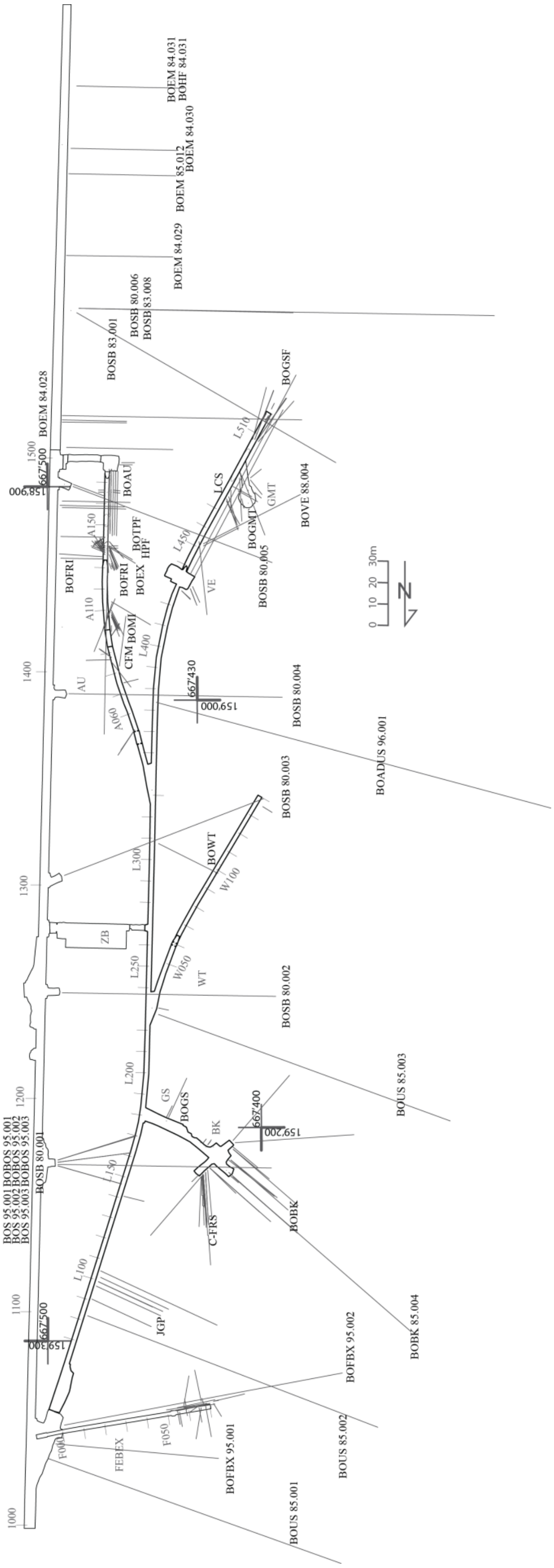

Figure 2.8. Plan of the GTS with the Swiss coordinate grid, the different drifts, some major boreholes, and the tunnel meters.

2.4. Description of the mapped units

2.4.1. Petrographic description

The different rock types occurring in the GTS and at the surface are described in detail in the following subchapters. The organisation follows the differentiation series presented in Chapter 2.2.

Mafic enclaves

As seen in Enclosure 1, mafic enclaves occur all throughout the GTS, but are visually more prominent within the CAGr. They are relicts of mafic dykes and are aligned on a plane. This gives an orientation to the mafic enclaves (Fig. 2.9).

The mafic enclaves show lentoid shapes and have very dark appearances (Fig. 2.9). Their dimensions range from a few cm to a few dm. They are predominantly composed of biotite, plagioclase and titanite (Stalder, 1964).

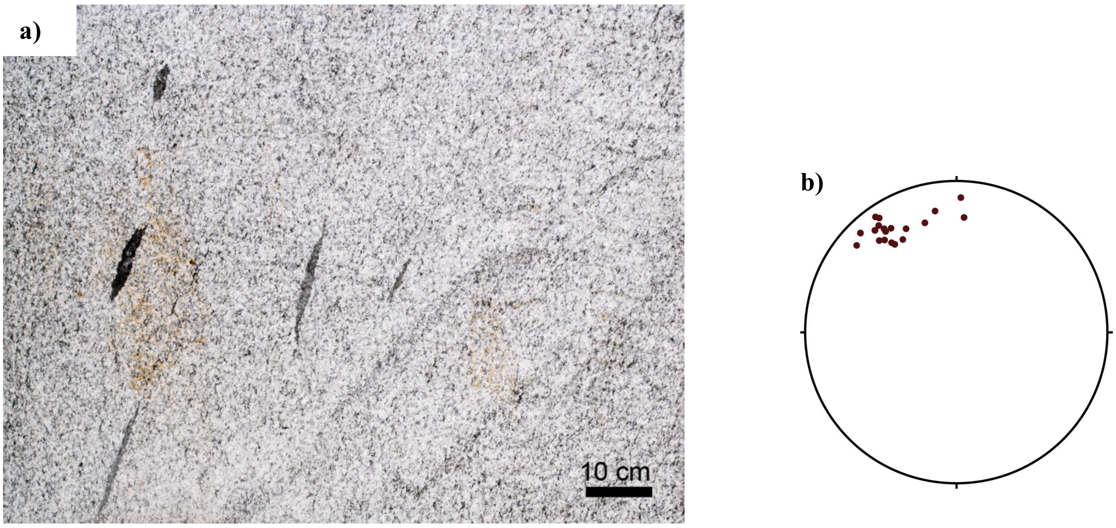

Figure 2.9. (a) Photograph showing mafic enclaves in the CAGr at L145 in the GTS. (b) Stereoplot with the measured orientations of the mafic enclaves from the entire GTS.

The poles of the planes are shown in the stereoplot (total number: 22). An equal area projection was used.

Based on visual estimation, the sampled mafic enclave (sampled at GTS L153, Fig. 2.8) is mainly composed of feldspars (25 vol %), biotite (20 vol %), quartz (20 vol %), white mica (20 vol %) and epidote (15 vol %). The feldspar grains are large (< 0.9 mm), occur as relicts and are pervasively transformed to epidote (< 40 μm) and sericite (Fig. 2.10). Some of the K-feldspar grains show perthitic lamellae. Neither epidote nor white mica was observed outside relict feldspar grains. Biotite grains are large (< 0.75 mm) and aligned, forming a weak foliation. Quartz is arranged in aggregates and shows equigranular shapes, which is probably due to annealing (Fig. 2.10).

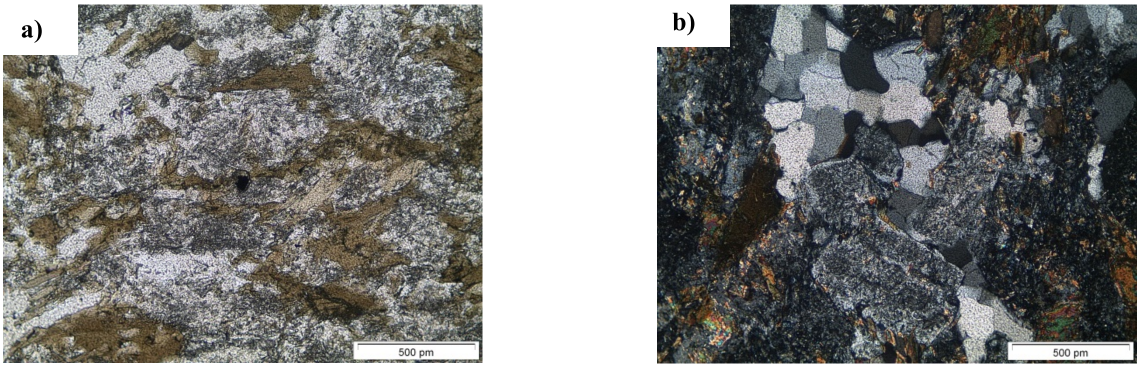

Figure 2.10. Thin section images taken under cross-polarized light. Image (a) shows a relicit feldspar grain surrounded by biotite. The feldspar grain is transformed to sericite and epidote. Image (b) shows a dynamically recrystallized quartz aggregate with annealed equigranular grain boundaries.

Melanocratic meta-granitoid – Grimsel Granodiorite (GrGr)

As mentioned in Chapter 2.1, the magmatic term granodiorite is not perfectly appropriate as the GrGr shows a pervasive foliation. The term melanocratic expresses the fact that the GrGr is the visually darkest meta-granitoid observed within the GTS because of its high biotite content 10 - 15 vol % (Keusen et al., 1989; Schaltegger, 1989).

It is a dark, moderately to strongly foliated meta-granite (Fig. 2.11) with Augengneis-type appearance in some rare cases. It is composed of quartz, K-feldspar, plagioclase, biotite, chlorite, white mica, epidote, titanite and some accessories such as apatite, zircon, pyrite, ilmenite and calcite (Keusen et al., 1989, see also Tab. 2.1).

Figure 2.11. Picture from the GTS showing the typical appearance of Grimsel Granodiorite. Photograph taken at L510.

Quartz occurs as magmatic relict or as ductile deformed dynamically recrystallized grains of small size (Fig. 2.12). The magmatic relicts are up to 2 mm large and xenomorph, whereas the dynamically recrystallized quartz grains are on average 0.18 mm in size (Wehrens, 2015). Commonly, they form aggregates (Fig. 2.12). The shape of the recrystallized quartz grains is lobate to equigranular. Next to quartz, the rock is mainly composed of K-feldspar and albite. They occur in magmatic shapes and are in the range of 0.5 - 3.25 mm (Wehrens, 2015). The K-feldspars show karlsbader twinning and strong sericitization (Fig. 2.13). The magmatic plagioclases are idiomorphic and show evidence for saussuritization (Stalder, 1964). Biotite is the major mafic mineral in the GrGr. It is up to 0.25 mm large (long axis) and occurs preferentially along planes defining a foliation (Fig. 2.12), developed during solid-state deformation. Along with biotite, also white micas are aligned but slightly smaller (< 0.2 mm, long axis) than the biotite grains. In addition, epidote minerals occur both in veins crosscutting the rock (Fig. 2.14) and as single crystals within the granitic matrix. In the veins, their average grain size is between 0.2 and 0.4 mm, whereas the single crystals are up to 0.75 mm in size. Chlorite occurs close to biotite. In some locations, biotite is transformed to chlorite. The alignment of biotite and white mica grains defines a pervasive foliation. A shape preferred orientation (SPO) of the quartz grains also develops a foliation with similar orientation.

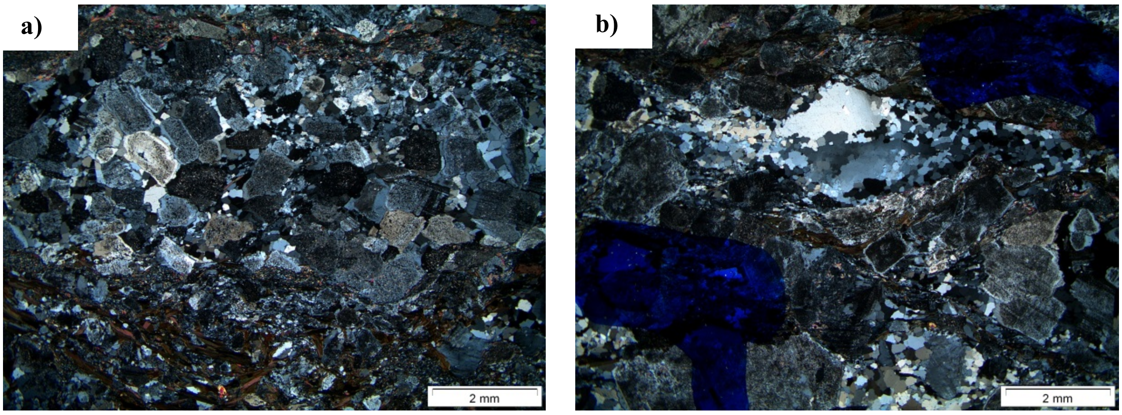

Figure 2.12. Thin sections (P6, Fig. 2.24) under crossed nicols of GrGr. Image (a) shows the typical texture of the GrGr. Image (b) shows magmatic quartz with recrystallized quartz around it.

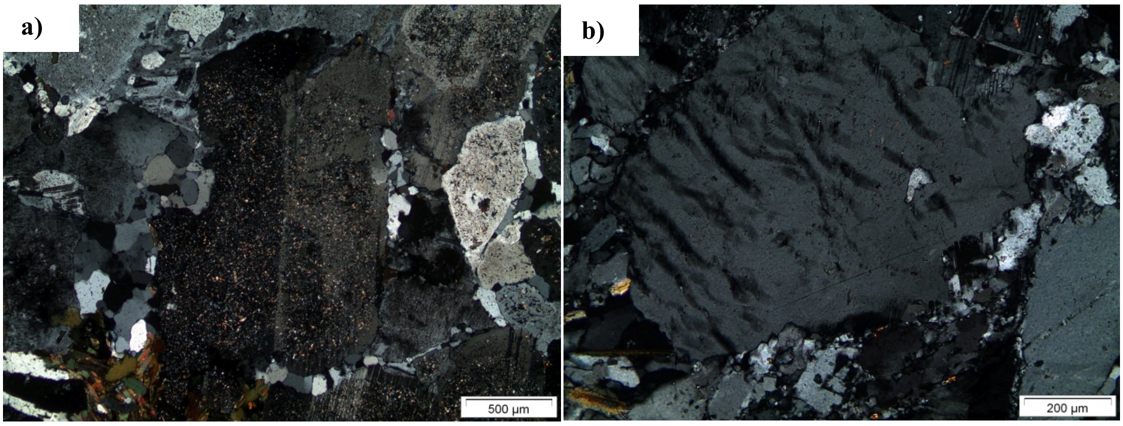

Figure 2.13. Picture under crossed nicols of a GrGr thin section (P6). Image (a) shows a sericitied K-feldspars twin. Image (b) shows perthitic lamellae in a K-feldspar.

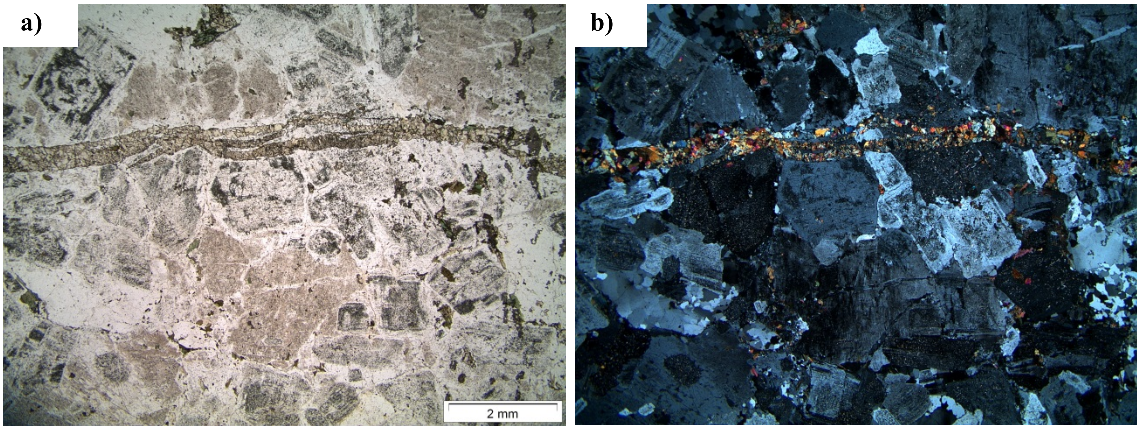

Figure 2.14. Epidote vein in a GrGr thin section (P6) under simple polarized light (a) and under crossed nicols (b).

Mesocratic meta-granite

While mapping, an intermediate type between the GrGr and the CAGr was defined. As the mapping differentiation criterion was the visible biotite content, i.e. the darkness versus brightness of the host rock, a biotite content of ca. 8 vol % was used to define the intermediate type (Fig. 2.15, Enclosures 1 to 3). It is composed of quartz, K-feldspar, albite, biotite, chlorite, white mica, epidote, and titanite.

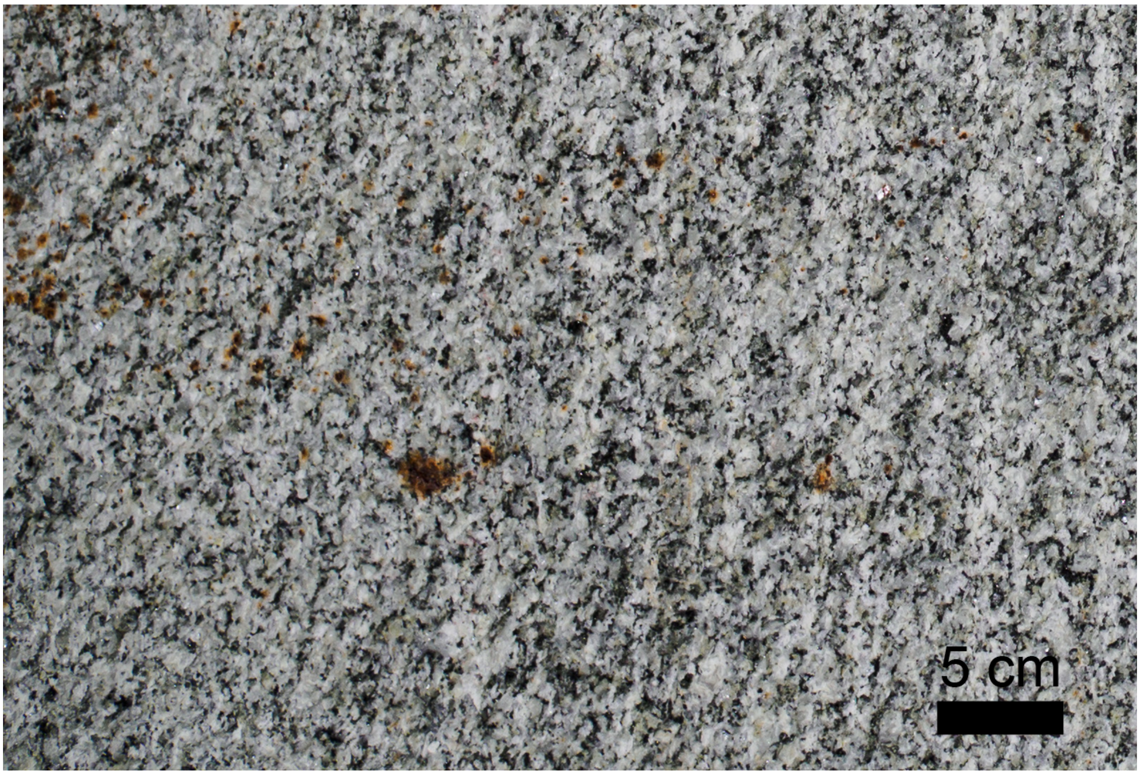

Figure 2.15. Mesocratic meta-granite from the GTS.

Photograph taken at L153.

Leucocratic meta-granite – Central Aar Granite (CAGr)

In domains affected only weakly by Alpine deformation (e.g. L200 - L290), the CAGr shows a massy to slightly parallel-bedded fabric and uniform to slightly porphyritic texture. It appears as bright rock mass with few dark inclusions. The mineralogical composition is similar to the one of the GrGr, but the relative amounts differ (Tab. 2.1; Fig. 2.16). The CAGr is composed of quartz, feldspars, biotite, chlorite, white mica, epidote, titanite and some accessories such as apatite, zircon, pyrite, garnet and calcite (Keusen et al., 1989).

Feldspars are bright and sometimes slightly greenish. Quartz is translucent (Labhart, 1977). Biotite represents the major mafic phase (Schaltegger, 1990).

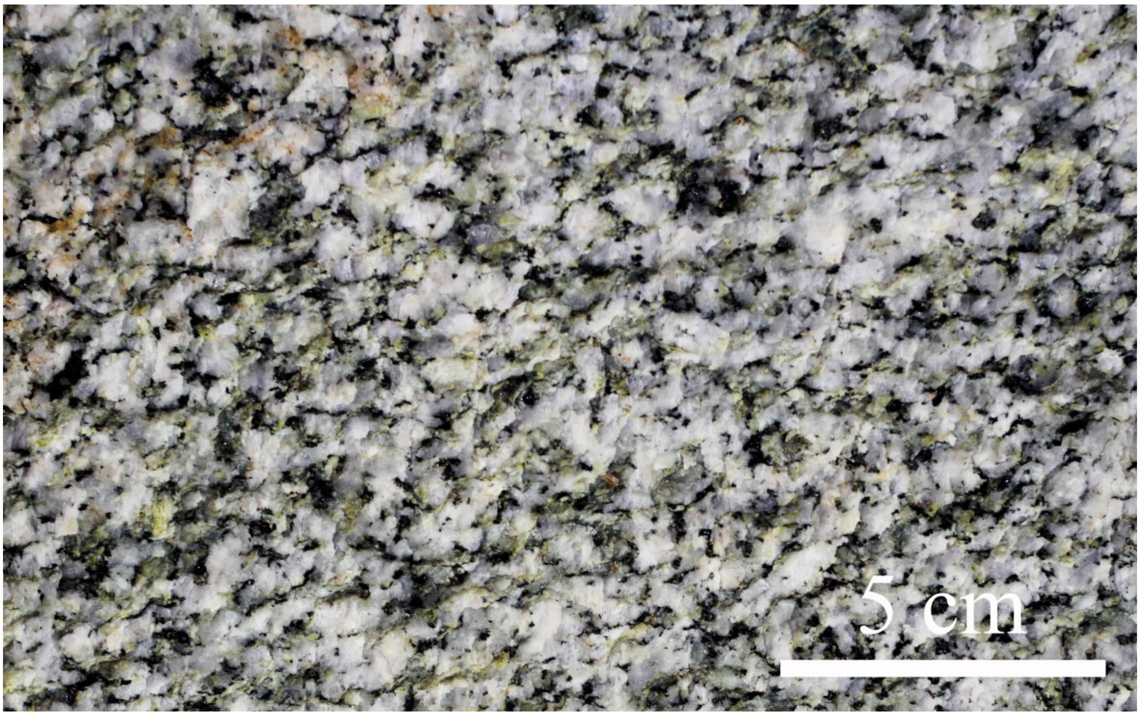

Figure 2.16. Leucocratic meta-granite from GTS (CAGr).
Photograph taken at L120.

Under the microscope, the CAGr is composed of approximately 30 vol % quartz (Tab. 2.1), which occurs either as magmatic relict or as deformed smaller grains (Fig. 2.17). The magmatic relicts are up to 2 mm in size. The deformed quartz grains normally are lobate to equigranular, form aggregates (Fig. 2.17) and are smaller on average (0.17 mm) due to dynamic recrystallization (Wehrens, 2015). Smaller quartz grains within larger aggregates are evidence for subgrain rotation, as a dynamic recrystallization process, whereas the equigranular shape indicates static recrystallization as annealing.

K-feldspar and plagioclase occur in magmatic idiomorphic shapes and are up to 3 mm in size. K-feldspars show alteration towards sericite (Fig. 2.17) and plagioclases are saussuritized. Biotite grains define a foliation and are up to 0.5 mm in size (Fig. 2.17). Besides biotite, white mica grains are also aligned, thereby defining a foliation. They are up to 2 mm long (Fig. 2.18).

Chlorite occurs in the vicinity of biotite, but not restricted to the biotite rich bands. It is also found between feldspar grains. In some locations grains of chlorite replace biotite. Chlorite is up to 2 mm long. Predominantly, epidote is found in the bands enriched in sheet silicate. In those bands epidote has a size of 100 µm.

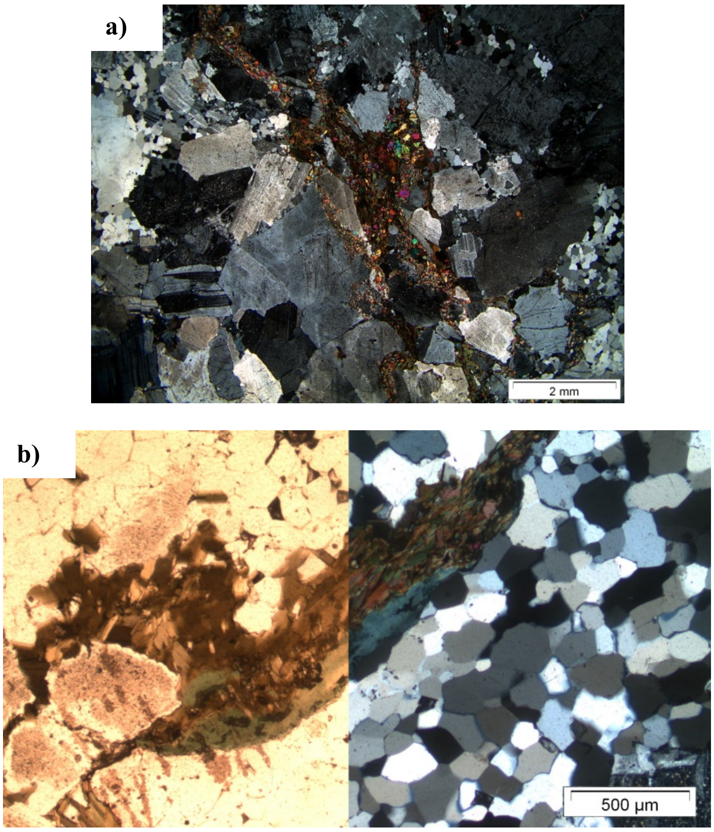

Figure 2.17. (a) Thin section (Gr0) photograph showing magmatic feldspar (karlsbader twin) and quartz aggregates with equigranular to lobate grain boundaries. Biotite and white mica occur along planes with epidote. (b) Chlorite bordering mica band in annealed quartz aggregate.

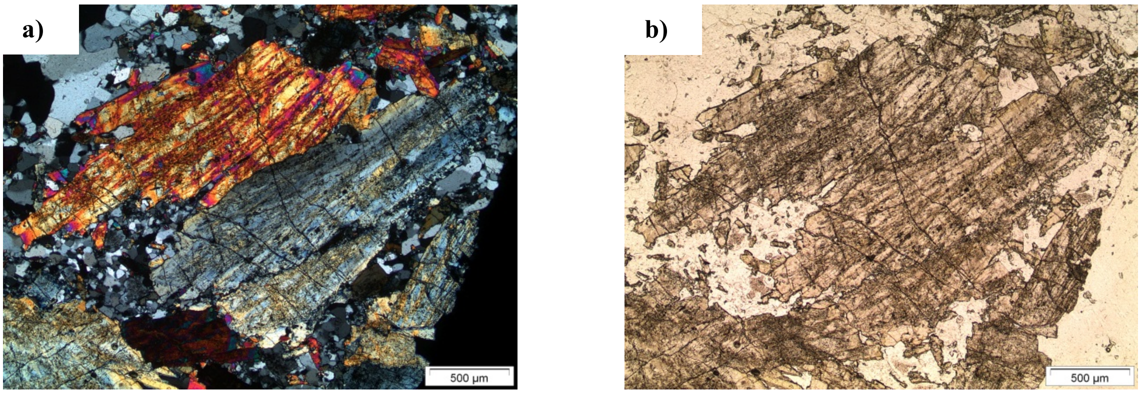

Figure 2.18. White mica in CAGr sample (Gr0) under crossed nicols (a) and single polarized light (b).

Mineral chemistry of the main granitoids in the Haslital group

Despite the difference in modal abundance of the different minerals between the members of the Haslital group, their mineral chemistry does not change significantly (Tabs. 2.3 and 2.4). We analysed two key examples, one for the GrGr (P6, Fig. 2.24) and one for the CAGr (sample KAW2214 from Schaltegger, 1989). The magmatic shaped feldspars are K-feldspar (97 % K-feldspar) and albite (> 93 % albite; Tab. 2.3) indicating that the samples are on the lower side of their persterite gap. However, all the feldspars show mineral alteration products as described before and primary (magmatic) compositions are not available anymore. The metamorphic alteration minerals show a larger spread in compositions, which also is the case inside each single sample. This variation is mainly caused by the local equilibrium volumes for these newly formed minerals like metamorphic epidote and white mica. The biotite is less variable and has X_{Mg} of ~0.6 and a relatively high F content. The measured Cl content is close to detection limit and should not be considered.

Table 2.3. Microprobe analyses of some minerals for GrGr (P6) and CAGr (KAW2214).

Mineral	**Units**	**Feldspar**	**Feldspar**	**Feldspar**	**Feldspar**	**Epidote**	**Epidote**
Probe		P6	KAW2214	P6	KAW2214	P6	KAW2214
SiO_2	wt-%	67.89	67.18	63.93	64.92	39.27	39.67
TiO_2	wt-%	0.01		0.0		0.11	0.07
Al_2O_3	wt-%	20.10	19.9	18.75	18.37	26.16	32.49
FeO	wt-%	0.06	0.13	0.10	0.06	9.10	1.47
MnO	wt-%				0.02	0.28	0.05
MgO	wt-%	0.04			0.03		
CaO	wt-%	0.62	1.27		0.02	23.67	24.62
Na_2O	wt-%	10.76	10.46	0.69	0.35	0.10	0.01
K_2O	wt-%	0.19	0.08	16.19	17.33	0.11	
Cl	wt-%				0.01		
F	wt-%		0.04		0.28		
Sum	%	99.69	99.07	100.49	101.39	98.80	98.38

Table 2.4. Microprobe analyses of sheet silicates for GrGr (P6) and CAGr (KAW2214).

Mineral	**Units**	**White mica**	**White mica**	**Biotite**	**Biotite**	**Chlorite**
Probe		P6	KAW2214	P6	KAW2214	P6
SiO_2	wt-%	50.53	47.17	35.99	37.22	25.91
TiO_2	wt-%	0.11	0.04	1.68	1.67	0.01
Al_2O_3	wt-%	28.58	33.37	16.89	17.60	20.50
FeO	wt-%	3.74	2.88	23.92	21.84	34.06
MnO	wt-%	0.04		0.94	1.68	1.52
MgO	wt-%	1.76	0.94	6.86	7.98	8.37
CaO	wt-%	0.02	0.08			0.07
Na_2O	wt-%	1.37	0.64	0.11	0.08	0.07
K_2O	wt-%	10.37	10.97	10.22	10.17	0.03
Cl	wt-%			0.02	0.04	
F	wt-%			0.56	0.27	
Sum	%	96.52	96.09	96.61	98.24	90.56

Aplitic dykes

Aplitic dykes or patches are found in the GTS within the Febex drift, at L075, L104, L291, L311, L363, AU107, AU120, and AU160 (Fig. 2.8). Thus they are spatially distributed equally over the CAGr dominated northern part and the GrGr dominated southern part. Aplitic dykes form the most differentiated part of the Haslital magmatic suite. Aplitic dykes are composed of quartz, plagioclase, K-feldspar and very little biotite (Tab. 2.1). Even though the magma forming the aplitic dyke is a differentiation product of the Haslital magmatic suite, it intrudes the magmatic suite with sharp contacts and thus the intruded rock behaved at the time of dyke injection already in a brittle manner. As the regional extent of the aplitic dykes is limited, the aplitic dykes were not further investigated within the current study. For example, an observed dyke at L363 shows no continuation in the AU drift.

Metabasic dykes

The metabasic dykes are manifold in the GTS (Fig. 2.19). They occur as groups and form three swarms in the GTS, L085 – L135, L303 – L371 and L461 – L500 (Fig. 2.8, Enclosure 1). The southernmost swarm is strongly deformed and dissected by Alpine deformation structures and therefore lacks lateral extent. At the surface only one swarm of dykes was observed (Enclosure 4). This implies that dykes end between the GTS and the surface, or that all swarms combine to a single swarm, or that dykes are not appropriately exposed at the surface.

The dykes form macroscopically homogeneous dark greenish dykes with a sharp contact to the granites (Fig. 2.19). Occasionally, magmatic relicts such as apophyses or hooks occur (Fig. 2.19). The dykes' thickness varies from cm to several m with no systematic occurrences.

Figure 2.19. Metabasic dykes at AU051 in the GTS.

The metabasic dykes are predominantly composed of plagioclase and biotite (Keusen et al., 1989), with biotite being the major rock-forming mineral in the two investigated samples. The investigated thin sections were obtained from dykes at AU045 and at L055. The AU045 sample shows up to ~ 70 % biotite (Fig. 2.20). Biotite grains are up to 40 μm long and strongly aligned. Some biotite grains are larger (> 0.4 mm) and interpreted as relicts of a former texture. Besides biotite, quartz, feldspars and epidote form the matrix. Quartz is fine-grained (few μm) and scarce. Feldspars occur as relicts and are transformed to sericite and epidote (Fig. 2.21). In the pressure shadow of the feldspar relicts grew epidote, white mica and biotite. Three different forms of epidote were observed. Epidote grains are found in the matrix, in veins and in the aforementioned transformation of feldspar (Fig. 2.21). The matrix epidote is larger than the matrix biotite grains and overgrows the strongly foliated texture. Therefore, epidote growth is younger than the foliation's formation. Very little white mica was observed aside from the white mica in the sericitization of the feldspars.

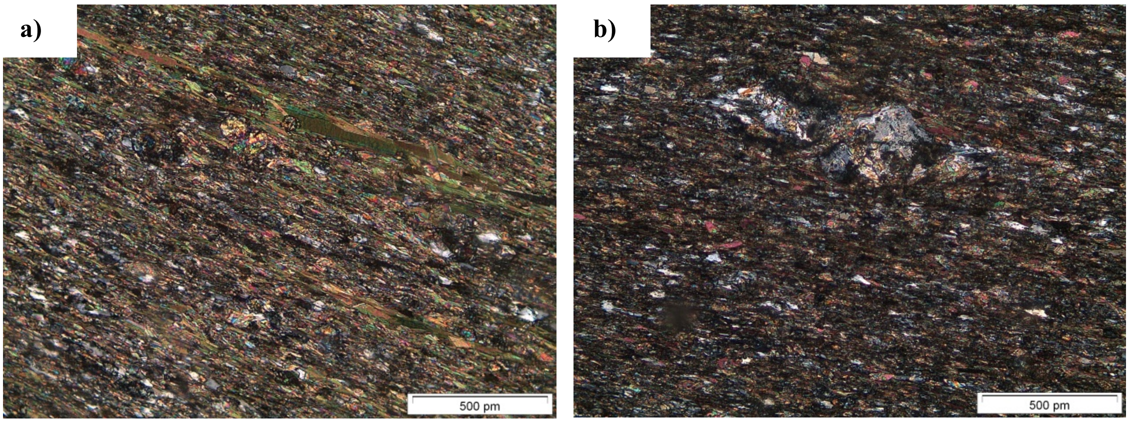

Figure 2.20. Image (a) indicates different sizes of biotite in thin section from dyke at AU045. Image (b) shows a feldpar relict with foliation bending around and crystal growth in the pressure shadow.

The dyke from L055 shows several calcite and epidote veins. The calcite veins are related to a hydrothermal overprint. Pyrite overgrows the foliation (Fig. 2.22) and thus is a later precipitation product. The foliation is expressed by the alignment of grains within the fine-grained matrix. The matrix is composed amongst others of biotite, quartz, white mica and feldspars.

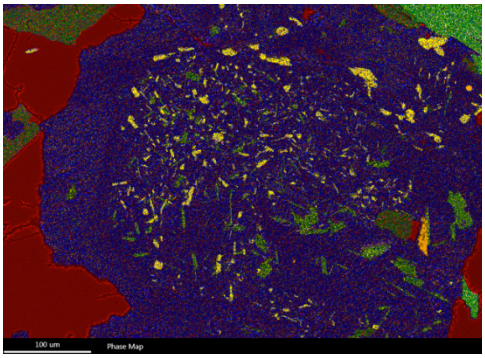

Figure 2.21. Phase map of a feldspar grain showing sericitization.

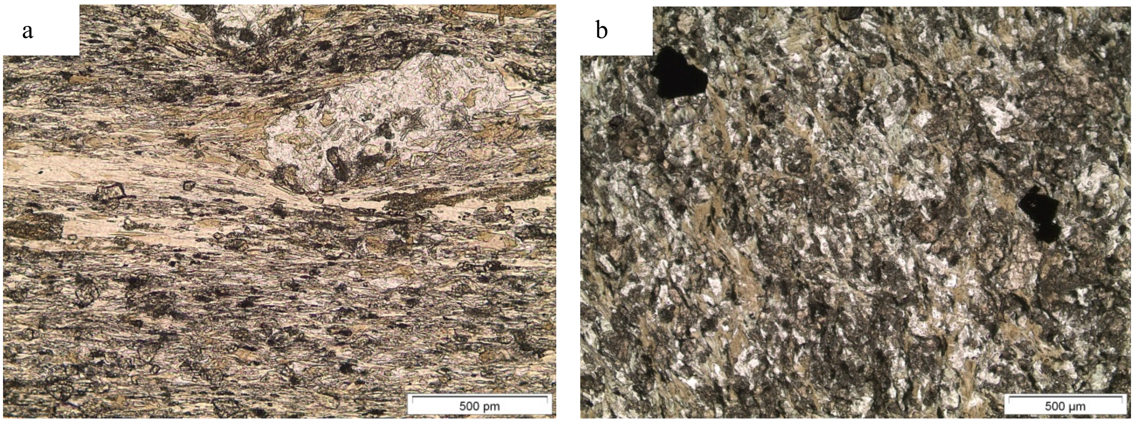

Figure 2.22. Image (a) indicates different kinds of epidote in thin section of dyke AU045. Image (b) shows overgrowing pyrite in thin section of dyke at L055.

Quartz veins

Quartz veins are ubiquitous in the GTS and at the surface. The mapping of quartz veins focussed on the GTS only. Quartz veins are indicators for fluid circulation and brittle fracturing within the Haslital group. In general, quartz veins occur throughout the entire tunnel system of the GTS (Enclosure 3). Their orientation varies strongly. Nevertheless, the occurrence of veins is spatially heterogeneously distributed, and frequently related to mechanical anisotropies like ductile shear zones and metabasic dykes.

Three main types of quartz veins were observed within the GTS: (i) open-quartz-cleft type with inherent, cm-sized quartz crystals and chlorite precipitation. (ii) Undeformed or only brittely fractured veins represent the smallest group and are randomly distributed in the tunnel system. (iii) Ductile overprinted veins form the largest group and are frequently restricted to ductile shear zones and metabasic dykes. Their orientation is similar to the orientation of the ductile shear zones. They have a high width-to-aperture ratio and often appear as elongated lenses. Type (ii) could also represent the start or end of an open cleft, where the opening is either within the rock mass or removed by drilling the tunnels.

Epidote veins

As mentioned in the microscopic description of the metabasic dyke, epidote prevails in different manners (Fig. 2.22). It outcrops not only in the metabasic dykes, but also in the Haslital group as mineral in the matrix. Moreover, it also occurs as epidote veins. For example at L153, where an epidote vein borders a quartz vein, which itself formed within a ductile shear zone (Fig. 2.23). Epidote is a hydrothermal mineral, implying circulation of hydrothermal fluids after brittle deformation within the CAGr. As the aforementioned quartz vein is overprinted by ductile deformation, the epidote vein is older than the ductile deformation of the quartz vein. The exact age of the epidote vein is unknown. Epidote veins offset by a ductile shear zone occur at L153 and provide evidence that epidote veining is older than the Alpine ductile deformation.

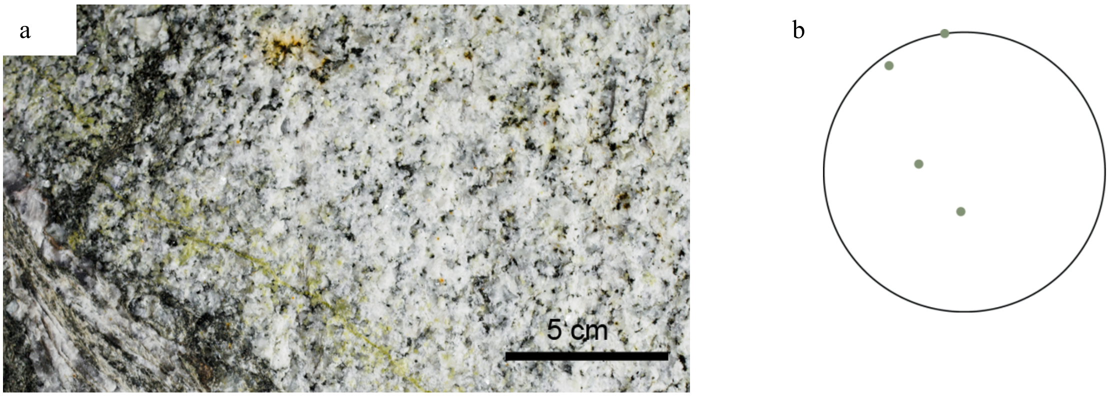

Figure 2.23. (a) The photograph taken at the same location as is mapped in Fig. 2.24 shows a quartz vein at L153 bordered by an epidote vein. (b) Stereoplot with measured orientations of epidote veins in the GTS.

The stereoplot is an equal area projection with the poles of the planes. Total number of measurements: 4.

2.4.2. Geochemistry of the mapped rocks

After looking at the petrographic aspects of the rock mass, the next subchapters focus on the geochemical description of the exposed rocks in the investigated area. This part combines literature data, mainly from Keusen et al. (1989), Oberhänsli (1986) and Schaltegger (1989), but also contains the results of new analyses performed in this study on samples from the GTS and the mapped surface area. In contrast to the spatially more extensive dataset of Schaltegger (1990), we concentrate on the near vicinity of the GTS only, by covering the area between Lake Räterichsboden and Grimsel Hospiz (Fig. 2.1). This area includes the transition from the Grimsel Granodiorite to the Central Aar Granite but also shows abundant occurrence of mafic dykes along this contact area. The geochemistry section is split into two parts, the Haslital-granite suite and the metabasic dykes, based on their different geochemical provenances (Schaltegger 1990).

Haslital-granite suite

The primary post-Variscan magmatic suite in the GTS, making up 95 % of the area (Keusen et al., 1989), is part of the Haslital group. The Haslital group includes granodiorite and granites, but also mafic enclaves and aplites. This magmatic association has already been investigated and discussed in detail by Schaltegger (1989). We will recall the data of Keusen et al. (1989), Oberhänsli (1986), Schaltegger (1989), and add some new data of our own (Tab. 2.5). The new data stem from an outcrop around L153 (Fig. 2.24).

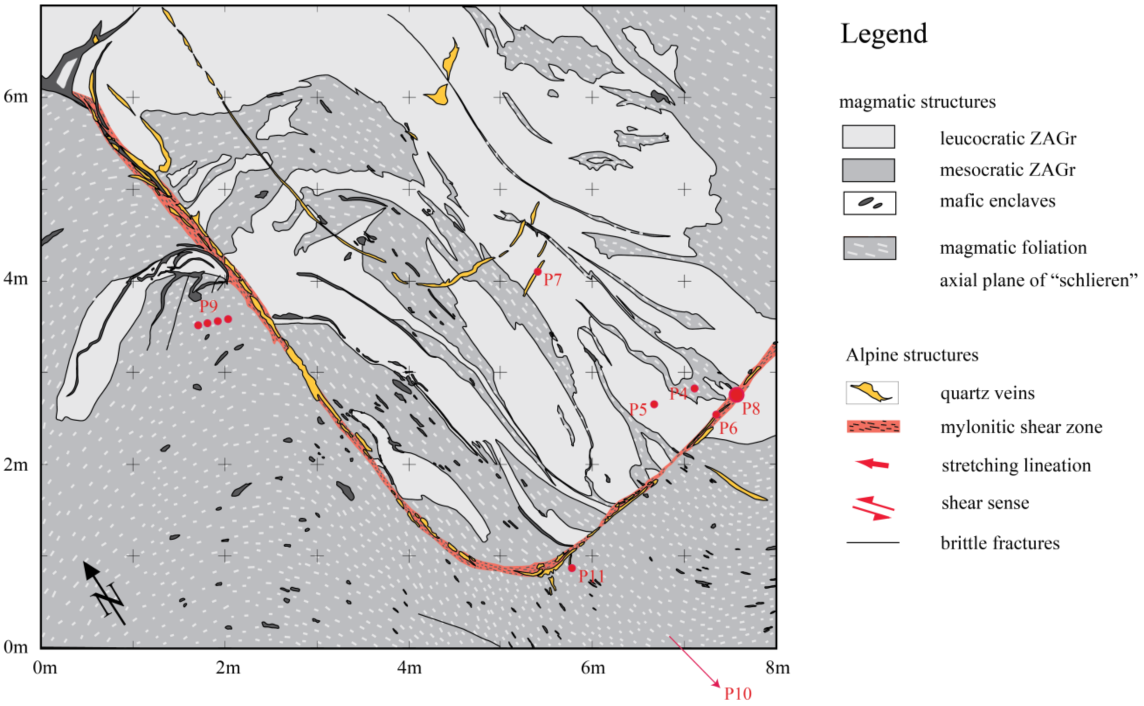

Figure 2.24. Map of outcrop at L153 with locations of samples analysed within this study (Map by Marco Herwegh).

P10 is approximatively 4m from P11 away.

The geochemical data derived from the spatially rather limited mapped area, indicates the general calc-alkaline magmatic trend (Fig. 2.25) which has been documented for the entire Haslital group (e.g. Debon and Lemmet, 1999; Schaltegger, 1990). In this respect, the extended GTS area enforces the trend observed overall. The data are grouped into Grimsel Granodiorite (GrGr) and Central Aare Granite (CAGr) and show that the geochemical signatures represent a continuous geochemical evolution (Fig. 2.25). This observation is consistent with a common genesis of a calc-alkaline magmatic suite and certain structural observations such as schlieren. We kept the separation between GrGr and CAGr for the sake of continuity.

In addition to the geochemical evolution within the magmatic environment, geochemical gradients are observed across Alpine shear zones with cm- to meter-scale thicknesses (Goncalves et al., 2012; Marquer et al., 1985). These variations are attributed to deformation / metamorphism-induced local mass transfer processes which alter the magmatic composition. The geochemical changes mainly affect the concentrations in MgO, K_2O and to a minor extent the concentration in CaO (Marquer et al. 1985).

As shown in Fig. 2.25, the SiO_2 content of the plotted data spreads from 60 wt % (mafic enclave) to 75 wt % (the leucocratic CAGr). The leucocratic members are poor in CaO, TiO_2 and MgO and relatively enriched in K_2O. The analysed mafic enclave and potentially some of the metabasic dykes (see next subchapter) may represent primitive intermediates of the Assimilation and Fractional Crystallization (AFC) evolution (Fig. 2.26). The Zr-TiO_2 diagram shows the typical bell shaped evolution for AFC processes. This bell shape results from an initial enrichment in TiO_2 and Zr until saturation of Zr and TiO_2 rich minerals as zircon or titanite, respectively, is reached. However, the mafic members of the differentiation suite are only represented by rare data, such as mafic enclaves. Moreover, numerous metabasic dykes occur in the GTS. As mentioned previously, not all metabasic dykes are part of the calc-alkaline trend of the Haslital granite magmatic association (Schaltegger, 1990) and will thus be discussed separately in the next chapter.

Table 2.5. Geochemical analyses of country rocks from the P shear zone around L153.

P shear zone is a name given randomly. The exact locations of the samples are shown in Fig. 2.24.

Sample	P-4	P-5	P-10	Sample	P-4	P-5	P-10
Location	Country rocks from the P-shear zone			Location	Country rocks from the P-shear zone		
Rock type	GrGr	CAGr	enclave	Rock type	GrGr	CAGr	enclave
Unit	[wt %]	[wt %]	[wt %]	Unit	[ppm]	[ppm]	[ppm]
SiO_2	68.24	73.58	60.15	Ba	886	416	168
TiO_2	0.5	0.19	1.16	Co	5.5	5.3	10.8
Al_2O_3	15.17	13.57	16.36	Cs	3.5	3	7.9
Fe_2O_3	3.23	1.52	6.73	Ga	17.2	14.9	23.2
MnO	0.08	0.04	0.21	Hf	7.3	3.7	4.4
MgO	1.54	0.25	2.09	Nb	35.6	12.9	52.4
CaO	1.31	1.07	4.26	Rb	180.7	170.8	233.7
Na_2O	4.36	3.64	4.92	Sn	7	3	8
K_2O	4.13	5.43	2.56	Sr	156.1	98.1	207.8
P_2O_5	0.16	0.05	0.4	Ta	5.3	1.3	2.3
LOI	1	0.5	1	Th	14.5	24	8.3
Sum	99.73	99.84	99.81	U	5.1	7	3.7
				Zr	260.5	102.8	187.9
				Y	72.6	19	81.3
				La	54.2	34.9	11.5
				Ce	107.1	67.4	37.7
				Pr	12.96	7.53	7.03
				Nd	49.1	25.6	36.3
				Sm	10.79	4.36	11.74
				Eu	1.28	0.59	1.05
				Gd	9.38	3.48	11.98
				Tb	1.96	0.53	2.34
				Dy	13.05	2.76	15.55
				Ho	2.72	0.6	3.06
				Er	8.25	1.76	8.54
				Tm	1.22	0.32	1.25
				Yb	7.73	2.33	7.57
				Lu	1.01	0.43	1.09

LOI: loss on ignition, GrGr: Grimsel Granodiorite, CAGr: Central Aar Granite, enclave: mafic enclave.

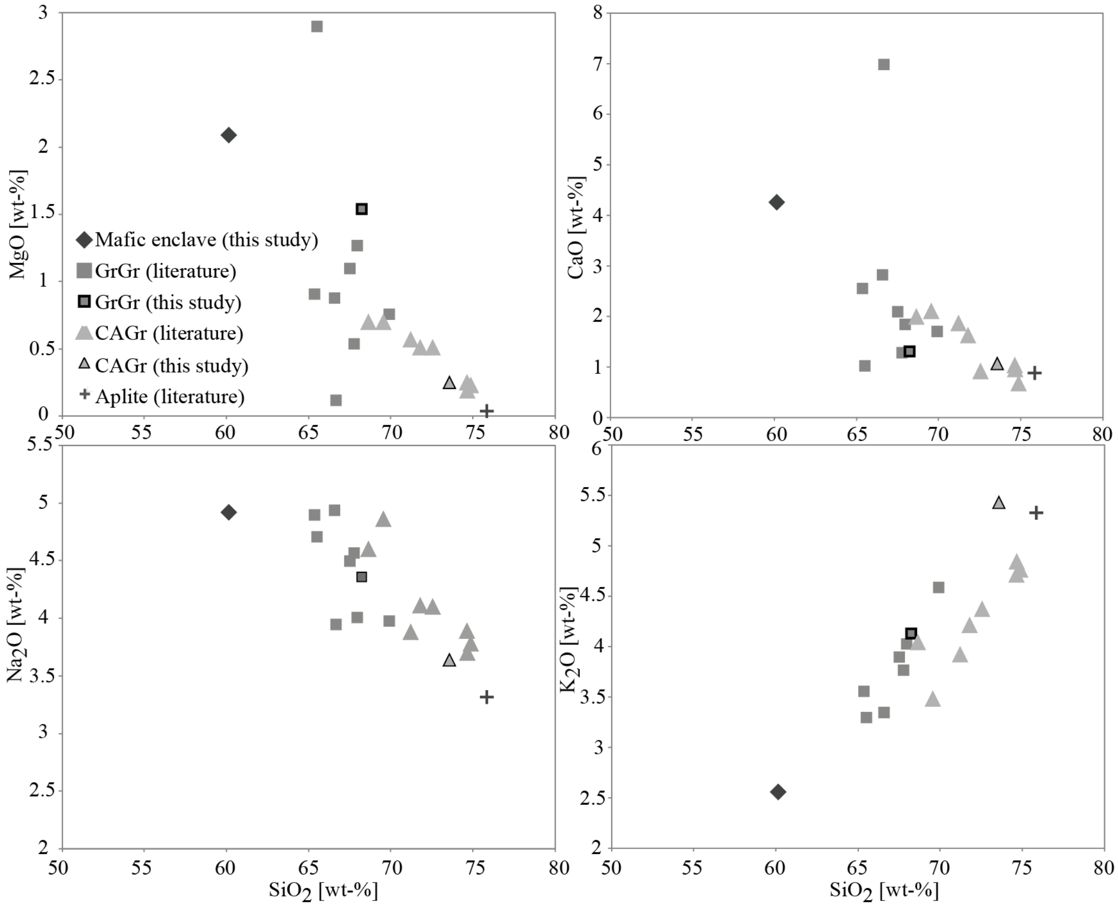

Figure 2.25. Selected Harker diagrams for the Haslital group, showing the magmatic evolution.

The literature data is from Keusen et al. (1989), Oberhänsli (1986), Schaltegger (1990) and Stalder (1964).

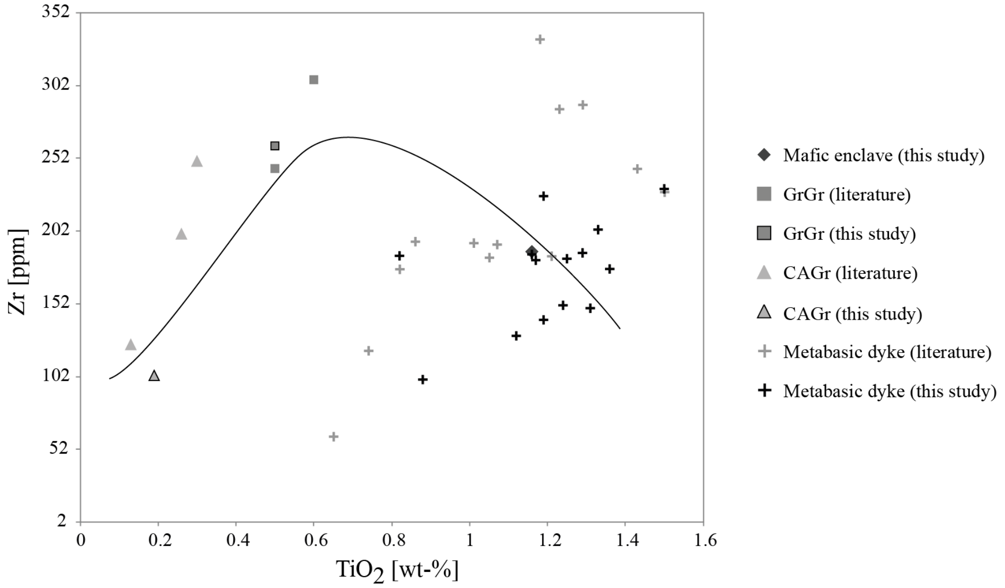

Figure 2.26. TiO$_2$ vs Zr diagram with AFC trend line.

Data sources as in Fig. 2.25. Line represents AFC evolution.

Metabasic dykes

The metabasic dykes show a large spread in compositions (Fig. 2.7). Unfortunately, the nomenclature of the dykes based on geochemical data including alkali and calcalkali elements is impossible. This is mainly due to the mobility of these elements during metamorphism and deformation (Oberhänsli, 1986). The metamorphic, and in some cases also the deformational overprint of all inspected dykes is significant. However, some observations are important:

- The chemical spread of the GTS samples is similar to the spread observed by Oberhänsli (1986) at the surface and by Hegner et al. (1998) in the Black Forest area.
- Metabasic dykes are alkaline as well as calc-alkaline; some might represent a primitive intermediate representative of the Haslital magmatic suite (Fig. 2.26).
- Metabasic dykes spread from high potassium to shoshonitic.
- High Mg# (MgO > 5 wt %) dykes have Ni concentrations above 100 ppm (with one exception), indicating relatively primary magmas (Oberhänsli, 1986).

The TiO_2 versus MgO diagram (Fig. 2.27) may be used to discriminate between different dyke types, because these two elements are considered to be relatively "immobile". Thus observed differences probably indicate differences in the chemical composition of the source magmas. Based on the entire TiO_2 / MgO dataset from all magmatic rocks, two trends can be discriminated: (i) a high-Ti trend and (ii) a low-Ti trend (Fig. 2.27).

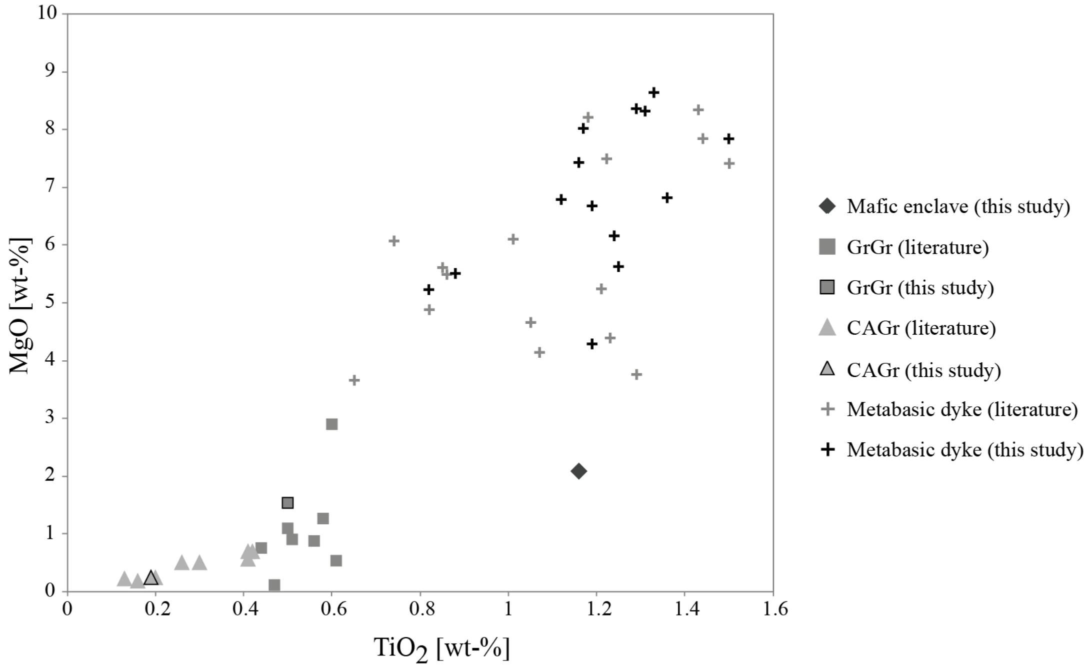

Figure 2.27. TiO_2 vs MgO diagram showing high-Ti and low-Ti trends for metabasic dykes. Data sources as in Fig. 2.25.

Based on the TiO_2 / Zr diagram, metabasic samples, which would fit in an AFC process connecting the mafic enclaves, GrGr and CAGr are found to be high in CaO (Fig. 2.26). Assuming minor CaO mobility during deformation, these dykes can be related to the Haslital magmatic suite and would represent a primitive part of the magma evolution. However, not all dykes match such an evolution (Fig. 2.26) and thus the origin of the dykes is manifold.

2.5. Deformation structures

As mentioned in Chapter 2.2, the rock mass surrounding the GTS and exposed at the surface is heterogeneously deformed by Alpine orogeny. The heterogeneous deformation results in background deformation and localized deformation. We understand background deformation as the least deformation present. This chapter is organized according to the deformation features introduced in Chapter 2.3. First, planar structures are presented, with background strain features in Chapter 2.5.1 and localized ductile shear zones and brittle features in Chapter 2.5.2. Lineations observed along deformation planes are discussed in Chapter 2.5.3 and give an opportunity to compare the observed structures with the kinematic framework proposed by Wehrens (2015). As a last paragraph, some major rock mechanical properties are summarized based on Keusen et al. (1989).

2.5.1. Planar fabrics

We use foliation to describe a planar rock texture. Foliation in the Haslital granitic suite has to be discriminated into a (i) magmatic foliation of pre-Alpine origin and (ii) solid-state foliation related to Alpine orogenic deformation.

Magmatic foliation

Magmatic foliation is marked by the shape-preferred orientation of large K-feldspar and plagioclase grains as well as by the planar arrangement of the lentoid-shaped mafic enclaves (Blumenfeld and Bouchez, 1988; Paterson et al., 1989). These structures are locally preserved in the GTS and at the surface (Ambrosio, 2011; Wehrens, 2015). The measured orientation of the magmatic foliations is on average 145 / 80 (Fig. 2.28), clustering within little variation (Fig. 2.28). The mean orientation corresponds to the general orientation of the solid-state foliation. Some of the magmatic structures are associated with schlieren expressed by magma-mingling between ‘meso-‘ and ‘leucocratic’ melts and small-scale phenomena, typical for magmatic systems (Paterson et al., 1989).

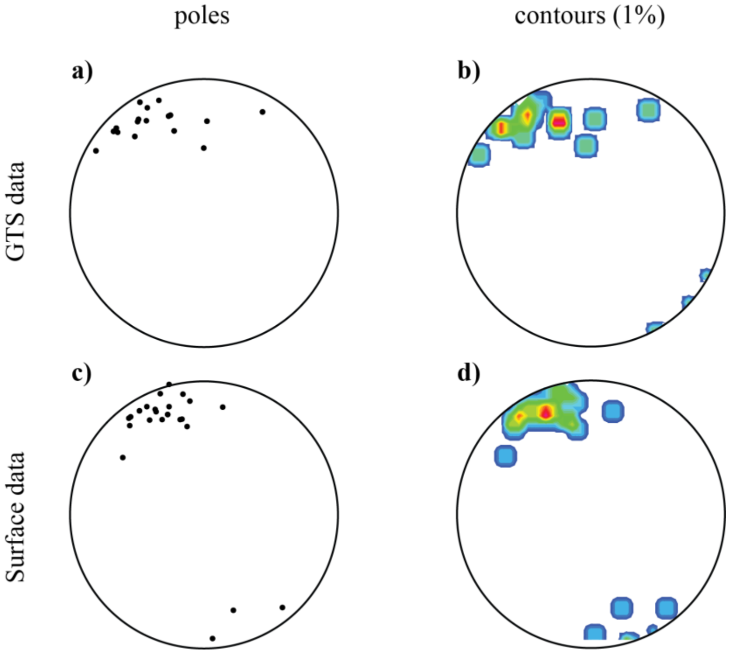

Figure 2.28. Stereoplots for measured orientation of magmatic foliation within the GTS (a) and at the surface (c). Poles are contoured with 1 % density lines for the GTS data (b) and the surface data (d).

An equal area projection was used and the poles of the planes are displayed. GTS data have a total number of 29 magmatic foliation measurements, whereas surface data have 25 measurements. Surface data are compiled from this study and literature data (Baumberger, 2015; Schubert, 2013; Wehrens, 2015; Wicki, 2011).

Dyke intrusion

Along with magmatic deformation of the Haslital group, there is also early dyke intrusion and veining within the bedrock. The exact timing of the dyke intrusion (metabasic dykes) is not known. Metabasic dykes (lamprophyres) within the Sambuco nappe are dated to 290.5 ± 3.7 Ma (Bussien et al., 2011), which corresponds to slightly younger ages than for the Haslital group.

Within the GTS, the metabasic dykes occur as swarms which strike NW-SE. Individual measurements of metabasic dykes are more variable in strike than suggested by the strike of the swarms (Fig. 2.29). Commonly, the dykes are steeply dipping (Fig. 2.29). As the orientation pattern of dykes reflects the local stress regime during intrusion, the steep orientation of the dyke can serve as evidence for an intrusion at great depth. While no information on σ1 and σ2 can be obtained from a planar dyke, σ3 is located perpendicular to its walls. In the case of an isotropic stress field, intrusion of randomly oriented dykes would be the consequence, where only the steeply oriented dykes reach today's topography. Strikingly, the orientation pattern of the surface data is close to randomly steeply oriented, which could indicate an isotropic stress field during intrusion. Therefore this dataset was used and a rotation along a horizontal orogen-parallel rotation axis (65°) was performed. The rotation angle was continuously increased from 0 to 30° (Fig. 2.30). A steep random orientation was found when the dykes were rotated by 20° around a horizontal 65° striking rotation axis. Those values were subsequently used with the

GTS dataset and the combination of both datasets (Fig. 2.30). The addition of the GTS dataset did not improve the results. The dyke's rotation could be evidence for a rotation of the Aar massif by about 20° since the dyke's intrusion. Paleo-magnetic studies could provide further insight, but were not within the scope of this study.

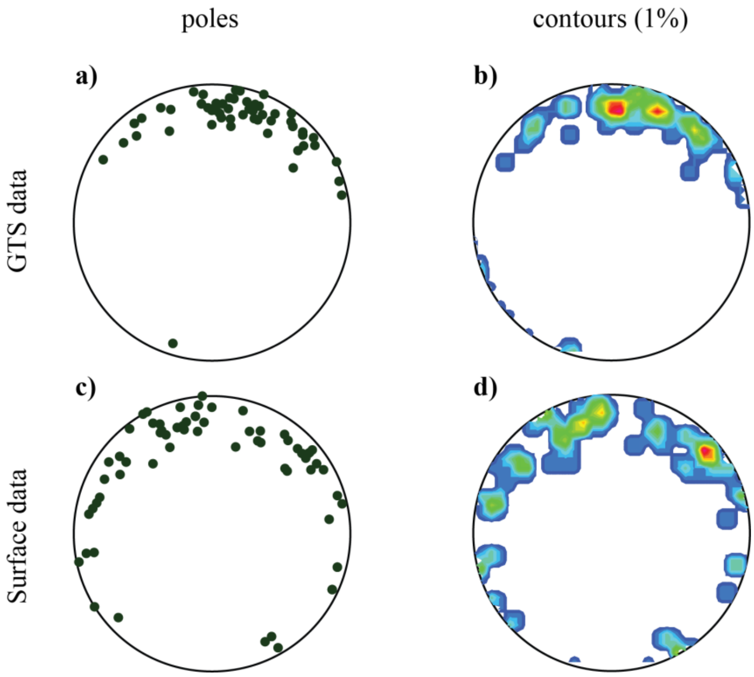

Figure 2.29. Stereoplots with measured orientations of metabasic dykes for the GTS (a) and the surface (c). The poles of the planes are contoured with 1 % for the GTS (b) and the surface (d).

An equal area projection was used for the stereoplots. The poles of the planes are displayed (total number: 64 for the GTS and 68 for the surface).

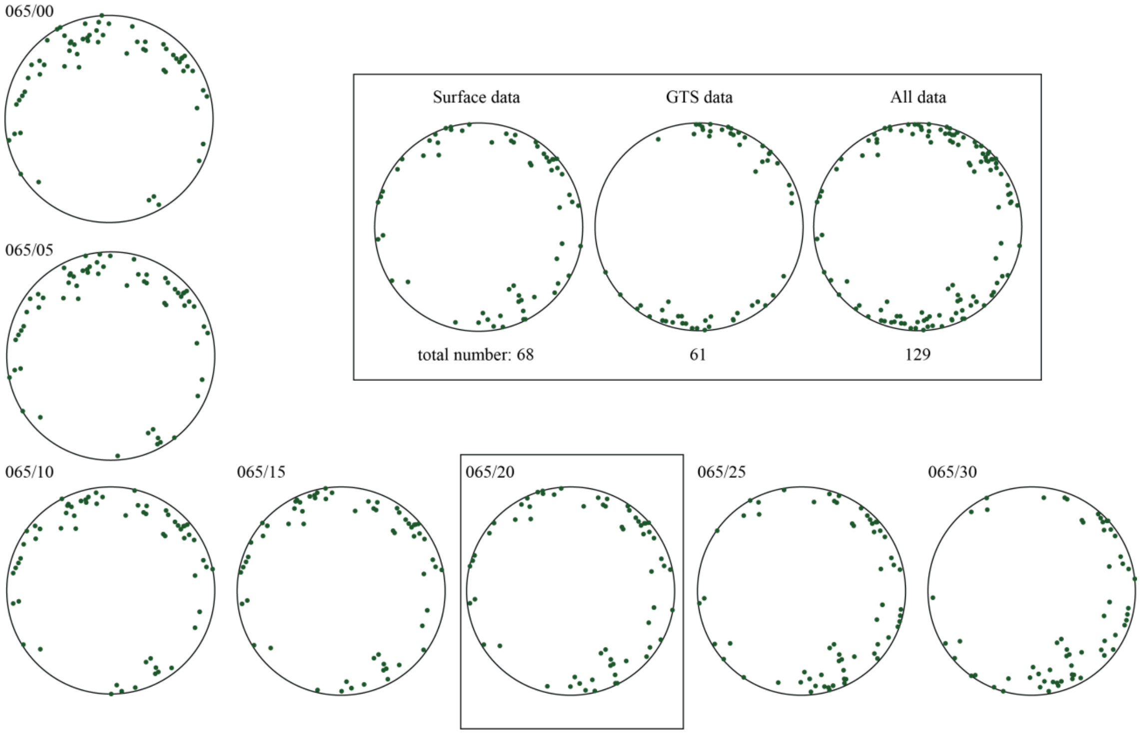

Figure 2.30. Surface dataset for orientations of metabasic dykes rotated around a 65° striking axis with increasing rotation angle.

Numbers top-left of stereoplots show plunge azimuth of rotation axis and rotation angle. An equal area projection was used for the stereoplot and the total number of points is 68.

Furthermore, the Haslital group is dissected by quartz veins of either Alpine or pre-Alpine age. Pre-Alpine quartz veins are strongly overprinted by deformation related to the Alpine orogeny. Their measured orientation (Fig. 2.31) clusters around steeply south dipping, therefore slightly at an angle to the magmatic foliation. Numerous veins within the GTS are presumably products of Alpine deformation with Alpine quartz clefts as the most prominent examples. The flat orientation of the veins is evidence for a vertical σ3. This is in good agreement with the kinematic evolution described in Chapter 2.2.2. Veins crosscutting Alpine foliation and not showing any ductile overprint must belong to this group. As mentioned in Chapter 2.2.2, the temperature and pressure conditions were suitable for ductile deformation of quartz during high temperature stages of Alpine deformation, thus quartz veins without evidence of ductile deformation are younger than the Alpine ductile deformation.

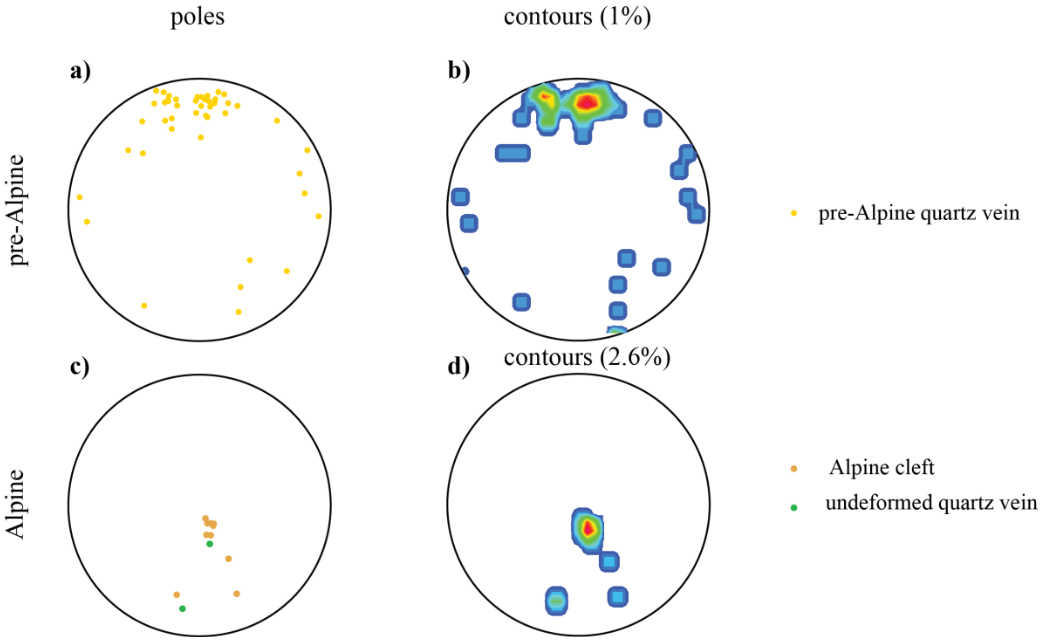

Figure 2.31. Measured orientations of quartz veins within the GTS. Veins overprinted by Alpine ductile deformation are shown in (a) and contoured in (b). Veins undeformed by Alpine ductile deformation are presented in (c) and (d).

An equal area plot was used, where the poles of the planes are displayed. The contours are 1 % density lines. In total 47 pre-Alpine quartz veins and 12 Alpine quartz veins are shown.

Alpine foliation

Solid-state foliation related to Alpine orogenic overprint is pervasive. It is marked by the orientation of biotite, white mica, shape preferred orientation of recrystallized quartz, and neo-crystallization of sheet silicates and quartz e.g. Schubert (2013), Wehrens (2015). The orientation is subparallel to the magmatic foliation (Fig. 2.32). The higher content of biotite in the GrGr compared to the CAGr leads to a more strongly expressed foliation in the S part of the GTS (Enclosure 2). The southward increasing foliation intensity therefore expresses a southward increasing strain gradient (Choukroune and Gapais, 1983; Wehrens, 2015).

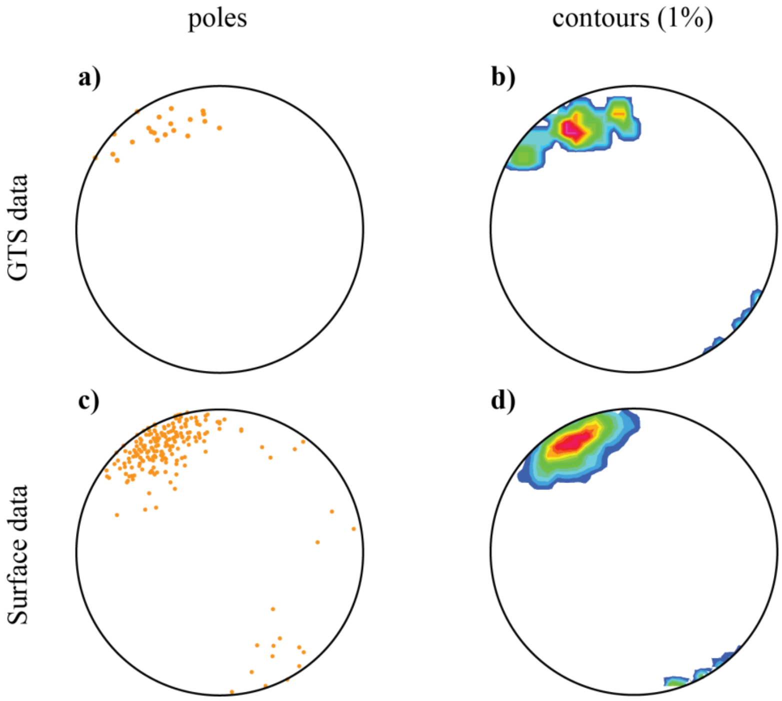

Figure 2.32. Stereoplots for Alpine foliation in the GTS (a) and at the surface (b). The poles of the planes are displayed and contoured with 1% density lines (GTS data, b; surface data, d).

An equal area projection was used and the poles of the planes are displayed. The GTS dataset has a total number of 22 foliation measurements, whereas surface dataset is composed of 240 measurements. Surface data are compiled from this study and literature (Baumberger, 2015; Schubert, 2013; Wehrens, 2015; Wicki, 2011).

2.5.2. Shear zones

Next to the pervasive foliation, shear zones and brittle faults record the highly localized deformation. We use shear zones to describe ductile high strain zones, whereas brittle faults mimic the brittle overprint of the ductile shear zones in the area investigated. Strain localization is enforced by the enrichment of sheet silicates within the shear zones (Fig. 2.33), which results in structural weakening of the zone (Wehrens, 2015).

Shear zones of three different deformation stages occur in the surroundings of the GTS, one magmatic stage and two stages of Alpine solid-state deformation.

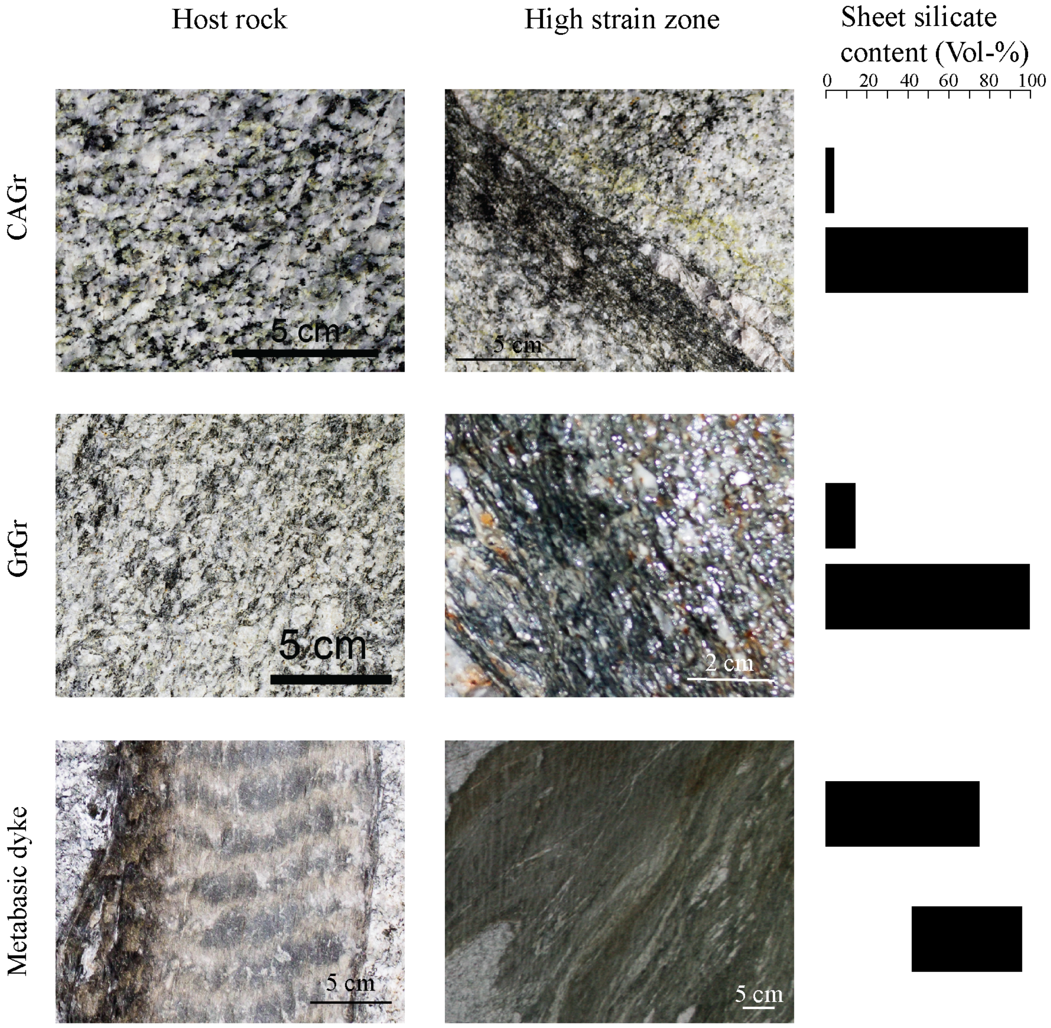

Figure 2.33. Sheet silicate content in deformed and undeformed bedrock.
Modified after Wehrens (2015).

Magmatic shear zones

As may be seen in Enclosure 2, Alpine deformation is heterogeneously distributed throughout the GTS. This deformation pattern results in deformed and undeformed parts under Alpine conditions. Within the undeformed parts magmatic features such as schlieren, magmatic foliation and magmatic shear zones were observed. Alpine undeformed parts are of variable thickness. A thick Alpine undeformed part is found between L200 and L290.

Deformation during the viscous state of the magma yields rotation of early-formed crystals such as feldspars or biotite. Strain is concentrated within the matrix surrounding the crystals (Blumenfeld and Bouchez, 1988). Therefore, magmatic shear zones are recognized due to changes in magmatic foliation defined by either feldspar grains or mafic enclaves (Fig. 2.34). Magmatic shear zones and more generally magmatic features were thoroughly described by

Ambrosio (2011). An example of feldspar grain rotation is found at ca. L176 and an example of rotating mafic enclaves at ca. L190.

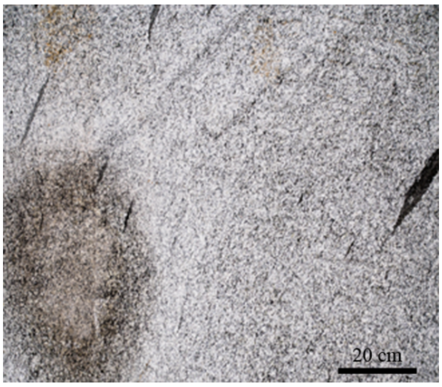

Figure 2.34. Photograph of a magmatic shear zone at L145.

Ductile shear zones

Some of the Alpine ductile shear zones are expressed as discrete planes with a small shear zone width (mm to cm) and others as asymmetric shear zones with visible strain gradients (Rolland et al., 2009; Steck, 1968; Wehrens, 2015). The strain gradient is macroscopically expressed by a reduction in grain size, an increase in foliation intensity and, if present, an increasing elongation of quartz aggregates (Fig. 2.35). In the case of the GrGr, this strain gradient sometimes results in an Augengneis type appearance.

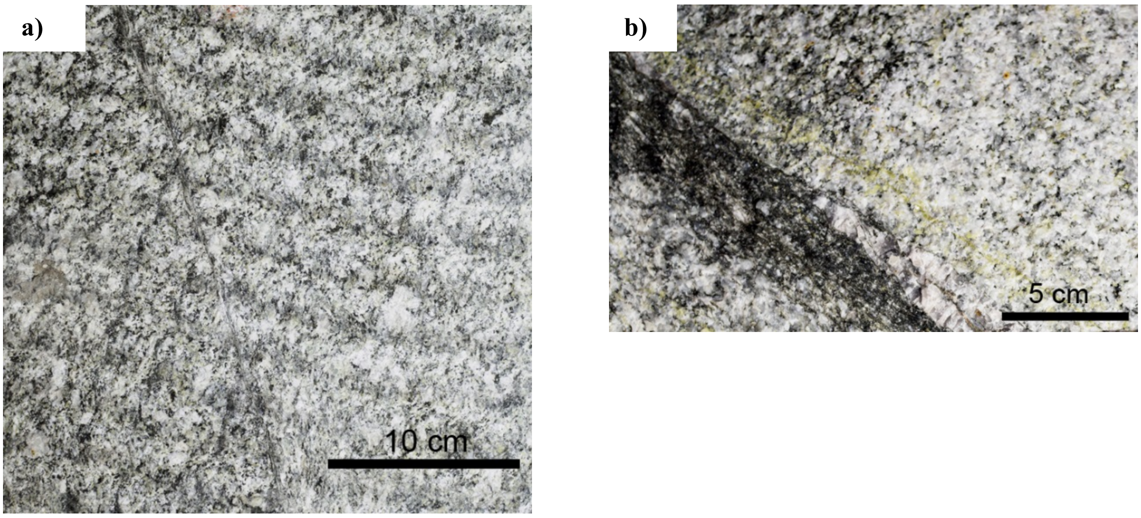

Figure 2.35. Photographs showing the different appearances of Alpine ductile shear zones: discrete shear zone (a) and asymmetric shear zone with strain gradient (b).

Discrete shear zones (Fig. 2.35) probably have a brittle fracture as a precursor structure (Mancktelow and Pennacchioni, 2005; Wehrens, 2015), which was then reactivated in a ductile manner. The origin as a brittle precursor is very realistic because of the low width to length ratio. In the case of the shear zones with strain gradient (Fig. 2.35) a brittle precursor cannot be excluded but also pure strain localization out of a homogeneous state (Peters et al., 2016, 2015) or along pre-existing mechanical anisotropies e.g. variations in lithological composition (Wehrens, 2015), are possible origins. The thickness of the shear zones varies from mm to cm in size or even to the meter scale, when several smaller shear zones contribute to the formation of a deformation zone. Ductile shear zones are recognized by their dark colour which is due to grain size reduction. Not only the smaller grain size renders the appearance of the ductile shear zones darker, also the content of sheet silicate is increased in the ductile shear zones as compared to the undeformed host rock (Wehrens, 2015, Fig. 2.33). If the sheet silicate enrichment occurred prior to the deformation or is a result of the deformation remains unclear. The increased concentration of sheet silicate in the shear zones leads to a strain weakening and thus enables further strain localization (Passchier and Trouw, 2005).

In the GTS, ductile shear zones prevail in two spatially separated zones (Enclosure 2). The zones are located from L050 to L185 and from L417 to L517. Ductile shear zones within the Haslital group are commonly oriented NE-SW, whereas the ductile shear zones within the metabasic dykes follow the strike of the dykes (NW-SE). Rarely, shear zones oriented E-W are found either located within metabasic dykes (L178, L465) or the Haslital group (L175, L517). A total of 65 shear zones were observed within the 517 m along the GTS' main gallery, yielding a density of ca. 120 shear zones per km. This is similar to the density of 90 to 125 features per km reported by Wehrens (2015) from the Transitgas tunnel system between Lake Räterichsboden and Grimsel Pass at the E side of the Haslital. At the surface the density of shear zones per km appears to be lower (approx. 24 features per km). This is an artefact, however, based on incomplete outcrop exposures and the coverage of shear zones by debris and vegetation, owing to the preferential erosion potential of these zones (Baumberger, 2015). Strikes observed in map view are also visible in Fig. 2.36, where ductile shear zones' orientations as measured in this study and compiled from literature (Baumberger, 2015; Vouillomaz, 2009; Wehrens, 2015; Wicki, 2011) for at the surface and in the GTS are reported. The surface data show one major cluster, about steeply SE dipping (Fig. 2.36). Orientations measured within the GTS reveal three to four clusters, all steeply dipping. The major cluster dips towards SE, whereas smaller clusters dip towards S and SW. The smallest cluster dips towards ESE.

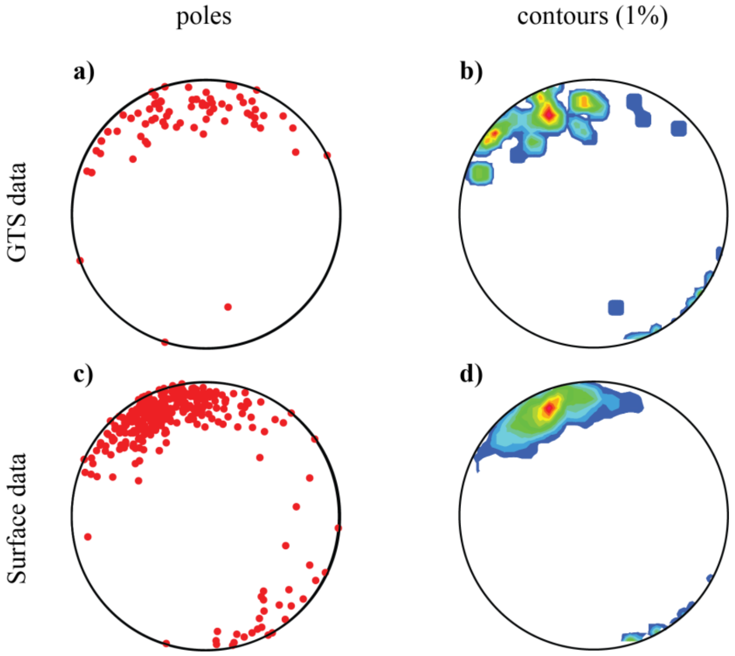

Figure 2.36. Stereoplots showing measured orientations of ductile shear zones in the GTS (a) and at the surface (c) and the 1 % contours for the pole for the GTS data (b) and the surface data (d).

An equal area projection was used. GTS data: Ductile shear zones are either located within a metabasic dyke or within the Haslital group (total number of points: 103). Surface data: Ductile shear zones are located within the Haslital group (total number of points: 378).

The thickness distribution of observed ductile shear zones reveals two maxima for the GTS data and surface data. Numerous shear zones are less than 5 cm across (Fig. 2.37) but also shear zones wider than 100 cm are often observed. It has to be noted that zones of deformation composed of several shear zones having similar orientations are summarized as one measurement and appear as a very thick shear zone, which in actual fact is composed of several thinner shear zones. Accordingly, the thickness indicated is to be interpreted as that of a deformation zone and not as that of a single feature.

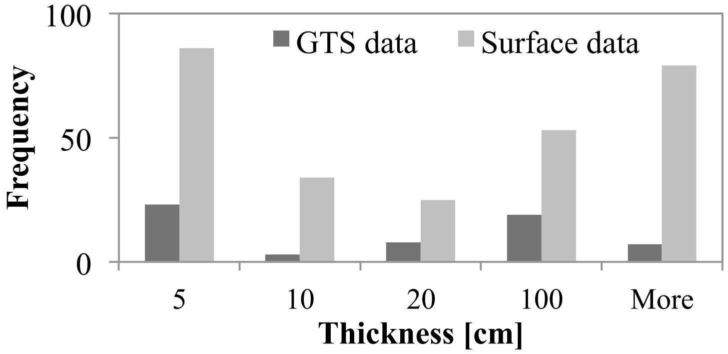

Figure 2.37. Histogramm showing the thickness distribution of ductile shear zones in the GTS and at the surface.

GTS data represent all data collected within the GTS (approx. 1 km galleries). Surface data represent data collected at the surface above the GTS (approx. 9 km^2).

Brittle reactivated ductile shear zones

During uplift of the Aar massif (Chapter 2.2.3), temperature and pressure conditions decreased and thus the deformation changed progressively from the ductile regime into a brittle regime. Numerous brittle structures overprint former ductile structures, forming cohesionless fault gouges and cohesive cataclasites. Cataclasites were only observed in drillcores, but not in the galleries or at the surface. Fault gouges formed by grinding down of the mylonitic material (Bossart and Mazurek, 1991; Kralik et al., 1992; Wehrens, 2015). The occurrence of smectite in the fault gouge implies formation at low temperature (Wehrens, 2015). The fault gouges found at the surface and in the GTS have similar orientations as the ductile precursors (Fig. 2.38).

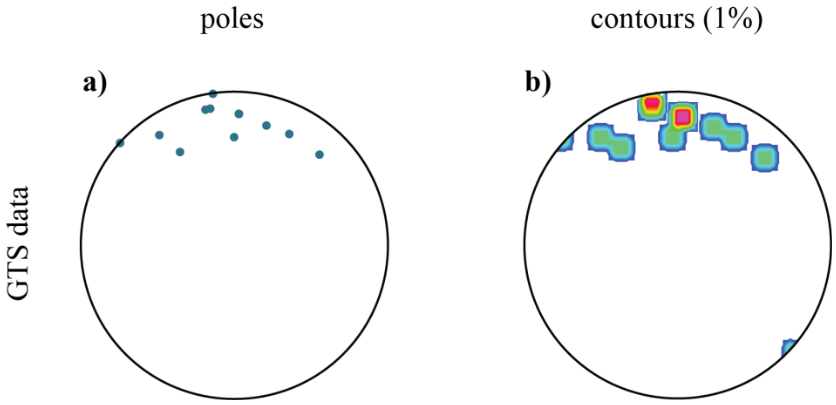

Figure. 2.38. Stereoplot with measured orientations of fault gouges within the GTS (a) and contoured data with 1 % density lines (b).

An equal area plot was used. The poles of the planes are displayed. Total number of points: 13.

Brittle shear zones and brittle fracturing

Brittle fabrics without any interplay with ductile deformation are represented by biotite-coated fractures, brittle fractures and Alpine clefts.

Biotite-coated fractures are expressed by a discrete fracture with biotite coating on the fracture planes (Fig. 2.39). Commonly biotite is a secondary coating of the fracture; more rarely primary magmatic enrichment could promote a subsequent brittle fracturing. If the coating is secondary, then the fracturing occurs in the stability field of biotite (> 400°C). In that case those fractures can be related to Alpine deformation, more exactly to the Oberaarphase. This is based on an outcrop at L465 (Fig. 2.40). If the fracturing happens along primary magmatic accumulation of biotite then no specific age relations can be infer

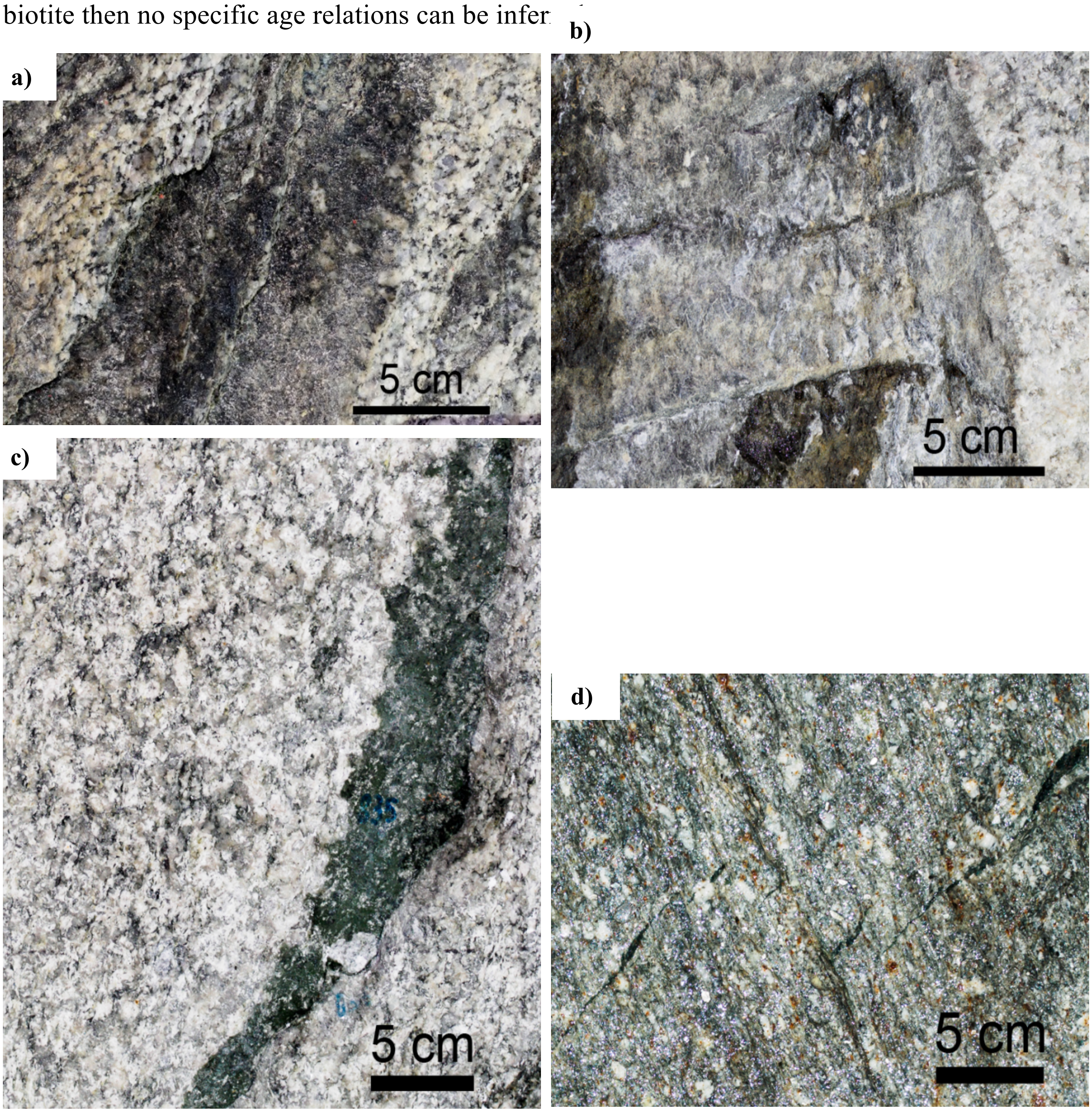

Figure 2.39. Photographs of different brittle fractures in the GTS.

(a) Brittle fractures in CAGr at L070, (b) brittle fractures in a metabasic dyke (water-conducting) at W114, (c) biotite coated fracture in CAGr at L202, and (d) biotite coated fractures in ductile shear zone within GrGr at L465.

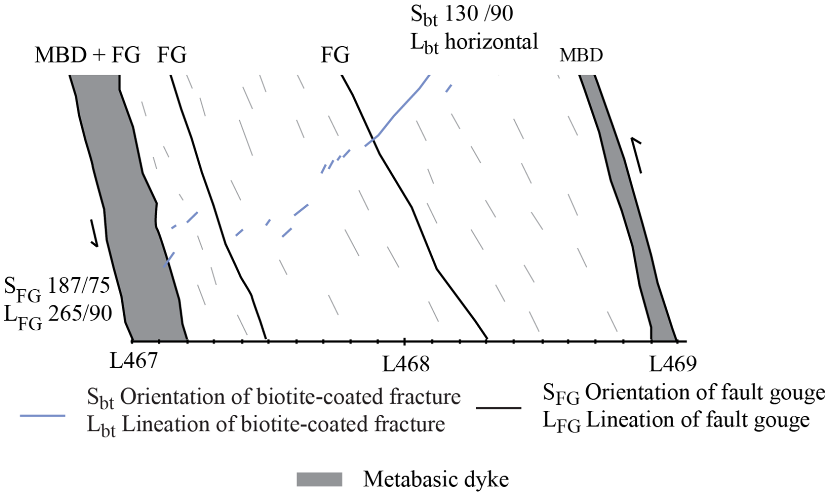

Figure 2.40. Detailed outcrop mapping at L467 to L469 within the GrGr showing biotite-coated fractures crosscutting a ductile shear zone with steep lineation.

Brittle fracturing is ubiquitous in the GTS (Fig. 2.39) and at the surface. Brittle fractures occur along pre-existing structures (e.g. quartz veins, metabasic dykes, ductile shear zones), but do also occur within intact host rock. Measured orientations vary significantly in dip azimuth but all are steeply dipping (Fig. 2.41).

Brittle fractures might have originated at very different times. As mentioned earlier, the biotite-coated fracture might be formed under biotite stable conditions and thus at a different time than the brittle fracture separates the host rock without altering it. Some of the brittle fractures may have also been caused by the excavation activities. Not all galleries were drilled using a tunnel boring machine, e.g. the BK cavern was blasted.

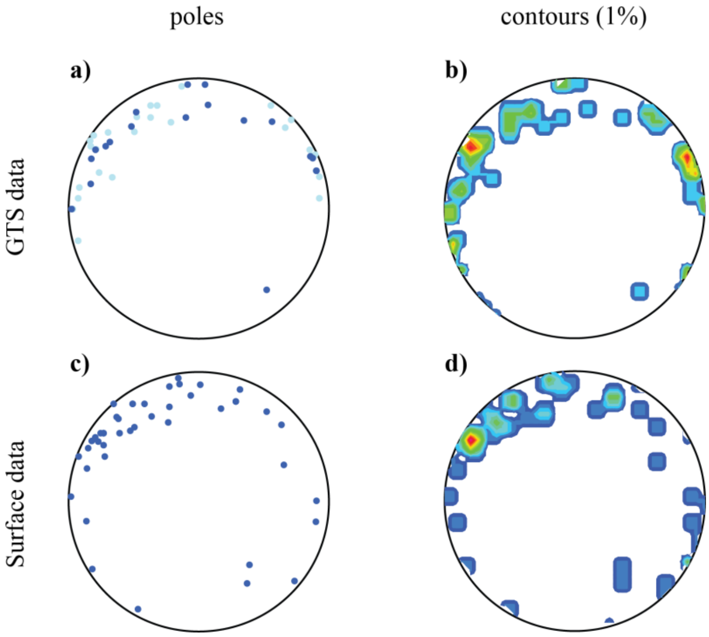

Figure 2.41. Measured orientations of brittle fractures in the GTS (a, b) and at the surface (c, d). The data is contoured with 1 % density lines.

An equal area projection was used. The poles of the planes are displayed. In the GTS a distinction between brittle fractures in general (dark blue, total number: 20) and biotite-coated fractures (light blue, total number: 27) was made. At the surface only brittle faults in general are reported (total number: 44).

In addition to decreasing temperatures, uplift formed exfoliation joints due to changes in stress conditions. These joints generally form close to the surface but appear with increasing spacing down to depths of 200 m below today's surface (Ziegler et al., 2013). The mean overburden above the GTS (ca. 450 m) is higher and thus the GTS is unaffected by exfoliation joints. Exfoliation joints are part of the youngest and ongoing brittle deformation in the Grimsel area. Exfoliation joints occur close to today's topography and are partly open. Thus, they also strongly influence the present day's infiltration pattern of meteoric water at the surface, building a funnel system. Alpine clefts are amongst the youngest brittle features observed in the mapped area. They have been described in Chapter 2.5.1.2 with the pre-Alpine quartz veins.

2.5.3. Linear structures

At the surface, rocks have been polished glacially while in the GTS they appear polished due to the tunnel drilling machine. Either way, observations of lineation are difficult. Nevertheless, lineations were observed within the GTS and at the surface along fractured fault/shear planes, fracture planes as well as foliations. Lineations were found as stretching lineations or slickensides. Along biotite-coated fractures the lineations were slickensides, indicating relative displacements during brittle deformation. The lineations are orientated from sub-horizontal to steep (Fig. 2.42). The available data indicate three clusters (one steep and two flat groups) but also a few transitional data occur (Fig. 2.42).

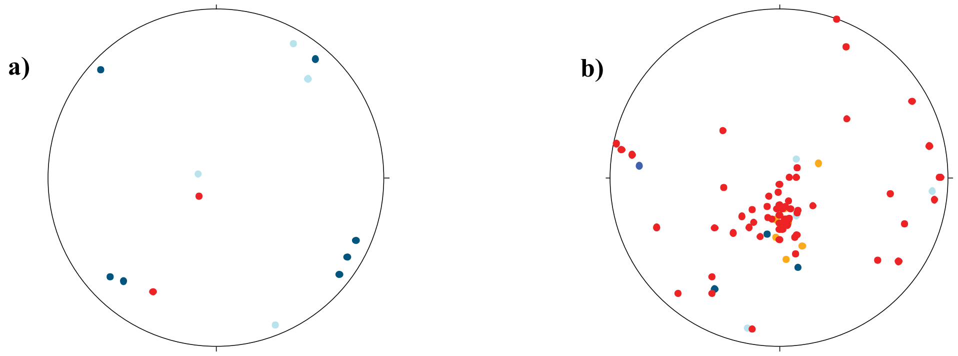

Figure 2.42. Stereoplots show (a) the lineations within the GTS and (b) the measured lineations at the surface.

Red dots: lineation along ductile shear zone, orange dots: lineation measured along foliation, petrol dots: lineation measured along fault gouge, light blue dots: lineations measured along biotite-coated fractures.

2.5.4. Rock mechanical properties

Within the scope of this study no rock mechanical properties were measured. For purposes of completeness, various values measured by Keusen et al. (1989) are reported in Tab. 2.6.

Table 2.6. Some rock mechanical properties for the main rock types in the Grimsel region.

	GrGr	CAGr	Aplitic dyke	Metabasic dyke
Density [kg/m^3]	2706 ± 13.6	2660 ± 23.8	2599 ± 17.4	2909 ± 31.0
Porosity [vol %]		0.4-1.0		
Young's modulus [GPa]	47.3 ± 15.4	53.3 ± 11.0	60.2 ± 8.9	42.4 ± 8.5
Poisson ratio	0.33 ± 0.15	0.37 ± 0.12	0.40 ± 0.12	0.33 ± 0.17
Internal friction angle [°]	29	33	36	32.5 ± 3.5

Young's modulus is one of the two elastic constants needed to characterize the elastic behaviour of an isotropic rock. Typically, it has values between 50 to 150 GPa in rocks (Twiss and Moores, 1992). The Poisson ratio is the other elastic constant used to characterize the elastic behaviour of an isotropic material. For most rocks, the Poisson ratio ranges from 0.25 to 0.33 (Twiss and Moores, 1992). It would be 0.5 for a perfectly incompressible material.

2.6. Surface / Underground correlation

Along with the mapping of the underground rock laboratory and the surface, we intended to correlate deformation structures observed at the surface with the structures observed underground. This was attempted in order to constraint the geometry of the deformation structures in 3D, which may serve as a base for further studies, e.g., an investigation of fluid flow paths, stress simulations, or fault reactivation analyses around the GTS.

We used the pattern of deformation structures mapped at the surface and projected it down to the GTS. The projection was done either using fieldwork derived orientations or using remote-sensing based information combined with a projection algorithm (Delaunay triangulation or Ribbon tool). Delaunay triangulation is based on the work of Delaunay (1934) and is a triangulation method. Ribbon tool is a Move^{TM}, Midland Valley internal algorithm that is based on moment of inertia analysis (Fernández, 2005).

What we obtained was an intersection pattern of the surface pattern (Fig. 2.43) and the mapped GTS pattern. To link a surface deformation feature with a feature underground, we used a minimum distance and a minimum angle misfit and inferred a best link (Fig. 2.44). Depending on the scale of consideration the attempt was more or less successful. The maximum distance between a projected surface structure and a used underground structure was 140 m, but the average was around 20 m (Fig. 2.44). Considering a mean overburden of 450 m this yields an average uncertainty of ca. 4.5 %. Average angular misfit was ca. 6°, implying an uncertainty of ca. 4.3 %. At the current status of the investigations, kinematic indicators such as lineation, thickness of structure, or shear sense indicators were not considered when performing the interpolation between the surface and the underground structure patterns. The different densities of structures were also not taken into account. In general, more structures were observed in the GTS as compared to at the surface. Furthermore, examples of ending structures within the GTS were observed (e.g. metabasic dyke at W109).

Using for every surface trace the best fitting underground feature, we were able to build a best-estimate model (Fig. 2.45). This model is a first working hypothesis as modelling continues.

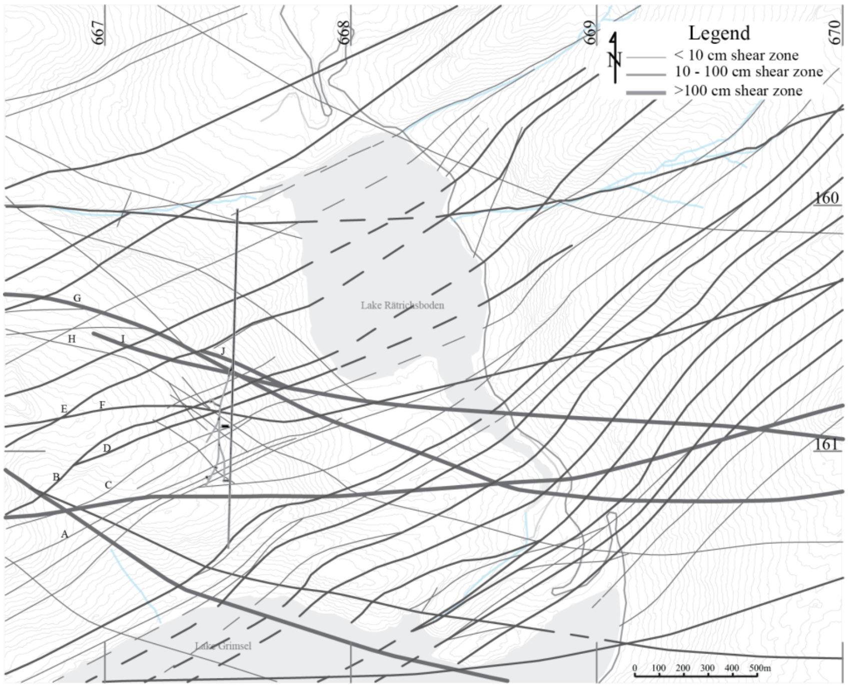

Figure 2.43. Surface map with ductile shear zones in grey with labels corresponding to labels in the histogram (Fig. 2.44).

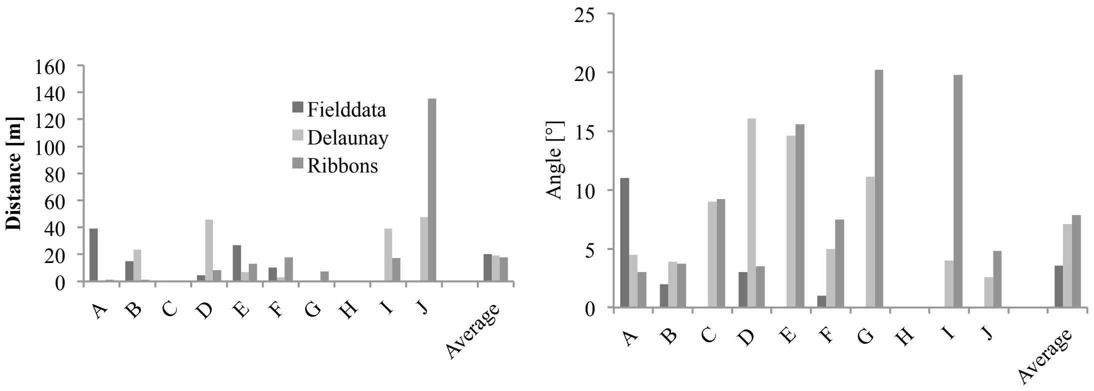

Figure 2.44. Histograms showing the distance and the angular misfit of selected surface deformation structures with mapped deformation structures in the underground.

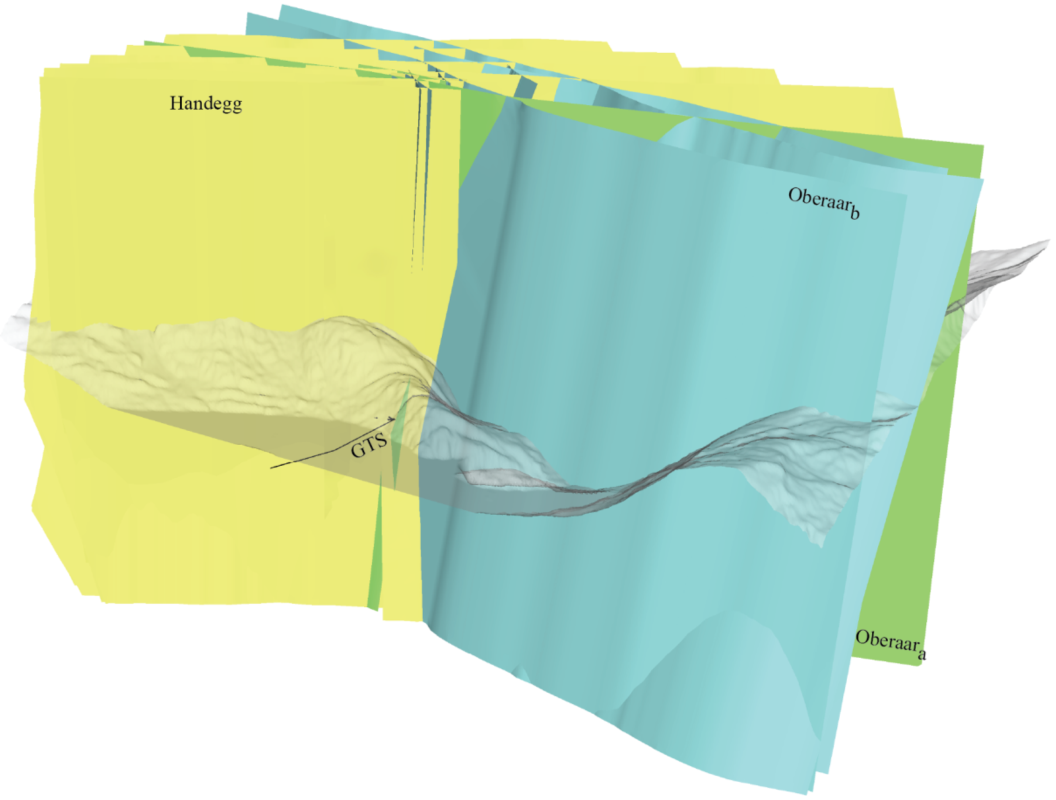

Figure 2.45. 3D visualization of fault zones from the surface to the GTS.

Digital elevation model with 25 m resolution (swisstopo).

2.7. Water-conducting features

In crystalline rocks, water inflows are generally constrained to water-conducting features (e.g. Caine et al., 1996). In the galleries, wet spots and spots with active water dripping are considered water inflow points. In this investigation we focussed on the spatial correlation between deformation structures and water inflows. For specifics about the composition of the fracture water the reader is referred to Frick et al. (1992), Keppler (1994) or Mäder & Ekberg (2006).

Water inflow points at the GTS were mapped at two different times, in July 2014 and in January 2016. The mapping was performed based on visual inspection of the galleries. This implies that the features mapped as water conducting were wet at the time of mapping. The ventilation in the tunnel system dries the tunnel surface. In order for water conducting features to be wet, their minimum hydraulic transmissivity needs to exceed the drying capacity of the ventilation system. This minimum hydraulic transmissivity was estimated by Mazurek (2000) to be ca. $3 \cdot 10^{-8}$ m/s. The ventilation capacity of the tunnel system is constant over the year, but may be sporadically enhanced due to more intense human activity such as drilling.

The number of water inflow points mapped in the two mapping campaigns was comparable. In July 2014, 64 water inflow points were mapped as compared to 62 in January 2016. In January 2016 only the water inflow points were mapped, whereas in July 2014 wet floor was mapped without specification of the number of inflow points. Some differences were observed:

- The mapping in July 2014 shows an enhanced water inflow into the AU drift that was not found in January 2016. This may be related to more work (e.g. drilling) being done in the AU drift.
- Some specific features such as a fault gouge at AU060 or the metabasic dyke reactivated as fault gouge in L176 were water conducting in July 2014 and not in January 2016.

As already reported by Mazurek (2000), the CAGr dominated part presents a higher density of water conducting features. This is due to the greater number of brittle features located within the CAGr than in the GrGr. Numerous water inflows are related to the occurrence of metabasic dykes, which is in good agreement with the observed localization of ductile and brittle deformation within the dykes. Therefore, not the composition of the host influences the water pathways but the deformation style, which might in turn be related to the host rock composition (Schneeberger et al. in prep). The map of inflow points reveals a close spatial relationship between the inflow points and the exposure line of zones deformed in a brittle manner, as already mentioned by Keusen et al. (1989). Not all brittle features are water-conducting, but water inflows not bound to a brittle feature were observed only at two locations, L314 and L321. The brittle feature in the host rock responsible for the increased permeability, which is necessary to allow for sufficient water flow, was not identified. The deduced feature most probably ends a short distance behind the tunnel wall.

The ductile deformation has little influence on water percolation (Mazurek, 2000) as the formation of mylonites does not increase the open porosity (Bossart and Mazurek, 1991). Thus, it is primarily the brittle deformation that is responsible for increases in the permeability (Caine et al., 1996; Kull et al., 1993). As mentioned above, brittle deformation often reactivates ductile deformed zones. This reactivation is heterogeneously distributed among the ductile shear zones (Bossart and Mazurek, 1991). In order to estimate the heterogeneity of the brittle reactivation the channelling fraction was recorded. This expresses the fraction along the circumference of the gallery of a specific feature, which is water conducting. Most of the water conducting features are very short (>50 cm) and in general the entire feature was water conducting. In the case of longer water conducting features, mostly the part of the feature close to the bottom was wet. Very rarely water was dripping from the ceiling. This heterogeneous distribution of the water conducting parts in a feature emphasizes the heterogeneity of the water pathways within a brittle feature. The above mentioned heterogeneity of the brittle reactivation in ductile features renders a possible up scaling more complex.

2.8. Summary

The host rock holding the GTS is composed of four rock types: GrGr, CAGr, aplitic dykes and metabasic dykes. Whereas the GrGr, CAGr and the aplitic dykes form a calc-alkaline differentiation series, the magmatic origin of the metabasic dykes is manifold. Some of them may represent a primitive intermediate of the Haslital magmatic suite. Even though the CAGr is more differentiated than the GrGr, the contact between the two rock types is gradual and marked by numerous schlieren, which implies a coeval magmatic state and emplacement. Therefore, instead of drawing the contact between the two as a sharp line, it is mapped as an intermediate rock type. Certainly, the two rock types differ sufficiently to make it possible and reasonable to differentiate between predominantly GrGr-composed areas and predominantly CAGr-composed areas.

Petrographically speaking, it is mostly the change in biotite content that expresses the transition between the different members of the Haslital group and thus was used as a mapping criterion. Other than that, the rocks show up to cm-sized feldspar grains and smaller quartz grains. The greenschist metamorphism yielded in saussuritization of the plagioclase and sericitization of the K-feldspars. Epidote is found as vein material, as a breakdown product of feldspars and within the matrix of metabasic dykes.

The ductile Alpine deformation is portrayed by increased foliation and by numerous planar ductile shear zones. The number of ductile shear zones increases southwards with increasing biotite content and strain gradient (Wehrens, 2015). The orientation of Alpine deformation structures is similar to the orientation of magmatic deformation structures, which points to a magmatic preconditioning of the location of Alpine deformation. Furthermore, some Alpine ductile shear zones show large length/width ratios which suggest brittle precursor structures.

Uplift causes a decrease in temperature and pressure and, as a result, deformation shifts from the ductile regime to the brittle regime. Brittle structures overprint ductile structures via brittle fracturing or cataclasis. The products are fault gouge, cohesive cataclasites and brittle fractures.

This late brittle overprint governs today’s water flow pattern in the rock mass. Nearly all mapped water inflow points in the GTS correlate spatially with a brittle structure. This is evidence for the well-known correlation between brittle deformation and permeability increase in low-porosity crystalline rock formations.

Further work should be done on a petrogenetic model of the metabasic dykes and their influence on the localization of deformation, both ductile and brittle. Furthermore, the small-scale characterization of the link between water flow paths and brittle deformation would allow for more specific and more accurate extrapolations and predictions of fluid pathways through the rock mass.

2. App. Geochemical analyses of metabasic dykes

Table 2.A-1. Major elements of selected metabasic dykes in the GTS.

Sample	SiO_2 wt-%	TiO_2 wt-%	Al_2O_3 wt-%	Fe_2O_3 wt-%	MnO wt-%	MgO wt-%	CaO wt-%	Na_2O wt-%	K_2O wt-%	P_2O_5 wt-%	Sum %
L058	51.57	1.17	16.19	8.87	0.21	8.02	4.99	2.95	6.2	0.38	100.82
L107	43.7	1.5	19.79	12.75	0.38	7.84	1.63	1.31	9.48	0.29	99.02
L059	51.04	1.16	16.39	8.89	0.18	7.43	8.5	1.68	4.09	0.37	99.98
L037	54.58	1.12	17.42	8.71	0.21	6.79	3.05	3.09	5.09	0.44	100.68
W120	58.71	0.82	15.63	6.14	0.12	5.23	6.15	2.84	3.33	0.35	99.52
L176	50.12	1.29	15.58	9.48	0.2	8.36	1.02	0.58	7.7	0.42	94.92
L085	49.93	1.36	17.37	9.52	0.18	6.82	8.71	2.33	3.08	0.45	99.99
W91	49.32	1.33	16.88	10.03	0.21	8.64	4.11	2.43	5.83	0.44	99.48
L115	57.83	1.19	17.42	8.36	0.16	4.29	5.32	3.87	3.11	0.41	102.17
L023	64.84	0.88	11.9	7.73	0.22	5.51	1.33	1.72	5.15	0.35	99.79
L030	46.8	1.31	19.3	11.08	0.32	8.32	1.43	0.47	9.32	0.51	99.14
W092	56.41	1.51	19.77	10.66	0.22	8.58	10.12	2.79	2.19	0.49	112.94
L083	57.31	1.19	14.7	8.57	0.21	6.68	2.03	1.27	6.56	0.43	99.2
L057	50.49	1.24	17.39	8.88	0.16	6.16	10.68	1.79	1.58	0.47	99.04
L125	59.36	1.25	15.23	8.5	0.18	5.63	1.69	2.42	4.68	0.41	99.52

Table 2.A-2. Trace elements of selected metabasic dykes in the GTS.

Name	Ba ppm	Cr ppm	Cu ppm	Nb ppm	Ni ppm	Pb ppm	Rb ppm	Sr ppm	V ppm	Y ppm	Zn ppm	Zr Ppm
L058	833	352	24	16	131	31	453	185	268	28	144	182
L107	958	430	2	38	138	19	881	94	254	33	329	231
L059	428	367	60	15	146	32	357	496	273	29	118	186
L037	505	236	29	15	135	17	355	174	232	25	133	130
W120	435	176	11	12	38	29	275	551	134	24	100	185
L176	487	49	13	18	28	10	453	32	224	57	151	187
L085	570	234	47	13	107	27	145	613	302	29	103	176
W91	625	320	18	18	142	19	531	245	262	31	160	203
L115	644	62	62	14	33	34	149	463	229	33	136	226
L023	249	187	19	14	117	14	455	45	187	24	150	100
L030	614	273	37	21	159	17	1144	26	266	27	221	149
W092	429	274	24	16	127	12	120	425	310	31	160	188
L083	1024	218	3	17	123	16	456	131	227	29	157	141
L057	265	181	36	11	100	34	79	772	289	27	100	151
L125	816	45	5	13	29	10	217	81	221	33	150	183

Chapter 3

Long-term chemical composition and evolution of groundwater in crystalline bedrock: A case study (Grimsel, Switzerland).

Raphael Schneeberger[1], Urs K. Mäder[1], H. Niklaus Waber[1], Florian Kober[2], Alfons Berger[1] & Marco Herwegh[1]

[1]: Institute of Geological Sciences, University of Bern, Switzerland
[2]: Nagra, Wettingen, Switzerland

Abstract Groundwater in crystalline rocks is ubiquitous and knowledge of its flow behaviour is of paramount importance for technical projects such as underground constructions, geothermal energy, groundwater supply or the deep disposal of radioactive waste. In crystalline rocks, water-rock interactions are limited by slow reaction kinetics and low solubility of the majority of minerals occurring along the flow paths. As a result, crystalline groundwater is commonly of low mineralisation also at long residence times, except for situations where mixing with higher mineralised groundwater occurs. In spite of the limited reactivity of crystalline rocks, the composition of crystalline groundwater differs as a function of the mineralogy along the flow paths what allows deciphering different groundwater flow regimes.

In an attempt to decipher recharge areas, recharge conditions and connectivity of fracture networks, we monitored fracture groundwater from different test intervals in boreholes in the underground laboratory at the Grimsel Test Site (GTS, Switzerland) and compared them to older data of similar locations. Over the two years period and – where literature data is available – over more than 20 years, the chemical composition of the fracture groundwater remained constant at specific locations, but differs as a function of host rock. Fracture groundwater collected from the Central Aar granite (CAGr) persistently differs in pH, concentrations of Na^+, Ca^{2+}, Cl^-, Li^+, and $\delta^{18}O$, δ^2H values compared to that collected from the Grimsel granodiorite (GrGr). This suggests that groundwater mixing along flow paths from different fracture networks is virtually absent.

In both host rocks, fracture groundwater is of meteoric origin with minimum ^3H-residence times of more than 50 years. The degree of mineral reaction differs between the host rocks and their water-conducting zones and mineral reactions include dissolution of plagioclase, fluorite, muscovite and pyrite, and the precipitation of quartz, kaolinite and K-montmorillionite. In addition, calcite may be dissolved or precipitated depending on the progress of plagioclase hydrolysis. Based on the similarity in host rock mineralogy and comparable flow rates in water-conducting zones, the differences in fracture groundwater mineralisation are attributed to differences in groundwater residence time related to the larger overburden of the Grimsel granodiorite and thus longer pathways of groundwater in this host lithology.

3.1. Introduction

Fracture groundwater in crystalline environments with little topography is characterised by increasingly alkaline pH conditions and evolves from slightly alkaline (pH 7-8) and Ca-(Na)-HCO_3 recharge water to higher pH (8-9) and Na-(Ca)-CO_3 groundwater in a granitic batholith in the Canadian Shield (Gascoyne, 2004) or from a Ca-HCO_3 (<300 m depth) groundwater to a Na-Ca-Cl groundwater (> 700 m depth) within granitic host rock of the Scandinavian shield (Nordstrom et al., 1989). In contrast to crystalline environments lacking topography, groundwater has been described as high-pH Na-TIC water, with lower chloride concentration (e.g. Bucher et al., 2012; Bucher and Stober, 2010; Ofterdinger et al., 2004; Pastorelli et al., 2001; Seelig and Bucher, 2010; Wanner et al., 2017).

Given the fractured nature of crystalline rocks the chemical evolution of crystalline groundwater is controlled to a large degree by mixing of differently evolved groundwater from different fracture networks (e.g. Edmunds et al., 1985; Gimeno et al., 2014). Water-rock interactions experienced by the individual end-members commonly include the dissolution of primary quartz, Al-silicate minerals and dissolution / precipitation of calcite combined with the formation of secondary hydrated-aluminosilicates, e.g. kaolinite, and quartz depending on the geological setting (e.g. Banks and Frengstad, 2006; Bucher and Stober, 2010; Gascoyne, 2004; Gimeno et al., 2014; Nordstrom et al., 1989; Ofterdinger et al., 2004; Seelig and Bucher, 2010; Wanner et al., 2017). In addition to mixing of differently composed groundwaters in different fracture networks, exchange with porewater residing in the low-permeability rock matrix notably modifies the groundwater compositions with increasing residence time (Waber et al., 2012; Waber and Smellie, 2008).

Water conducting zones in crystalline rocks are restricted to brittle deformation features. These features allow advective flow of groundwater (e.g. Bense et al., 2013; Caine et al., 1996; Evans et al., 1997; Lützenkirchen, 2002; Mazurek, 2000; Zhu and Wong, 1997; Zoback and Byerlee, 1975). It is commonly agreed that permeability decreases with an increasing overburden (Bucher and Stober, 2010; Martin and Follin, 2011; Saar and Manga, 2004). For example in the Oregon Cascades, the permeability decreases from ca. 10^{-10} m^2 at 200 m depth to 10^{-20} m^2 at 10 km depth (Saar and Manga, 2004). Thus, the occurrence of potential fluid pathways related to brittle deformation structures decreases non-linearly with increasing depth. The decrease in permeability with depth directly influence the residence time of the groundwater and consequently also the degree of groundwater mineralisation.

In this study, we utilise the data set from the Grimsel Test Site (GTS) collected since 1980s and enlarged over the last years to inspect the different factors influencing the groundwater composition in Alpine crystalline basement rocks characterised by a distinct topography. The GTS is an underground rock laboratory run by the Swiss National Cooperative for the Disposal of Radioactive Waste (Nagra). It is petrographically, structurally and geochemically well characterized at small and large scale and thus allows for the testing and refining of concepts of groundwater flow and water-rock interactions in a rugged crystalline rock environment. The excellent 3D rock outcrop conditions in the underground facility offer the possibility to study both the spatial and temporal characteristics of fluid pathways from surface recharge to depth. Over the last three years groundwater was collected from several packed-off intervals in boreholes drilled in different host rocks at variable overburden. The deformation structures that act as water-conducting features are described in detail by Schneeberger et al. (2016). Groundwater chemical and isotope compositions are used in combination with structural and mineralogical data and geochemical inverse and forward modelling approaches to decipher the recharge area, groundwater flow paths and their connectivity in the individual host rocks.

3.2. Hydro-geological setting

3.2.1. Geological Setting

The GTS is located in the upper part of the Hasli valley in the Central Swiss Alps within the Aar massif (Fig. 3.1). The Aar massif is composed of Palaeozoic basement rocks, Late to Post-Variscan intrusives and Mesozoic cover rocks (Abrecht, 1994; Berger et al., 2017a; Labhart, 1977; Schaltegger, 1994). Two main lithologies occur within the GTS, the Central Aar granite (CAGr) in the northern sections and the Grimsel granodiorite (GrGr) in the southern domain (Keusen et al., 1989). Metabasic dykes intrude into the granitoid rocks (Oberhänsli, 1986; Schneeberger et al., 2016). Both the CAGr and GrGr have been age dated to 299 ± 2 Ma (Schaltegger and Corfu, 1992) and are part of a Late to Post-Variscan calc-alkaline differentiation suite (Schaltegger, 1994).

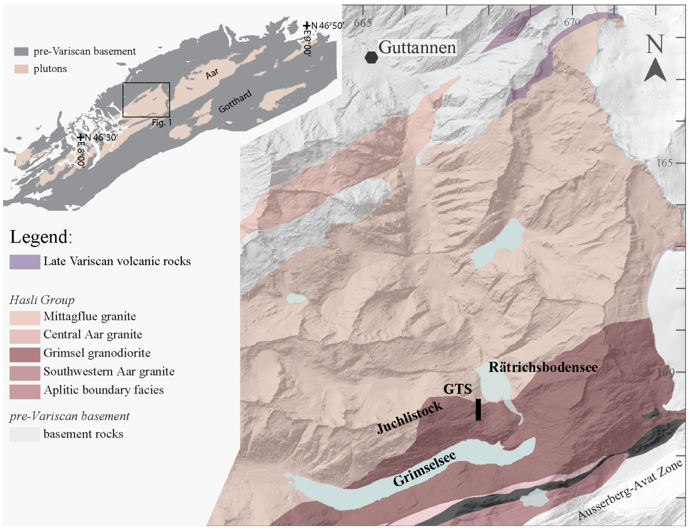

Figure 3.1. Regional geological map based on Berger et al. (2017b).

3.2.2. Mineralogy

The CAGr differs mainly from the GrGr by the biotite, white mica and plagioclase content (Keusen et al., 1989; Schneeberger et al., 2016; Wehrens et al., 2017). Metabasic dykes, however, are mainly composed of biotite and feldspars (Keusen et al., 1989; Oberhänsli, 1986) and thus differ substantially in composition.

Table 3.1. Mineralogy of the different rock types around GTS. The units are [wt-%] unless specified. Data for CAGr and metabasic dyke (MBD) is from Keusen et al. (1989), the data for GrGr from Mäder and Ekberg (2006).

Property / mineral	CAGr	GrGr			MBD
	Host rock	Host rock	Mylonite	Fault gouge	Host rock
Quartz	32.0 [vol-%]	31	27	22	
K-feldspar	34.1 [vol-%]	28	17	18	0-10 [vol-%]
Plagioclase	20.9 [vol-%]	25	18	17	10-25 [vol-%]
Biotite	5.5 [vol-%]	8	10	12	50-70 [vol-%]
Chlorite (metamorphic)	1 [vol-%]	0.1	0	0	
Muscovite	1 [vol-%]	6	24	27	
Epidote	2.3 [vol-%]	0.4	0.3	0.3	10-20 [vol-%]
Titanite	0.2 [vol-%]	1	0.3	0.3	
accessories	< 1 [vol-%]	0.2	3	3	
Smectite (hydrothermal)		0	0.2	0.2	
Chlorite (clay mineral)		0	0.1	0.1	
Illite / smectite mixed layers		0	0.1	0.1	
Surface, external (BET) [m^2/g]		0.5-1.3	0.6-1.5	0.7-1.6	
Surface, total (EGME) [m^2/g]		5	11	10	

Most of the magmatic minerals are transformed either by Alpine metamorphism or earlier phases of metamorphism. Alpine metamorphism reached greenschist facies conditions in the study area (Challandes et al., 2008; Frey, 1980; Keusen et al., 1989). Major mineral alterations are: (i) sericitization of K-feldspar, (ii) saussuritization and albitisation of plagioclase, (iii) and the presence of, partially chloritized, biotite. These transformations lead to the observed mineral compositions: Biotite is composed of 59% phlogopite and 41% annite; plagioclase contains 95% albite and 5% anorthite; K-feldspar is a mixture of 97% orthoclase and 3% albite (Schneeberger et al., 2016).

Furthermore, pyrite was observed in certain thin sections (Schneeberger et al., 2016). In only few locations smectite was detected within brittle fault rocks (Mäder and Ekberg, 2006; Wehrens et al., 2016).

In addition, enhanced sheet silicate (biotite and muscovite, Tab. 3.1) concentrations are reported in highly deformed ductile zones (Mäder and Ekberg, 2006; Wehrens et al., 2017), leading to differences between matrix rock composition and fault rock composition.

One last important mineralogical entity is formed by the Alpine clefts, which are related to Alpine deformation history and postdate metamorphism. They are filled with quartz, adularia, chlorite, fluorite, minor calcite, and rarely sulphides, surrounded by leached wall rock depleted in quartz and biotite (Keusen et al., 1989).

3.2.4. Deformation history

The bedrock of the Aar massif records Alpine solid-state deformation (Challandes et al., 2008; Choukroune and Gapais, 1983; Herwegh et al., 2017; Keusen et al., 1989; Rolland et al., 2009; Steck, 1968; Wehrens, 2015). Alpine ductile deformation is expressed by a pervasive foliation and discrete high strain shear zones, which increase in frequency towards the south, i.e. the GrGr shows more intense ductile deformation than the CAGr (Choukroune and Gapais, 1983; Rolland et al., 2009; Wehrens et al., 2017). Ductile shear zones related to Alpine deformation are planar, steeply SE, S or SW dipping, and show widths of few centimetres up to several meters (in few cases tens of meters) with lateral extensions in the range of km to tens of kilometres (Herwegh et al., 2017; Wehrens et al., 2017). In the case of the GTS, shear zones range from 50 cm to maximal 3.5 m in width.

On-going exhumation of the Aar massif led to cooling and to brittle overprint of formerly ductile shear zones (Baumberger, 2015; Michalski and Soom, 1990; Vernon et al., 2008; Wehrens et al., 2016). Brittle deformation is expressed by fractures, cataclasites and fault gouges that are mostly younger than 8 Ma (Kralik et al., 1992; Pleuger et al., 2012).

Ductile shearing as well as subsequent brittle faulting resulted in a decrease in grain size within deformed rocks compared to the pre-Alpine host rock (Fig. 3.2). This grain size reduction within fault rocks resulted in an increase of reactive mineral surface areas and thereby catalyses water-rock interactions.

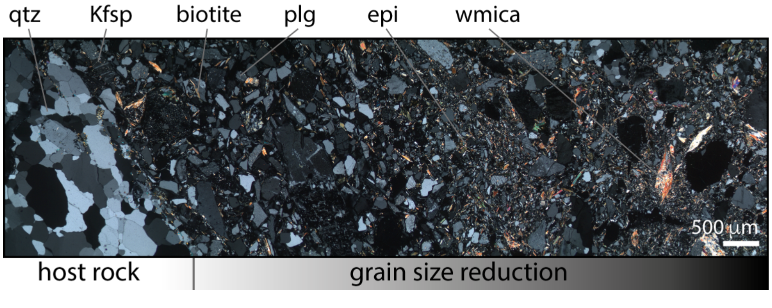

Figure 3.2. Brittle fault zone bordering a quartz aggregate. qtz: quartz, Kfsp: K-feldspar, plg: plagioclase, epi: epidote, wmica: white mica.

Latest deformation features are exfoliation joints, which are formed by a combination of denudation, glacial carving and deglaciation-induced unloading and affect the uppermost 200 m of the bedrock

(Ziegler et al., 2013). Such depth interval is comparable to that observed in granitoid rocks with little topography in the Scandinavian Shield at Forsmark, Sweden (Martin, 2007). Forming an interconnected network of tensile fractures these youngest deformation features are thought to constitute the dominant infiltration pathways for meteoric recharge in the upper part of the rock mass.

3.2.4. Hydraulic regime

The GTS is located next to an access tunnel built for the local hydropower plant. This tunnel was completed by 1954. The GTS is operational since 1984. For the last 63 years, the tunnels from artificial pressure sinks in the rock mass and drain the mountainside (Bucher et al., 2012; Maréchal and Etcheverry, 2003), potentially resulting in a transient state. This transient state is illustrated in borehole interval pressures decrease reported for the period 1980-1987 (Wyss, 1989).

The hydraulic regime around GTS has been reported previously (e.g. Frick et al., 1992; Frieg and Blaser, 2012; Hoehn et al., 1990; Keppler, 1994; Voborny et al., 1991) as heterogeneous with low porosity rock matrix (porosity: 0.8-1.53 vol%) and higher porosity faults (ca. 10-30 vol%; Bossart and Mazurek, 1991). An average hydraulic conductivity for test intervals sampling rock matrix is ca. 10^{-10} m s^{-1} (Hoehn et al., 1998). Transmissivity values obtained for selected borehole test intervals are indicated in Table 3.2. From hydraulic modelling it is known that the GTS forms a pressure sink and drains the mountainside, whereas in "undisturbed" conditions the river Aare in the valley floor would act as sink (Voborny et al., 1991).

3.3. Sample Locations and Methods

3.3.1. Sampling locations

For the long-term monitoring 14 test intervals from previously drilled boreholes within the underground facility covering different structural and lithological features were selected (Fig. 3.3). The test intervals are isolated by standard hydraulic packers and connected by polyamide or steel tubes with the gallery instrumentation for water sampling and hydraulic testing. Test intervals along the selected boreholes were classified, based on available geological information (Geotest AG, 1981; Mäder and Ekberg, 2006; Vomvoris et al., 1992). The classification aimed at the distinction of mineralogical differences along water-conducting features that potentially result in differences in groundwater chemical compositions. The first criterion was the occurrence of metabasic dykes, CAGr or GrGr. If no metabasic dyke was identified within the test interval then the test interval was classified based on the occurrence of fault gouge, ductile shear zone and / or brittle fractures. In this classification the amount of fault gouge may be underestimated, because specific drilling techniques are required to retrieve fault gouge in drill core samples. Only borehole G was drilled accordingly, whereas other boreholes were drilling without focus on core recovery.

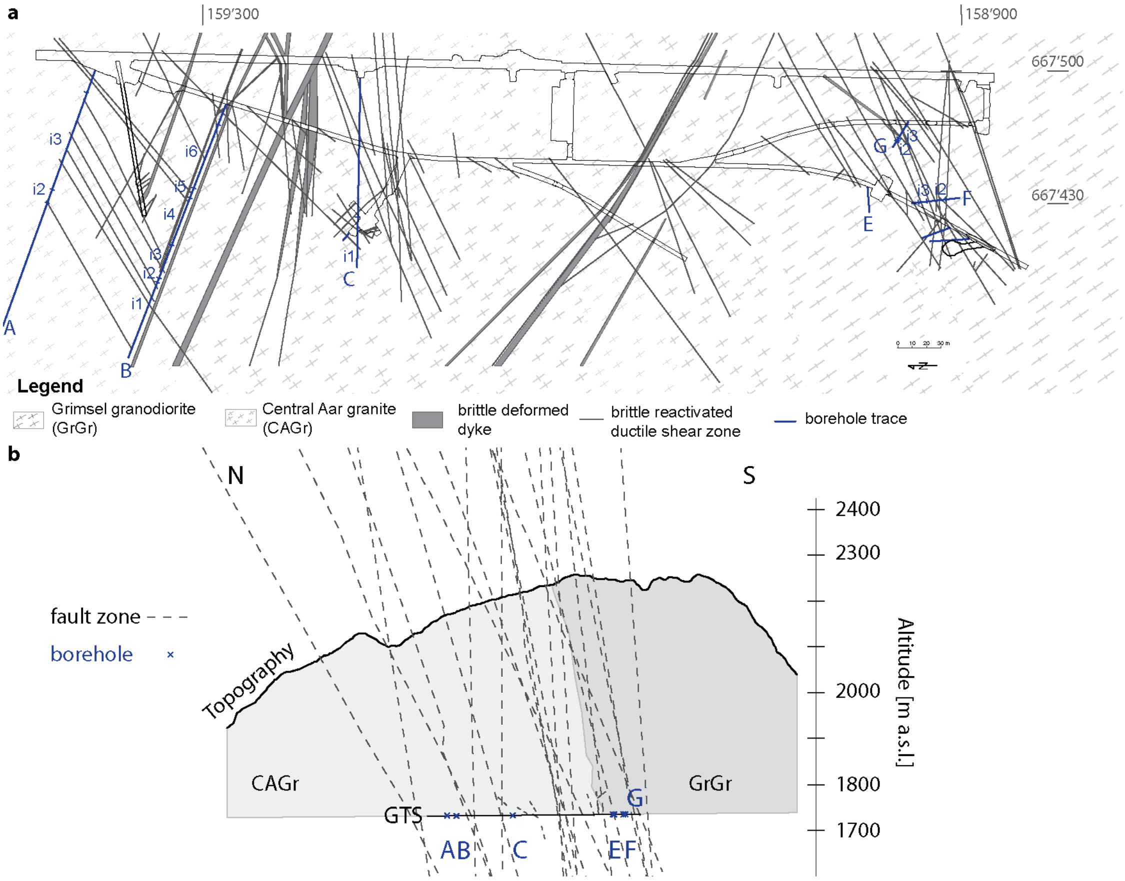

Figure 3.3. GTS map (a) and underground facility parallel cross section (b) showing the topography and occurring faults that crosscut the entire bedrock. Sampled boreholes are labelled in blue. A = BOUS 85.001, B = BOUS 85.002, C = SB 80.001, E = VE 13.001, F = VE 88.003, G = HP 98.007.

3.3.2. Groundwater sampling

Groundwater was sampled from hard polyamide or stainless steel flow lines installed during emplacement of the packers to delimit the test intervals. Interval pressures were monitored with pressure gauges mounted on the outflow lines.

Samples were taken with a 50 ml syringe directly from the outflow valve from the sampled test interval in order to prevent air contamination. Samples for cations, anions, and stable water isotopes were filtered with a 45 μm CE filter into a 30 ml or 125 ml polypropylene (PP) bottle. Cation samples were acidified with HNO_3 to prevent precipitation. Samples for total inorganic/organic carbon (TIC/TOC) were taken unfiltered in a PS bottle.

3.3.3. Chemical and isotope analyses

On-site measurements included temperature, pH, Eh, and electric conductivity [EC]. All these parameters were measured in-line during sampling of each test interval with electrodes mounted in a flow-through chain (Mäder and Ekberg, 2006) to avoid atmospheric contamination with respect to pH and Eh measurements.

Chemical analyses of own samples were performed at Institute for Geological Sciences, University of Bern. Major anions and cations (F^-, Cl^-, Br^-, NO_3^-, SO_4^{2-}, Na^+, NH_4^+, Ca^{2+}, K^+, Sr^{2+}, Mg^{2+}) were analysed by ion chromatography (Metrohm 850 Professional IC). The detection limit is 0.016 mg/L for anions and 0.1 mg/L for cations, with an analytical uncertainty of ± 5%. Concentrations of K^+, Mg^{2+} and Sr^{2+}, which are close to or below the detection limit by IC techniques, were re-analysed along with trace elements (Al^{3+}, Si, Mn_{tot}, Fe_{tot}) using inductively coupled plasma optical emission spectrometry (ICP-OES, Varian 720-ES). Detection limits of this technique are 1 µg/L for Sr^{2+} and Fe_{tot}, and 5 µg/L for K^+, Mg^{2+}, Al^{3+}, Si, and Mn_{tot} with an analytical uncertainty of ± 5–10% depending on element concentration and sample matrix. Concentrations of Si were additionally determined by colorimetric techniques using a spectro-photometer (Varian UV/VIS Cary 50) in order to avoid any colloidal Si. The detection limit for Si is 0.005 mg/L with an analytical uncertainty of ± 5%. Li^+ concentration was measured via graphite furnace atomic absorption spectroscopy (GFAAS) with a detection limit of 1.25 µg/L and an analytical uncertainty of ± 5%. Total inorganic and organic carbon concentrations were determined using a TIC/TOC analyser (Analytic Jena multi N/C 2100S) with a detection limit of 0.1 mg/L for total carbon and an analytical uncertainty of ± 5%. The amount of total organic carbon was deduced from the difference between total carbon and total inorganic carbon. Stable water isotopic compositions were analysed by cavity ring down spectroscopy (Picarro) and are reported relative to VSMOW standard as $\delta^{18}O$, δ^2H. Analytical uncertainty (2σ) is 0.1‰ VSMOW for $\delta^{18}O$ and 1.5 ‰ VSMOW for δ^2H. Samples for Tritium were analysed by Hydroisotop GmbH via liquid scintillation spectroscopy after electrolytic enrichment, with a detection limit of 0.6 TU.

3.3.4. Geochemical modelling

Geochemical model calculations were conducted using the software PhreeqC (Parkhurst and Appelo, 2013) with the thermodynamic database Wateq4F (Ball and Nordstrom, 1992 updated version 2005-08-23). Initial modelling included speciation and saturation index calculations for quality control, and to correct for sampling artefacts, as in gassing of atmospheric CO_2. Saturation indexes were calculated based on field pH measurements and carbon was integrated from the measured TIC concentration after correction for potential in-gassing of CO_2.

Element mass-balance calculations (inverse modelling) were done using the software NETPATH (Plummer et al., 1994) to identify major water-rock interactions that may occur from precipitation infiltration to the groundwater sampled at depth (Garrels and Mackenzie, 1967).

Forward modelling approaches implementing reaction kinetics were performed using PhreeqC in order to evaluate the results of the mass-balance approach and to elucidate the time scales that may be involved in the groundwater evolution. Kinetic rates for the different minerals reactions were taken from the Wateq4F database (Ball and Nordstrom, 1992), and additional rates are from Palandri and Kharaka (2004). Models were run for 100 years at a constant temperature of 12°C.

3.4. Results

3.4.1. Sampling sites

Six boreholes (A-C, E-G; Fig. 3.3) were chosen from the existing boreholes at the GTS for sampling. Boreholes (A, B, C) are located within the CAGr, whereas boreholes (E, F, G) are located within the GrGr. Test intervals were isolated by multi-packer systems, boreholes A and B were instrumented in 1996, boreholes C and F in 1994, borehole E in 2013, and borehole G in 2000. Multiple test intervals in the same borehole are labelled with increasing numbers from deepest interval (i1) towards the borehole mouth. Test interval lengths vary from 0.4 to 60.5 m (Tab. 3.1).

During six groundwater sampling campaigns, performed in April, August, October 2014, January, August 2015, and January 2016, 75 groundwater samples were taken. Time series of sample per locality were taken in order to discriminate analytical artefacts from natural variations.

3.4.2. Physical parameters measured onsite

Flow rates vary greatly between the different test intervals (Geotest AG, 1981; Keppler, 1994; Keusen et al., 1989; Vomvoris et al., 1992). The flow rate in the Ci1 interval is strikingly higher compared to other passive outflow rates measured within GTS (4 L/min; Tab. 3.2).

Water samples from the northern CAGr-dominated section (CAGr waters) show on average lower temperatures (12.4°C ± 0.6°C; Tab. 3.2) and have a smaller overburden (Fig. 3.3) compared to groundwater sampled in the southern, GrGr-dominated domain (13.5°C ± 0.9; GrGr waters).

Table 3.2. Compilation of physical properties describing sampled test intervals and their groundwater. Yields and transmissivity values are taken from literature (Geotest AG, 1981; Hoehn et al., 1990; Keppler, 1994; Keusen et al., 1989; Vomvoris et al., 1992). BF: brittle fault, DS: ductile shear zone, FG: fault gouge, MD: metabasic dyke.

Sample ID	Host rock	Geology	Interval length	Interval diameter	Samples	EC	flow rate	Transmissivity	Overburden
			[m]	[m]	nb	[µS/cm]	[ml/min]	[m^2/s]	[m]
Ai2	CAGr	BF	9.5	0.101	6	69.3-74.7	n.m.	1.5e-9	445
Ai3	CAGr	DS	60.5	0.101	4	67.9-74.7	n.m.	2.4e-10	436
Bi1	CAGr	DS	36.27	0.101	2	71.7-78.2	9.4	7.4e-10	494
Bi2	CAGr	DS	2	0.101	6	62.1-70.0	186	1.7e-8	488
Bi3	CAGr	MD	20	0.101	6	63.2-67.0	16.5	7.0e-9	485
Bi4	CAGr	MD	29	0.101	6	61.5-65.5	162	6.0e-8	479
Bi5	CAGr	DS	5	0.101	6	59.4-62.2	31	4.2e-8	474
Bi6	CAGr	DS	40	0.101	6	64.1-67.0	264	1.8e-6	468
Ci1	CAGr	DS	28	0.086	6	58.2-63.8	4000	n.m.	482
Ei2	GrGr	DS	0.4	0.086	3	69.1-71.8	n.m.	n.m.	518
Fi2	GrGr	MD	13.5	0.086	6	65.7-127.5	n.m.	2.7e-9	499
Fi3	GrGr	DS	5	0.086	6	63.1-70.9	n.m.	6.6e-11	510
Gi2	GrGr	FG	0.65	0.086	6	63.8-73.5	6	2.4e-8	518
Gi3	GrGr	BF	1	0.086	6	64.6-71.8	n.m.	1.8e-8	518

3.4.3. Modern chemical composition of groundwater

Groundwater is of low total mineralisation with total dissolved solids (TDS) between 48.4 and 81.4 mg/L and remained nearly constant in all sampled intervals over the two years of sampling (Fig. 3.4). However, borehole A (Ai2 and Ai3) is characterized by higher TDS (Fig. 3.4).

The range in chemical composition of each sampled test interval is reported in Tables 3.3 and 3.4.

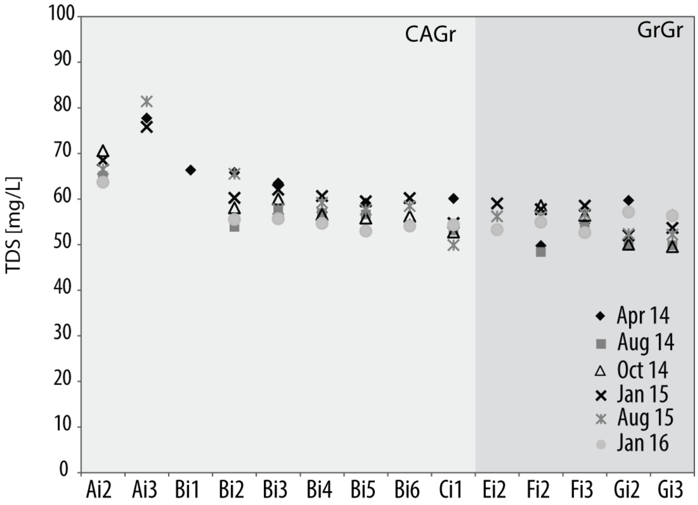

Figure 3.4. Total mineralisation (TDS) of groundwater for each sampling campaign plotted against the location of the borehole test interval from N to S in the GTS.

Table 3.3. Ranges in composition of groundwater collected between April 2014 and January 2016 from the different borehole test intervals within the CAGr. The borehole test intervals are listed from N to S. (n.m. not measured).

Entity	Units	Ai2	Ai3	Bi1	Bi2	Bi3	Bi4	Bi5	Bi6	Ci1
T	°C	11.6-13.0	11.9-13.8	11.5	11.7-13.2	11.8-13.0	11.9-13.2	11.8-13.1	11.8-13.6	12.3-13.7
pH		7.27-8.13	6.62-6.83	9.08	9.08-9.37	8.54-9.38	8.80-9.40	8.85-9.40	9.15-9.61	8.52-9.43
Eh (Ag/AgCl)	mV	-170 to -46	93 to 186	-176	-238 to -81	-234 to -115	-248 to -17	-235 to -19	-233 to 2	-189 to 147
Li^+	µg/L	18.4-21.5	21.1-21.4	n.m	7.7-8.2	6.2-8.4	7.0-8.0	6.6-7.7	13.8-20.1	7.4-8.8
Na^+	mg/L	12.25-12.57	15.00-15.15	10.17	9.75-10.32	8.94-9.30	8.97-9.27	8.42-8.64	9.30-10.58	6.29-6.63
K^+	mg/L	0.20-0.32	0.16-0.86	0.16	0.36-0.48	0.14-0.16	0.12-1.73	0.22-0.34	0.11-0.18	0.20-0.24
NH_4^+	mg/L	<0.1	<0.1	<0.1	<0.1	<0.1	<0.1	<0.1	<0.1	<0.1
Mg^{2+}	mg/L	0.004-0.338	0.023-0.035	0.023	0.024-0.026	0.023-0.024	0.020-0.023	0.016-0.018	0.012-0.016	0.041-0.043
Ca^{2+}	mg/L	6.35-6.95	4.38-4.72	8.86	6.72-7.04	7.79-9.60	7.37-7.69	7.33-7.60	6.58-7.27	8.43-9.24
Sr^{2+}	mg/L	0.13-0.16	0.11-0.12	0.21	0.18-0.20	0.21-0.24	0.22-0.25	0.18-0.20	0.17-0.18	0.16-0.17
Fe_{tot}	mg/L	0.697-1.949	<0.005-0.032	0.023	0.06-0.016	0.007-0.009	<0.005-0.011	0.006-0.041	<0.005-0.009	<0.005-0.009
Mn_{tot}	mg/L	0.019-0.051	<0.005-0.026	<0.005	<0.005	<0.005	<0.005	<0.005-0.005	<0.005-0.009	<0.005
Al^{3+}	mg/L	<0.001-0.80	<0.001-0.022	0.041	0.012-0.018	<0.001-0.006	<0.001-0.013	<0.001-0.004	0.005-0.017	0.028-0.057
F^-	mg/L	5.76-5.92	6.08-6.20	5.54	4.53-4.96	4.24-4.44	4.17-4.31	3.86-4.00	4.73-4.96	3.67-3.79
Cl^-	mg/L	0.83-0.87	0.69-0.79	0.44	0.34-0.36	0.31-0.32	0.33-0.44	0.27-0.31	0.33-0.66	0.22-0.52
Br^-	mg/L	<0.016	<0.016	<0.016	<0.016	<0.016	<0.016	<0.016	<0.016	<0.016
SO_4^{2-}	mg/L	6.79-7.30	7.12-7.27	8.67	5.52-6.48	6.35-6.58	5.98-6.76	6.17-7.10	7.34-7.77	6.99-11.05
NO_3^-	mg/L	0.032-0.764	0.020-0.061	<0.016	0.024-0.043	0.031-0.045	0.017-0.041	0.026-0.042	0.018-0.053	0.030-0.803
Tot. Alk.	meq/L	0.51-0.73	0.49-0.76	0.63	0.50-0.81	0.52-0.87	0.50-0.85	0.49-0.83	0.50-0.69	0.48-0.83
TIC	mg/L	5.58-6.81	6.45-6.72	5.97	4.51-5.86	4.81-6.34	4.74-6.09	4.70-6.04	4.33-5.10	4.35-5.52
Si	mg/L	3.28-3.87	3.66-4.28	4.82	4.67-5.19	4.35-5.08	4.35-5.04	4.30-4.59	4.39-5.02	4.04-4.68
TDS	mg/L	63.7-70.6	75.8-81.4	66.3	53.9-60.3	55.6-63.5	54.6-60.6	53.0-59.50	54.1-60.2	49.9-60.1

Table 3.4. Ranges of composition of groundwater collected from the different borehole intervals within the GrGr and for a surface water ("Totensee"). The intervals are listed from N to S. (n.m. = not measured).

Entity	Units	Ei2	Fi2	Fi3	Gi2	Gi3	Totensee
Temp	°C	13.2-14.6	13.2-15.5	12.2-15.0	11.9-13.8	12.1-13.6	12.5
pH		9.19-9.59	9.03-9.78	9.23-9.40	8.85-9.75	9.00-9.79	9.27
Eh (Ag/AgCl)	mV	-92 to -16	-198 to 62	-238 to -91	-203 to -56	-180 to -65	23
Li^+	µg/L	42.8-43.8	28.1-35.5	31.1-32.1	32.0-39.0	33.0-36.4	n.m.
Na^+	mg/L	12.51-12.70	11.05-11.83	11.14-11.83	11.71-12.01	11.78-11.95	0.65
K^+	mg/L	0.28-0.34	0.44-0.57	0.30-0.38	0.37-2.35	0.39-0.52	0.38
NH_4^+	mg/L	<0.1	<0.1	<0.1	<0.1	<0.1	<0.1
Mg^{2+}	mg/L	0.019-0.028	0.018-0.022	0.025-0.036	0.016-0.019	0.016-0.018	0.086
Ca^{2+}	mg/L	5.35-5.53	5.45-6.41	5.58-6.76	4.89-5.90	4.29-5.18	2.27
Sr^{2+}	mg/L	0.19-0.20	0.17-0.25	0.15-0.21	0.16-0.17	0.16-0.17	0.01
Fe_{tot}	mg/L	0.010-0.052	0.005-0.018	0.013-0.360	<0.005	<0.005	<0.005
Mn_{tot}	mg/L	<0.005	<0.005	<0.005-0.007	<0.005	<0.005	<0.005
Al^{3+}	mg/L	0.040-0.082	0.008-0.016	0.007-0.015	0.019-0.020	0.021-0.034	0.011
F^-	mg/L	5.67-5.82	4.12-4.60	5.60-6.06	4.54-4.67	4.53-4.66	0.045
Cl^-	mg/L	2.96-3.14	1.51-1.69	1.90-2.24	1.94-2.01	1.95-2.59	0.285
Br^-	mg/L	0.027-0.03	<0.016	0.019-0.034	0.016-0.024	0.018-0.018	<0.016
SO_4^{2-}	mg/L	4.67-4.81	5.66-7.35	0.45-1.87	4.96-5.12	5.00-5.21	0.876
NO_3^-	mg/L	0.016-0.092	0.025-0.043	0.017-0.047	0.021-0.068	0.016-0.064	0.345
Tot. Alk.	meq/L	0.47-0.61	0.52-0.71	0.56-0.86	0.49-0.61	0.52-0.68	0.37
TIC	mg/L	3.71-4.79	3.91-5.36	4.56-6.27	3.64-5.09	3.61-4.95	1.92
Si	mg/L	4.63-5.27	4.53-5.38	2.87-3.50	4.51-5.21	4.45-5.17	1.02
TDS	mg/L	53.3-59.0	48.4-58.5	52.6-58.5	50.1-59.7	49.6-56.6	15.7

Eh measurements vary between different samplings, however not systematically. This variation may result from analytical difficulties, as the concentrations of redox-sensitive elements (Fe_{tot}, Mn_{tot}) are low in the majority of the measured groundwater. Except for interval Ai3 and first two sampling campaigns (April and August 2014) in Ci1, reducing conditions were measured in all samples (Tabs. 3.3 and 3.4). Reducing conditions are confirmed by smell of HS^- during one sampling in Fi3 and Bi4.

Rust-coloured water during sampling of Ai2 and Ai3 in combination with oxidizing conditions in Ai3 may indicate contamination of borehole A by for example corrosion of the steel tubing. This also may explain the higher TDS observed for those samples (Fig. 3.4). As a contamination cannot be ruled out, borehole A is not considered for further discussion.

Several differences between CAGr and GrGr waters are revealed by the chemical composition (Tabs. 3.3, 3.4; Fig. 3.5). (i) Measured pH is significantly lower in the CAGr (8.53 - 9.61, mean ± σ: 9.16 ± 0.27) waters compared with GrGr waters (8.85 - 9.79, mean ± σ: 9.45 ± 0.23). (ii) Molar Na^+/Ca^{2+} is lower for CAGr waters (2.45 ± 1.04) compared to GrGr waters (3.62 ± 0.56). (iii) Concentrations in

Cl^- and Li^+ are lower in CAGr waters than in GrGr waters. (iv) Calculated partial pressure in CO_2 using the measured TIC concentrations is higher in CAGr waters than in GrGr waters ($P(CO_2)_{[CAGr]} = 10^{-4.72}$ to $10^{-5.13}$ bar; $P(CO_2)_{[GrGr]} = 10^{-4.88}$ to $10^{-5.66}$ bar).

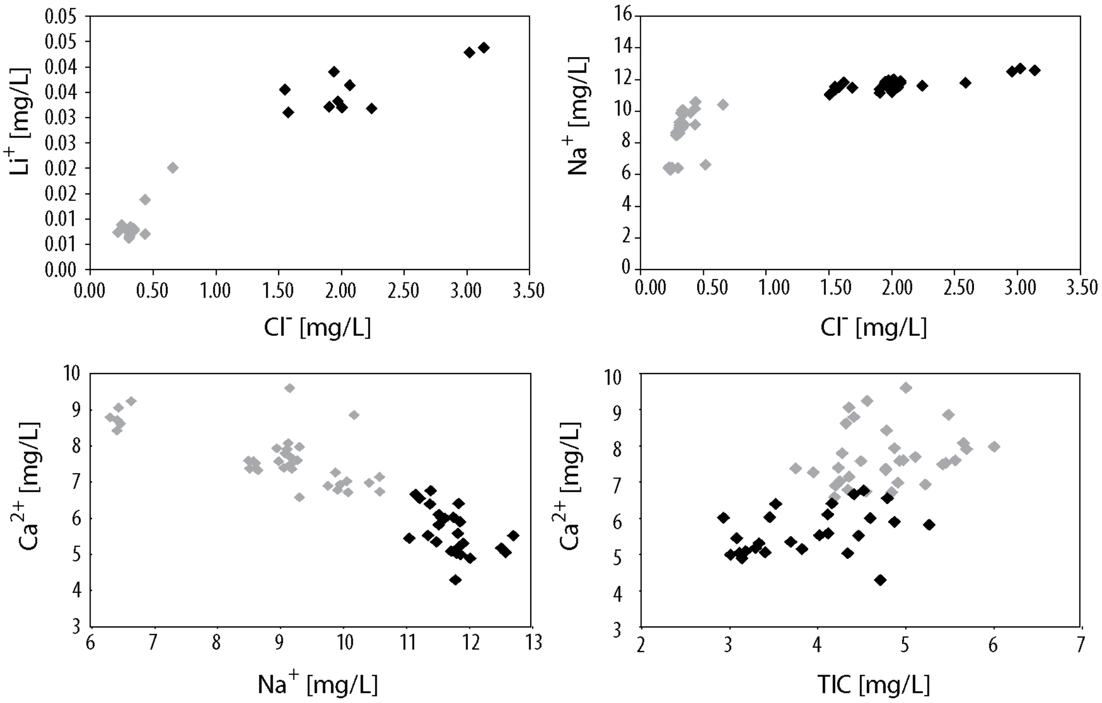

Figure 3.5. Selected ions showing difference in chemical composition between CAGr (grey) and GrGr (black) waters.

Li^+ and Na^+ concentrations are plotted against Cl^- concentration, as Cl^- is considered to be a conservative element (e.g. Nordstrom et al., 1989) and is clearly distinguishable between CAGr and GrGr waters. Cl^- concentration in the CAGr water corresponds closely to the meteoric input (Tab. 3.4). Na^+ and Li^+ seem to correlate linearly with Cl^- in the GrGr waters, this indicates a linked evolution.

Further Ca^{2+} against Na^+ plot shows lower Na/Ca molar ratio for the CAGr waters (Fig. 3.5). The weakly linear relationship between Ca^{2+} and TIC may indicate a common evolution as would be precipitation or dissolution of calcite.

All analysed groundwater samples are saturated with respect to quartz (CAGr waters: median $SI_{quartz} = -0.02$; GrGr waters: median $SI_{quartz} = -0.10$) and calcite (CAGr waters: median $SI_{calcite} = -0.05$; GrGr waters: median $SI_{calcite} = -0.04$). Groundwater is undersaturated with respect to plagioclase, K-feldspar, and fluorite (Tab. 3.5). Saturation indices for kaolinite vary strongly between different sampling locations and range from -1.5 to 1.5 for CAGr and GrGr waters, excluding borehole A (Tab. 3.5). Most of CAGr waters are saturated with respect to kaolinite (median $SI_{kaolinite} = 0.0$). GrGr waters, however, are generally undersaturated in kaolinite (median $SI_{kaolinite} = -0.6$).

Table 3.5. Range of pH and saturation indexes for selected phases per specific interval. Phases containing Al are only reported if Al concentration was above detection limit.

			CAGr							**GrGr**				
	Ai2	**Ai3**	**Bi1**	**Bi2**	**Bi3**	**Bi4**	**Bi5**	**Bi6**	**Ci1**	**Ei2**	**Fi2**	**Fi3**	**Gi2**	**Gi3**
pH	7.27 to 8.13	6.62 to 6.83	9.08	9.08 to 9.37	8.54 to 9.38	8.80 to 9.40	8.85 to 9.40	9.15 to 9.61	8.52 to 9.43	9.19 to 9.59	9.03 to 9.78	9.23 to 9.40	8.85 to 9.75	9.00 to 9.79
Calcite	-2.08 to -1.11	-2.81 to -2.6	-0.09	-0.31 to 0.06	-0.61 to 0.10	-0.43 to 0.07	-0.40 to 0.05	-0.20 to 0.43	-0.70 to 0.19	-0.34 to -0.04	-0.39 to 0.12	-0.10 to 0.04	-0.52 to 0.13	-0.52 to 0.19
Log pCO_2	-3.8 to -3.0	-2.5 to -2.3	-4.7	-5.1 to -4.8	-5.2 to -4.1	-5.2 to -4.5	-5.2 to -4.5	-5.1 to -4.9	-5.2 to -4.2	-5.5 to -5.0	-5.8 to -4.8	-5.2 to -4.9	-5.7 to -4.5	-5.8 to -4.7
Adularia	-1.8	-5.9 to -5.8	-2.0	-2.3 to -2.1	-3.3 to -3.1	-2.9 to -2.0	-3.0	-3.3 to -2.5	-2.6 to -2.1	-2.1 to -1.6	-2.7 to -2.3	-3.4 to -3.1	-2.3 to -1.5	-2.4 to -1.9
Albite	-2.7	-7.0 to -6.4	-2.7	-3.4 to -3.2	-4.0 to -3.9	-3.7 to -3.4	-4.0	-3.9 to -3.2	-3.6 to -3.1	-3.0 to -2.5	-3.8 to -3.5	-4.4 to -4.1	-3.4 to -2.9	-3.5 to -2.9
Anorthite	-3.3	-12.4 to -11.3	-3.6	-4.7 to -4.4	-6.0 to -5.4	-5.1 to -4.7	-5.8	-5.6 to -4.5	-4.1 to -3.5	-4.0 to -3.2	-5.3 to -4.9	-5.9 to -5.3	-4.6 to -4.2	-4.8 to -4.2
$Fe(OH)_3$ (a)	-0.3 to 3.3	-0.6 to 1.5	1.8	0.7 to 1.7	-0.2 to 1.8	0.6 to 1.8	0.8 to 1.9	0.4 to 1.8	0.7 to 1.2	1.2 to 2.0	0.4 to 1.5	0.6 to 1.9	0.2 to 0.8	0.5 to 0.8
Fluorite	-0.42 to -0.13	-0.28 to -0.24	-0.07	-0.35 to -0.30	-0.34 to -0.23	-0.39 to -0.37	-0.45 to -0.42	-0.33 to -0.29	-0.46 to -0.40	-0.28 to -0.26	-0.59 to -0.40	-0.23 to -0.13	-0.51 to -0.40	-0.54 to -0.48
Illite	1.5	-8.1 to -7.3	-1.4	-2.8 to -2.1	-4.0 to -3.7	-3.6 to -2.4	-3.7	-4.3 to -2.6	-2.6 to -1.1	-2.4 to 1.0	-3.8 to -2.7	-4.6 to -3.8	-3.1 to -1.5	-3.3 to -1.6
Kaolinite	5.5	-2.2 to -1.4	1.5	-0.1 to 0.8	-0.9 to -0.1	-0.6 to 1.0	-0.3	-1.1 to 0.4	0.1 to 2.2	0.1 to 1.5	-1.3 to 0.2	-1.5 to -0.8	-0.7 to 1.5	-1.0 to 1.3
Muscovite	8.6	-3.1 to -2.57	4.2	2.4 to 3.4	0.8 to 1.4	1.3 to 3.0	1.4	0.5 to 2.7	2.7 to 4.8	2.9 to 4.6	1.2 to 2.6	0.4 to 1.3	2.0 to 4.3	1.8 to 4.1
Quartz	-0.08 to -0.02	-0.03 to 0.01	0.05	-0.02 to 0.04	-0.02 to 0.05	-0.05 to 0.03	-0.04 to 0.02	-0.06 to 0.02	-0.10 to 0.00	-0.07 to 0.02	-0.16 to -0.02	-0.29 to -0.17	-0.13 to 0.03	-0.14 to 0.00

3.4.4. δ^2H, δ^{18}O, ^{3}H values

Stable water isotopic composition of samples was analysed in order to evaluate conditions of infiltration of groundwater. Measured δ^{18}O and δ^2H values are constant over the two year sampling period. Therefore, the average δ^{18}O and δ^2H values are reported per interval (Tab. 3.6).

Further, they are comparable with values for the precipitation (Fig. 3.6). The mean δ^{18}O and δ^2H value for the precipitation data from 1993 to 2014 is slightly lower ($\delta^{18}O = -13.40$, $\delta^2H = -95.5$) than the measured mean values in the groundwater data (Tab. 3.6). However, the sampling location for the precipitation is located higher in altitude (Grimselpass; Bundesamt für Umwelt (BAFU), 2014) then the direct infiltration area for the groundwater in the GTS.

The spread of the precipitation data is larger (Fig. 3.6), where the obtained values for the CAGr and the GrGr waters are well enclosed. The groundwater values might result from homogenization of the precipitation input due to mixing of different rain waters in the unsaturated zone.

All analysed samples plot along the local Grimsel meteoric water line (LMWL, Fig. 3.6).

$$\text{LMWL: } \delta^2H = 8.082 \times \delta^{18}O + 12.751 \text{ (Schotterer et al., 2010)} \qquad (1)$$

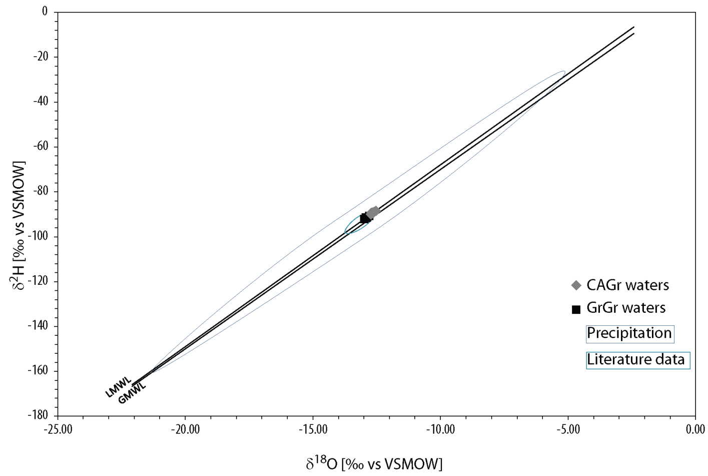

Figure 3.6. Average δ^{18}O and δ^2H values per sampling location grouped according to chemical composition (CAGr or GrGr water). Enveloppe of precipitation data (1993 to 2014) taken from Schweizerische Eidgenossenschaft, Bundesamt für Umwelt (BAFU), 2014. Values are compared to the Local Meteoric Water Line (LMWL, Schotterer et al., 2010) and the Global Meteoric Water Line (GMWL) which is defined as: $\delta 2H = 8\ \delta^{18}O + 10$ (Craig, 1961).

The D-excess for both the CAGr (11.9 ± 0.5) and the GrGr (11.8 ± 0.5) waters is similar to the mean of the local precipitation between 1993 and 2014 (D-excess: 11.7 ± 2.9; Bundesamt für Umwelt (BAFU), 2014)). This indicates a meteoric origin from the same moisture source for the CAGr and the GrGr waters. Further, this is evidence for restricted or absent mixing between the meteoric input water with another non-meteoric water source.

Despite observed similarities, CAGr waters differ systematically from GrGr waters. The CAGr waters are isotopically heavier ($\delta^{18}O = -12.65$, $\delta^2H = -89.28$) than the GrGr waters (Fig. 3.6; $\delta^{18}O = -12.85$, $\delta^2H = -91.18$).

During the sampling campaign in January 2016, samples for the analysis of tritium were taken from several test intervals (Tab. 3.6). One sample within the CAGr waters shows measurable tritium activity (Ci1 = 3.1 TU), whereas all other samples have activities at or below detection limit (<0.6 TU, see Tab. 3.6). Measured tritium activity indicates a recent recharge component within the sampled groundwater.

Table 3.6. Compilation of the average $\delta^{18}O$ and $\delta^{2}H$ values and measured ^{3}H concentrations. Precipitation data from Schweizerische Eigenossenschaft, Bundesamt für Umwelt (BAFU) (2014). CAGr: Central Aar granite, GrGr: Grimsel granodiorite, n.m.: not measured.

Sample ID		Sampling date	$\delta^{18}O$		$\delta^{2}H$		Sampling date	^{3}H	
			Mean ‰ vs VSMOW	St.dev ‰ vs VSMOW	Mean ‰ vs VSMOW	St.dev ‰ vs VSMOW		Activity TU	2σ TU
CAGr	Ai2	14.04.14 to 28.01.16	-12.72	0.42	-90.08	3.93	27.01.16	<0.6	
	Ai3	14.04.14 to 28.01.16	-12.71	0.05	-89.42	0.21		n.m.	
CAGr	Bi1	14.04.14 to 28.01.16	-12.53	0.07	-88.45	0.52	27.01.16	<0.6	
	Bi2	14.04.14 to 28.01.16	-12.67	0.05	-89.30	0.21	27.01.16	<0.6	
	Bi3	14.04.14 to 28.01.16	-12.65	0.06	-89.28	0.14	27.01.16	<0.6	
	Bi4	14.04.14 to 28.01.16	-12.68	0.06	-89.40	0.20	27.01.16	<0.6	
	Bi5	14.04.14 to 28.01.16	-12.64	0.09	-89.33	0.54	27.01.16	<0.6	
	Bi6	14.04.14 to 28.01.16	-12.65	0.31	-89.51	2.55	27.01.16	<0.6	
	Ci1	14.04.14 to 28.01.16	-12.60	0.08	-88.89	0.31	27.01.16	3.1	0.6
GrGr	Ei2	14.04.14 to 28.01.16	-12.93	0.01	-91.37	0.23	27.01.16	<0.6	
	Fi2	14.04.14 to 28.01.16	-13.00	0.04	-92.04	0.38	27.01.16	<0.6	
	Fi3	14.04.14 to 28.01.16	-12.79	0.06	-90.66	0.18	27.01.16	<0.6	
	Gi2	14.04.14 to 28.01.16	-12.91	0.20	-91.56	1.56	28.01.16	<0.6	
	Gi3	14.04.14 to 28.01.16	-12.89	0.61	-91.35	4.47	28.01.16	<0.6	
Precipitation	mean	1993	-12.48	2.89	-87.94	22.26	1993	14.8	
	mean	2000	-12.47	2.98	-89.87	23.75	2000	8.8	
	mean	2010	-15.12	3.35	-108.42	26.57	2010	10.2	
	mean	2013	-13.82	4.13	-98.39	33.42	2013	n.m	

3.5. Discussion

3.5.1. Infiltration conditions of fracture water

Measured stable isotopic composition in precipitation data shows a seasonal variation (Fig. 3.6; Bundesamt für Umwelt (BAFU), 2014; Schotterer et al., 2010), however this seasonal variation is erased in the groundwater. The stable isotopic composition of the groundwater corresponds closely to the mean isotopic composition of the precipitation. This attenuation of the seasonal variation is known to occur in unsaturated zone in crystalline environments (Clark and Fritz, 1997). Exfoliation joints that occur within the uppermost 200 m may form the unsaturated zone, as they occur in diverse orientations and form an interconnected network of joints and thus potential flow paths (Ziegler et al., 2013).

The comparability between the mean isotopic composition of the rainwater and of the groundwater indicates that the groundwater is solely composed by rainwater without significant addition of another water source. A close fit between groundwater samples and the LMWL, as already observed by Frick et al. (1992) and Keppler (1994), is further evidence for a meteoric origin of all sampled fracture groundwater (Fig. 3.6). The leftward shift of the LMWL with respect to the GMWL (Fig. 3.6) could result from hydration of silicate minerals (Geyh et al., 2001). The D-excess for the groundwater as well as for the rainwater is slightly above 10, which indicate relatively dryer air conditions during fractionation (Schotterer, 2000).

Despite being of meteoric origin and from a similar moisture source, we observe significant differences when comparing stable water isotopic composition of the CAGr waters with the GrGr waters (Fig. 3.6). Consistent differences over two years of sampling between CAGr and GrGr waters indicate that no mixing occurs between the two flow fields.

From the difference in mean $\delta^{18}O$ values between CAGr and GrGr waters (0.2 ‰), a difference of ca. 75 m in infiltration altitude results using the relationship between $\delta^{18}O$ and infiltration altitude 0.27‰ / 100m (Maréchal and Etcheverry, 2003).

Differences in infiltration altitude yield differences in flow path length, as the water-conducting structures are similar between the CAGr and the GrGr (Schneeberger et al., 2016). This difference in flow path length is supported by the observed overburden (Tab. 3.2) and by measured differences in temperature. CAGr waters show lower temperatures than GrGr waters. Using a geothermal gradient of 25 °C / km (Vernon et al., 2008), differences in overburden between the CAGr and the GrGr results in higher temperature for the GrGr domain of similar magnitude (ca. 2°C) as observed.

No differences are observed within reported transmissivity values for CAGr and GrGr waters, therefore longer residence time for GrGr waters would follow from the inferred longer flow path. Tritium measurements potentially allow for an estimation of the mean residence time of groundwater. It was found that 12 out of 13 samples from January 2016 are tritium-free, which indicates infiltration times prior the tritium activity peak in the atmosphere due to bomb tests in the early 1950s (Tab. 3.6) and residence time of over 65 years. Within the measured samples, only the sample from Ci1 shows measurable ^3H activity (Tab. 3.6). However, the borehole history is not entirely clear for Ci1 and a possible contamination cannot be ruled out (Keppler, 1994).

Tritium activity was also measured within another borehole in the GTS (27.04.2017: 2.3 ± 0.4 TU). Accounting for the variance in ^3H input of precipitation (Waber et al., 2017) and applying - as an approximation - a piston flow model, a infiltration around November 1960 is inferred for the groundwater in specific borehole, which yields a mean transit time of ca. 57 years for this specific borehole.

3.5.2. Geochemical evolution

The chemical as well as the isotopic compositions (see above) do not vary between the different samplings. Therefore, the seasonal variation that is observed in the $\delta^{18}O$ and δ^2H values of the precipitation data (see chapter 4.4) is erased by homogenization without addition of non-meteoric water. The observed chemical composition is, hence, a product of water-rock interactions on the downwards path of the groundwater.

The measured chemical compositions are comparable to previously reported groundwater chemistry (Fig. 3.7; Keppler 1994). Unfortunately, no direct comparison can be performed, as different borehole test intervals were sampled. However, the comparable chemical composition of the groundwater since the 1990s indicates constant water-rock interactions since 1990s. Therefore, the water-rock interactions leading to observed chemical composition seems to be constant for the last 20 years. Combination of homogeneous recharge inferred from $\delta^{18}O$ and δ^2H values and the constant water-rock interaction indicate a stable system since 1990s.

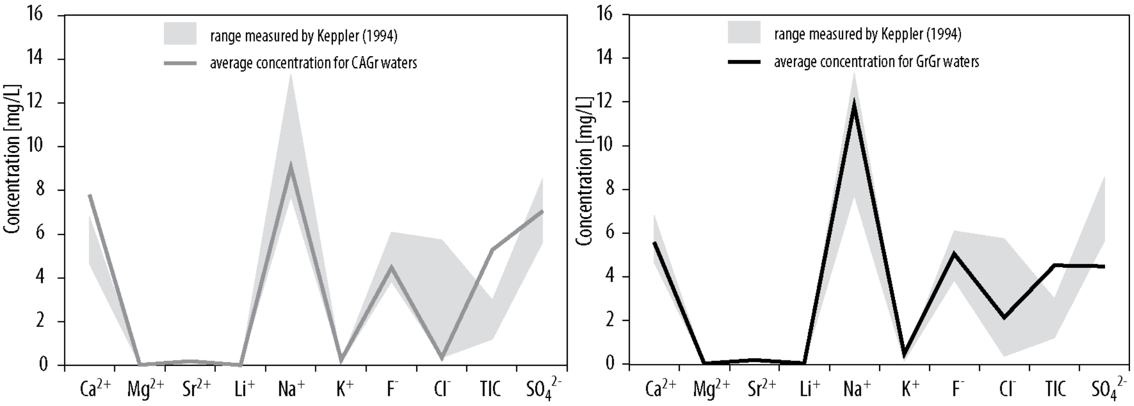

Figure 3.7. Schoeller diagrams illustrating the comparison of recent groundwater chemical composition (average concentrations) with concentrations measured previously (Keppler, 1994).

Despite, comparable chemical composition per test interval over time, we observed, also in the chemical composition, differences between CAGr and GrGr waters. CAGr waters reveal higher Ca^{2+}, but lower Na^+, Li^+ and Cl^- concentrations, and higher CO_2 partial pressure compared to GrGr waters.

Observed differences in chemical composition could not be related to the differences in mineralogical composition of the water-conducting fault rock, as illustrated by following two examples. Test intervals Bi4 and Bi5 show similar groundwater chemical composition and transmissivity value (Tab. 3.2), but within Bi4 metabasic dykes occur and probably are water conducting, whereas Bi5 is characterized by fractures in a ductile shear zone forming the flow path. Further, the chemical composition of groundwater in Gi2 and Gi3 is comparable, but the probable flow path is formed by a fault gouge in Gi2 and by fractures in a ductile shear zone in Gi3.

As inferred from $\delta^{18}O$ values and measured overburden, longer residence times for the GrGr waters yield longer reaction time for interactions between water and granitoid host rock. It is commonly agreed, that hydrolysis of plagioclase is the major source for Na^+ in high-topography crystalline environments (e.g. Bucher and Stober, 2010; Maréchal and Etcheverry, 2003; Seelig and Bucher, 2010; Wanner et al., 2017). Coupled albite dissolution and kaolinite precipitation is (Wanner et al., 2017):

$$NaAlSi_3O_8 + H^+ + 0.5H_2O = 0.5Al_2Si_2O_5(OH)_4 + Na^+ + 2SiO_{2(aq)} \quad (2)$$

This reaction implies an increase of pH with on-going reaction, which agrees with measured pH values for both rock types. Increasing pH results in higher solubility of quartz (Wanner et al., 2017), which correlates with the lower quartz saturation indexes for GrGr waters compared to CAGr waters. Furthermore, albite undersaturation observed in both type of water (CAGr and GrGr) indicates that plagioclase is probable to be dissolved.

Saturation of groundwater with respect to kaolinite (Tab. 3.5) implies precipitation of kaolinite with on-going dissolution of plagioclase. Precipitation of kaolinite seems plausible, as sporadic observations are reported within GTS (Wehrens et al., 2016) and in weathering experiments of granitoid bedrock (White et al., 2017).

Dissolution of CO_2 is a possible source for protons (reaction 3) required for dissolution of plagioclase and has been proposed by Wanner et al. (2017) as a driving force for reaction 2.

$$HCO_3^-{}_{(aq)} + Ca^{2+}{}_{(aq)} = CaCO_{3\,(s)} + H^+{}_{(aq)} \quad (3)$$

TIC and Ca^{2+} concentrations correlate linearly in measured groundwater (Fig. 3.5), which agrees with precipitation of calcite required by dissolution of CO_2 as source for protons. Further, dissolution of CO_2 decreases the partial pressure of CO_2 in the water, which is in line with observed partial pressures of CO_2 being under atmospheric CO_2 partial pressure ($P(CO_2)_{atm}$: $10^{-3.4}$ bar).

Linked to calcite precipitation (reaction 4) is the observed undersaturation with respect to fluorite, which has been reported previously (Mäder and Ekberg, 2006). Precipitation of calcite decreases the Ca^{2+} concentration in the groundwater, which acts as driving force for dissolution of fluorite (reaction 4).

$$CaF_{2\,(s)} = Ca^{2+}_{(aq)} + 2\ F^{-}_{(aq)} \qquad (4)$$

Fluorite occurs within Alpine clefts (Keusen et al., 1989), which are distributed over the entire rock mass. Therefore, dissolution of fluorite from Alpine clefts is a probable source for observed F^-. No differences in F^- concentration between CAGr and GrGr waters were observed.

Lower CO_2 partial pressure, higher measured pH, higher Na^+ concentrations and lower Ca^{2+} concentration indicate more advanced progress of reaction 2 and 3 in GrGr waters compared to CAGr waters. Moreover, CAGr waters show lower Cl^- concentrations than GrGr waters. Cl^- and Li^+ concentrations seem to evolve parallel ($R^2 = 0.8$, Fig. 3.5), which might indicate a similar source for Cl^- and Li^+. Neither Li^+ nor Cl^- concentrations show a correlation with K^+ or Mg^{2+} concentrations, which excludes sheet silicates as a potential source. As no other Cl-bearing mineral is known to occur around GTS, Cl^- and Li^+ in waters are probably added to the groundwater from another source as potentially an exchange with matrix pore water. Moderately mineralised pore water ($Cl^- \approx 330\text{-}440$ mg/kg$_{H2O}$) is known to occur within GrGr in the GTS (Eichinger, 2009), the Li^+ concentration of the rock matrix pore water is unknown. When using the reported Cl^- concentration an exchange ratio of approximately 1/188 is inferred for GrGr waters. Even though the rock matrix pore water is known not to plot along the LMWL in a $\delta^{18}O$-$\delta^{2}H$ plot (Eichinger, 2009), such low exchange ratio only slightly alter the isotopic composition of the groundwater and are not detected on the $\delta^{18}O$-$\delta^{2}H$ plot.

As the mineralogical compositions of the two host rocks (CAGr and GrGr) are very similar, ions ratios can be used to deduce the evolution and the fracture water's reaction progress within both lithologies.

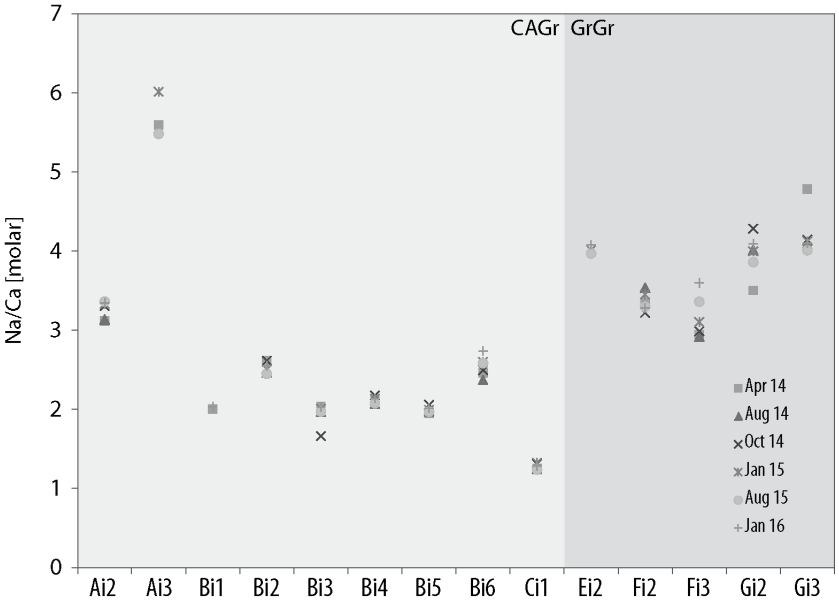

Figure 3.8. Molar Na^+/Ca^{2+} ratio per sampling campaign plotted against test interval position from N (left) to S (right) along GTS.

As demonstrated before, dissolution of plagioclase leads to increased Na^+ concentration in water. In addition, precipitation of calcite decreases the Ca^{2+} concentration. Therefore, Na^+ /Ca^{2+} increases with interaction time between water and host rock.

Furthermore, ion exchange from potentially occurring clays would additionally increase the Na^+ concentration (Banks and Frengstad, 2006; Gascoyne, 2004; Gimeno et al., 2014). However, ion exchange due to surface complexations might be a short term alteration (Mazurek et al., 2003). These observations suggest a molar Na^+/Ca^{2+} increase with groundwater evolution. Applied to our water samples, the CAGr waters are therefore less evolved compared to the more evolved GrGr waters (Fig. 3.8).

Strikingly, the lowest Na^+/Ca^{2+} ratio is found in interval Ci1, which is the interval with the highest outflow rates (Fig. 3.8, Tab. 3.2) and with measurable tritium activity. This confirms that groundwater evolves towards higher Na^+/Ca^{2+} along reaction with granitoid host rock and that the observed differences in chemical composition are likely due to differences in residence time.

In order to quantify the differences in reaction progress of water-rock interactions inferred from chemical composition of sampled groundwater, we performed element mass-balance calculations between surface water (Tab. 3.4) and the groundwater.

Inverse modelling was performed using Na^+, K^+, Ca^{2+}, Al^{3+}, F^-, Cl^-, SO_4^{2-}, TIC and Si and the mineral phases Ca-albite (local plagioclase), quartz, calcite, fluorite, kaolinite, $CO_2(g)$, pyrite, NaCl and either dissolution of muscovite (increase K^+ concentration) or precipitation of K-montmorillonite (decrease K^+ concentration). Plagioclase composition was adapted to the local composition; else the pure end-members were used.

As mentioned before, Cl^- concentration is likely to be due to exchange with another water source; therefore, NaCl was added to the inverse models, as a proxy. The observed linear relationship between Na^+ and Cl^- in GrGr waters (Fig. 3.5) depicts a linked evolution of Na^+ and Cl^- in the GrGr waters.

For both the CAGr and the GrGr waters inverse modelling was performed on groundwater sample with (i) minimal Cl^- concentration and (ii) maximal Cl^- concentration, as Cl^- is considered as conservative tracer (Tab. 3.7). The composition of meteoric water was taken from one sample collected from a nearby lake (Tab. 3.4; Totensee).

Table 3.7. Phase mole transfer inferred from inverse modelling for minimal and maximal Cl^- concentration for CAGr and GrGr waters. Positive values indicate dissolution, negative precipitation.

Phase	Units	CAGr min	CAGr max	GrGr min	GrGr max
Kaolinite	mmol/L	-0.1154	-0.1957	-0.2225	-0.2293
Albite-Ca	mmol/L	0.2574	0.4203	0.4286	0.4502
Pyrite	mmol/L	0.0319	0.0404	0.0249	0.0204
CO_2(g)	mmol/L	-0.0218	0.0801	-0.0732	-0.0070
Calcite	mmol/L	0.04983	0.0069	-0.0408	-0.0800
Quartz	mmol/L	-0.3531	-0.6601	-0.7070	-0.7443
Fluorite	mmol/L	0.0958	0.0490	0.1073	0.1478
NaCl	mmol/L	0.0000	0.0060	0.0360	0.0820
K-Montmorillonite	mmol/L	-0.0141	-0.0171		-0.0019
Muscovite	mmol/L			0.0014	

From inverse models for CAGr waters, we infer that groundwater composition is achieved by dissolution of Ca-albite (plagioclase adapted to local stoichiometry), fluorite, calcite, pyrite and halite in conjunction with the precipitation of quartz, kaolinite, CO_2(g) and K-Montmorillionite (Tab. 3.7).

Inverse models for GrGr waters differ only slightly, as calcite is not dissolved, but precipitated (Tab 3.7). Inverse model for GrGr max shows slightly higher K^+ than meteoric input water, therefore muscovite is dissolved. Most GrGr waters have similar K^+ concentration as the GrGr max sample, therefore dissolution of muscovite is probable to occur in most GrGr waters. Furthermore, a comparison of the inverse models with saturation indexes revealed that all suggested reactions are plausible considering the saturation index of every single mineral (Tab. 3.5).

We propose a similar dissolution / precipitation pattern for the CAGr waters as for the GrGr waters, except for precipitation of calcite needed in the case of GrGr waters. However, the differences in progress of plagioclase (Ca-Albite) inferred from the chemical compositions are confirmed by the inverse models, as the phase mole transfers are higher for the GrGr waters (Tab. 3.7). Coupled to the increase dissolution of plagioclase is the increased precipitation of kaolinite and quartz in the GrGr waters (reaction 4). Further, the precipitation of calcite within the GrGr waters indicates that calcite precipitation was required as proton source in the GrGr waters, whereas in the CAGr the dissolution of plagioclase occurred without precipitation of calcite as driving force.

Performed inverse models confirm that the different chemical compositions in GrGr waters than in the CAGr result from differences in progress of comparable water-rock interactions.

3.5.3. Kinetic modelling of meteoric water interaction with granitic host rock

From inverse modelling we inferred major water-rock interactions. However, the inverse modelling does not allow any conclusion on whether proposed reactions are feasible within the inferred residence time for the groundwater (around 60 years).

By kinetically modelling the interaction between local granite with pure water buffered with atmospheric O_2 and slightly lower partial pressure of CO_2 than the atmosphere, we were able to reach concentrations similar to measured ones (Fig. 3.9). Input parameters of the model and the code are attached as supplementary material.

After 100 years, pH attained a value of 9.6, which corresponds to observed pH values for GrGr waters (Fig. 3.9). The increase of pH with time shows that GrGr waters, with higher pH values compared to CAGr waters, have a longer evolution.

Calcite is precipitated during the entire model simulation time, however with the rate of precipitation decreasing with model run time. This agrees with evolution inferred from inverse modelling and ion ratios for the GrGr waters, where calcite precipitation is required for the hydrolysis of aluminosilicates.

On-going reaction time leads to an increase in Na^+, Si, and Mg^{2+} concentrations, as primary minerals are dissolved. The solution is oversaturated with respect to quartz, saturated with respect to calcite and kaolinite, close to saturation with albite-Ca and fluorite, and undersaturated with respect to plagioclase, K-feldspar and fluorite. The modelled saturation indexes correspond to observed mineral saturation indexes with exception of oversaturation in quartz.

The indicated time scales have to be considered only in a relative sense because the model results strongly depend on the employed rates and reactive mineral surfaces, which are not well constraint in the GTS. The model's input parameters have been stretched to fit the probable time evolution of local water.

Those kinetic inferences consolidated the main conclusions from the chemical composition. Hydrolysis of albite is the fastest dissolution reaction of the abundant minerals and calcite precipitation plays an important role as source for protons, as suggested previously (e.g. Wanner et al., 2017).

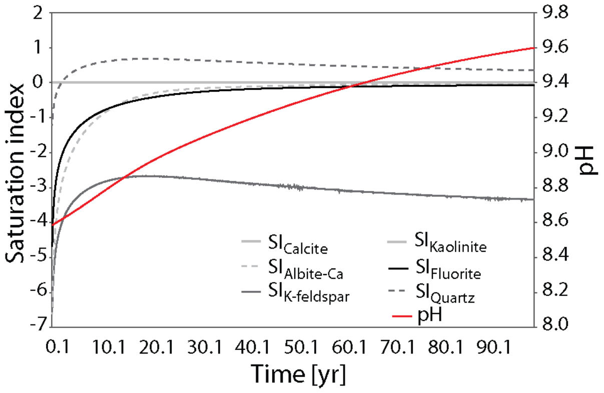

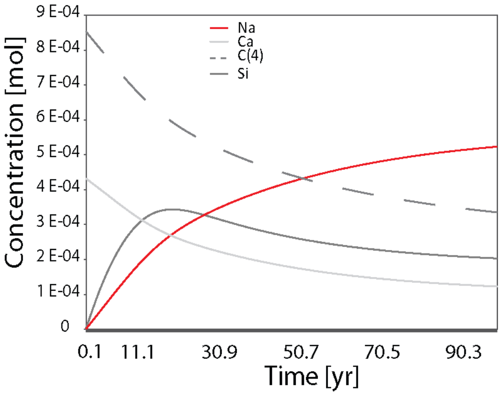

Figure 3.9. Kinetic modelling results with saturation index of selected minerals and pH in (a) and concentrations of major elements shown in (b).

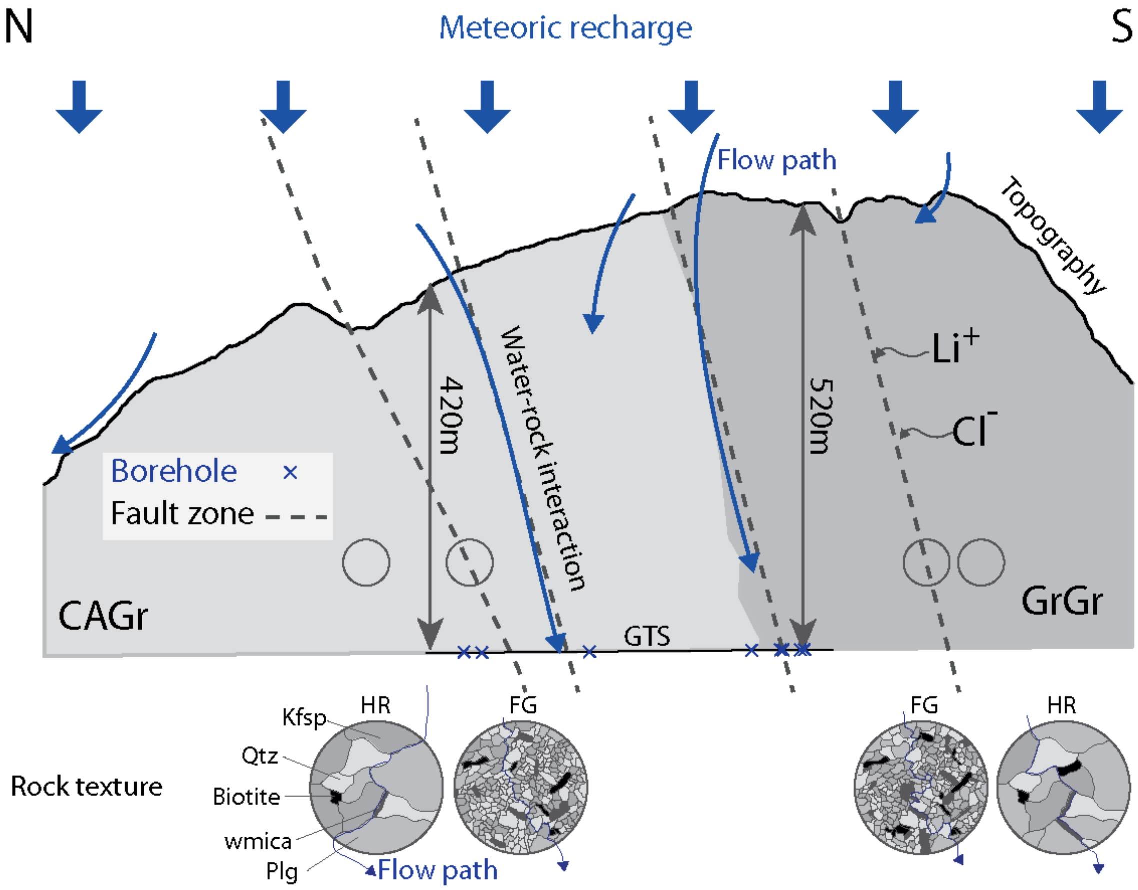

Figure 3.10. Schematic drawing summarizing major findings. GTS marks the underground facility where groundwater was sampled. Two different rock types (CAGr, GrGr) with crosscutting fault zones, which focus groundwater flow towards depth. Fault zone are characterized by smaller grain sizes than the host rock, as indicated by small inlets at the bottom. The figure is not to scale.

CAGr: Central Aare Granite, GrGr: Grimsel Granodiorte, GTS: Grimsel Test Site, HR : Host rock, FG: fault gouge, Kfsp : K-feldspar, Qtz: quartz, wmica : white mica, Plg: plagioclase.

3.6. Conclusion

Based on stable water isotopic composition, sampled groundwater is assigned to a meteoric origin (Fig. 3.10). The absence of seasonal variation in the $\delta^{18}O$ and δ^2H values indicates homogenization of the rainwater in the unsaturated zone. Further, the D-excess indicate similar moisture source for the CAGr and the GrGr waters. Therefore, observed differences between CAGr and GrGr waters are likely due to differences in infiltration altitude.

We suggest that, gravity-driven, water flows along the localized faults (Keusen et al., 1989; Seelig and Bucher, 2010) and interacts with host rock during circulation (Fig. 3.10). The grainsize reduction in the fault zones increases the water-rock interface and thus potentially catalyses the water-rock interactions. No link between chemical composition of sampled groundwater and mineralogical composition of faults (ductile shear zone, metabasic dykes, fault gouge, brittle fracture) was observed.

The flow field above GTS is heterogeneous, and faults are poorly interconnected as evidenced by consistent differences in physical parameters, chemical and isotopic composition between CAGr and GrGr waters. CAGr and GrGr waters were defined based on several parameters (pH, Li^+ and Cl^- concentrations, Na^+/Ca^{2+} molar ratio and water stable isotopic composition). Furthermore, we were able to show that differences between CAGr and GrGr waters are caused by varying progress of major water-rock interactions. Major water-rock interactions are the dissolution of plagioclase, fluorite, pyrite and muscovite in combination with precipitation of kaolinite, quartz, K-montmorillonite and $CO_2(g)$. Calcite is precipitated or dissolved depending on progress of albite hydrolysis. Suggested major water-rock interactions agree with saturation indices, as groundwater samples were found to be in equilibrium with calcite, quartz and kaolinite and undersaturated in fluorite, plagioclase and K-feldspar. In addition to dissolution-precipitation reactions, exchange with another water source is probably responsible for observed differences in Cl^- and Li^+ concentration.

Differences in reaction progress and exchange with matrix pore water may result from differences in residence time. Longer residence times follow from an increased overburden with similar flow rates and a decrease in permeability with depth, as reported from elsewhere (e.g. Manning and Ingebritsen, 1999; Martin, 2007). The assumption of constant flow rates is based on reported transmissivity values for the GTS (Tab. 3.2).

In summary, we can state that meteoric water evolves purely by water-rock interactions with minor mixing with non-meteoric water towards higher Na^+/Ca^{2+}, higher pH and lower $P[CO_2]$, which is evidence for a more advanced progress of hydrolysis of plagioclase. Proposed evolution is comparable to already suggested groundwater evolutions (e.g. Bucher et al., 2012; Ofterdinger et al., 2004; Seelig and Bucher, 2010; Wanner et al., 2017). Furthermore, in this case study, the evolution does not imply more saline waters as evidenced by similar total dissolved solids between both groundwater groups.

Future work might focus on elucidating observed differences between CAGr and GrGr waters by (i) developing reaction path models, where the groundwater chemistry evolves as function of distance along water-conducting features. (ii) Acquire knowledge about chemistry and texture of fault gouge and other water-conducting features (e.g. cataclasites, fractures) within the CAGr and the GrGr for better constrain the reactive mineral surface and the mineralogical composition of the flow paths. (iii) Additional tritium sampling campaigns might unravel residence time of both groundwater types (CAGr and GrGr waters).

3.7. Acknowledgments

This study was financed and supported by the Swiss National Cooperative for the Disposal of Radioactive Waste, Nagra. Particular appreciation is given to the very supportive field team at GTS (H. Ablanalp, R. Dorrer, T. Baer, A. Dorrer, M. Treuthard). Analytical work performed by Priska Bähler and Stefan Weissen is very much appreciated. Special thanks are given to Christoph Wanner for stimulating discussions. James Gilgannon is thanked for English corrections.

Chapter 4

Methods and uncertainty-estimations of 3D structural modelling in crystalline rocks: A case study

Raphael Schneeberger[1], Miguel de La Varga[2], Daniel Egli[1], Alfons Berger[1], Florian Kober[3], Florian Wellmann[2], & Marco Herwegh[1]

[1]Institute for Geological Sciences, University of Bern, Baltzerstrasse 1+3, CH-3012 Bern
[2]Graduate School AICES, RWTH Aachen University, Schinkelstrasse 2, D-52062 Aachen
[3]Nagra, Hardstrasse 73, CH-5430 Wettingen

Abstract. Exhumed basement rocks are often dissected by faults, controlling physical parameters such as rock strength, porosity, or permeability. Knowledge on the three dimensional (3D) geometry of the fault pattern and its continuation with depth is therefore of paramount importance for projects of applied geology (e.g. tunnelling, nuclear waste disposals) in crystalline bedrock. The central Aar massif (Central Switzerland) serves as a study area, where we investigate the 3D geometry of the Alpine fault pattern by means of both surface (fieldwork and remote sensing) and underground (mapping of the Grimsel Test Site) investigations. The fault zone pattern consists of planar steep major faults (kilometre-scale) being interconnected with secondary relay faults (hectometre-scale). Starting with surface data, we present a workflow for structural 3D modelling of the primary faults based on a comparison of three extrapolation approaches based on: a) field data, b) Delaunay triangulation and c) a best fitting moment of inertia analysis. The quality of these surface-data-based-3D models is then tested with respect to the fit of the predictions with the underground appearance of faults. All three extrapolation approaches result in < 6% distance misfit when compared with underground rock laboratory mapping. Subsequently, we performed a statistically interpolation based on Bayesian inference in order to validate and further constrain the uncertainty of the extrapolation approaches. This comparison indicates that fieldwork at the surface is key for accurately constraining the geometry of the fault pattern enabling a proper extrapolation of major faults towards depth. Considerable uncertainties, however, persist with respect to smaller-sized secondary structures because of their limited spatial extensions and unknown reoccurrence intervals.

4.1. Introduction

Geological information is inherently three dimensional (3D) in space, but often represented in 2D (Jones et al., 2009). With increasing available computer power, 3D modelling or geometrical visualizations became widespread, as they can be performed on a desktop computer (e.g. Bistacchi et al., 2008; Caumon et al., 2009; Hassen et al., 2016; Sausse et al., 2010; Stephens et al., 2015). 3D models widely serve as basis for subsequent investigations such as stress modelling or fluid flow modelling (e.g. Hassen et al., 2016; Stephens et al., 2015). Two different approaches are mainly used for modelling 3D geological problems: explicit modelling or implicit modelling. An implicit model is built by an interpolation function defining a solid throughout space. In contrast, an explicit model uses a patchwork of 3D meshes formed by interconnected triangles (Cowan et al., 2003). Implicit modelling allows for faster re-calculation of the model and thus faster model updating with new data (Lindsay et al., 2012). Explicit modelling, however, allows for easier visualization. Structural modelling can further be subdivided into stochastic and deterministic models. Deterministic approaches try to represent the actual occurrence of geological features, analogous to drawing a map, producing a single output (e.g. Stephens et al., 2015), whereas as in stochastic approaches parameters are defined by a probability density function. Therefore, the thereout derived mathematical instances are also probabilistic distributions (e.g. González-Garcia and Jessell, 2016; Jørgensen et al., 2015; Koike et al., 2015).

When modelling a certain volume of Earth's intermediate deep subsurface (tens of meters to kilometres), as often done for planning nuclear waste repositories, geothermal projects or tunnelling work, 3D structural modelling commonly starts from a known lithological and structural dataset, may it be from the Earth surface or underground facilities such as tunnels or boreholes. Known information is then extrapolated towards the unknown. At the time of extrapolation, its validity cannot be proven unless additional information such as geophysical, borehole or excavation data is integrated later.

Previous studies report that this extrapolation represents the main uncertainty within 3D structural modelling (e.g. Baumberger, 2015; Bistacchi et al., 2008). More generally, uncertainties in accuracy related to input data (i.e. GPS location, dip / dip azimuth measurements) are small compared to the uncertainty related to the data interpolation between known locations or to data extrapolation (Bond, 2015).

Uncertainties play an important role when considering decision-making based on information available from a 3D model and have therefore been subject to extensive studies in the past (e.g. Bistacchi et al., 2008; Clare E. Bond et al., 2007; Lindsay et al., 2012; Tacher et al., 2006; Wellmann et al., 2014, 2010; Wellmann and Regenauer-Lieb, 2012; Yamamoto et al., 2014). Since models are a function of the used data, some of the approaches tend to analyse uncertainties of the input data before modelling (e.g. C. E. Bond et al., 2007; Jones et al., 2009). Other approaches investigate the error propagation into the models inferring the uncertainty after modelling (Jessell et al., 2010; Lindsay et al., 2012; Viard et al., 2011; Wellmann et al., 2010). Most of these published studies were performed within sedimentary environments where information such as stratigraphy, layer thickness, layer orientation is known and the overall tectonic setting is rather simple. Uncertainty estimation and its potential reduction are less well constrained for structural modelling of basement rocks (e.g. Svensk Kärnbränslehantering AB, 2009), which are characterized by intrusive contacts and a complex arrangements of deformation structures.

In this study, we focus on deformed basement rocks and the extrapolation of faults. We follow three main goals: i) development of an extrapolation workflow for different techniques for projection of surface structures to depth, ii) estimation of related uncertainties using underground information, and iii) design and application of a probabilistic approach to validate the generated model.

We focus specifically on the combination of observations in outcrops at the surface with observations in an underground facility allowing for an extrapolation modelling approach and propose that it is possible to link these two types of observations in a probabilistic context, taking into account uncertainties in measurements, as well as the exact tie between observed features at the surface and in the underground facility. We investigate a local case study in a relatively simple setting in crystalline rocks. The study area is characterized by well-exposed crystalline rocks of the Aar massif in the Central Swiss Alps (Fig. 4.1) and furthermore greatly benefits from subsurface information from the Grimsel Test Site (GTS) underground rock laboratory run by the Swiss Cooperative for Disposal of Radioactive Waste (Nagra).

This combination of good outcrop conditions at the surface and independent high quality subsurface information allows for an extrapolation modelling approach and subsequent validation in a relatively simple and well-constrained setting.

4.2. Geological setting

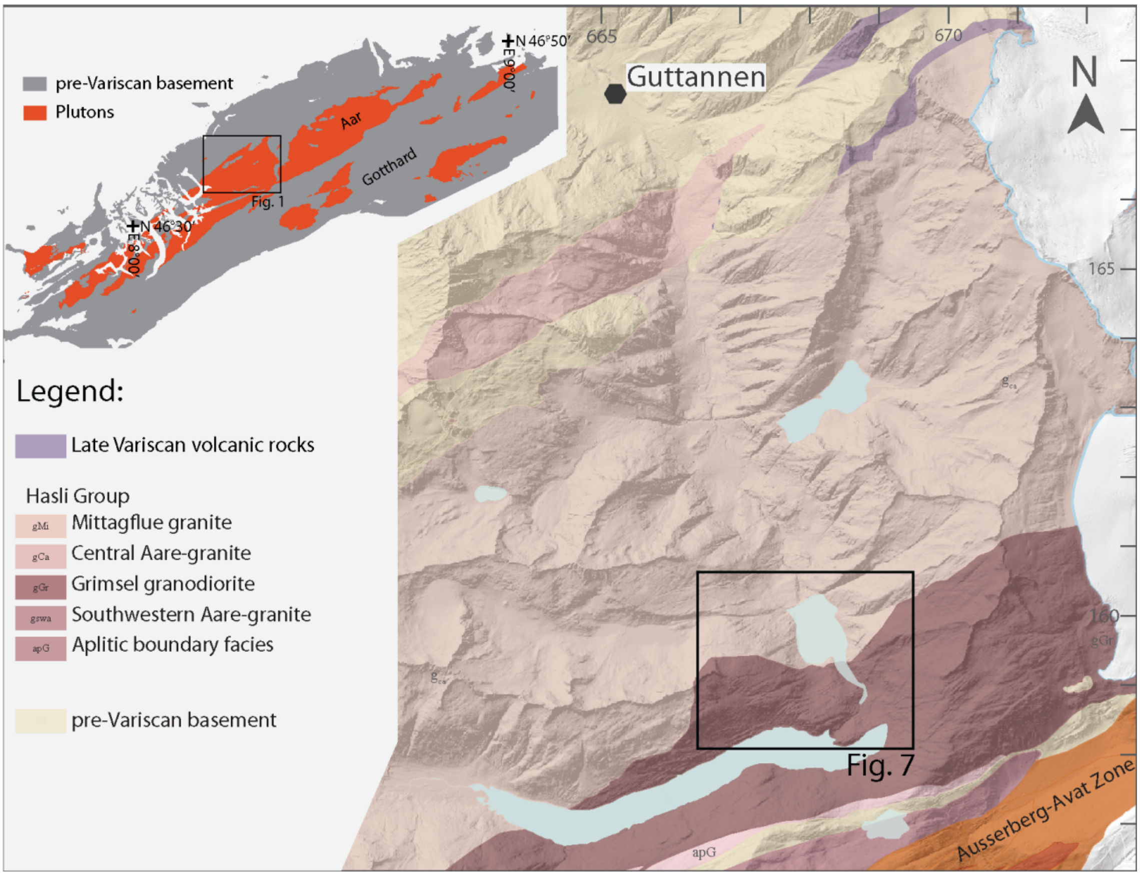

Figure 4.1. Geological map of the study area (modified after Berger et al. 2017).

The study site is located in the Haslital in the Central Alps (Switzerland, Fig. 4.1) within the Aar massif, an External Crystalline Massif of the Alps, representing exhumed basement rocks of the former European continental margin and thus belonging to the paleogeographic Helvetic domain of the Alps (e.g. Mercolli and Oberhänsli, 1988; Pfiffner, 2009; von Raumer et al., 2009)..

Three different host rocks of magmatic origin occur in the study area: (i) Grimsel granodiorite (GrGr), (ii) Central Aar granite (CAGr), and (iii) meta-basic dykes (e.g. Abrecht, 1994; Keusen et al., 1989; Labhart, 1977; Stalder, 1964). The GrGr and the CAGr belong to the Haslital group, which is a Permian calc-alkaline magmatic differentiation suite (Berger et al., 2017a; Schaltegger, 1990; Schaltegger and Corfu, 1992), the GrGr being the more primitive member. The two host rocks mainly differ in the relative amount of biotite, with ca. 11 vol% biotite in the GrGr compared to ca. 5 vol% biotite in the CAGr (Keusen et al., 1989). Intermingling structures observed in the field indicate coeval viscous state (Schneeberger et al., 2016). Furthermore, the concordant zircon and titanite U/Pb intrusion ages of both rock units are overlapping within error, where the GrGr intrusion has a concordant titanite U/Pb intrusion age of 299±2 Ma and the CAGr an age of 299± 2Ma (Schaltegger and Corfu, 1992). The granitoids intruded during Late to Post-Variscan extensional tectonics into a polymetamorphic pre-Variscan basement (Abrecht, 1994; Berger et al., 2017a; Labhart, 1977; Schaltegger, 1994, 1990; von Raumer et al., 2009).

Meta-basic dykes, formerly called lamprophyres (Oberhänsli, 1986), intrude into the granitoid bedrock without altering the granitoid indicating only slightly younger intrusion ages of former basic dykes with respect to the calc-alkaline granitoids.

Aforementioned rock types are subsequently overprinted by metamorphism and deformation related to Alpine orogeny. Peak metamorphic conditions reached 450 ± 30 °C and 6 ± 1 kbar (Challandes et al., 2008) at 22 - 20 Ma (Challandes et al., 2008; Rolland et al., 2009).

Several authors have described the deformation related to Alpine orogeny in the vicinity of the study area (e.g. Baumberger, 2015; Challandes et al., 2008; Choukroune and Gapais, 1983; Goncalves et al., 2012; Keusen et al., 1989; Marquer et al., 1985; Rolland et al., 2009; Steck, 1968; Wehrens et al., 2017, 2016). Ductile deformation is expressed by a pervasive foliation and by localized high strain zones (shear zones). The exact geometry of the 3D shear zone network, which occurs at a variety of scales ranging from several kilometres down to millimetres, is complex (Choukroune and Gapais, 1983). It is, however, possible to extract a pattern of km-long major shear zones interconnected by hectometre-long subordinate bridging structures. The major shear zones tend to be quasi-planar (Baumberger, 2015; Wehrens et al., 2017) and we therefore assume a considerably simplified shear zone pattern with quasi-planar to planar geometries of the major shear zones grouped according to their strike orientation (Fig. 4.2).

The kinematic framework of Alpine deformation is controversial. Several kinematic models have been proposed for the shear zone network genesis in the study area, including single phase (Choukroune and Gapais, 1983) and multistage evolution models (Herwegh et al., 2017; Rolland et al., 2009; Steck, 1968; Wehrens et al., 2017, 2016). This study aims at reconstructing the present day 3D geometry and the kinematic evolution is thus of secondary interest. The different orientations of the structures are therefore used without kinematic implications. Major orientation of structures within the area are NE-SW (group A), E-W (group B) and NW-SE (group C) trending (Fig. 4.2; Schneeberger et al., 2016; Wehrens et al., 2017).

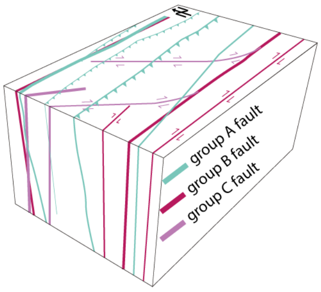

Figure 4.2. Schematic bloc diagram showing geometrical relationships between faults of different orientation groups (modified after Wehrens et al. 2017).

The pervasive foliation and the highly localized shear zones form mechanical anisotropies, which favour subsequent brittle localization (Belgrano et al., 2016; Kralik et al., 1992).

Deformation in the brittle regime is expressed by fracturing and cataclasis, often resulting in fault gouges (Bense et al., 2014; Wehrens et al., 2016). The spatial distribution of fractures as well as their reactivation in the form of fault gouge development is heterogeneous (Bossart and Mazurek, 1991; Mazurek, 2000).

Although the shear zones experienced a severe ductile deformation history, most of them were reactivated in a brittle manner during the exhumation history (Wehrens et al., 2017). Subsequently, we therefore use the term fault as summary terms for high T ductile shear zones, low T ductile shear zones and their reactivation by brittle shearing leading to cohesive (protocataclasite, cataclasite) or non-cohesive (fault gouge) fault rocks.

Present day seismic activity (Pfiffner and Deichmann, 2014) indicate on-going recent tectonic activity in the deep subsurface of the Aar massif.

Glaciation and glacial retreat contributed to the latest history of the area (Wirsig et al., 2016). Basal erosion and the latest young (17.7 ka, Wirsig et al. 2016) retreat ages produced excellent outcrop conditions, as most outcrops are glacially polished and above the treeline, exposing bare bedrock.

Owing to deglaciation, exfoliation jointing occurred (Ziegler et al., 2013). Given the restricted near-surface occurrence of these exfoliation joints and their small dimensions, we exclude these deformation features from further consideration in this study.

4.3. Methods

4.3.1. Extrapolation workflow

In order to represent the 3D geometry of faults, we developed a workflow based on a combination of remote sensing and fieldwork (Fig. 4.3).

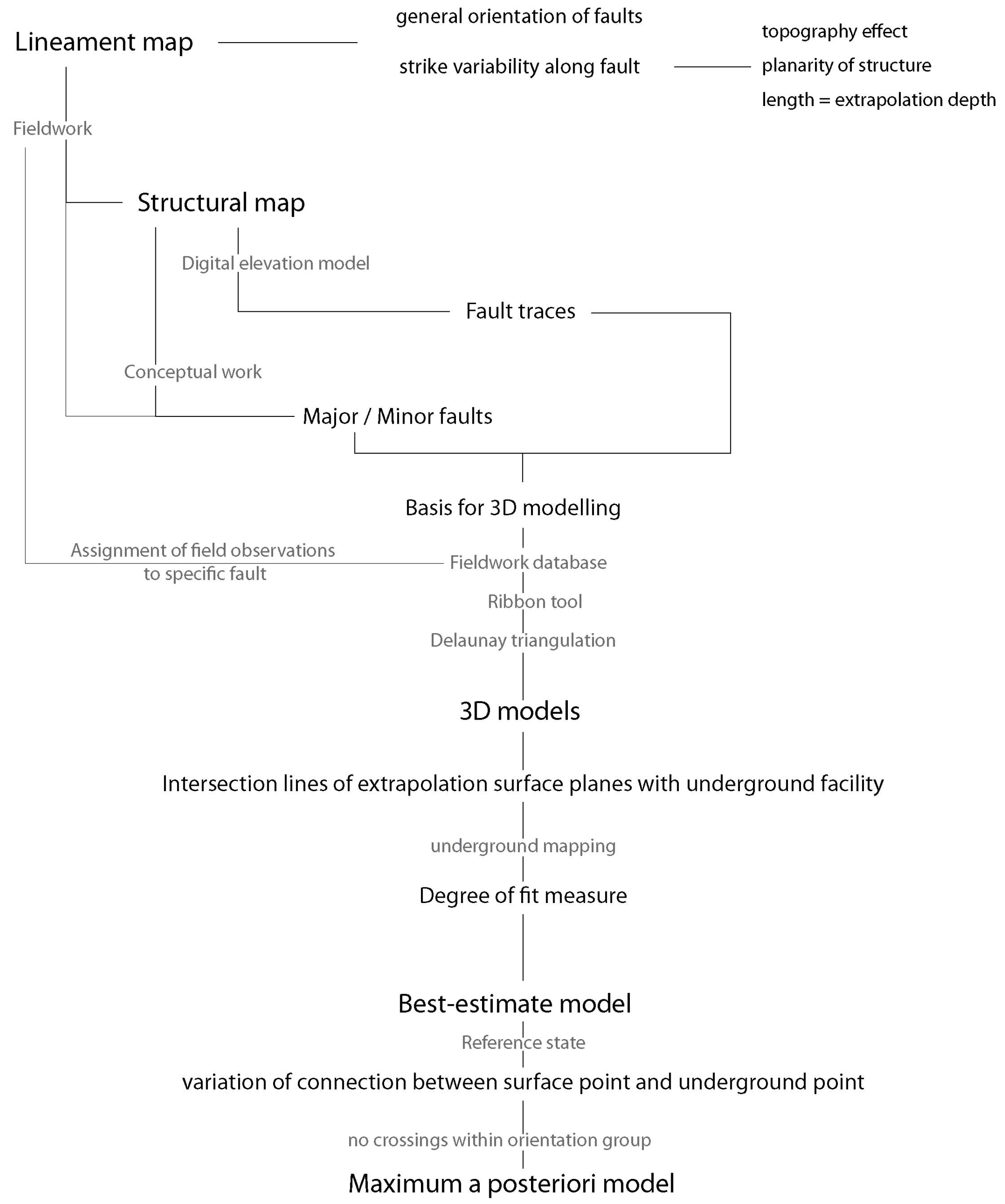

Figure 4.3. Modelling workflow.

As a first step, we generated a lineament map using remote sensing data. We use the term lineament as defined by Gabrielsen et al. (2014) and O'Leary et al. (1976), where a lineament is a mappable linear or curvilinear feature identified by remote sensing, possibly representing the intersection between a planar to subplanar structural anisotropy and the Earth surface. Lineament mapping followed the methodology presented by Baumberger (2015). Aerial photographs (Swisstopo) and digital elevation model (DEM; Swisstopo) with resolutions of 0.5 m and 2 m, respectively, served as basis.

Using the DEM, hillshade images (i.e. greyscale relief images) with distinct illumination angles (0°-360° illumination azimuth with 45° steps and constant at 30° altitude angle) were calculated, resulting in eight hillshade images, illuminating different areas of the investigation area. On a pixel-based map, the possible strike angle of a line depends on the number of pixels of the raster matrix in which the line is enclosed (Heilbronner and Barrett, 2014). Our approach requires an angular resolution <10°, thus a minimum length of 10 pixels for a specific lineament was necessary to fulfil this criterion. Hence, shorter lineaments (< 5 m) were discarded. Lineaments were manually digitized and are composed of minimum 2 endpoints and potentially several points in between.

The strike of lineaments was defined as the angle measured clockwise from north. Two different approaches to analyse the strike of lineaments were compared: i) single strike values from endpoint to endpoint, and ii) strike values for individual segments between a lineament's nodes. In both approaches, a weight is added to the strike proportional to the length of the lineament.

In addition to the aforementioned remote sensing approach, conventional structural surface mapping over an area of 13 km^2 was performed. Spatially restricted outcrop observations at the surface were extrapolated along strike using the lineament map, thus combining fieldwork and remote sensing allowed a structural surface map to be obtained. Ductile deformation was mapped differentiating pervasive background strain and localized high strain zones (shear zones). At the surface, mapping of brittle deformation focused on the occurrence of fault gouges. In addition, mapping in the GTS underground facility was performed similarly to surface mapping on dm-scale and in more detail regarding brittle structures (Schneeberger et al., 2016).

Structural modelling was performed using Move^{TM} software (Midland Valley) on two distinct scales: at a local (decametre) scale for the GTS and at a regional scale (km-scale) for the entire study area. Underground 3D structural modelling was performed on the basis of underground mapping and drill core data, which resulted in fault traces and orientations. This information provided the base for the 3D reconstruction of fault planes. Regional 3D structural modelling was performed following published workflows using the surface fault map as a basis (e.g. Baumberger, 2015; Bistacchi et al., 2008; Kaufmann and Martin, 2009; Zanchi et al., 2009). Surface faults were extrapolated to depth by assigning a dip value to individual surface traces, where a trace is the intersection between the Earth’s surface and a fault. Three different extrapolation approaches were applied: (i) extrapolation along measured dip and dip azimuth (fieldwork-based approach). Data from outcrops were considered within an orthogonal distance of <20 m to inferred fault traces and a strike differing less than 20° compared to the fault’s mean strike as defined by remote sensing. The fault’s mean strike was calculated via linear regression through all points defining its trace. (ii) Delaunay triangulation is a 3D meshing algorithm, where triangulation for a given point cloud is calculated such as no point of the point cloud is inside the circumcircle of any triangle connecting three points of the point cloud (Delaunay, 1934). (iii) The ribbon tool is a Move^{TM} internal interpolation algorithm based on a three points approach, where three points form a triangle and the orientation is averaged over a defined number of triangles (Midland Valley). The maximum dip orientation of each average triangle is represented as a stick at the location of the starting point. Combination of all sticks along a trace results in a plane for the given trace. More details on the ribbon tool are given in Fernandez (2005) and Baumberger (2015).

For each approach, the surface fault trace was extrapolated to depth using the obtained specific orientation. Subsequently, the intersection line between the extrapolated plane and a horizontal plane at GTS elevation (approx. 1730 m a.s.l.) was calculated. Then, the resulting intersection lines were compared with the underground structural map in order to find the 'best fitting' underground structure to the obtained intersection line. The degree of fit between the intersection line at the surface and the trace of the underground structure was estimated using the orthogonal distance (distance misfit), starting from the intersection with the main gallery, and the angular difference (angle misfit) between the two linear features (Fig. 4.4). Only structures within an orientation group (group A, B, C) were compared.

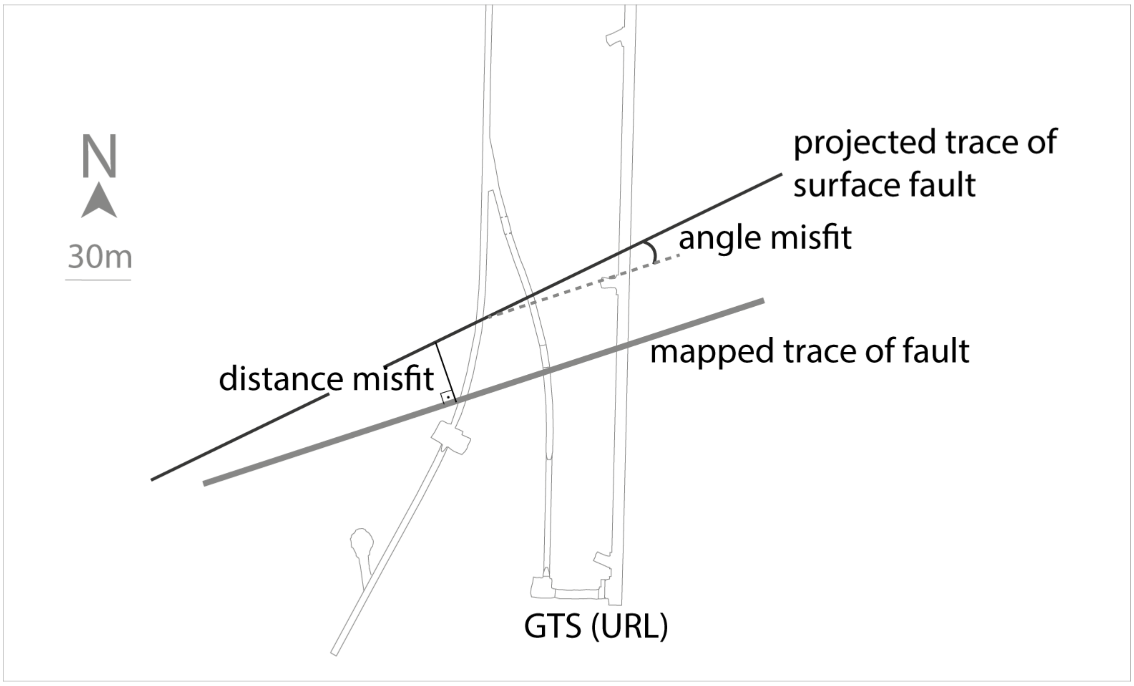

Figure 4.4. Schematic drawing of hypothetical example for validation of 3D models based on angular and distance misfit.

Furthermore, the degree of fit was compared between the different extrapolation approaches and thus for every surface fault. Considering all approaches, a 'best fitting' underground fault was assigned based on the aforementioned criteria. This assignment served as basis for the following structural modelling step, where every surface fault was linearly interpolated with the assigned 'best fitting' underground fault, yielding a 'best estimate' model.

4.3.2. Bayesian Inference

For a better description of the system taking into consideration the inherent uncertainty on the extrapolation methods above, we performed a Bayesian inference. Bayes' theorem

$$p(\theta|\,\mathrm{y}) = \frac{p(\theta)p(y|\theta)}{p(y)}$$

provides a formal way to update probability distributions for model parameters θ when new data y is obtained. The final goal is to obtain the posterior distribution $p(\theta|\,\mathrm{y})$ of the parameters θ, given the observations y. This distribution is proportional to the distribution of prior parameters $p(\theta)$, and likelihood functions, $p(y|\theta)$ which determine how likely these parameters are, given specific observations y. The term $p(y)$ is a normalisation constant and commonly referred to as evidence or marginal likelihood (see for example MacKay, 2003, for more details).

In this study's scenario, we assign a parameter to each surface fault at the tunnel level. We represented the uncertainty about the exact value with a Gaussian distribution and a constant standard deviation of 40 m in the horizontal axis (Fig. 4.5), based on the dip uncertainty of 10° based on the dip variation in multiple orientation measurements along a single fault (Fig. 4.5). As a mean value, we assign the 'best estimate' model from the previous interpolation. Interpolated planes were grouped according to their orientation into three separate groups (identified by A, B, C following, Fig. 4.2).

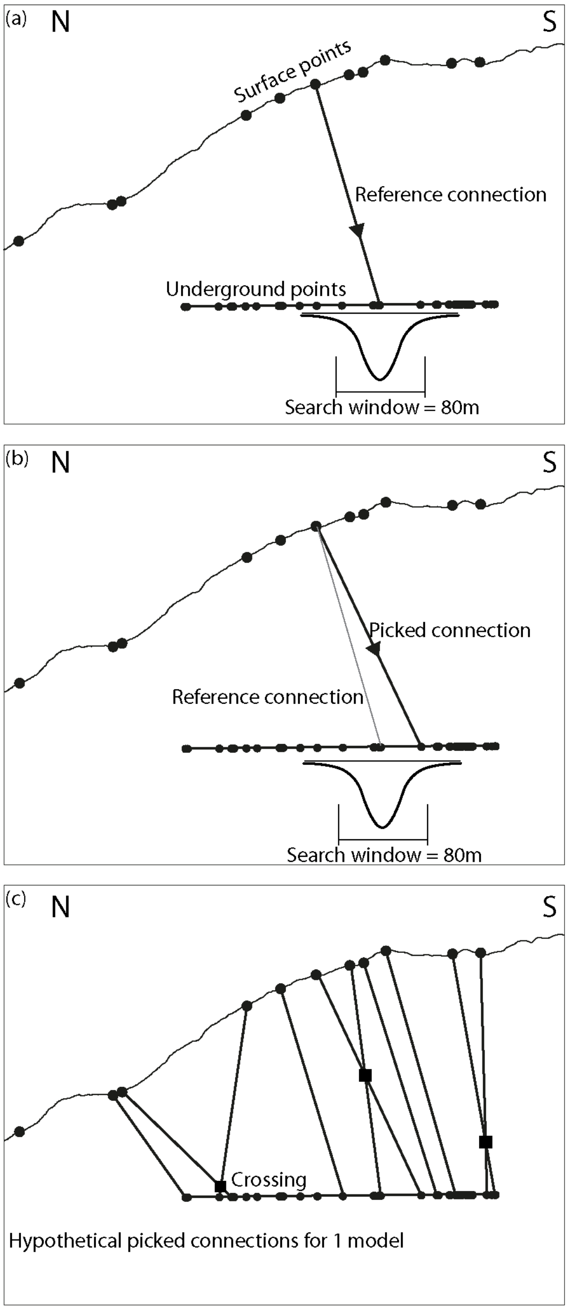

Figure 4.5. Schematic cross-section illustrating the statistical modelling methodology for one example. (a) Reference state is defined by aforementioned workflow. A search window of 80 m is assigned to the reference underground point. (b) The code picks a possible underground point within the 80 m search window based on a normal Gaussian distribution and calculates the connection. (c) For every surface point a corresponding underground point is picked resulting in a connection pattern. This pattern building is performed 10'000 times and all patterns are compared based on the number of crossings within the specific pattern, yielding in a probability for connecting a certain surface point to a certain underground point.

Within each orientation group, we expect faults to be mostly parallel with limited intersections based on field observations. To capture this idea, we assigned a penalty factor that reduces the log-likelihood of a parameter set for an increasing number of intersections (by 0.05 per intersection, to be precise). The number of intersections per iteration was calculated using the Bentley-Ottmann algorithm (Supplement; Balaban, 1995; Bentley and Ottmann, 1979).

The described Bayesian inference cannot be performed directly due to the complexity of multiple parameters in several groups and the non-linearities due to the fault intersections. We therefore apply a computational sampling method based on an Adaptive Metropolis MCMC approach (Haario et al., 2001) implemented in the probabilistic programming package PyMC 2 (Patil et al., 2010).

Final posteriors were discretized to match the locations of measured faults in the underground tunnel by a simple nearest location classifier (Fig. 4.5). Therefore, the final result of the inference is a discretise distribution of each of the parameters. In order to compare the 3D models obtained by the three extrapolations approaches, we then use the maximum a posteriori value, i.e. the highest probability value of the posterior distributions.

4.4. Results

4.4.1. Lineament map

In total, 5198 lineaments with a spatially heterogeneous distribution and lengths ranging from 5 m to 1941 m were mapped (Fig. 4.6a). Lineaments are generally more concentrated along topographic highs and lows. Within certain areas (areas (i) and (ii) in Fig. 4.6a), the lineament's strike tends to be parallel to the dip azimuth of the slopes yielding uniform orientations. In contrast, in domains with relatively low topographic variations a variety of strike orientations become discernible (area (iii) in Fig. 4.6a).

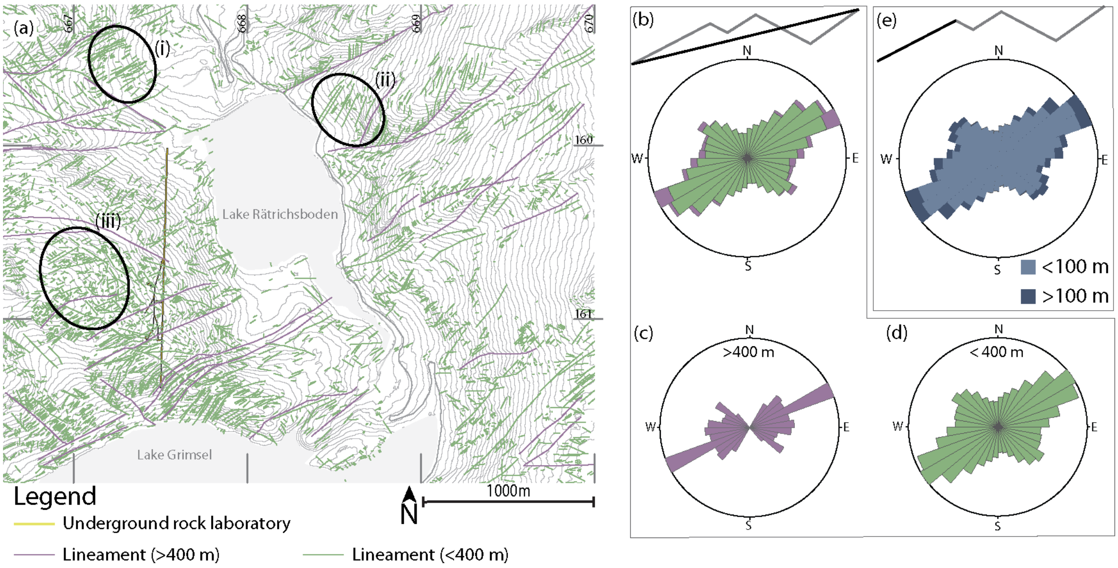

Figure 4.6. (a) Lineament map of the study area with underground rock laboratory. Topography contours are based on SwissAlti3D (reproduced by permission of swisstopo (BA17063)). (b-d) Length-weighted rose diagrams showing endpoint to endpoint strike of all lineaments (b), of lineaments longer than 400m (c) and of lineaments shorter than 400m (d). (e) Length-weighted rose diagram showing the orientation of each segment of all lineaments.

Looking at the bulk data, lineaments show a major NE-SW and a minor NW-SE trend (Fig. 4.6b). Long lineaments (>400 m) are mainly oriented NE-SW (Fig. 4.6c), whereas short lineaments show a considerable variation in strike (Fig. 4.6d). When comparing the two different approaches for strike measurement, the calculated strike distributions are comparable (Figs. 4.6b and e).

4.4.2. Field observations and data

Data obtained by fieldwork combined with a compilation of several published maps (Baumberger, 2015; Keusen et al., 1989; Vouillomaz, 2009; Wehrens et al., 2017; Wicki, 2011) yielded a surface fault map (Fig. 4.7, see also Schneeberger et al., 2016).

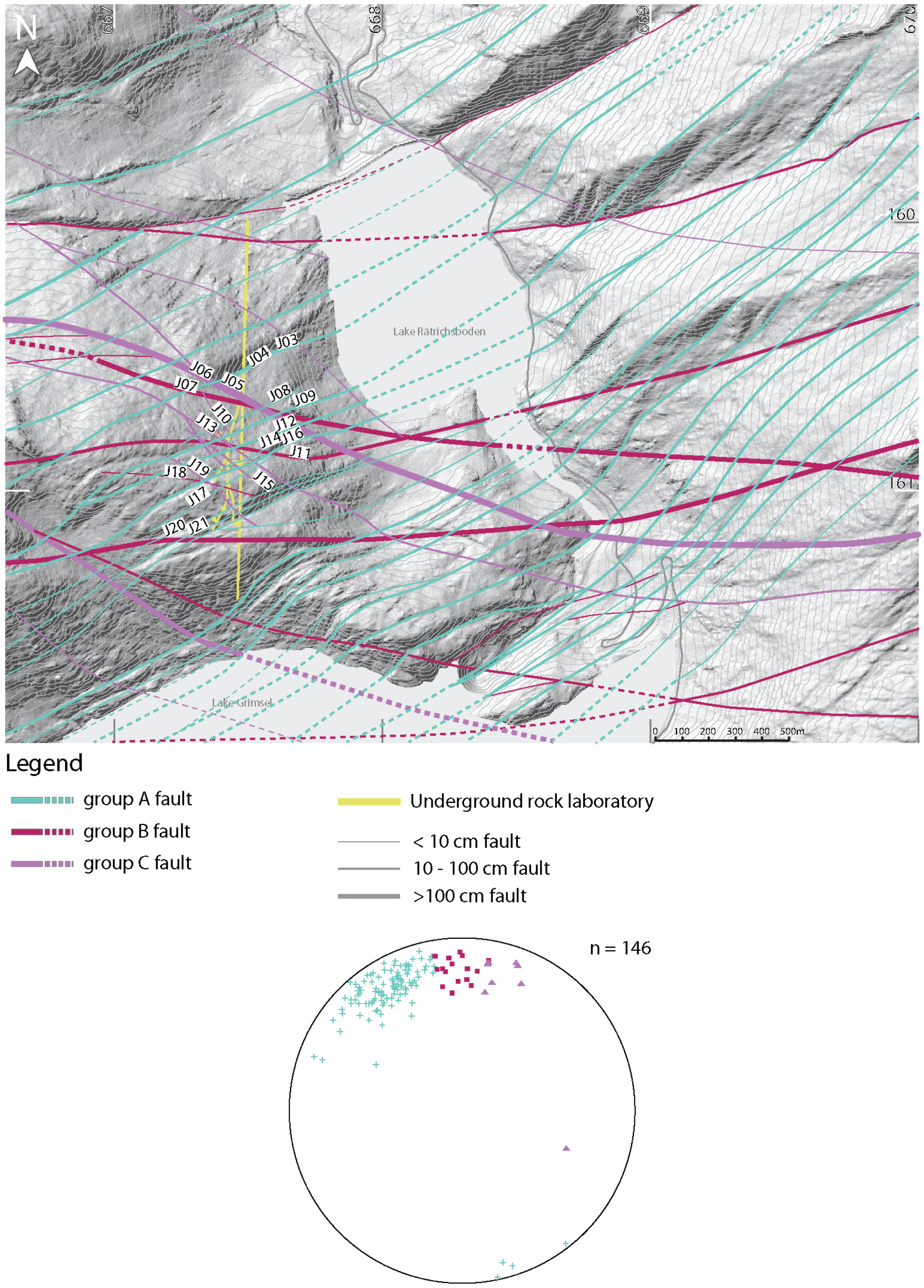

Figure 4.7. Surface fault map with faults grouped by strike orientation (group A, B, C). Hillshade image underlying the map is based on SwissAlti3D (reproduced by permission of swisstopo (BA17063)). Fault exposure lines are dashed over uncertain areas and are labelled in cases where a connection to GTS exists. Lower hemisphere equal area projection with planes poles grouped according to strike. Map is based on Swiss coordinate system.

Based on their orientation, we discriminated different groups of faults (Fig. 4.7): group A are mainly steep SE-dipping faults. Their average orientation (dip azimuth / dip) is 149/74. Group A faults mostly show steeply plunging stretching-lineations resulting from ductile shearing. Group A can be correlated with faults formed during the Handegg phase (22 – 17 Ma) as defined by Wehrens et al. (2017) while group B and group C would correspond to faults formed during the Oberaar phase (14 – 12 Ma, Wehrens et al., 2017). Group B are mainly steep S-dipping (mean orientation: 178/72) faults. Lastly, group C are SW-dipping faults coeval with group B, with an average orientation of 196/72. Group C faults are subparallel to meta-basic dykes and often co-occur spatially with the latter. Group B and C mostly show oblique to horizontal stretching-lineations. For multiple orientation measurements along individual faults the standard deviation of the mean dip azimuth was below 15° and of the mean dip below 10°. Generally, the GrGr dominated southern area shows an increased number of faults (Figs 4.7 and 4.8). Detailed underground mapping resulted in a lithological (Fig. 4.8a) and in a structural map of the GTS (Fig. 4.8b).

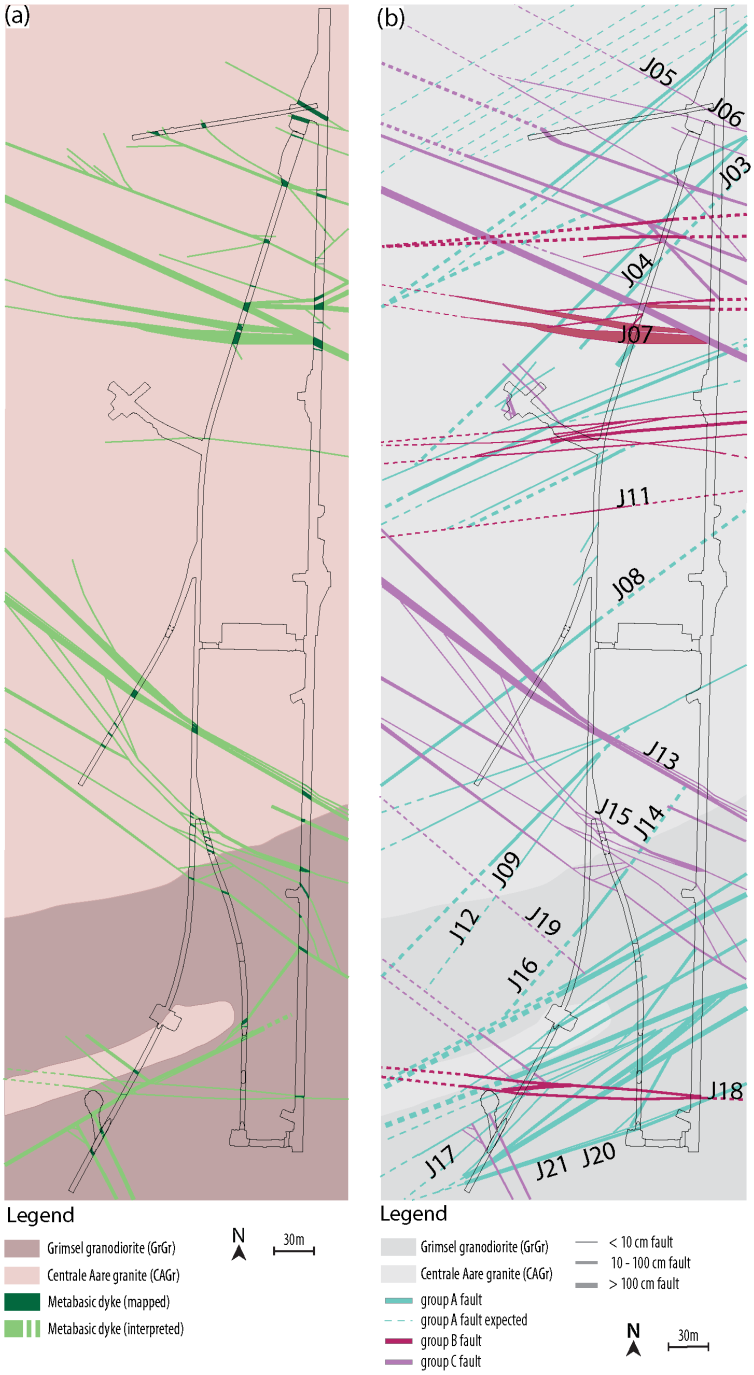

Figure 4.8. (a) Petrographic underground map. (b) Structural mapping (1:1000) of the underground rock laboratory (GTS) with faults grouped according to their strike. Indicated labels correspond to surface fault labelling and represent 'maximum a posteriori' interpolation.

Meta-basic dykes occur as three distinct swarms, two being located within the CAGr domain (Fig. 4.8a). The northern two swarms strike NW-SE, whereas the southern swarm strikes E-W, however, less clearly marked. Numerous dykes are overprinted by an Alpine foliation, which sometimes is oblique to the dyke boundary. Furthermore, dykes are often overprinted by localized ductile as well as brittle deformation, expressed by shear zones and fault gouges.

Faults occur along three NE-SW trending swarms, two E-W trending swarms and along two NW-SE trending swarms, leading to a heterogeneous strain distribution along the underground facility (Fig. 4.8b).

The NE-SW trending swarms correspond to group A faults with an average spacing of ca. 16 m. In total 31 group A data were mapped in the underground (GTS facility). They can be further subdivided into 17 moderately to steeply dipping faults (between 45 and 75°) and 14 sub-vertically dipping ones (>80°).

The E-W trending swarms correspond to faults with orientations that are similar to group B. In total, 12 of these E-W striking faults were mapped.

The NW-SE trending fault swarms are localized mainly along dykes (Fig. 4.8) and represent group C structures. In total, 25 NW-SE striking faults occur within GTS.

Faults in the CAGr (northern part) seem to preferentially localize along pre-existing anisotropies, i.e. high-temperature brittle fractures (biotite coating) or meta-basic dykes and thus form discrete faults (cm-sized) with marked contacts to the host rock. In contrast, faults in the GrGr dominated southern part form strain gradients over larger distances (m-sized). This observation is in agreement with findings of Wehrens et al. (2017).

4.4.3. 3D structural modelling

The GTS model size is 600x250x100 m, whereas the regional model size was 4x3 km with a projection depth of 1000 m. The projection depth was defined arbitrarily, but no larger than half of the fault trace's length.

4.4.3.1. GTS model

Combination of the underground map with measured surface orientation data resulted in a 3D geometric visualization of meta-basic dykes and faults. Swarms of meta-basic dykes tend to join towards less numerous dykes with depth. Based on geometrical considerations, we infer the occurrence of three major dykes from which all others either fan out or form relay structures in-between the major dykes. Based on the field observation that the major faults and relay structures dip steeply to sub-vertically towards the south, we discriminated 8 major group A faults and 23 relay structures. Major group A faults occur within each NE-SW trending swarm discriminated on map view. Group B deformation structures can be further subdivided into 6 major and 7 relay faults. Group C deformation structures can be subdivided into 6 major and 32 relay deformation structures, some of which are very short (14 m).

4.4.3.2. Regional model

The surface fault map (Fig. 4.7) served as a basis for the generation of the three different km-scale 3D models (see above). All three modelling approaches yielded the 3D geometrical visualization of the surface fault pattern. They all share the same fault traces at the model surface. As mentioned above, projection specific dip values were used for each of the models. However, not all surface faults were extrapolated with each approach. Of the 22 possible surface faults, 15 were extrapolated with the fieldwork-based approach, 12 using the Delaunay triangulation and 21 with the ribbon tool method. Missing projections can be due to lack of outcrop description or absence of sufficient topographic relief for remote sensing based approaches.

By combining all three approaches at least one, but up to three degrees of fit with underground faults were calculated for each surface fault. Based on the different degrees of fit a ‘best fitting’ underground structure was assigned to each surface fault. By linearly interpolating the two traces, we obtained a model, which we called "best estimate" model. In total, 11 group A faults reach the GTS. From the total 11, 7 have a dip <80°, which would correspond to the major structures defined in the above presented GTS-scale model, whereas the 4 steeper faults correspond to relay structures. Moreover, 2 group B and 8 group C faults connect the surface with the GTS. Combination of all faults yields an average spacing of 25.4 m. Furthermore, faults appear to converge with depth.

4.4.3.3. Bayesian inference

For each model that is obtained when each surface point (intersection between surface fault and 2D section along GTS) is interpolated with a specific underground point, the number of intersections was calculated and the likelihood of the model compiled based on the number of intersections. In total 10’000 models were calculated and for each a probability for a certain interpolation of a specific surface point with an underground point was obtained (Fig. 4.9). For certain surface points, a clear maximum a posteriori value was found (Fig.4.9a-d), however, for other surface points no underground point could be assigned unambiguously (Fig. 4.9e).

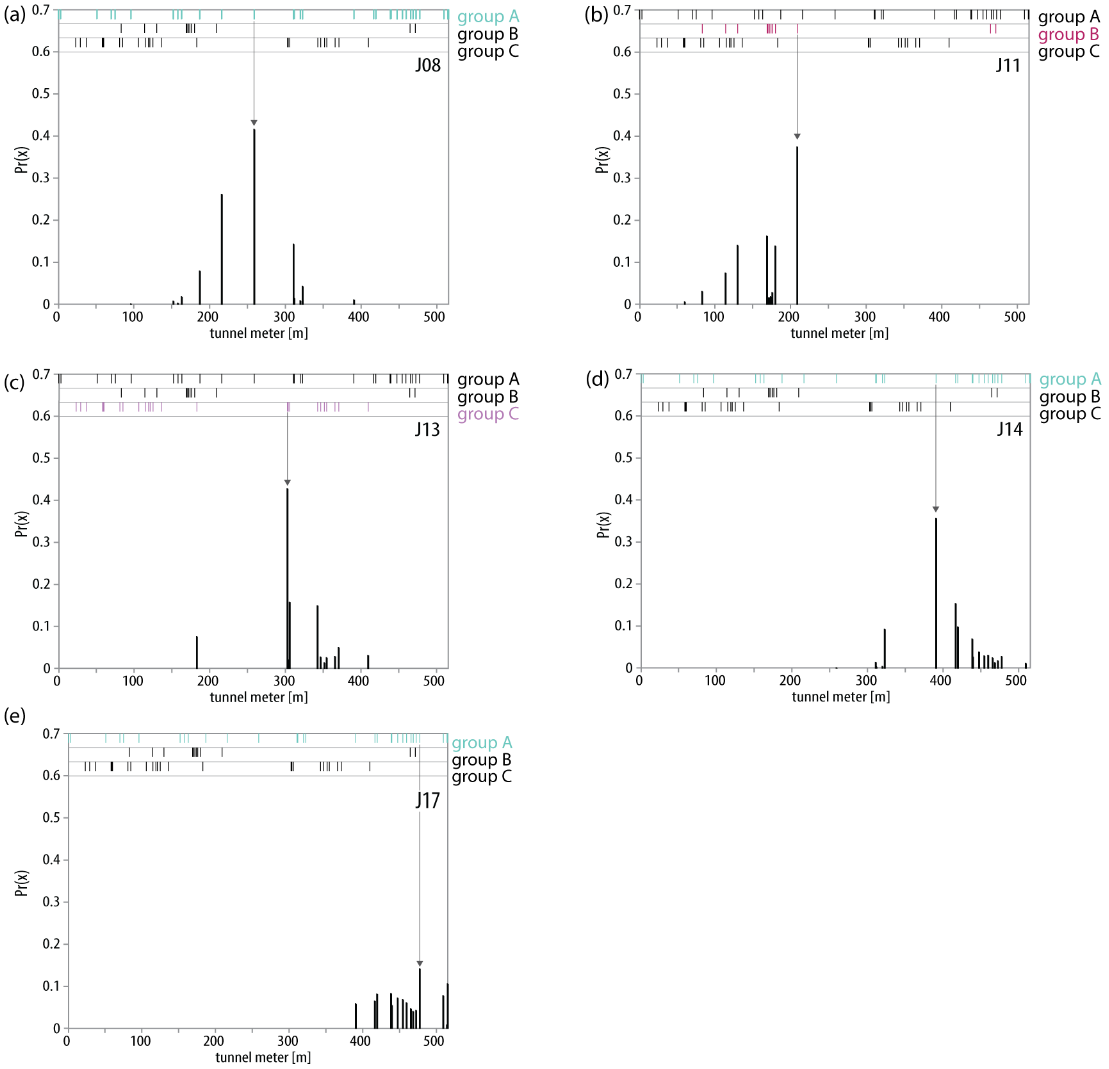

Figure 4.9. Probability distributions of five selected examples: (a) to (d) with highest probabilities achieved, whereas (e) shows an example without clear maximum probability. On top are indicated the positions of the underground deformations zones, grouped according to their strike. Additionally, the 'maximum a posteriori' interpolation is highlighted with an arrow.

Based on the maximum a posteriori value a 3D structural model was obtained by linearly interpolating each surface point to the underground point with the maximum a posteriori value. We call this model the 'maximum a posteriori' model (Fig. 4.10). Notice that the 'maximum a posteriori' model only adds information to the initial model through consideration of a likelihood, i.e. the assumption that crossing faults at large-scale are unlikely. Note that the smaller scaled relay structures are not considered in this approach.

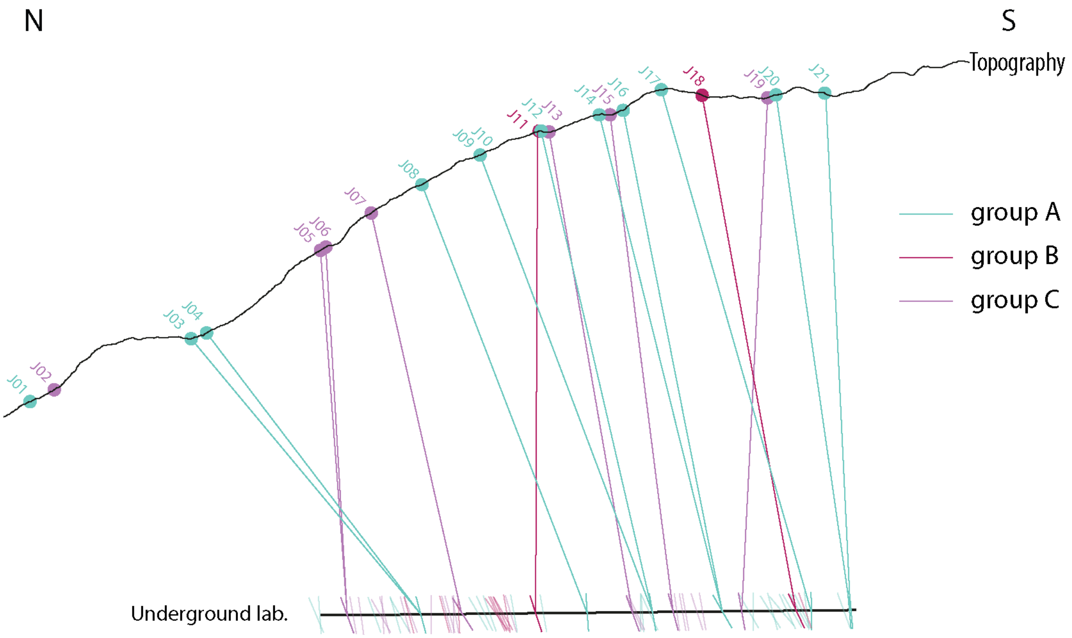

Figure 4.10. Cross section showing 'maximum a posteriori' connections between surface and underground faults. Faults are grouped and coloured according to their strike. Underground faults are represented by short ticks where the less transparent are the ones with connection to the surface.

This 'maximum a posteriori' interpolation model served as basis for comparing different employed extrapolation approaches. The comparison did not yield a clear 'best' extrapolation approach, however, it seems that fieldwork-based approach results in most accurate extrapolation.

4.5. Discussion

4.5.1. Lineament map

Comparison of the remote-sensing based lineament map and field data showed that in intact granitic rocks, purely ductile shear zones without later brittle overprint are not detected by remote sensing. Brittle deformation generating fractures, cataclasites or even fault gouges responsible for mechanical weakening is necessary to form morphologically detectable structures (Fig. 4.11a; Baumberger, 2015). Moreover, the orientations of the slopes play an important role, as faults striking down dip directions of slopes are prone to most effective erosion processes driven by gravity. Different orientations observed on the lineament map (Fig. 4.6a, areas (i) and (ii)) for the eastern and western flank of the Hasli valley are interpreted to result from such preferential erosion. In contrast, surface area (iii) in Fig. 4.6a is nearly horizontal and thus reflecting a homogeneously eroded pattern of intersection for lineaments. The dependence on erosion for the formation of morphological incisions leads to the observed heterogeneous lineament density distribution as ridges and valleys show higher lineament densities.

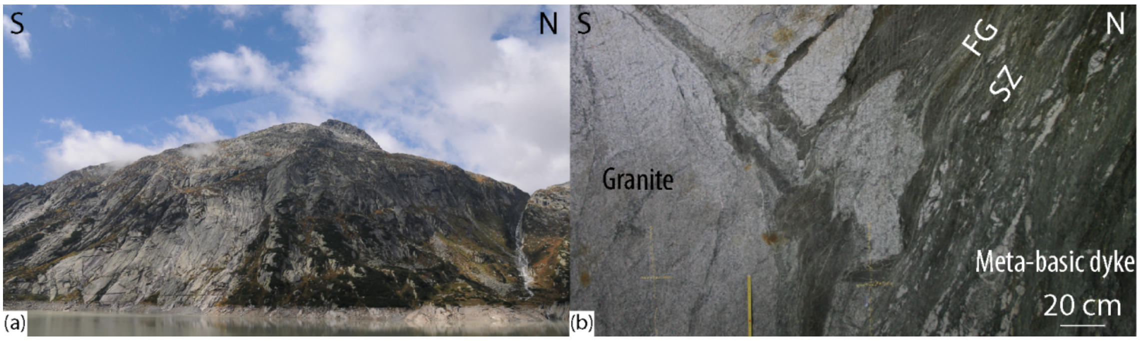

Figure 4.11. (a) Mountainside with incisions and exfoliation joints. b) detailed picture of underground outcrop showing outcrop conditions and key structural features:, ductile shear zone (SZ) and a fault gouge (FG).

Endpoint-to-endpoint strike and strikes of individual segments of lineaments are very similar (Fig. 4.6b and e) indicating only small variation in strike of the lineaments themselves. Therefore, underlying structures should be quasilinear to linear in 2D and planar in 3D. We also observe that the longest lineaments are NE-SW striking and that the variability shown in Fig. 4.6e is mostly due to varying strike orientations of very short lineaments (< 20m). In addition to the NE-SW striking maximum, few long lineaments strike NW-SE. Both major orientations are similar to those reported from field observations (Figs. 4.7 and 4.8) and correlate with previous studies (Rolland et al., 2009; Steck, 1968; Wehrens et al., 2017), indicating that lineament maps are suitable to obtain the general trend of steep faults in well exposed crystalline terrain. Much care is needed, however, when further interpreting lineament maps as the geologic meaning of the lineament is ambiguous and as lineament maps are strongly operator dependent (e.g. Scheiber et al., 2015).

4.5.2. Field observations and data

Differences between the surface map and the underground map are relatively small. The spacing of faults at the surface is lower, but general orientations are comparable (Figs. 4.7 and 4.8) and the two mappings are thus discussed conjointly.

Faults commonly show little variation in orientation along strike as evidenced by consistent orientations of dip and dip azimuth of multiple outcrop descriptions along the same fault. In conjunction with the small variability in strike for lineaments, this is clear evidence for the planarity of large-scale faults. At the surface, the 2D length of faults is between 229 and 5591 m (mean 2199 ± 1603 m). Therefore, extrapolation of surface faults to depths similar to depths of the underground faults, which have an overburden between 420 and 520 m, is well in the projection depth range, assuming a circular shape for the plane as a minimum estimation for their lateral extent.

Localization processes seem to differ between the two host rocks (CAGr and GrGr; Wehrens et al., 2017). The higher amount of biotite in the GrGr could influence the rock's rheology towards more ductile behaviour. In contrast, the relatively higher amount of quartz and K-feldspars renders the CAGr more brittle than GrGr at similar P-T conditions and thus enforces brittle fracturing and possible subsequent ductile shear zone widening, as observed in other crystalline rocks (Guermani and Pennacchioni, 1998; Mancktelow and Pennacchioni, 2005; Wehrens et al., 2017, 2016). Hence any mechanical anisotropy, such as along pre-existing structures in form of magmatic shear zones, meta-basic dykes or aplitic dykes served in the CAGr as sites for strain localization when suitably oriented with respect to the stress field.

4.5.3. 3D structural modelling

Our 3D structural models were generated as contribution to a project monitoring several parameters such as micro-seismicity and in-situ stress conditions on the km-scale (Large Scale Monitoring, Nagra). Therefore, 3D structural models were required mostly for visualization purposes. A deterministic explicit modelling workflow was required, as often used in applied projects. It is, however, clear that for model updating an implicit modelling approach would result in faster data handling. The deterministic approach was chosen, because we attempted to obtain a geometrically satisfying product within the simplest geological setting possible, without requiring statistical approximations for representing fault patterns. Furthermore, we were interested in the actual geometry of the faults dissecting granitoid rock bodies.

4.5.3.1. Three different approaches to obtain extrapolation 3D structural models (km-scale models)

Uncertainty related to the assignment of specific dip values to lineament traces (Baumberger, 2015; Bistacchi et al., 2008) led to the comparison of three different approaches. Validation attempts by comparison with underground mapping are purely geometrical and were based on two criteria, namely angle and distance misfit (Fig. 4.4). All three extrapolation approaches yielded similar results and no significant differences were observed. Moreover, in order to allow for a thorough comparison between the different extrapolation approaches solely based on the angle and distance misfit, the underground faults would need to be homogeneously distributed, which is not the case (Fig. 4.8).

The validation procedure could be refined using fault thickness. However, fault thickness varies substantially along strike and thus is not a clear distinction criterion.

In addition to the average dip, the maximum and minimum dips could be used, which would yield a projection cone, similar to uncertainty visualization suggested by Baumberger (2015). Applying this approach to a restricted area such as the underground rock laboratory investigated in this study, resulted in a total coverage and no possible distinction between different faults. However, for a final representation of the uncertainty related to the dip value on a regional scale (km-scale) the approach to visualize projection cones would suit.

4.5.3.2. GTS (decametre scale model) compared with km-scale 'best-estimate' model

As a result of differences in outcrop conditions, the number of observed faults is significantly higher in the underground laboratory compared to the surface (Fig. 4.12). In the underground, nearly 100% of polished outcrop is accessible along the tunnel walls (Fig. 4.11b), whereas at the surface faults are often covered with vegetation, even in relatively vegetation-poor domains.

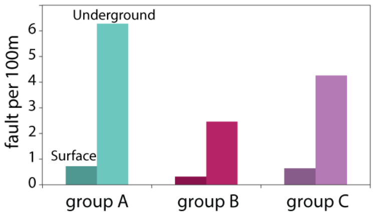

Figure 4.12. Histogram showing number of faults grouped per strike at the Earth's surface and in the underground (GTS).

Furthermore, we observe convergence of surface faults with depth in our 'best estimate' model, which could be a modelling artefact, as only surface faults that occurred spatially close to the underground facility were selected. Subsequently, the degree of fit of each surface fault was calculated to the closest underground fault. Therefore, faults were potentially passively rotated, yielding a 'pseudo' convergence. Moreover, no similar pattern was observed in the GTS model (decametre scale). We therefore conclude that the 'best estimate' interpolation model suffers from boundary effects, altering the fault orientation at the margin of the GTS and thus only faults in the central part will be further considered.

4.5.4.3. 'Maximum a posteriori' model

Comparison of numerous models obtained from Bayesian inference was performed calculating the number of intersections. The fewer intersections the more probable the model was considered. Assuming no intersections between large-scale fault set is simplistic, but from field observations seems plausible as a first approach for faults belonging to a specific orientation group (group A, B, C). This simplistic representation of nature enabled us to obtain a probability for all possible interpolations between a specific surface point and all underground points of the corresponding orientation group. As previously mentioned, the margins of the interpolation space show boundary artefacts and thus following surface points at model margin were not further considered: J03, J04, J05, J06, J19, J20, and J21 (Fig. 4.8). As expected, probability densities are skewed towards the area of lesser fault density (Fig. 4.9). At this point it is important to recall that probability density is given as area and therefore we cannot directly compare the discretized posteriors since they are function of the distance between nearby faults.

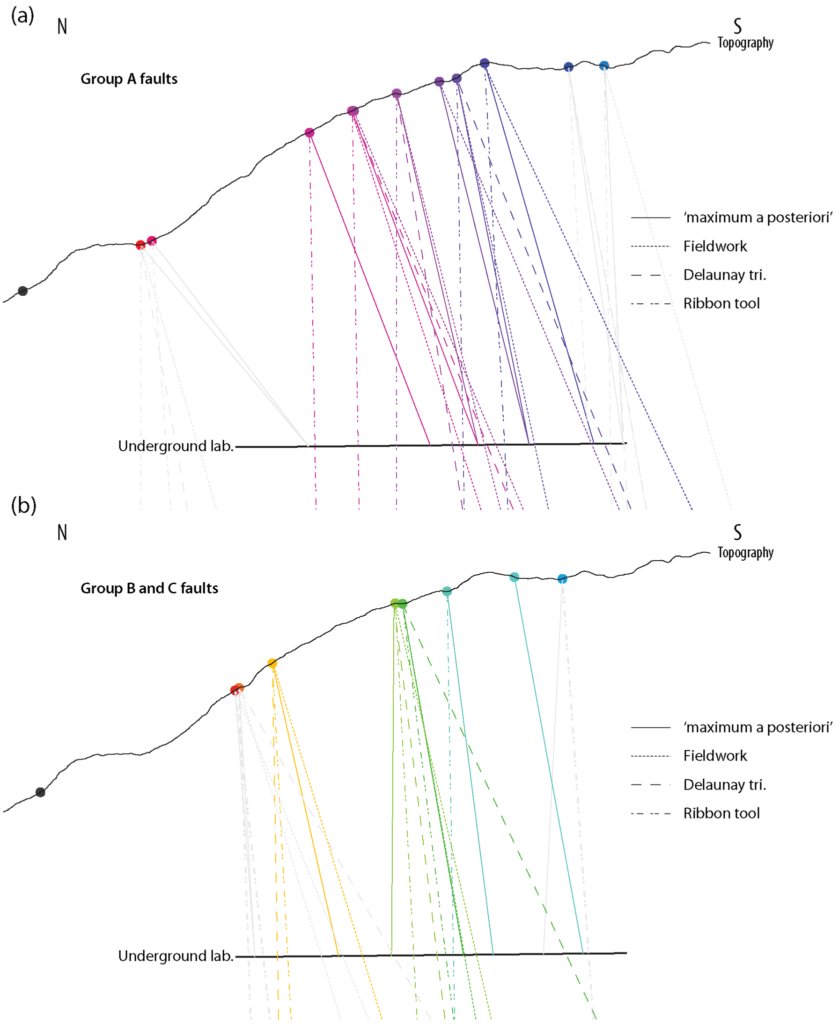

Figure 4.13. Comparison of 'maximum a posteriori' interpolation with three extrapolation approaches used to assign dip to fault exposure line. Figure subdivided in: (a) group A (NE-SW) and (b) group B (E-W) and group C (NW-SE). group B and group C are display conjointly as group B contains only two faults.

We initially compared the three extrapolation techniques based on the 'maximum a posteriori' model (Fig. 4.13). When comparing group A faults, fieldwork-based extrapolation closely fit the 'maximum a posteriori' interpolation, which indicates either that the fieldwork-based model yields 'best' results or validates the Bayesian inference approach depending if the reference state is the statistical interpolation or the measured field data. Generally, dips of 'maximum a posteriori' models are slightly steeper than measured dips during fieldwork (Fig. 4.14a). However, the dip differences between the fieldwork-based extrapolation 3D structural model and the 'maximum a posteriori' interpolation model are small (Fig. 4.14b). Also the dip differences between the ribbon tool based 3D structural model and the 'maximum a posteriori' interpolation model are small, but dips obtained via the ribbon tool are systematically steeper, which do not correspond to the measured dips (Fig. 4.14a). The extrapolation 3D structural model obtained via Delaunay triangulation is less close to 'maximum a posteriori' interpolation model and obtained dips vary substantially.

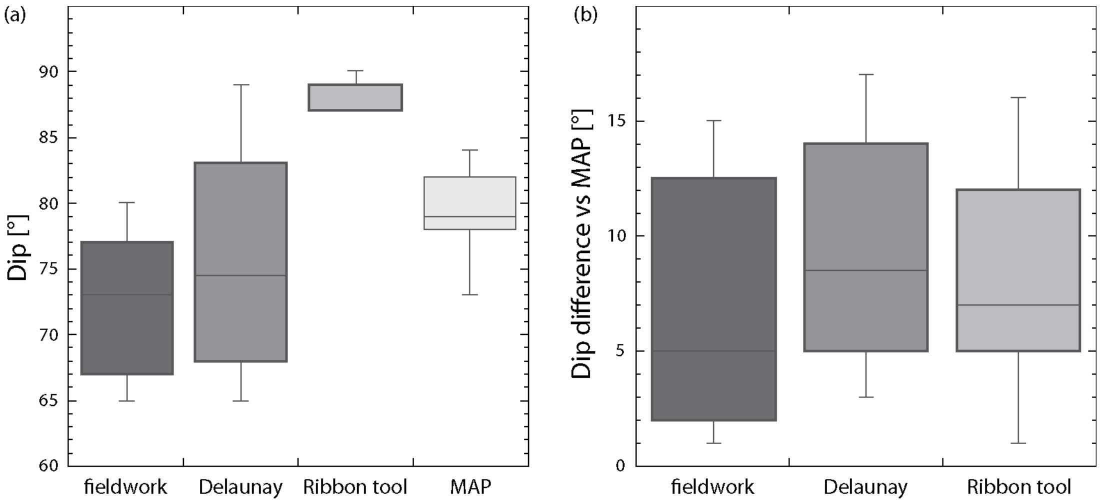

Figure 4.14. (a) Box plot showing dip value for different extrapolation approaches and for 'maximum a posteriori' (MAP) interpolation. (b) Box plots for dip comparison between different extrapolation approaches and the 'maximum a posteriori' (MAP) interpolation.

Comparison for the group B and C faults is less clear. Fieldwork-based and ribbon tool extrapolations are close to the 'maximum a posteriori' model (Fig. 4.13). Therefore, we conclude that fieldwork is still necessary for 3D structural modelling in crystalline environments and that the ribbon tool (Move^{TM}) offers numerous options to tune the obtained plane, however, this tuning requires a profound conceptual background model.

4.5.4.4. Possible model refinements

Presented surface models include only major faults (Fig. 4.15). However, for further applications such as for example groundwater flow modelling or slip tendency analysis not solely major faults are of interest but also their relay structures. Based on the orientation information gained from the regional km-scale models and on the intersection pattern observed during lineament mapping it is possible to infer a near surface 3D model not only with the major fault but also the relay structure. Furthermore, the increased level of detail in the GTS model (decametre scale) forms a similar model in the underground. The unknown space between both models would require probabilistic modelling with several key parameters as for example fault spacing, fault orientations, apertures or crosscutting relationships.

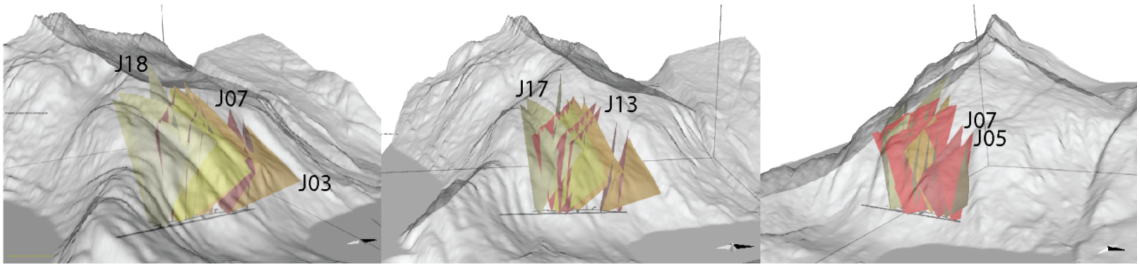

Figure 4.15. Representation in 3D of the 'maximum a posteriori' model of fault geometry with three different angle of view. N is indicated by the black triangle. The black tunnel is 717 m long.

4.6. Conclusions

The exceptional opportunity of surface and underground data comparison over 3D structural modelling approaches led us to the following conclusions:

- Lineament maps enable identification of major faults, but are highly sensitive to preferential erosion.
- Structural surface mapping allowed a discrimination of three orientation groups of faults.
- Comparison based on geometrical criteria (distance and angle misfit) of three approaches to extrapolate to depth surface traces yielded comparable results for all extrapolation approaches and less than 6% distance misfit.
- Interpolation of surface data with underground data based on a Bayesian inference problem showed that the fieldwork-based approach is the most accurate extrapolation technique. However, this could also validate the interpolation approach.

We conclude, similarly to Zanchi et al. (2009) that for 3D structural modelling an area within crystalline bedrock classical fieldwork is required not only for field measurements but also as base for a conceptual background model on which interpolations or extrapolations performed within 3D structural modelling can be examined for their validity.

4.7. Acknowledgments

This study was funded by the LASMO project run by NAGRA, RWM and SURAO. We thank NAGRA staff in the underground rock laboratory for excellent working environment. We thank the reviewers, Clare Bond, Gautier Laurent and an anonymous reviewer, whose comments greatly improved the manuscript.

Chapter 5

Structural permeability favourability in crystalline rocks: Implications for groundwater flow paths, a case study (Aar massif, Central Switzerland).

R. Schneeberger[1], D. Egli[1], G.W. Lanyon[2], U.K. Mäder[1], A. Berger[1], F. Kober[3], & M. Herwegh[1]

[1]Institute for Geological Sciences, University of Bern, Baltzerstrasse 1+3, CH-3012 Bern
[2] Fracture Systems Ltd, St Ives, Cornwall, UK
[3]Nagra, Hardstrasse 73, CH-5430 Wettingen

Abstract Groundwater flow in granitic bedrock is of major interest for applied projects such as deep-seated geothermal energy projects or underground disposal of radioactive waste. It is generally accepted that granitic basement rocks of the upper crust are characterized by faulted, low porosity rocks showing fault-related permeability.

In this study, we investigate the influence of existing fault patterns on the current water flow in the Grimsel Test Site (GTS), an underground rock laboratory located in crystalline bedrock. Structural mapping was carried out at the surface and in the underground and incorporated in a kilometre-scale model and in a GTS scale model (decametre scale). In the underground, water discharge points were mapped and compared with the mapped structures. Further, we evaluated the link between water flow and faults considering slip-tendency analysis and fault intersections. High slip-tendency faults and fault intersections were combined in a structural permeability favourability map.

Faults occur as three groups of orientations, NE-SW, E-W, and NW-SE, all steeply dipping southwards. Fault intersections are steeply plunging southwards. Water discharge points are located along faults or fault intersections. In total, 100 water discharge points were mapped in summer, whereas 85 were mapped in winter. Numerous water discharge points occur along faults located within former ductile shear zones or metabasic dykes.

A comparison of mapped underground water discharge points with density maps of (i) high slip-tendency fault segments and (ii) fault intersections shows that over 50 % of the water discharge points occur along (i), whereas 30-60 % occur within (ii). Water fluxes, however, are enhanced along (ii). Comparison of the structural permeability favourability map with the mapped water discharge points showed that over 90% of the discharge points occur within a domain of enhanced favourability.

We, therefore, conclude that the structural permeability favourability map is a suitable representation for constraining water discharging areas. Moreover, we infer, from the water flux measurements, that fault intersections are favoured locations for higher water circulation.

5.1. Introduction

Fractured media in low porosity crystalline bedrock play an important role in numerous applications such as the disposal of radioactive waste or enhanced geothermal power plants (e.g. Bredehoeft, 1997). Permeability in low porosity fractured media is considered to be anisotropic (Snow, 1969) consisting of high permeable fractures and low permeable rock matrix. Thus, advective fluid flow mostly concentrates along permeable faults (and their damage zones) with their enhanced fracture densities of granular fault cores (e.g. Barton et al., 1995; Bense et al., 2013; Berkowitz, 2002; Bisdom et al., 2016; Blessent et al., 2011; Burnside et al., 2013; Caine et al., 1996; Curewitz and Karson, 1997; Dockrill and Shipton, 2010; Eichhubl et al., 2009; Evans et al., 1997; Faulkner et al., 2010; Flint et al., 2001; Forster and Evans, 1991; Mazurek, 2000; Mazurek et al., 2003; Seaton and Burbey, 2005; Siler et al., 2016; Townend and Zoback, 2000; Walker et al., 2013).

Faults are formed in response to a non-uniform stress state when the rock is stressed beyond a rock-specific differential stress (e.g. Mandl, 2000). The type of faulting and the orientation of resulting faults are influenced by the stress state. In fractured bedrock, the current stress state influences whether a fault will be potentially reactivated, responds elastically or remains undeformed (Byerlee, 1978; Jaeger and Cook, 1971). Associated with deformation, elastic dilation or shear reactivation of a rough fault may increase its permeability (Bense et al., 2013; Wibberley et al., 2008). Previous studies have shown that the reactivation of a fault surface can strongly influence its water conduction behaviour (e.g. Barton et al., 1995; Townend and Zoback, 2000; Zoback and Townend, 2001). Tube-like channels have also been proposed for the geometry of water-conducting features (e.g. Curewitz and Karson, 1997; Figueiredo et al., 2016; Sibson, 1996; Siler et al., 2016) as an alternative to planar geometries.

In this study, we present a conceptual flow model for crystalline bedrock, where fault intersections and high slip-tendency faults are the two relevant features for water flow. We performed a case study where the concept of permeability favourability map, introduced by Siler et al. (2016) for geothermal exploration, and the 3D patterns of fault and fault intersections (Schneeberger et al., n.d.), are combined and crosschecked against water discharge mapping.

In order to perform this crosscheck the Grimsel Test Site (GTS), an underground rock laboratory, was selected as the study site. The Swiss National Cooperative for the Disposal of Radioactive Waste (Nagra) operates the GTS since more than 30 years (Blechschmidt and Vomvoris, 2010). The GTS has a long lasting research background and is structurally, geochemically and hydrologically well-characterized (e.g. Frick et al., 1992; Frieg and Blaser, 2012; Hoehn et al., 1990; Keppler, 1994; Keusen et al., 1989; Kralik et al., 1992; Schneeberger et al., 2016; Vomvoris et al., 1992) and therefore offers an ideal study site to test the structural permeability favourability map as a prediction tool for water conductivity of faults.

5.2. Geological setting

5.2.1. Geology

The GTS is located within the Central Swiss Alps in the Haslital (Fig. 5.1). Geologically, it is within the Aar massif, one of the External Crystalline massifs of the Alps (e.g. Pfiffner, 1993; von Raumer et al., 2009, 1993). The country rock is composed of (i) two granitoids from a calc-alkaline magmatic suite (Berger et al., 2017b; Keusen et al., 1989; Schaltegger, 1994), the Grimsel granodiorite (GrGr) and the Central Aar granite (CAGr), and (ii) of metabasic dykes (Keusen et al., 1989; Oberhänsli, 1986). The granitoids have Permian concordant U/Pb intrusion ages of 299 ± 2 Ma (Schaltegger and Corfu, 1992). The GrGr is characterized by a higher biotite content compared to the CAGr (Keusen et al., 1989; Wehrens et al., 2017). The granitoids are intruded by metabasic dykes, which are mainly composed of biotite and plagioclase (Keusen et al., 1989; Oberhänsli, 1987). The metabasic dykes are mainly oriented NW-SE or E-W (Schneeberger et al., 2016).

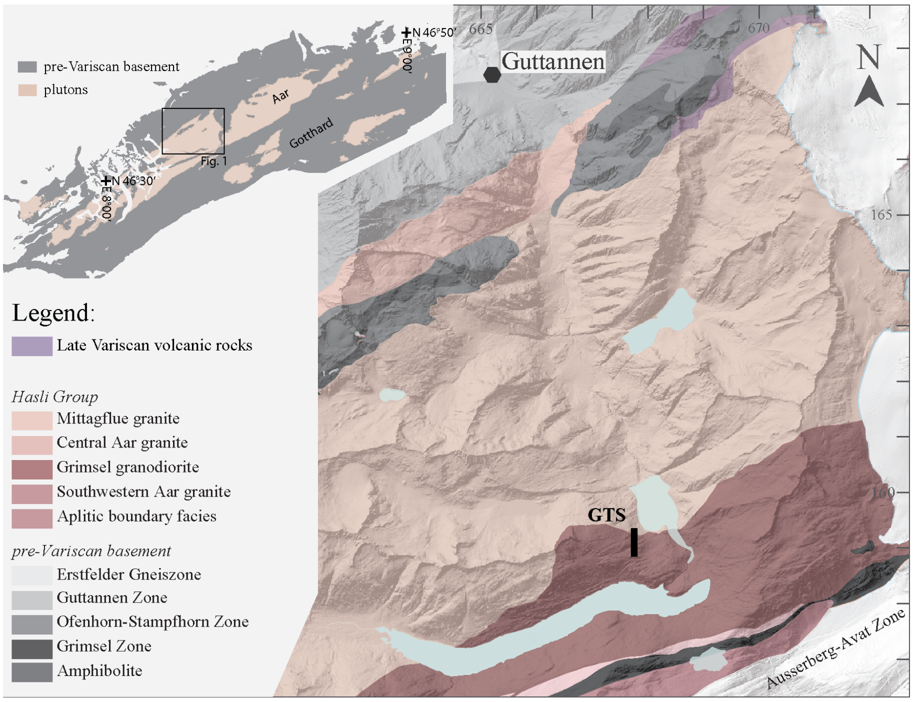

Figure 5.1. Geological map of the Haslital modified after Berger et al. (2017). The location of the GTS is marked with a black line. Inlet shows the basement rocks for the Alpine orogeny.

5.2.2. Deformation history – metamorphism

The granitoids (CAGr and GrGr) show pervasive saussuritization and sericitization (Keusen et al., 1989; Wehrens et al., 2017). Peak metamorphic overprint related to the Alpine orogeny was estimated to 450 ± 30°C and 6 ± 1 kbar (Challandes et al., 2008). Alpine deformational overprint is expressed by pervasive foliation that was formed as a consequence of ductile deformation. In addition, highly localized ductile deformation led to the formation of km-sized high strain zones, ductile shear zones (Fig. 5.2; e.g. Choukroune and Gapais 1983; Herwegh et al. 2017; Rolland et al. 2009; Wehrens et al. 2017). Ductile shear zones occur in three distinct orientations, NE-SW, E-W and NW-SE striking, all steeply S dipping (Fig. 5.3). Most ductile shear zones show down dip lineations indicating vertical transport directions, however oblique to horizontal lineations have also been observed suggesting strike-slip movements (Schneeberger et al., 2016; Wehrens et al., 2017). NE-SW striking shear zones can be associated with the Handegg phase, whereas the E-W and the NW-SE striking shear zones formed during the Oberaar phase (Wehrens et al., 2017).

During exhumation and cooling of the Aar massif (e.g. Diamond and Tarantola, 2015; Glotzbach et al., 2010; Reinecker et al., 2008), the ductile shear zone as mechanical anisotropies were broadly reactivated by brittle fracturing leading to the development of cataclasites, fault gouges and brittle fractures (Fig. 5.2; e.g. Belgrano et al., 2016; Bense et al., 2014; Bossart and Mazurek, 1991; Keusen et al., 1989; Kralik et al., 1992; Steck, 1968; Wehrens et al., 2017). Fault gouges being non-cohesive zones of enhanced porosity (10-30 Vol%; Fig. 5.2) are prone for water flow (Bossart and Mazurek, 1991; Sibson, 1996; Zhu and Wong, 1997). The mineralogy of the fault gouges is almost identical to the mineralogy of the ductile shear zones, but sporadic formation of clay minerals has been observed (Bossart and Mazurek, 1991; Kralik et al., 1992; Wehrens, 2015).

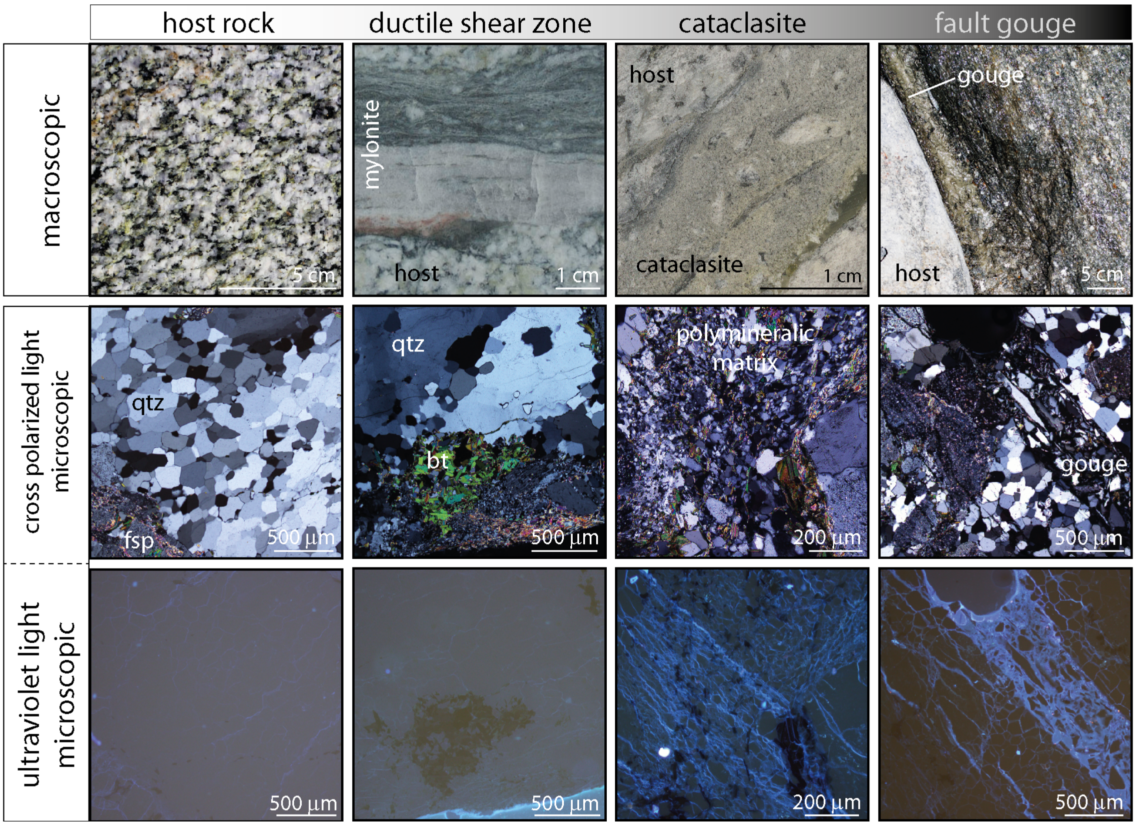

Figure 5.2. Deformation sequence of CAGr from weakly deformed host rock over ductile deformed shear zone to brittle cataclasite eventually leading to non-cohesive fault gouge. Microscopic images taken under cross polarized light (central row) or UV light (bottom row).

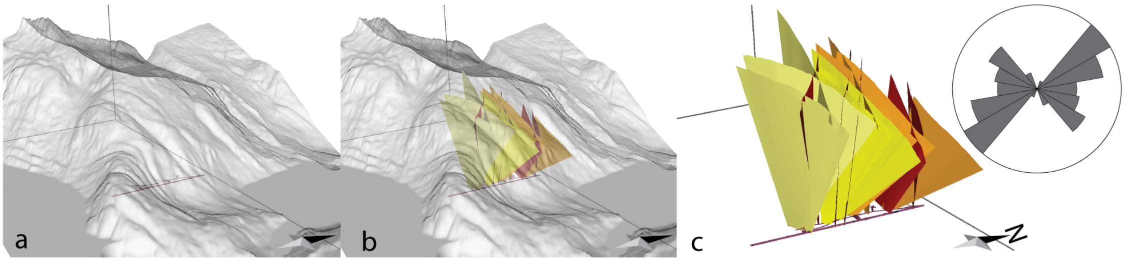

Figure 5.3. (a) 3D elevation model of the mountainside and the GTS. (b) 3D view of the GTS with the major fault zones connecting fault-surface intersections with fault exposed at GTS. (c) Close up on the fault zones and the GTS of (b) additionally displaying a rose diagram of the strike of the faults. (Tunnel length is ca. 700m).

From here onwards, we use the term fault as a summary term for different types of structures related to brittle deformation such as fault zone, fault gouge, cataclasite, fracture or joint. The geometrical pattern of faults around the GTS has been reported previously (Schneeberger et al. in prep.; Schneeberger et al., 2016). A structural 3D model of the area around the GTS is shown in Figure 5.3 and can be found in the supplementary material for more details.

5.2.3. Infiltration conditions, water hydro-geochemistry and residence time estimations

Groundwater flow into the GTS has been previously documented indicating inflowing waters being of meteoric origin and mostly tritium free, suggesting infiltration before the tritium peak in the early 1950s (Fig. 5.4; Frick et al., 1992; Keppler, 1994; Keusen et al., 1989; Schneeberger et al. in prep.).

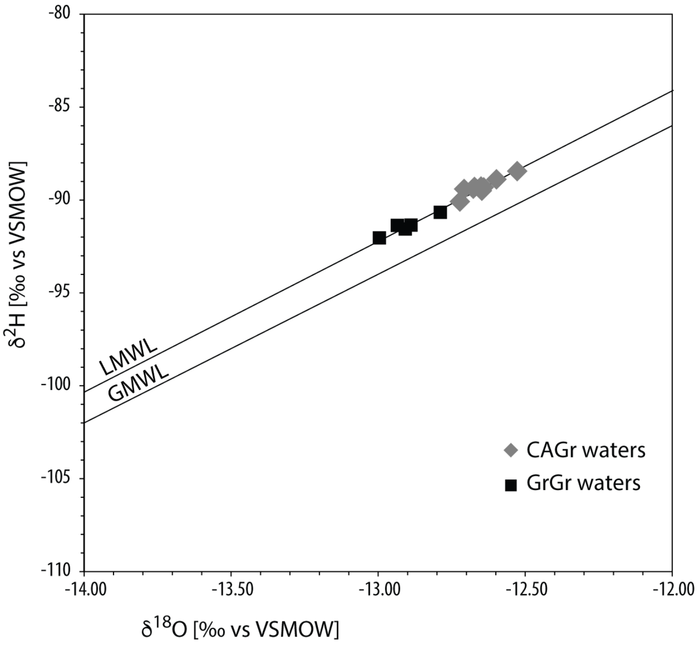

Figure 5.4. Stable isotope composition of sampled groundwater. All values are displayed as small crosses (Data from Schneeberger et al. in prep.). Average (av.) values per sampling location are highlighted. LMWL: Local Meteoric Water line (Schotterer et al. 2010); GMWL: Global Meteoric Water Line (Craig, 1960).

During downwards circulation water interacts with the bedrock (Fig. 5.5) and dissolves minor amounts of its components, mainly plagioclase. Water sampled within the CAGr differs geochemically from water sampled within the GrGr (Schneeberger et al. in prep.) when sampled at the GTS level. These differences probably result from differences in water residence time, i.e. flow path length.

Under "undisturbed" conditions, i.e. without an underground lab draining the mountainside, water would discharge in the valley floor, the Haslital-Aare (Frick et al., 1992; Voborny et al., 1991; Vomvoris et al., 1992).

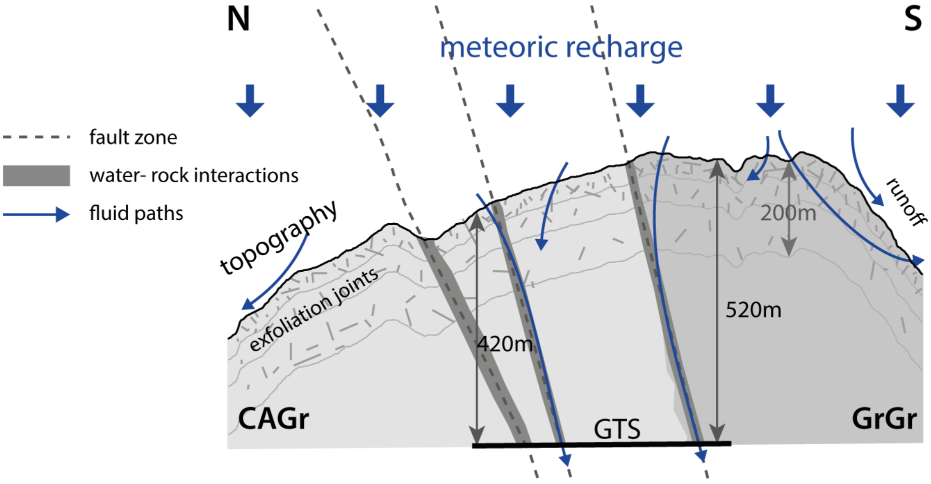

Figure 5.5. Schematic cross section above GTS (Grimsel Test Site) showing (i) highly fractured near surface zones (exfoliation joints) and (ii) large-scale steep fault zones. Pervasive and localized flow of meteoric water occurs along (i) and (ii), respectively.

5.3. Methods & concepts

In order to examine the interplay between brittle deformation and water flow within crystalline bedrock and to test the application of a structural permeability favourability map, we mapped water discharge points in the gallery system of the GTS. The water discharge point map was compared with previous mappings of water discharges in the GTS (Keusen et al., 1989) and with the most recent structural mapping of the GTS (Schneeberger et al., 2016) in order to check for the structural link and changes in water flow with time. Water discharge points were mapped where, at minimum, a visible moisture spot occurred.

In order to be recognized as distinct moisture spot a water-conducting fault requires a minimum flux from the rock, which is higher than the evaporation. For the GTS this is estimated to be ~1ml/min/m^2 equivalent to a minimum hydraulic conductivity of approximately. 3×10^{-8} m/s (Mazurek, 2000), which is significantly greater than the inflow expected given the estimated matrix hydraulic conductivity of ~5×10^{-12}m/s (Finsterle and Pruess, 1995). However, the required flux to maintain a wet-spot varies with the ventilation with generally dryer air in winter times (Gimmi et al., 1997). Therefore, two mapping campaigns were performed, in summer (June 2014) and in winter (January 2016). The total number of discharge points is smaller in winter compared to summer.

While mapping, the water discharge points were attributed to the respective water-bearing structural features, which were metabasic dykes, ductile shear zones, fault gouges, brittle fractures, or tunnel walls. The water discharge points were assigned to the category "wall" in cases where no apparent structure was observed at the discharge point.

Previous studies have demonstrated that the slip-tendency of a fault represents an important parameter to explain differences between water-conducting and non-water-conducting faults (e.g. Barton et al., 1995; Hennings et al., 2012; Townend and Zoback, 2000; Zoback and Townend, 2001). Surface roughness of fault planes being prone for slip allow for openings after the slip event providing new paths for fluid flow (e.g. Brown, 1987).

Slip-tendency (μ) is defined as the ratio of shear stress (τ) to effective normal stress (σ_n) acting on a given surface (e.g. Bott, 1959; Jaeger and Cook, 1971; Morris et al., 1996; Wallace, 1951):

$$\mu = \tau/\sigma_n$$

Faults with slip-tendency above 0.6 ($\mu>0.6$) are considered as high slip-tendency faults (e.g. Barton et al., 1995), i.e. they are favourable to be activated . $\mu > 0.6$ was chosen, which corresponds to a rather low slip tendency, but represents a worst-case scenario for the disposal of radioactive waste. We calculated the slip-tendency (Bott, 1959; Jaeger, 1969; Jaeger and Cook, 1971; Morris et al., 1996; Wallace, 1951) of mapped faults, such as brittle fractures, fault gouge, brittle reactivated former ductile shear zones or brittle overprinted metabasic dykes, based on estimations of the current stress tensor (Frieg and Blaser, 2012; Krietsch et al., 2017; Pahl et al., 1986), assuming a constant pore fluid pressure of 4MPa. The latter corresponds approximately to the maximum reported hydraulic pressure in the GTS, which correlates with an overburden of about 400 m.

The high slip-tendency (with $\mu \geq 0.6$) faults were selected and used to develop a line density map using ArcMap™. The density map was calculated on the base of a grid with 10 m x 10m cells.

$$Cell\ value\ =\ {}^{l_{slip}}\!/_{A_{cell}}$$

where, l_{slip} is the total length of high slip-tendency fault segments cutting the cell and A_{cell} the cell area. The values within the density map were subsequently normalized using a linear fuzzy membership function. This function assigns a probability to each density value. In the case of the linear function, the largest entered value obtains the value 1 and the smallest is set to 0. All values in between are assigned to a probability, which decreases linearly as the difference between the specific density value and the maximum density value increases (e.g. Pradhan et al., 2009; Zadeh, 1965).

Moreover, the intersections between faults were calculated and a point density map was generated. The cell size of the orthogonal grid was 10x10 m. Subsequently, the point density map was normalized using a linear fuzzy membership function (e.g. Zadeh, 1965).

Lastly, both density maps were combined by a weighted sum, where each raster was weighted 0.5, resulting in a structural permeability favourability map.

5.4. Results

5.4.1. Mapping water-conducting features

Water discharge points co-occur spatially with faults (Figs. 5.6a, 5.7). In total, 100 water discharge points were mapped during the summer mapping and 85 during the winter mapping. Among the summer discharge points, 37 were mapped along faults in metabasic dykes, 48 along faults localized in ductile shear zones, 9 along fault gouges, 5 along brittle fractures and 1 with no underlying apparent structure (Fig. 5.6b). In the winter mapping, 27 discharge points occurred along metabasic dykes, 49 along faults in ductile shear zones, 4 along fault gouge, 4 along fractures and 1 with no underlying apparent structure.

Water discharge points mapped along faults mostly occur within 1 m distance to the associated structure (Fig. 5.6 c, d and e). This corresponds approx. to the mapping accuracy.

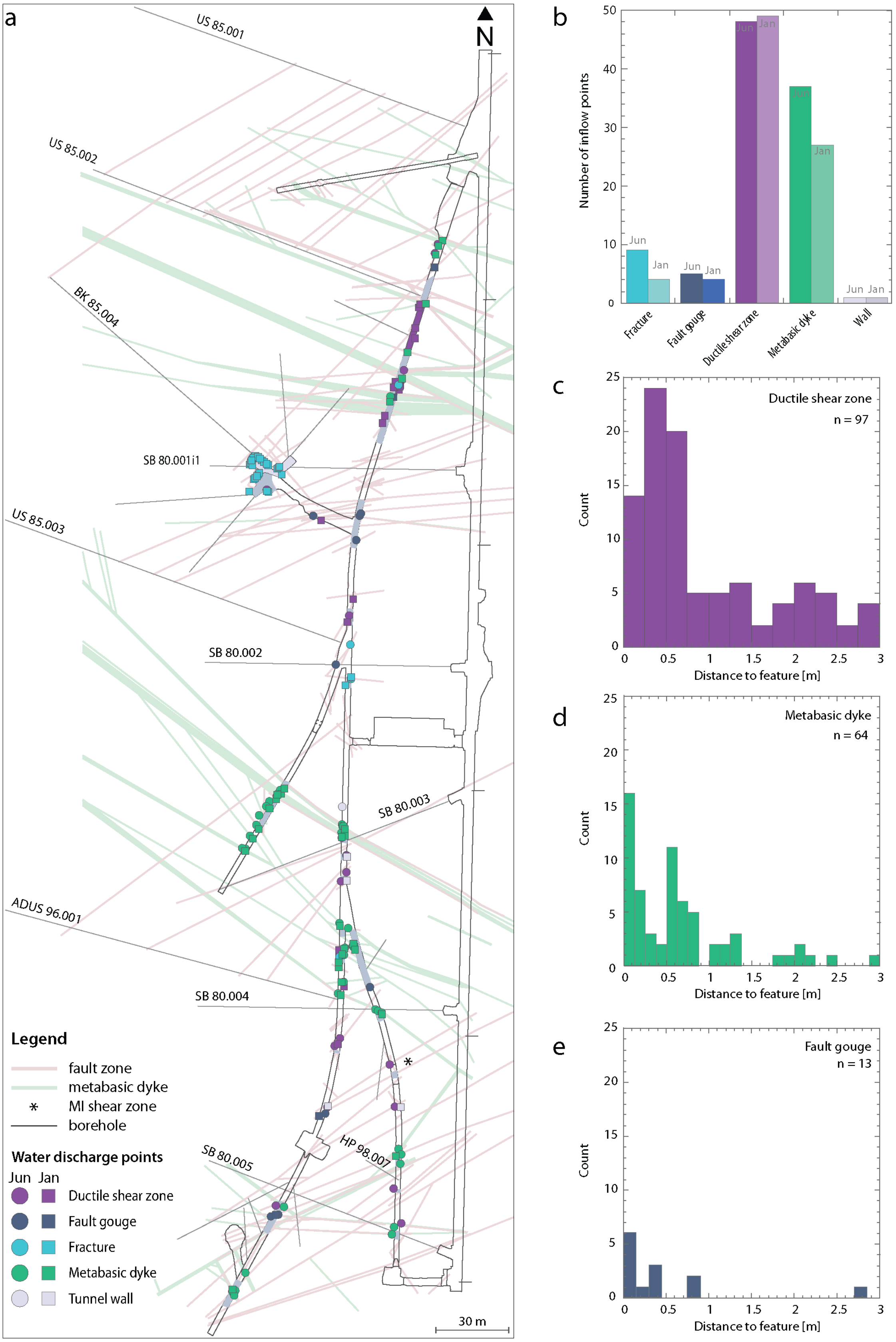
a
N
US 85.001
US 85.002
BK 85.004
SB 80.001i1
US 85.003
SB 80.002
SB 80.003
ADUS 96.001
SB 80.004
SB 80.005
HP 98.007
*
30 m
Legend
fault zone
metabasic dyke
* MI shear zone
borehole
Water discharge points
Jun Jan
Ductile shear zone
Fault gouge
Fracture
Metabasic dyke
Tunnel wall
b
Number of inflow points
0
10
20
30
40
50
Jun
Jan
Fracture
Fault gouge
Ductile shear zone
Metabasic dyke
Wall
c
Ductile shear zone
n = 97
Count
0
5
10
15
20
25
Distance to feature [m]
0
0.5
1
1.5
2
2.5
3
d
Metabasic dyke
n = 64
Count
Distance to feature [m]
e
Fault gouge
n = 13
Count
Distance to feature [m]

Figure 5.6. (a) GTS map showing major deformation features and water discharge points mapped in June 2014 and Jan 2016. (b) Histogram showing water discharge points grouped by mapped underlying structure. Histograms showing the distance between mapped water discharge point and underlying structure, (c) ductile shear zone, (d) metabasic dyke or (e) fault gouge.

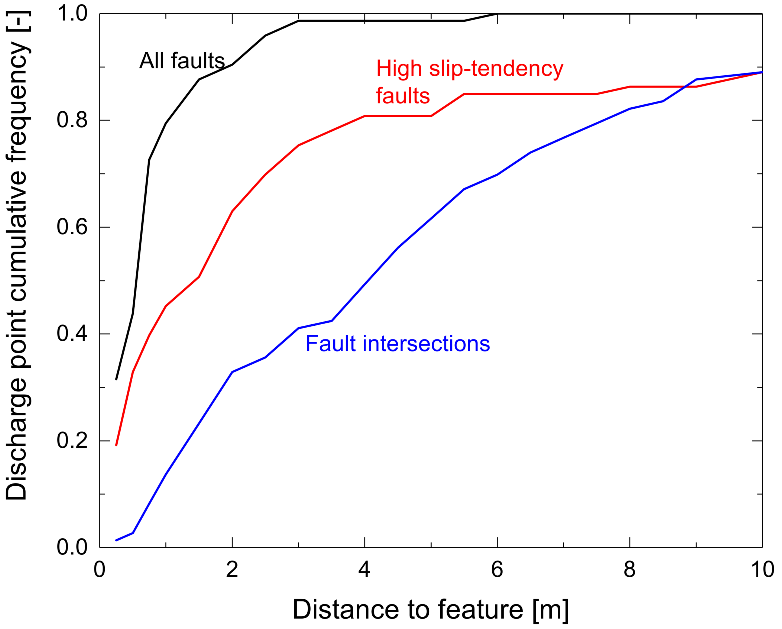

Figure 5.7. Cumulative frequency diagram showing distance from a water discharge point to the nearest structural feature (all faults, high slip-tendency faults, fault intersections).

Faults occur with three distinct strike orientations, NE-SW, E-W and NW-SE (Schneeberger et al., 2016; Wehrens et al., 2017, 2016) with water discharges coinciding with faults of all three orientations (Fig. 5.6a). In total 113 faults crossing the circumcircle of the tunnel were mapped within GTS, 53 NE-SW striking, 25 E-W trending and 35 NW-SE striking.

Relative to the number of mapped discharge points, 51.4 % (summer and winter) of NW-SE striking faults are water conducting and therefore NW-SE striking faults appear to be the preferred orientation for water flow paths. In summer 39.6% of the NE-SW striking faults were water conducting and 24% of E-W striking faults. In winter 35.8% of the NE-SW and 36% of the E-W striking faults were water conducting.

While mapping in January 2016, special focus was payed to whether the entire fault intersection with the tunnel wall was water conducting or whether only a portion of the fault discharges water to the tunnel. Most water discharges were observed in the lower half of the tunnel circumference and no punctual discharges were observed within the tunnel. However, water discharges in the tunnel are affected by a skin effect (Mazurek, 2000), which changes the hydraulic properties in the near-field of a tunnel (ca. one tunnel diameter), and punctual discharges are known from borehole images (Fig. 5.8) and from the MI shear zone (star in Fig. 5.6a), which could not be mapped as it had been sealed in 2005. Flow into the tunnel from the MI shear zone had previously been identified at 4 points around the shear zone intersection (Meier et al., 2001).

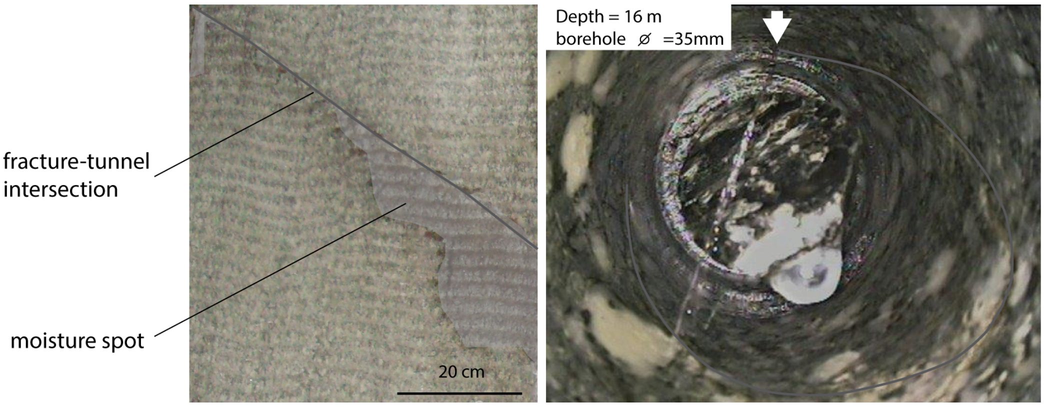

Figure 5.8. (a) Image of a water-conducting fault. (b) Borehole image showing a fault with punctual water discharge (arrow, photo courtesy by Nagra).

5.4.2. Structural permeability favourability map

Water discharge mapping revealed clustering of discharge points along faults. However, not all faults observed within the GTS, are associated with discharge points. In the following, different effects potentially influencing the water conductivity of a fault are examined.

5.4.2.1. Water discharge points compared with high slip-tendency faults

Different stress estimations of the current stress state for the GTS are available (Fig. 5.9; Frieg and Blaser, 2012; Krietsch et al., 2017). The orientations of the principal stress axes (σ_1) are similar for both stress tensors, the main principal stress being sub horizontally NW trending. Although the exact magnitudes of the stresses show some variations (Tab. 5.1), it is possible to evaluate the reactivation potential of faults qualitatively based on their orientation to the stress tensor.

The two stress tensors result in a range in magnitude for the principal stresses (Tab. 5.1). The maximum and minimum values of this range were used and both stress measurement campaigns compared (Fig. 5.9).

Based on the stress tensor estimated by Krietsch et al. (2017) and assuming 4MPa pore fluid pressure, the slip-tendency (μ) was calculated in 3D for all major faults occurring in the GTS. The minimum magnitude stress tensor by Krietsch et al. (2017) was chosen as only with this stress tensor any faults displayed slip-tendency above 0.6.

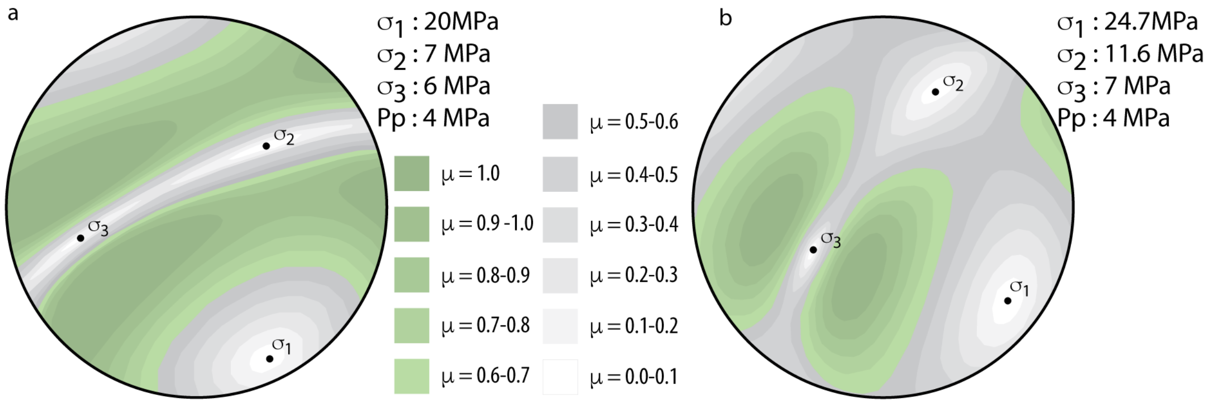

Figure 5.9. Stress tensor estimation with minimum magnitude, where orientations favourable to slip ($\mu>0.6$) are colour coded (contour interval is 0.1). (a) Stress tensor estimations taken from Krietsch et al. 2017 and (b) from Frieg & Blaser (2012).

Table 5.1. Site-specific stress tensor estimation (Frieg & Blaser, 2012; Krietsch et al., 2017).

	Krietsch et al. (2017)			Frieg & Blaser (2012)		
	Plunge azimuth [°]	Plunge [°]	Magnitude [MPa]	Plunge azimuth [°]	Plunge [°]	Magnitude [MPa]
σ_1	155	13	20-24	125	16	24.7-30
σ_2	228	-50	7-15	024	32	11.6-14.1
σ_3	255	37	6-12	242	52	7-9.7

The 2D intersections of high slip-tendency ($\mu \geq 0.6$) 3D fault planes were calculated at the elevation of the GTS and used as the base for the high slip-tendency fault segment density map (Fig. 5.10a and b). Most faults are rather planar (Wehrens et al., 2017) and therefore a single slip-tendency characterizes the entire fault.

From the total 113 faults mapped within the GTS, 64 (~56%) are high slip-tendency faults using the criteria $\mu \geq 0.6$ (20 NE-SW, 9 E-W, 35 NW-SE). From the 64 high slip-tendency faults, 43 faults (70%) are water conducting, whereas only 18 show water discharge points along a low slip-tendency fault. Comparison of the high slip-tendency fault segment density map with the mapped water discharge points indicates a strong correlation between both (Figs. 5.7, 5.10a).

5.4.2.2. Intersections of faults

Next to the high slip-tendency fault segments also the intersection of faults are considered as potential water-conducting features (e.g. Belgrano et al., 2016; Curewitz and Karson, 1997; Sibson, 1996; Siler et al., 2016). Therefore, all fault intersections were calculated resulting in a steeply S plunging bundle of fault intersection lines (Fig. 5.11).

Fault intersections served as basis for a point density map (Fig. 5.10c). Comparison of the intersection density map with the mapped water discharge points revealed that high intersection density domains correlate with clusters of water discharge points, most prominently in the western cross-shaped gallery system (Fig. 5.7 and 5.10c).

5.4.2.3. Structural permeability favourability map

Combination of the high slip-tendency fault segment density map with the fault intersection density map resulted in a structural permeability favourability map (Fig. 5.10d). The structural permeability favourability map is conceptually similar to the geothermal favourability map presented by Siler et al. (2016).

Comparison of the structural permeability favourability map with the mapped water discharge points revealed a strong correlation.

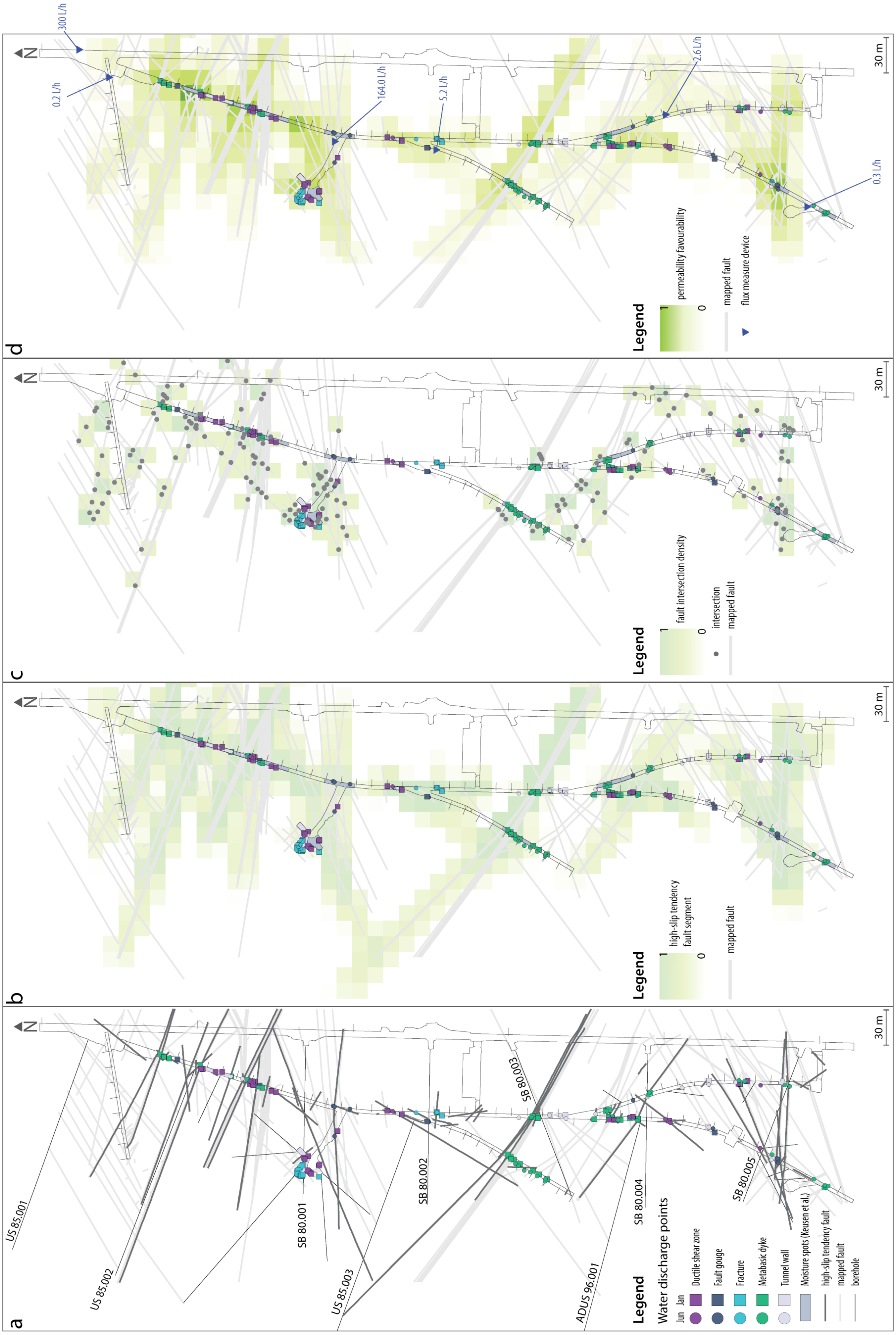
a
b
c
d
N
30 m
Legend
Water discharge points
Jun
Jan
Ductile shear zone
Fault gouge
Fracture
Metabasic dyke
Tunnel wall
Moisture spots (Keusen et al.)
high-slip tendency fault
mapped fault
borehole
US 85.001
US 85.002
US 85.003
SB 80.001
SB 80.002
SB 80.003
SB 80.004
SB 80.005
ADUS 96.001
high-slip tendency fault segment
1
0
fault intersection density
intersection
permeability favourability
flux measure device
300 L/h
0.2 L/h
164.0 L/h
5.2 L/h
2.6 L/h
0.3 L/h

Figure 5.10. (a) Map of the Grimsel Test Site with mapped water discharge points, mapped faults and dykes and high slip-tendency faults. (b) Density map of high slip-tendency fault segments. (c) Density map of fault intersections. (d) Sum of both density maps resulting in a structurally controlled permeability favourability map. Water fluxes measurements are indicated at the northeastern end of the measured gallery section (Kober and Härtel, 2014).

5.5. Discussion

5.5.1. Mapping water discharge points

Generally, the number of water discharge points is lower during winter compared to summer (Fig. 5.6b). This is due to ventilation with dryer air from outside the GTS during winter and thus significantly reduced relative humidity in the tunnel system (Kober and Härtel, 2014). As a consequence, the evaporation from the rock mass is higher and only domains of enhanced water flux are capable of maintaining moisture spots in winter.

The rare occurrence of water discharge points without an associated structural feature is probably a 3D problem, where in the third dimension beyond the tunnel wall a water-conducting structure may be present. Note that flow through the matrix in the solid host rock is too small to form wet spots, requiring the presence of a nearby water-conducting structure – the contrast in permeability may result in high hydraulic gradient between the structure and the tunnel wall.

The main water discharge domains within the GTS seem to persist over time considering that similar domains occurred in the mapping shortly after GTS construction (Keusen et al., 1989) and our own mapping (Fig. 5.6). Strikingly, Keusen et al. (1989) observed most discharges along NE-SW striking faults as well as along contact surface between metabasic dyke and the granitoid host rock (NW-SE striking). Also Martinez-Landa and Carrera (2005) identified rims of metabasic dykes as the main water flow paths in the GTS. These observations are in line with our statement that NE-SW and NW-SE striking faults represent the main water-conducting features.

5.5.2. Increase of permeability over brittle reactivation - link to permeability in low porosity bedrock

As already shown previously and confirmed by our study, faults are governing water flow in the crystalline bedrock around the GTS (e.g. Bossart and Mazurek, 1991; Keusen et al., 1989; Mazurek, 2000). Most importantly dilatation associated to brittle deformation increases the porosity of the fault compared to the protolith (Fig. 5.2; e.g. Bense et al., 2013; Bossart and Mazurek, 1991; Mazurek, 2000; Zhu and Wong, 1997). The increased connected porosity in turns leads to a higher permeability, which is inferred to be anisotropic being larger in-plane than out-of-plane of faults. Evidence for the existence of anisotropic permeability and low communication between different water-conducting features is twofold; (i) differences in chemical composition of the waters flowing along faults and (ii) from differences in hydraulic pressure between neighbouring faults (Keppler, 1994):

(i) An aqueous geochemical study performed earlier has shown persistent and significant differences in chemical composition between neighbouring faults (Schneeberger et al. in prep.). Therefore, low water exchange across faults is inferred.

(ii) Pressure monitoring along boreholes within the GTS have shown that large pressure differences are preserved between nearby faults (Schneeberger et al. in prep.). This indicates a low hydraulic communication between neighbouring faults and thus a hydraulic isolation of single faults.

5.5.3. High slip-tendency faults

Comparison of the water discharge point map with the high slip-tendency fault segment density map (Fig. 5.10a and b) revealed that 60 out of 100 (60.0%) water discharge points mapped in summer and 48 out of 85 (56.5%) water discharge points mapped in winter occur along a high slip-tendency fault. The majority (70%) of the high slip-tendency faults are water conducting and over 50% of the water discharge points occur along a high slip-tendency fault. This highlights the importance of high slip-tendency faults as water conduits in fractured low porosity bedrock.

If a fault has a high slip-tendency depends on the orientation of the fault and on the orientation and magnitude of the stress tensor (Jaeger and Cook, 1971; Morris et al., 1996). However, in situ stress tensor estimations are complex (e.g. Evans and Engelder, 1989; Krietsch et al., 2017; Martin and Christiansson, 1991; Martin, 2007). In the GTS, both stress tensor estimations were performed within the less deformed rock matrix between faults. However, it is known that stress state varies across faults (Faulkner et al., 2006; Flach and Noell, 1989; Hardebeck and Hauksson, 1999; Martin and Chandler, 1993). Thus potential variation in the orientation of the principal stress tensors between near fault (inter-block) and at fault intersections may occur.

Despite such local variations, the existing stress tensors provide a first-order estimate for the estimation of the slip-tendency of major fault orientations. Faults orientated perpendicular to the least principal stress (σ_3) are prone to be reactivated and potentially dilate creating open flow paths (Jaeger and Cook, 1971). The orientation of σ_3 is comparable between both stress tensor estimations (Frieg and Blaser, 2012; Krietsch et al., 2017) and gently plunges towards SW. Therefore faults striking NW-SE are favourably orientated for both dilation and reactivation.

Furthermore, the absolute magnitude of the principal stress axes may vary over time. Processes such as global earth tides, hydropower managed lake level changes and annual air pressure changes are known to influence the hydraulic pressure measured in boreholes in the GTS (Flach and Noell, 1989; Frieg and Blaser, 2012; Noell, 1994). However, the magnitude of those effects is rather small, as borehole test interval pressures vary as much as 5-15 mbar in response to tidal waves (Frieg and Blaser, 2012). Hence such effects are of secondary importance for slip-tendency estimations and are neglected for the further discussion.

5.5.4. Intersection density domains

Fault intersections are known to influence fluid flow (Belgrano et al., 2016; Curewitz and Karson, 1997; Figueiredo et al., 2016; Sibson, 1996; Siler et al., 2016). In the GTS most fault intersections are steeply S plunging. Assuming gravity-driven water flow, steeply dipping fault intersections (Fig. 5.11) form suitable channels for water flow from the topographic surface to the GTS.

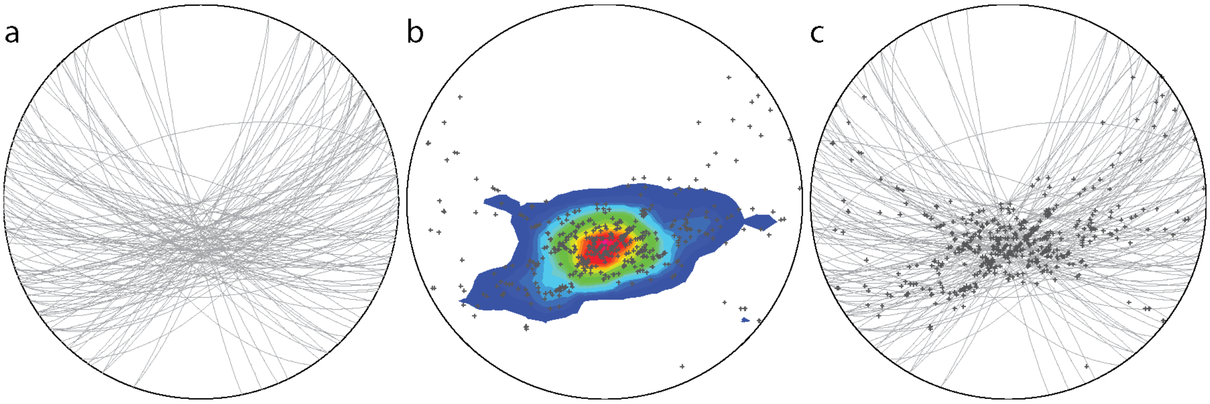

Figure 5.11. Stereoplots showing (a) the orientation (great circles) of all mapped faults in the GTS (n=160), (b) the intersections (dots) between faults in the GTS (contour interval 1 % of uniform distribution; n=573), and (c) the combination of the fault planes (great circles) and the intersections (dots). All stereoplots show equal area lower hemisphere projections.

In general, 26 out of 91 in summer and 46 out of 75 in winter mapped discharge points are located within a domain with increased fault intersection density (Fig. 5.10), which is a smaller fraction than the correlation between water discharge points and high slip-tendency faults. Also the distance from a water discharge point is typically larger to the nearest fault intersection than the distance to the nearest high slip-tendency fault (Fig. 5.7).

5.5.5. Correlation between structural permeability favourability map, water discharge mapping and actual discharge flux

Comparison of the structural permeability favourability map with the mapped water discharge points revealed a strong correlation between the favourability and the discharge points. 89.0% (81 out of 91) water discharge points mapped in summer and 90.6% (68 out of 75) mapped in winter times are located within a domain with increased favourability for acting as water flow path.

However, in the GTS a prominent water-conducting feature (Migration shear zone, Fig. 5.6a; Bradbury, 1989) reveals no structural permeability favourability despite being known as transmissive fault (hydraulic conductivity: $3.6x10^{-6}$; Hoehn et al., 1990). This structure is however highly channelled and is only observed as a significant discharge point in one of the 4 tunnels that it intersects This exception emphasizes the difficulty to predict water flow paths and highlights that the structural permeability favourability map describes only a favourability.

5.5.6. 1D versus 2D water flow

As shown before, high slip-tendency faults have a major effect on localization of water discharge. When comparing with the number of discharge points, the effect of fault intersections is less. However, comparison of the structural permeability map with the measured water discharge fluxes (Fig. 5.10d) showed that domains with enhanced density of fault intersection discharge ca. 195 L/h to the GTS, whereas domains with high density of high slip-tendency faults discharge ca. 97 L/h, and domains with high density of low slip-tendency faults 2.94 L/h (Kober and Härtel, 2014). These water flux measurements indicate a possible graded relevance for water flow, where fault intersections are the most important factor followed by high slip-tendency faults, followed by low slip-tendency faults. This hierarchy of importance of water-conducting features has been suggested previously for the GTS (Martel and Peterson, 1991).

On a smaller scale (single water-conducting fault), flow channelization within planar faults is inferred from geochemical analyses of groundwater from 2 nearby boreholes cutting the same fault revealing persistent differences between both water samples (Schneeberger et al. in prep.). This might indicate low in-plane exchange within a given fault. This could indicate a rather tube-like 1D flow channels located within planar faults. Similar tube-like channels are illustrated in Figure 5.11 showing a borehole image with a punctual discharge located within a planar fault and have been reported for the MI shear zone as mentioned previously(Bossart and Mazurek, 1991).

Further evidence for channelized flow in planar faults was found by microscopic studies of resin-injected overcored borehole in the GTS, which enabled sampling of the fault gouge (Bossart and Mazurek, 1991; Mazurek, 2000), in other crystalline environments (Belgrano et al., 2016; Mazurek et al., 2003; Siler et al., 2016), in analogue modelling (Lunn et al., 2008) as well as in other field studies (e.g. Annunziatellis et al., 2008; Barton et al., 1995; Dockrill and Shipton, 2010).

5.5.7. Application of the concept of the structural permeability favourability to the local 3D fault pattern

In order to verify the concept of the structural permeability favourability, surface data from above the GTS was used. A surface mapping revealed 18 faults that could be extrapolated towards depth matching faults in the GTS (Schneeberger et al. in review). From those faults the intersections were compiled in 3D and the slip-tendency was calculated using the same stress conditions as for the underground laboratory (Fig. 5.12). Comparison of the high slip-tendency faults (n=7) revealed that with one exception all high slip-tendency fault zones identified at the surface are water conducting within the GTS. Within the low slip-tendency faults, 2 faults (out of a total of 11) are water conducting.

Fault intersections highlight similar domains as being potentially water conducting within the GTS as indicated by water discharge mapping. An exception is the cross-shaped area (Fig. 5.6a), which is characterized by numerous fault intersections at the GTS scale, but not on a regional scale. The level of detail strongly influences the number of fault intersections. This application would strongly benefit from a probabilistic interpolation between the high level of detail at the surface and in the GTS, similar to approach employed elsewhere (e.g. Koike et al., 2015).

This application further showed that most domains with high water fluxes are recognized with the structural permeability favourability map. However, the prediction of single water-conducting faults remains difficult in that both a water-conducting feature may not be locally associated with an inflow at the tunnel intersection and that structural favourability may not guarantee the presence of a connected flow path.

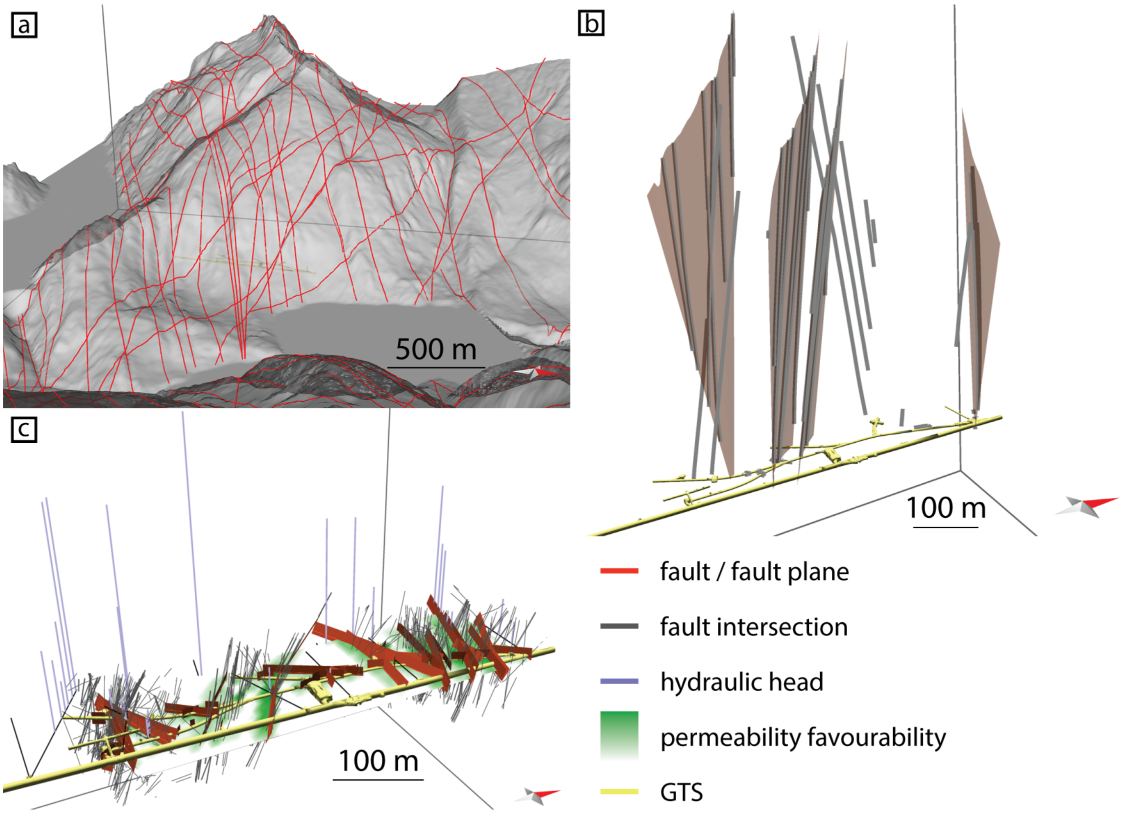

Figure 5.12. 3D models showing (a) fault traces and DEM at the regional (kilometre) scale, (b) fault intersections at the regional scale with selected fault planes for better representation, and (c) fault intersections and high slip-tendency faults at the GTS scale and the current hydraulic heads of key borehole test intervals.

5.6. Conclusions

Faults interplay intimately with the current stress state as variation in the stress state may induce opening or closure of a fault segment. Moreover, fault intersections result from interaction between faults where the resulting intersections potentially act as permeable tubes (Sibson, 1996). Because permeability within crystalline bedrock is mainly restricted to fractured domains, it follows that potential flow paths must be linked to the fault pattern. In the case of the GTS we can demonstrate that in the subsurface a combination of high slip-tendency faults and fault intersections can account for 90% of the water discharge points. The remaining 10%

of water inflow points are highly likely to be fault-related as well. In this light, potential local stress deflections (fault intersections, fault tips) may induce local variations in slip-tendency, a fact, which was not investigated by our approach. Moreover, faults terminating near the tunnel wall cannot be detected but may yield additional fault intersections. Furthermore, as shown by Bossart & Mazurek (1991), the detailed geometry of a water pathway on the small meter-scale is highly complex and thus prediction of water-conducting features highly depends on the considered scale. Our study demonstrates that on the hundred metres to kilometre scale, permeability favourability maps seem to represent a feasible prediction tool for crystalline basements and seem to be more accurate than using the general fracture pattern.

Conclusions

Deformation structures and associated brittle deformation processes occurring within the rock mass around GTS exert a first order control on the dimensions and geometry of groundwater flow paths. This influence can be seen most clearly in transmissivity values for borehole test intervals sampling faults. Transmissivity is recorded to be nine orders of magnitude higher in faults than within the undisturbed rock matrix at the GTS (Hoehn et al., 1998).

The water pathways formed by major fault structures can be correlated between the surface and the GTS, allowing for meteoric water recharge. This meteoric water interacts during downward circulation with the host rock mainly by dissolution of plagioclase and fluorite, and the precipitation of quartz and kaolinite. The amount of dissolved ions present in any sampled water is seen to relate directly with the length of the flow paths, i.e. with the residence time of meteoric water. Analysed chemical compositions and $\delta^{18}O$ and $\delta^{2}H$ values were stable over the two years sampling campaign and comparable with sampling in the early 1990s, which suggests homogenisation of groundwater after infiltration. However, persistent differences between individual sampling localities in the GTS indicate low lateral, out-of fault plane exchange of groundwater.

For the geometric characterization of flow paths of GTS, faults steeply dip mainly towards SE and SW. The orientation of first order faults at the surface is well estimated by lineament mapping. Structural 3D modelling, projecting data from the surface to depth, allowed for the visualisation of major faults crosscutting the entire rock mass above the GTS. Fieldwork has proven to be of paramount importance for both an accurate 3D structural modelling as well as for validating probabilistic approaches such as Bayesian Inference.

In light of a site characterization for a repository for radioactive waste, gained information is of major importance since faults, their geometric interplay, and orientation with respect to today's stress field define two main parameters for fault-related groundwater flow in rugged crystalline environments: occurrence of (i) fault intersections and (ii) high slip-tendency faults.

Aforementioned outcomes allowed for the development of a conceptual flow path model around the GTS. For future work, the resulting model could now be extended in several aspects in order to obtain a self-consistent hydrogeological flow model. The resulting model could comprise (i) the 3D structural model, representing the water-conducting faults, as base for the heterogeneous permeability of the rock mass, and (ii) different residence times of water based on overburden and flow rate. Such a hydraulic model could then be tested against measured groundwater chemical compositions and measured hydraulic parameters such as hydraulic heads, transmissivity or flow rates. In order to obtain such a self-consistent model diverse additional information is needed, which currently is not available. The information required would consist of:

(i) A probabilistic addition to the presented 3D structural model, bridging the detailed data at the surface and in the underground. This probabilistic approach would allow for extrapolating secondary faults based on observed fault patterns, particularly in the case of faults, which occur in between surface and GTS, i.e. which are too short to show intersections with accessible rock volumes. Moreover, the known exfoliation joints at the surface could be incorporated and complement the 3D structural model, as they may substantially affect water infiltration in the upper 100 to 200 m of the bedrock.

(ii) Further analyses of tritium in the groundwater around GTS could constraint its residence time and potential spatial variations. Information about residence would increase the accuracy of the flow model by adding constraints to the flow velocity.

(iii) A thorough hydraulic study would be needed to complement the structural geological consideration of water flow paths in order to characterize the permeability of major faults and to measure flow rates along water-conducting faults. This data would serve as boundary conditions for the flow model and as validation data for the obtained results.

Such a kilometre-scale flow model would add to the extensive site characterisation of the GTS, which in turn could serve as an additional example to already existing crystalline basement site characterisations for radioactive waste disposal sites (e.g. Svensk Kärnbränslehantering AB, 2009). These steps, outlined above, would greatly help for future planning of safe repositories for radioactive waste in basement rocks.

Last but not least, the newly gained knowledge about water-conducting faults could also be applied in the framework of geothermal exploration in hot dry rocks, as water-conducting faults are targeted for energy production. In such cases, similar mechano-structo-hydraulic knowledge is required and large-scale flow models for low-porosity crystalline rocks could serve as prediction tools for exploring geothermal energy in crystalline basement rocks.

References

Abrecht, J., 1994. Geologic units of the Aar massif and their pre-Alpine rock associations: a critical review. Schweizerische Mineral. und Petrogr. Mitteilungen 74, 5–27. doi:10.5169/seals-56328

Abrecht, J., 1975. Die Granit-Kontaktzone und die migmatischen Gesteine im Gebiet des Gruben- und des Aerlen-Gletschers. PhD thesis, University of Bern, Switzerland.

Ambrosio, J.J.Z., 2011. Magmatic structures in the Grimsel Test Site. Nagra Arbeitsbericht NAB 09-27, Wettingen, Switzerland.

Annunziatellis, A., Beaubien, S.E., Bigi, S., Ciotoli, G., Coltella, M., Lombardi, S., 2008. Gas migration along fault systems and through the vadose zone in the Latera caldera (central Italy): Implications for CO2 geological storage. Int. J. Greenh. Gas Control 2, 353–372. doi:10.1016/j.ijggc.2008.02.003

Balaban, I.J., 1995. An optimal algorithm for finding segments intersections, in: Proceedings of the Eleventh Annual Symposium on Computational Geometry - SCG ’95. ACM Press, New York, New York, USA, pp. 211–219. doi:10.1145/220279.220302

Ball, J.W., Nordstrom, D.K., 1992. User’s manual for WATEQ4F, with revised thermodynamic data base and test cases for calculating speciation of major, trace, and redox elements in natural waters., Open-File Report 91-183. Menlo Park: U.S. Geological Survey, California, United States of America.

Bambauer, H.U., Herwegh, M., Kroll, H., 2009. Quartz as indicator mineral in the Central Swiss Alps: the quartz recrystallization isograd in the rock series of the northern Aar massif. Swiss J. Geosci. 102, 345–351.

Banks, D., Frengstad, B., 2006. Evolution of groundwater chemical composition by plagioclase hydrolysis in Norwegian anorthosites. Geochim. Cosmochim. Acta 70, 1337–1355. doi:10.1016/j.gca.2005.11.025

Barton, C.A., Zoback, M.D., Moos, D., 1995. Fluid flow along potentially active faults in crystalline rock. Geology 23, 683–686. doi:10.1130/0091-7613(1995)023<0683

Baumberger, R., 2015. Quantification of lineaments: Link between internal 3D structure and surface evolution of the Hasli valley (Aar massif, Central Alps, Switzerland). PhD thesis, University of Bern, Switzerland.

Belgrano, T.M., Herwegh, M., Berger, A., 2016. Inherited structural controls on fault geometry, architecture and hydrothermal activity : an example from Grimsel Pass, Switzerland. Swiss J. Geosci. 109, 345–364. doi:10.1007/s00015-016-0212-9

Bense, F.A., Wemmer, K., Löbens, S., Siegesmund, S., 2014. Fault gouge analyses: K-Ar illite dating, clay mineralogy and tectonic significance-a study from the Sierras Pampeanas, Argentina. Int. J. Earth Sci. 103, 189–218. doi:10.1007/s00531-013-0956-7

Bense, V.F., Gleeson, T., Loveless, S.E., Bour, O., Scibek, J., 2013. Fault zone hydrogeology. Earth-Science Rev. 127, 171–192. doi:10.1016/j.earscirev.2013.09.008

Bentley, J.L., Ottmann, T.A., 1979. Algorithms for Reporting and Counting Geometric Intersections. IEEE Trans. Comput. C-28, 643–647. doi:10.1109/TC.1979.1675432

Berger, A., Mercolli, I., Herwegh, M., Gnos, E., 2017a. Explanatory notes accompanying the geological map of the Aar massif and the Tavetsch- and Gotthard Nappes. Geological Special Map 129, Swisstopo, Wabern, Switzerland.

Berger, A., Mercolli, I., Herwegh, M., Gnos, E., 2017b. Geological Map of the Aar massif, Tavetsch and Gotthard Nappes 1: 100 000. Geological Special Map 129, Swisstopo, Wabern, Switzerland.

Berkowitz, B., 2002. Characterizing flow and transport in fractured geological media: A review. Adv. Water Resour. 25, 861–884.

Best, M.G., 2013. Igneous and metamorphic petrology. John Wiley & Sons.

Bisdom, K., Bertotti, G., Nick, H.M., 2016. The impact of in-situ stress and outcrop-based fracture geometry on hydraulic aperture and upscaled permeability in fractured reservoirs. Tectonophysics 690, 63–75. doi:10.1016/j.tecto.2016.04.006

Bistacchi, A., Massironi, M., Dal Piaz, G. V, Dal Piaz, G., Monopoli, B., Schiavo, A., Toffolon, G., 2008. 3D fold and fault reconstruction with an uncertainty model: An example from an Alpine tunnel case study. Comput. Geosci. 34, 351–372. doi:10.1016/j.cageo.2007.04.002

Blechschmidt, I., Vomvoris, S., 2010. Underground research facilities and rock laboratories for the development of geological disposal concepts and repository systems, Woodhead P. ed.

Blechschmidt, I., Vomvoris, S., Rueedi, J., Martin, A.J., 2007. Grimsel Test Site - Phase VI: Review of accomplishments and next generation of in-situ experiments under repository relevant boundary conditions., in: Scientific Basis for Nuclear Waste Management XXXI. Sheffield, UK, pp. 547–555.

Blessent, D., Therrien, R., Gable, C.W., 2011. Large-scale numerical simulation of groundwater flow and solute transport in discretely-fractured crystalline bedrock. Adv. Water Resour. 34, 1539–1552. doi:10.1016/j.advwatres.2011.09.008

Blumenfeld, P., Bouchez, J.-L., 1988. Shear criteria in granite and migmatite deformed in the magmatic and solid states. J. Struct. Geol. 10, 361–372.

Bond, C.E., 2015. Uncertainty in structural interpretation: Lessons to be learnt. J. Struct. Geol. 74, 185–200. doi:10.1016/j.jsg.2015.03.003

Bond, C.E., Gibbs, A.D., Shipton, Z.K., Jones, S., 2007. What do you think this is? "Conceptual uncertainty" In geoscience interpretation. GSA Today 17, 4–10. doi:10.1130/GSAT01711A.1

Bond, C.E., Shipton, Z.K., Jones, R.R., Butler, R.W.H., Gibbs, A.D., 2007. Knowledge Transfer in a digital world: Field data acquisition, uncertainty and data management. Geosphere 3, 568–576. doi:10.1130/GES00094.1

Bossart, P., Mazurek, M., 1991. Structural geology and water flow-paths in the migration shear-zone. Nagra technical report NTB 91-12, Wettingen, Switzerland.

Bott, M.H.P., 1959. The Mechanics of Oblique Slip Faulting. Geol. Mag. 96, 109–117.

Bradbury, M.H., 1989. Grimsel Test Site: Laboratory investigations in support of the migration experiments. Nagra technical report, NTB 88-23, Baden, Switzerland.

Bredehoeft, J.D., 1997. Fault permeability near Yucca Mountain. Water Resour. Res. 33, 2459–2463. doi:10.1029/97WR01710

Brown, S.R., 1987. Fluid flow through rock joints: The effect of surface roughness. J. Geophys. Res. 92, 1337–1347. doi:10.1029/JB092iB02p01337

Bucher, K., Stober, I., 2010. Fluids in the upper continental crust. Geofluids 10, 241–253. doi:10.1002/9781444394900.ch17

Bucher, K., Stober, I., Seelig, U., 2012. Water deep inside the mountains: Unique water samples from the Gotthard rail base tunnel, Switzerland. Chem. Geol. 334, 240–253. doi:10.1016/j.chemgeo.2012.10.031

Bundesamt für Umwelt (BAFU), S.E., 2014. Nationale Grundwasserbeobachtung NAQUA, Modul ISOT.

Burnside, N.M., Shipton, Z.K., Dockrill, B., Ellam, R.M., 2013. Man-made versus natural CO2 leakage : A 400 k . y . history of an analogue for engineered geological storage of CO2. Geology 41, 471–474. doi:10.1130/G33738.1

Bussien, D., Bussy, F., Magna, T., Masson, H., 2011. Timing of Palaeozoic magmatism in the Maggia and Sambuco nappes and paleogeographic implications (Central Lepontine Alps). Swiss J. Geosci. 104, 1–29. doi:10.1007/s00015-010-0049-6

Byerlee, J., 1978. Friction of Rocks. pure Appl. Geophys. 615–626.

Caine, J.S., Evans, J.P., Forster, C.B., 1996. Fault zone architecture and permeability structure. Geology 24, 1025–1028.

Caumon, G., Collon-Drouaillet, P., Le Carlier de Veslud, C., Viseur, S., Sausse, J., 2009. Surface-Based 3D Modeling of Geological Structures. Math. Geosci. 41, 927–945. doi:10.1007/s11004-009-9244-2

Challandes, N., Marquer, D., Villa, I.M., 2008. P-T-t modelling, fluid circulation, and 39Ar-40Ar and Rb-Sr mica ages in the Aar Massif shear zones (Swiss Alps). Swiss J. Geosci. 101, 269–288. doi:10.1007/s00015-008-1260-6

Choukroune, P., Gapais, D., 1983. Strain pattern in the Aar Granite (Central Alps): orthogneiss developed by bulk inhomogeneous flattening. J. Struct. Geol. 5, 411–418.

Clark, I., Fritz, P., 1997. Environmental isotopes in Hydrogeology. CRC press.

Cowan, J., Beatson, R., Ross, H., Fright, W.R., McLennan, T., Evans, T.R., Carr, J., Lane, R., Bright, D., Gillman, A., Oshust, P., Titley, M., 2003. Practical implicit geological modelling. 5th Int. Min. Geol. Conf. 89–99.

Curewitz, D., Karson, J.A., 1997. Structural settings of hydrothermal outflow: Fracture permeability maintained by fault propagation and interaction. J. Volcanol. Geotherm. Res. 79, 149–168. doi:10.1016/S0377-0273(97)00027-9

Debon, F., Lemmet, M., 1999. Evolution of Mg/Fe Ratios in Late Variscan Plutonic Rocks from the

External Crystalline Massifs of the Alps (France, Italy, Switzerland). J. Petrol. 40, 1151–1185.

Delaunay, B., 1934. Sur la sphère vide. A la mémoire de Georges Voronoi. Bull. l'Académie des Sci. l'URSS. Cl. des Sci. mathématiques Nat. 6, 793–800.

Dempster, T.J., 1986. Isotope systematics in minerals: biotite rejuvenation and exchange during Alpine metamorphism. Earth Planet. Sci. Lett. 78, 355–367.

Diamond, L.W., Tarantola, A., 2015. Interpretation of fluid inclusions in quartz deformed by weak ductile shearing: Reconstruction of differential stress magnitudes and pre-deformation fluid properties. Earth Planet. Sci. Lett. 417, 107–119. doi:10.1016/j.epsl.2015.02.019

Dockrill, B., Shipton, Z.K., 2010. Structural controls on leakage from a natural CO2 geologic storage site : Central Utah, U.S.A. J. Struct. Geol. 32, 1768–1782. doi:10.1016/j.jsg.2010.01.007

Edmunds, W.M., Kay, R.L.F., McCartney, R.A., 1985. Origin of saline groundwaters in the carnmenellis granite (Cornwall, England): Natural processes and reaction during hot dry rock reservoir circulation. Chem. Geol. 49, 287–301.

Eichhubl, P., Davatzes, N.C., Becker, S.P., 2009. Structural and diagenetic control of fluid migration and cementation along the Moab fault , Utah. Am. Assoc. Pet. Geol. Bull. 93, 653–681. doi:10.1306/02180908080

Eichinger, F., 2009. Matrix pore water - fracture groundwater interaction in crystalline bedrock based on natural tracers: An archive of long-term hydrogeological evolution. PhD thesis, University of Bern, Switzerland.

Esperanza, S., Holloway, J.R., 1987. On the origin of some mica-lamprophyres: experimental evidence from a mafic minette. Contrib. to Mineral. Petrol. 95, 207–216.

Evans, J.P., Forster, C.B., Goddard, J. V, 1997. Permeability of fault-related rocks, and implications for hydraulic structure of fault zones. J. Struct. Geol. 19, 1393–1404.

Evans, K.F., Engelder, T., 1989. Some problems in estimating horizontal stress magnitude in thurst regimes. Int. J. Rock Mech. Min. Sci. Geomech. Abstr. 26, 647–660.

Faulkner, D.R., Jackson, C.A.L., Lunn, R.J., Schlische, R.W., Shipton, Z.K., Wibberley, C.A.J., Withjack, M.O., 2010. A review of recent developments concerning the structure, mechanics and fluid flow properties of fault zones. J. Struct. Geol. 32, 1557–1575. doi:10.1016/j.jsg.2010.06.009

Faulkner, D.R., Mitchell, T.M., Healy, D., Heap, M.J., 2006. Slip on "weak" faults by the rotation of regional stress in the fracture damage zone. Nature 444, 922–925. doi:10.1038/nature05353

Fernández, O., 2005. Obtaining a best fitting plane through 3D georeferenced data. J. Struct. Geol. 27, 855–858. doi:10.1016/j.jsg.2004.12.004

Figueiredo, B., Tsang, C.-F., Niemi, A., Lindgren, G., 2016. Review: The state-of-art of sparse channel models and their applicability to performance assessment of radioactive waste repositories in fractured crystalline formations. Hydrogeol. J. 24, 1607–1622. doi:10.1007/s10040-016-1415-x

Finsterle, S., Pruess, K., 1995. Solving the Estimation-Identification Problem in 2-Phase Flow Modeling. Water Resour. Res. 31, 913–924.

Flach, U., Noell, U., 1989. Neigungsmessungen zur Ermittlung neotektonischer Vorgänge. Nagra technical report, NTB 89-11, Wettingen, Switzerland.

Flint, A.L., Flint, L.E., Kwicklis, E.M., Bodvarsson, G.S., Fabryka-Martin, J.M., 2001. Hydrology of Yucca Mountain, Nevada. Rev. Geophys. 39, 447–470. doi:10.1029/1999RG000075

Florineth, D., Schlüchter, C., 1998. Reconstructing the Last Glacial Maximum (LGM) ice surface geometry and flowlines in the Central Swiss Alps. Eclogae Geol. Helv. 91, 391–407.

Forster, C.B., Evans, J.P., 1991. Hydrogeology of thrust faults and crystalline thrust sheets: results of combined field and modeling studies. Geophys. Res. Lett. 18, 979–982.

Frey, M., 1980. Alpine metamorphism along the Geotraverse Basel-Chiasso- a review. Eclogae Geol. Helv. 73, 527–546.

Frick, U., Alexander, W.R., Baeyens, B., Bossart, P., Bradbury, M.H., Bühler, C., Eikenberg, J., Fierz, T., Heer, W., Hoehn, E., Mckinley, I.G., Smith, P.A., 1992. The radionuclide migration experiment - overview of investigations 1985-1990. Nagra technical report NTB 91-04, Wettingen, Switzerland.

Frieg, B., Blaser, P.C. (eds), 2012. Grimsel Test Site: Excavation Disturbed Zone Experiment (EDZ). Nagra technical report 98-01,Wettingen, Switzerland.

Gabrielsen, R.H., Braathen, A., 2014. Models of fracture lineaments - Joint swarms, fracture corridors and faults in crystalline rocks, and their genetic relations. Tectonophysics 628, 26–44. doi:10.1016/j.tecto.2014.04.022

Garrels, R.M., Mackenzie, F.T., 1967. Origin of the Chemical Compositions of Some Springs and Lakes. Adv. Chem. Ser. 67, 222–241.

Gascoyne, M., 2004. Hydrogeochemistry, groundwater ages and sources of salts in a granitic batholith on the Canadian Shield, southeastern Manitoba. Appl. Geochemistry 19, 519–560. doi:10.1016/s0883-2927(03)00155-0

Geotest AG, 1981. Sondierbohrungen Juchlistock - Grimsel. Nagra Technischer Bericht NTB 81-07, Baden, Switzerland.

Geyh, M., Amore, F.D., Darling, G., Paces, T., Pang, Z., Silar, J., 2001. Groundwater saturated and unsaturated zone, in: Environmental Isotopes in the Hydrological Cycle. International Atomic Energy Agency.

Gimeno, M.J., Auqué, L.F., Acero, P., Gómez, J.B., 2014. Hydrogeochemical characterisation and modelling of groundwaters in a potential geological repository for spent nuclear fuel in crystalline rocks (Laxemar, Sweden). Appl. Geochemistry 45, 50–71. doi:10.1016/j.apgeochem.2014.03.003

Gimmi, T., Schneebeli, M., Flühler, H., Wydler, H., Baer, T., 1997. Field-scale water transport in unsaturated crystalline rock. Water Resour. Res. 33, 589–598.

Glotzbach, C., Reinecker, J., Danišík, M., Rahn, M., Frisch, W., Spiegel, C., 2010. Thermal history of the central Gotthard and Aar massifs, European Alps: Evidence for steady state, long-term exhumation. J. Geophys. Res. 115, 1–24. doi:10.1029/2009jf001304

Goncalves, P., Oliot, E., Marquer, D., Connolly, J.A.D., 2012. Role of chemical processes on shear zone formation: an example from the Grimsel metagranodiorite (Aar massif, Central Alps). J. Metamorph. Geol. 30, 703–722. doi:10.1111/j.1525-1314.2012.00991.x

González-Garcia, J., Jessell, M., 2016. A 3D geological model for the Ruiz-Tolima Volcanic Massif (Colombia): Assessment of geological uncertainty using a stochastic approach based on Bézier curve design. Tectonophysics 687, 139–157. doi:10.1016/j.tecto.2016.09.011

Guermani, A., Pennacchioni, G., 1998. Brittle precursors of plastic deformation in a granite: an example from the Mont Blanc massif (Helvetic, western Alps). J. Struct. Geol. 20, 135–148. doi:10.1016/S0191-8141(97)00080-1

Haario, H., Saksman, E., Tamminen, J., 2001. An adaptive metropolis algorithm. Bernoulli 7, 223–242. doi:10.3318737

Hardebeck, J.L., Hauksson, E., 1999. Role of Fluids in Faulting Inferred from Stress Field Signatures. Science (80-.). 285, 236–239. doi:10.1126/science.285.5425.236

Hassen, I., Gibson, H., Hamzaoui-Azaza, F., Negro, F., Rachid, K., Bouhlila, R., 2016. 3D geological modeling of the Kasserine Aquifer System, Central Tunisia: New insights into aquifer-geometry and interconnections for a better assessment of groundwater resources. J. Hydrol. 539, 223–236. doi:10.1016/j.jhydrol.2016.05.034

Hegner, E., Kölbl-Ebert, M., Loeschke, J., 1998. Post-collisional Vasriscan lamprophyres (Black Forest, Germany): 40Ar/39Ar phlogopite dating, Nd, Pb, Sr isotope, and trace element characteristics. Lithos 45, 395–411.

Heilbronner, R., Barrett, S., 2014. Image Analysis in Earth Sciences. Springer, Berlin Heidelberg. doi:10.1007/978-3-642-10343-8

Hennings, P., Allwardt, P., Paul, P., Zahm, C., Reid, R., Alley, H., Kirschner, R., Lee, B., Hough, E., 2012. Relationship between fractures, fault zones, stress, and reservoir productivity in the Suban gas field, Sumatra, Indonesia. Am. Assoc. Pet. Geol. Bull. 96, 753–772. doi:10.1306/08161109084

Herwegh, M., Berger, A., Baumberger, R., Wehrens, P., Kissling, E., 2017. Large-Scale Crustal-Block-Extrusion During Late Alpine Collision. Sci. Rep. 7. doi:10.1038/s41598-017-00440-0

Hoehn, E., Eikenberg, J., Fierz, T., Drost, W., Reichlmayr, E., 1998. The Grimsel Migration Experiment: field injection - withdrawal experiments in fractured rock with sorbing tracers. J. Contam. Hydrol. 34, 85–106.

Hoehn, E., Fierz, T., Thorne, P., 1990. Hydrogeological characterisation of the migration experiment area at the Grimsel Test Site. Nagra technical report NTB 89-14, Wettingen, Switzerland.

Iwatsuki, T., Yoshida, H., 1999. Groundwater chemistry and fracture mineralogy in the basement granitic rock in the Tono uranium mine area, Gifu Prefecture, Japan -Groundwater composition, Eh evolution analysis by fracture filling minerals-. Geochem. J. 33, 19–32.

Jaeger, J.C., 1969. Elasticity fracture and flow, third edit. ed. Methuen & CO. Ltd, London.

Jaeger, J.C., Cook, N.G., 1971. Fundamentals of rock mechanics. Chapman & Hall Ltd, London.

Jessell, M.W., Aillères, L., de Kemp, E.A., 2010. Towards an integrated inversion of geoscientific data: What price of geology? Tectonophysics 490, 294–306. doi:10.1016/j.tecto.2010.05.020

Jones, R.R., McCaffrey, K.J.W., Clegg, P., Wilson, R.W., Holliman, N.S., Holdsworth, R.E., Imber, J., Waggott, S., 2009. Integration of regional to outcrop digital data: 3D visualisation of multi-scale geological models. Comput. Geosci. 35, 4–18. doi:10.1016/j.cageo.2007.09.007

Jørgensen, F., Høyer, A., Sandersen, P.B.E., He, X., 2015. Combining 3D geological modelling techniques to address variations in geology , data type and density – An example from Southern Denmark. Comput. Geosci. 81, 53–63. doi:10.1016/j.cageo.2015.04.010

Kaufmann, O., Martin, T., 2009. 3D geological modelling from boreholes, cross-sections and geological maps, application over former natural gas storages in coal mines. Comput. Geosci. 35, 70–82. doi:10.1016/S0098-3004(08)00227-6

Keppler, A., 1994. Hydrogeologische, hydrochemische und isotopenhydrologische Untersuchungen an den Oberflächen- und Kluftwässern im Grimselgebiet, Schweiz. PhD thesis, Ludwig-Maximilians-Universität, München, Germany.

Keusen, H.R., Ganguin, J., Schuler, P., Buletti, M., 1989. Felslabor Grimsel: Geologie. Nagra technical report NTB 87-14, Baden, Switzerland.

Kickmeier, W., Vomvoris, S., Mckinley, I.G., Alexander, W.R., 2005. Grimsel Test Site: challenges for the 21st century and beyond. Eur. Geol. 19, 19–22.

Kober, F., Härtel, M., 2014. Water flux measurement in the drainage system of the Grimsel Test Site (GTS) 2007 - 2012. Nagra Aktennotiz AN 14-467, Wettingen, Switzerland.

Koike, K., Kubo, T., Liu, C., Masoud, A., Amano, K., Kurihara, A., Matsuoka, T., Lanyon, B., 2015. 3D geostatistical modeling of fracture system in a granitic massif to characterize hydraulic properties and fracture distribution. Tectonophysics 660, 1–16. doi:10.1016/j.tecto.2015.06.008

Kralik, M., Clauer, N., Holnsteiner, R., Huemer, H., Kappel, F., 1992. Recurrent fault activity in the Grimsel Test Site (GTS, Switzerland): revealed by Rb-Sr, K-Ar and tritium isotope techniques. J. Geol. Soc. London. 149, 293–301.

Krietsch, H., Gischig, V., Jalali, M.R., Amann, F., Evans, K.F., Doetsch, J., Valley, B., 2017. Stress measurements in crystalline rock : Comparison of overcoring, hydraulic fracturing and induced seismicity results, in: American Rock Mechanics Association.

Kull, H., Brewitz, W., Klarr, K., 1993. Ventilationtest - In-situ-Experiment for Determination of Permeability in Crystalline Rock. Nagra technical report NTB 91-02E, Wettingen, Switzerland.

Labhart, T., 1977. Aarmassiv und Gotthardmassiv. Gebruder Borntraeger Verlagsbuchhandlung.

Lindsay, M.D., Aillères, L., Jessell, M.W., de Kemp, E.A., Betts, P.G., 2012. Locating and quantifying geological uncertainty in three-dimensional models: Analysis of the Gippsland Basin, southeastern Australia. Tectonophysics 546–547, 10–27. doi:10.1016/j.tecto.2012.04.007

Lunn, R.J., Shipton, Z.K., Bright, A.M., 2008. How can we improve estimates of bulk fault zone hydraulic properties ? Geol. Soc. London 299, 1–7.

Lützenkirchen, V.H., 2002. Structural Geology and Hydrogeology of Brittle Fault Zones in the Central and Eastern Gotthard Massif, Switzerland. PhD thesis, Swiss Federal Institute of Technology Zürich, Switzerland.

MacKay, D.J.C., 2003. Information Theory, Inference, and Learning Algorithms, 4th editio. ed. Cambridge University Press, Cambridge, UK.

Mäder, U.K., Ekberg, C., 2006. Geochemical evolution of porewater in the granitic shear zone AU-126 during 3 years of interaction with hyperalkaline fluid, and its interpretation. Nagra Arbeitsbericht NAB 06-08, Wettingen, Switzerland.

Mancktelow, N.S., Pennacchioni, G., 2005. The control of precursor brittle fracture and fluid–rock interaction on the development of single and paired ductile shear zones. J. Struct. Geol. 27, 645–661. doi:10.1016/j.jsg.2004.12.001

Mandl, G., 2000. Faulting in Brittle Rocks. Springer-Verlag Berlin Heidelberg.

Manning, C.E., Ingebritsen, S.E., 1999. Permeability Implications of the Continental of Geothermal Data Crust and Metamorphic Systems. Rev. Geophys. 37, 127–150.

Maréchal, J.C., Etcheverry, D., 2003. The use of 3H and 18O tracers to characterize water inflows in Alpine tunnels. Appl. Geochemistry 18, 339–351.

Marquer, D., 1990. Structures et déformation alpine dans les granites hercyniens du massif du Gotthard (Alpes centrales suisses). Eclogae Geol. Helv. 83, 77–97.

Marquer, D., Gapais, D., Capdevila, R., 1985. Chemical-changes and mylonitization of a granodiorite within low-grade metamorphism (Aar massif, central Alps). Bull. Mineral. 108, 209–221.

Martel, S.J., Peterson, J.E., 1991. Interdisciplinary characterization of fracture systems at the US/BK site, Grimsel Laboratory, Switzerland. Int. J. Rock Mech. Min. Sci. Geomech. Abstr. 28, 295–323. doi:10.1016/0148-9062(91)90596-E

Martin, C.D., Chandler, N.A., 1993. Stress heterogeneity and geological structures. Int. J. Rock Mech.

Min. Sci. Geomech. Abstr. 30, 993–999. doi:10.1016/0148-9062(93)90059-M

Martin, C.D., Christiansson, R., 1991. Overcoring in highly stressed granite - Comparison of the USBM and Modified CSIR devices. Rock Mech. Rock Eng. 24, 207–235.

Martin, D., 2007. Quantifying in situ stress magnitudes and orientations for Forsmark. Svensk kärnbränslehantering (SKB R-07-26).

Martin, D., Follin, S., 2011. Review of possible correlations between in situ stress and PFL fracture transmissivity data at Forsmark. Svensk kärnbränslehantering (SKB R-08-69).

Martinez-Landa, L., Carrera, J., 2005. An analysis of hydraulic conductivity scale effects in granite (Full-scale Engineered Barrier Experiment (FEBEX), Grimsel, Switzerland). Water Resour. Res. 41, n/a-n/a. doi:10.1029/2004wr003458

Mazurek, M., 2000. Geological and hydraulic properties of water-conducting features in crystalline rocks, in: Stober, I., Bucher, K. (Eds.), Hydrogeology of Crystalline Rocks. Springer Netherlands, pp. 3–26.

Mazurek, M., Jakob, A., Bossart, P., 2003. Solute transport in crystalline rocks at Aspo - I: Geological basis and model calibration. J. Contam. Hydrol. 61, 157–174.

McCombie, C., Mckinley, I.G., Vomvoris, S., 1995. Contributions of the Grimsel Test Site (GTS) to Swiss site characterisation programmes., in: Proceedings of the Sixth Annual International Conference. High Level Radioactive Waste Management. Las Vegas, Nevada, pp. 172–174.

Meier, P.M., Medina, A., Carrera, J., 2001. Geostatistical inversion of cross-hole pumping tests for identifying preferential flow channels within a shear zone. Ground Water 39, 10–17.

Mercolli, I., Oberhänsli, R., 1988. Variscan tectonic evolution in the Central Alps: a working hypothesis. Schweizerische Mineral. und Petrogr. Mitteilungen 68, 491–500. doi:10.5169/seals-52084

Michalski, I., Soom, M., 1990. The Alpine thermo-tectonic evolution of the Aar and Gotthard massifs, Central Switzerland: fission track ages on zircon and apatite and K-Ar mica ages. Schweizerische Mineral. und Petrogr. Mitteilungen 70, 373–387. doi:10.5169/seals-53628

Möri, A., Blechschmidt, I., 2006. CFM Experiment Structural geological model. Nagra Arbeitsbericht NAB 06-18, Wettingen, Switzerland.

Möri, A., Inderbitzin, L., Heugel, T., Mäder, U.K., 2005. GTS HPF: Over-coring, sampling, sample preparation, UV/VIS-photography, Beta/gamma- autoradiography and structural-geological model of the shear zone AU-126 and the dipole flow field. Nagra Arbeitsbericht NAB 05-018, Wettingen, Switzerland.

Morris, A., Ferrill, D.A., Henderson, D.B., 1996. Slip-tendency analysis and fault reactivation. Geology 24, 275–278. doi:10.1130/0091-7613(1996)024<0275

Niggli, E., Niggli, C., 1965. Karten der Verbreitung einiger Mineralien der alpidischen Metamorphose in den Schweizer Alpen (Stilpnomelan, Disthen, Sillimanit). Eclogae Geol. Helv. 58, 335–368.

Noell, U.H., 1994. Über den Einfluss elastischer Heterogenitäten auf Gezeitenneigungen am Beispiel des Messungen im Felslabor Grimsel. PhD thesis, Universtität Stuttgart, Germany.

Nordstrom, D.K., Ball, J.W., Donahoe, R.J., Whittemore, D., 1989. Groundwater chemistry and water-rock interactions at Stripa. Geochim. Cosmochim. Acta 53, 1727–1740.

O'Leary, D.W., Friedman, J.D., Pohn, H.A., 1976. Lineament , linear , lineation : Some proposed new standards for old terms. Geol. Soc. Am. Bull. 87, 1463–1469. doi:10.1130/0016-7606(1976)87<1463

Oberhänsli, R., 1987. Mineralogy and Alpine Metamorphism of meta-lamprophyres from the Central Swiss Alps. Schweizerische Mineral. und Petrogr. Mitteilungen 67, 321–338.

Oberhänsli, R., 1986. Geochemistry of meta-lamprophyres from the Central Swiss Alps. Schweizerische Mineral. und Petrogr. Mitteilungen 66, 315–342.

Oberhänsli, R., Schenker, F., Mercolli, I., 1988. Indications of Variscan nappe tectonics in the Aar massif. Schweizerische Mineral. und Petrogr. Mitteilungen 68, 509–520.

Ofterdinger, U.S., Balderer, W., Loew, S., Renard, P., 2004. Environmental Isotopes as Indicators for Ground Water Recharge to Fractured Granite. Ground Water 42, 868–879.

Pahl, A., Bräuer, V., Heusermann, S., Kilger, B., Liedtke, L., 1986. Results of engineering geological research in granite. Bull. Int. Assoc. Eng. Geol. 34, 59–65.

Palandri, J.L., Kharaka, Y.K., 2004. A compilation of rate parameters of water-mineral interaction kinetics for application to geochemical modeling. U.S. Geol. Surv. Open file Rep. 2004–1068, 71. doi:10.1098/rspb.2004.2754

Parkhurst, D.L., Appelo, C.A.J., 2013. Description of input and examples for PHREEQC version 3: A computer program for speciation, batch-reaction, one-dimensional transport, and inverse geochemical calculations.

Passchier, C.W., Trouw, R.A.J., 2005. Microtectonics, 2nd, Revis ed. Springer, Berlin Heidelberg New York.

Pastorelli, S., Marini, L., Hunziker, J., 2001. Chemistry, isotope values (dD, d18O, d34 SSO4) and temperatures of the water inflows in two Gotthard tunnels, Swiss Alps. Appl. Geochemistry 16, 633–649.

Paterson, S.R., Vernon, R.H., Tobisch, O.T., 1989. A review of criteria for the identification of magmatic and tectonic foliations in granitoids. J. Struct. Geol. 11, 349–363.

Patil, A., Huard, D., Fonnesbeck, C.J., 2010. PyMC: Bayesian stochastic modelling in Python. J. Stat. Softw. 35, 1.

Peters, M., 2011. Spatial distribution of quartz recrystallization microstructures across the Aar massif (Swiss Central Alps). Master thesis, University of Bern, Switzerland.

Peters, M., Berger, A., Herwegh, M., Regenauer-Lieb, K., 2016. Strain localization in ductile rocks : A comparison of natural and simulated pinch-and-swell structures. Tectonophysics 680, 140–154. doi:10.1016/j.tecto.2016.04.049

Peters, M., Veveakis, M., Poulet, T., Karrech, A., Herwegh, M., Regenauer-Lieb, K., 2015. Boudinage as a material instability of elasto-visco-plastic rocks. J. Struct. Geol. 78, 86–102. doi:10.1016/j.jsg.2015.06.005

Pfiffner, O.A., 2009. Geologie der Alpen. Haupt Verlag, Bern, Stuttgart, Wien.

Pfiffner, O.A., 1993. The Structure of the Alps: An Introduction, in: von Raumer, J.F., Neubauer, F. (Eds.), Pre-Mesozoic Geology of the Alps. Springer-Verlag Berlin Heidelberg.

Pfiffner, O.A., Deichmann, N., 2014. Seismotektonik der Zentralschweiz. Wettingen, Switzerland.

Pleuger, J., Mancktelow, N., Zwingmann, H., Manser, M., 2012. K-Ar dating of synkinematic clay gouges from Neoalpine faults of the Central, Western and Eastern Alps. Tectonophysics 550, 1–16. doi:10.1016/j.tecto.2012.05.001

Plummer, L.N., Prestemon, E.C., Parkhurst, D.L., 1994. An Interactive Code (NETPATH) for Modeling NET Geochemical Reactions Along a Flow PATH— Version 2.0.

Pradhan, B., Lee, S., Buchroithner, M.F., 2009. Use of geospatial data and fuzzy algebraic operators to landslide-hazard mapping. Appl. Geomatics 1, 3–15. doi:10.1007/s12518-009-0001-5

Reinecker, J., Danišík, M., Schmid, C., Glotzbach, C., Rahn, M., Frisch, W., Spiegel, C., 2008. Tectonic control on the late stage exhumation of the Aar Massif (Switzerland): Constraints from apatite fission track and (U-Th)/He data. Tectonics 27, 1–17. doi:10.1029/2007tc002247

Rolland, Y., Cox, S.F., Corsini, M., 2009. Constraining deformation stages in brittle–ductile shear zones from combined field mapping and 40Ar/39Ar dating: The structural evolution of the Grimsel Pass area (Aar Massif, Swiss Alps). J. Struct. Geol. 31, 1377–1394. doi:10.1016/j.jsg.2009.08.003

Saar, M.O., Manga, M., 2004. Depth dependence of permeability in the Oregon Cascades inferred from hydrogeologic, thermal, seismic, and magmatic modeling constraints. J. Geophys. Res. B Solid Earth 109, 1–19. doi:10.1029/2003JB002855

Sausse, J., Dezayes, C., Dorbath, L., Genter, A., Place, J., 2010. 3D model of fracture zones at Soultz-sous-Forêts based on geological data, image logs, induced microseismicity and vertical seismic profiles. Comptes Rendus - Geosci. 342, 531–545. doi:10.1016/j.crte.2010.01.011

Schaltegger, U., 1994. Unravelling the pre-Mesozoic history of Aar and Gotthard massifs (Central Alps) by isotopic dating: a review. Schweizerische Mineral. und Petrogr. Mitteilungen 74, 41–51. doi:10.5169/seals-56330

Schaltegger, U., 1990. The Central Aar Granite: Highly differentiated calc-alkaline magmatism in the Aar massif (Central Alps, Switzerland). Eur. J. Mineral. 2, 245–259.

Schaltegger, U., 1989. Geochemische und isotopengeochemische Untersuchungen am Zentralen Aaregranit und seinen assoziierten Gesteinen zwischen Aare und Reuss (Aarmassiv, Schweiz). PhD thesis, University of Bern, Switzerland.

Schaltegger, U., Corfu, F., 1992. The age and source of late Hercynian magmatism in the central Alps: evidence from precise U-Pb ages and initial Hf isotopes. Contrib. to Mineral. Petrol. 111, 329–344.

Scheiber, T., Fredin, O., Viola, G., Jarna, A., Gasser, D., Łapińska-Viola, R., 2015. Manual extraction of bedrock lineaments from high-resolution LiDAR data: methodological bias and human perception. Gff 5897, 1–11. doi:10.1080/11035897.2015.1085434

Schneeberger, R., Berger, A., Herwegh, M., Eugster, A., Kober, F., Spillmann, T., Blechschmidt, I., 2016. GTS Phase VI - LASMO: Geology and structures of the GTS and Grimsel region. Nagra Arbeitsbericht NAB 16-27, Wettingen, Switzerland.

Schneeberger, R., de la Varga, M., Egli, D., Berger, A., Kober, F., Wellmann, J.F., Herwegh, M., n.d. Methods and uncertainty-estimations of 3D structural modelling in crystalline rocks: A case study. Solid Earth Discuss. 2017. doi:https://doi.org/10.5194/se-2017-47

Schneeberger, R., Mäder, U.K., Waber, H.N., 2017. Hydrochemical and isotopic (d2H, d18O, 3H) characterization of fracture water in crystalline rock (Grimsel, Switzerland), in: 15th Water-Rock Interaction International Symposium. pp. 738–741. doi:dx.doi.org/10.1016/j.proeps.2016.12.187

Schotterer, U., 2000. Das Schweizer Isotopen-Messnetz. GWA Gas, Wasser, Abwasser 10.

Schotterer, U., Schuerch, M., Rickli, R., 2010. Water isotopes in Switzerland: Latest Findings of the National ISOT Network. GWA Gas, Wasser, Abwasser 12.

Schubert, R., 2013. Shear zone pattern and 3D geometry in the Gelmersee-Gruebensee transect (Grimsel, Switzerland). Master thesis, University of Bern, Switzerland.

Seaton, W.J., Burbey, T.J., 2005. Influence of ancient thrust faults on the hydrogeology of the blue ridge province. Ground Water 43, 301–313. doi:10.1111/j.1745-6584.2005.0026.x

Seelig, U., Bucher, K., 2010. Halogens in water from the crystalline basement of the Gotthard rail base tunnel (central Alps). Geochim. Cosmochim. Acta 74, 2581–2595. doi:10.1016/j.gca.2010.01.030

Sibson, R.H., 1996. Structural permeability of fluid-driven fault-fracture meshes. J. Struct. Geol. 18, 1031–1042. doi:10.1016/0191-8141(96)00032-6

Siler, D.L., Faulds, J.E., Mayhew, B., McNamara, D.D., 2016. Analysis of the favorability for geothermal fluid flow in 3D: Astor Pass geothermal prospect, Great Basin, northwestern Nevada, USA. Geothermics 60, 1–12. doi:10.1016/j.geothermics.2015.11.002

Snow, D.T., 1969. Anisotropic Permeability of Fractured Media. Water Resour. Res. 5, 1273–1289.

Stalder, H.A., 1964. Petrographische und mineralogische Untersuchungen im Grimselgebiet (Mittleres Aarmassiv). PhD thesis, University of Bern, Switzerland.

Steck, A., 1968. Die alpidischen Strukturen in den Zentralen Aaregranite des westlichen Aarmassivs. Eclogae Geol. Helv. 61, 19–48. doi:10.5169/seals-163584

Stephens, M.B., Follin, S., Petersson, J., Isaksson, H., Juhlin, C., Simeonov, A., 2015. Review of the deterministic modelling of deformation zones and fracture domains at the site proposed for a spent nuclear fuel repository, Sweden, and consequences of structural anisotropy. Tectonophysics 653, 68–94. doi:10.1016/j.tecto.2015.03.027

Svensk Kärnbränslehantering AB, 2009. Site description of Laxemar a completion of the site investigation phase, TR-09-01.

Tacher, L., Pomian-Srzednicki, I., Parriaux, A., 2006. Geological uncertainties associated with 3-D subsurface models. Comput. Geosci. 32, 212–221. doi:10.1016/j.cageo.2005.06.010

Tchalenko, J.S., 1970. Similarities between shear zones at different magnitudes. Geol. Soc. Am. Bull. 81, 1625–1640. doi:10.1130/0016-7606(1970)81

Townend, J., Zoback, M.D., 2000. How faulting keeps the crust strong. Geology 28, 399–402. doi:10.1130/0091-7613(2000)28<399:HFKTCS>2.0.CO

Twiss, R.J., Moores, E.M., 1992. Structural geology. Macmillan.

Vernon, A.J., Beek, P.A. Van Der, Sinclair, H.D., Rahn, M.K., 2008. Increase in late Neogene denudation of the European Alps confirmed by analysis of a fission-track thermochronology database 270, 316–329. doi:10.1016/j.epsl.2008.03.053

Viard, T., Caumon, G., Lévy, B., 2011. Adjacent versus coincident representations of geospatial uncertainty: Which promote better decisions? Comput. Geosci. 37, 511–520. doi:10.1016/j.cageo.2010.08.004

Voborny, O., Adank, P., Hürlimann, W., Vomvoris, S., Mishra, S., 1991. Grimsel Test Site: Modeling of groundwater flow in the rock body surrounding the underground laboratory. Nagra technical report, NTB 91-03, Wettingen, Switzerland.

Vomvoris, S., Blechschmidt, I., Gaus, I., Rueedi, J., Martin, A., Spillmann, T., 2013. The Grimsel Test Site - Going into the fourth decade of applied RD & D. Integrating storage, transportation, and disposal, in: Proceedings of the Fourteenth International High-Level Radioactive Waste Management Conference. Albuquerque, New Mexico, pp. 150–157.

Vomvoris, S., Blechschmidt, I., Vietor, T., Müller, H., 2015. Nagra's activities at the Grimsel Test Site and Mont Terri project: Update and Outlook, in: Proceedings of the Fifthteen International High-Level Radioactive Waste Management Conference. Charlestone, South Carolina, pp. 379–289.

Vomvoris, S., Frieg, B., Bossart, P., Gmünder, C., Heiniger, P., Jaquet, O., Watanabe, K., 1992. Grimsel Test Site: Overview of Nagra field and modeling activities in the Ventilation Drift (1988-1990). Nagra technical report NTB 91-34, Wettingen, Switzerland.

von Raumer, J.F., Bussy, F., Stampfli, G.M., 2009. The Variscan evolution in the External massifs of the Alps and place in their Variscan framework. Comptes Rendus Geosci. 341, 239–252. doi:10.1016/j.crte.2008.11.007

von Raumer, J.F., Ménot, R.P., Abrecht, J., Biino, G., 1993. The Pre-Alpine Evolution of the External Massifs, in: von Raumer, J.F., Neubauer, F. (Eds.), Pre-Mesozoic Geology of the Alps. Springer-Verlag Berlin Heidelberg.

Vouillomaz, J., 2009. Strain localization along shear zones in the Juchlistock area. Master thesis, University of Bern, Switzerland.

Waber, H.N., Gimmi, T., Smellie, J.A.T., 2012. Reconstruction of palaeoinfiltration during the Holocene using porewater data (Laxemar, Sweden). Geochim. Cosmochim. Acta 94, 109–127. doi:10.1016/j.gca.2012.06.030

Waber, H.N., Schneeberger, R., Mäder, U.K., Wanner, C., 2017. Constraints on evolution and residence time of geothermal water in granitic rocks at Grimsel (Switzerland), in: 15th Water-Rock Interaction International Symposium.

Waber, H.N., Smellie, J.A.T., 2008. Characterisation of pore water in crystalline rocks. Appl. Geochemistry 23, 1834–1861. doi:10.1016/j.apgeochem.2008.02.007

Walker, R.J., Holdsworth, R.E., Armitage, P.J., Faulkner, D.R., 2013. Fault zone permeability structure evolution in basalts. Geology 41, 59–62. doi:10.1130/G33508.1

Wallace, R.E., 1951. Geometry of shearing stress and relation to faulting. J. Geol. 59, 118–130.

Wanner, C., Bucher, K., Pogge von Strandmann, P.A.E., Waber, H.N., Pettke, T., 2017. On the use of Li isotopes as a proxy for water-rock interaction in fractured crystalline rocks: a case study from the Gotthard rail base tunnel. Geochim. Cosmochim. Acta 198, 396–418. doi:http://dx.doi.org/10.1016/j.gca.2016.11.003

Wehrens, P., 2015. Structural evolution in the Aar Massif (Haslital transect): Implications for mid-crustal deformation. PhD thesis, University of Bern, Switzerland.

Wehrens, P., Baumberger, R., Berger, A., Herwegh, M., 2017. How is strain localized in a mid-crustal basement section ? Spatial distribution of deformation in the Aar massif (Switzerland). J. Struct. Geol. 94, 47–67. doi:10.1016/j.jsg.2016.11.004

Wehrens, P., Berger, A., Peters, M., Spillmann, T., Herwegh, M., 2016. Deformation at the frictional-viscous transition: Evidence for cycles of fluid-assisted embrittlement and ductile deformation in the granitoid crust. Tectonophysics 693, 66–84. doi:10.1016/j.tecto.2016.10.022

Weisenberger, T.B., Rahn, M., Lelij, R. Van Der, Spikings, R.A., Bucher, K., 2012. Timing of low-temperature mineral formation during exhumation and cooling in the Central Alps , Switzerland. Earth Planet. Sci. Lett. 327–328, 1–8. doi:10.1016/j.epsl.2012.01.007

Wellmann, J.F., Horowitz, F.G., Schill, E., Regenauer-Lieb, K., 2010. Towards incorporating uncertainty of structural data in 3D geological inversion. Tectonophysics 490, 141–151. doi:10.1016/j.tecto.2010.04.022

Wellmann, J.F., Lindsay, M., Poh, J., Jessell, M., 2014. Validating 3-D Structural Models with Geological Knowledge for Improved Uncertainty Evaluations. Energy Procedia 59, 374–381. doi:10.1016/j.egypro.2014.10.391

Wellmann, J.F., Regenauer-Lieb, K., 2012. Uncertainties have a meaning: Information entropy as a quality measure for 3-D geological models. Tectonophysics 526–529, 207–216. doi:10.1016/j.tecto.2011.05.001

White, A.F., Schulz, M.S., Lawrence, C.R., Vivit, D. V., Stonestrom, D.A., 2017. Long-term flow-through column experiments and their relevance to natural granitoid weathering rates. Geochim. Cosmochim. Acta 202, 190–214. doi:10.1016/j.gca.2016.11.042

Wibberley, C.A.J., Yielding, G., Di Toro, G., Umr, C., Antipolis, D.N.S., Einstein, A., House, N.B., Lane, N.B., Pe, L., Geoscienze, D., Giotto, V., Nazionale, I., Murata, V., 2008. Recent advances in the understanding of fault zone internal structure: a review. Geol. Soc. London, Spec. Publ. 299, 5–33. doi:10.1144/SP299.2

Wicki, T., 2011. 3D-shear zone pattern in the Grimsel area: ductile to brittle deformation in granitic rocks. Master thesis, University of Bern, Switzerland.

Wimmenauer, W., 1973. Lamprophyre, Semilamprophyre and achibasaltische Ganggesteine. Forschritte der Mineral. 51, 3–67.

Wirsig, C., Zasadni, J., Ivy-Ochs, S., Christl, M., Kober, F., Schlüchter, C., 2016. A deglaciation model of the Oberhasli, Switzerland. J. Quat. Sci. 31, 46–59. doi:10.1002/jqs.2831

Wyss, E., 1989. Felslabor Grimsel: hydrogeologische untersuchungen zur Bestimmung hydraulischer

Potentiale. Nagra technical report NTB 89-01, Baden, Switzerland.

Yamamoto, J.K., Koike, K., Kikuda, A.T., da Cruz Campanha, G.A., Endlen, A., 2014. Post-processing for uncertainty reduction in computed 3D geological models. Tectonophysics 633, 232–245. doi:10.1016/j.tecto.2014.07.013

Zadeh, L.A., 1965. Fuzzy sets. Inf. Control 8, 338–353.

Zanchi, A., Francesca, S., Stefano, Z., Simone, S., Graziano, G., 2009. 3D reconstruction of complex geological bodies: Examples from the Alps. Comput. Geosci. 35, 49–69. doi:10.1016/j.cageo.2007.09.003

Zhu, W., Wong, T., 1997. The transition from brittle faulting to cataclastic flow: Permeability evolution. J. Geophys. Res. 102, 3027–3041. doi:10.1029/96JB03282

Ziegler, M., Loew, S., Moore, J.R., 2013. Distribution and inferred age of exfoliation joints in the Aar Granite of the central Swiss Alps and relationship to Quaternary landscape evolution. Geomorphology 201, 344–362. doi:10.1016/j.geomorph.2013.07.010

Zoback, M.D., Byerlee, J.D., 1975. The effect of microcrack dilatancy on the permeability of westerly granite. J. Geophys. Res. 80, 752–755. doi:10.1029/JB080i005p00752

Zoback, M.D., Townend, J., 2001. Implications of hydrostatic pore pressures and high crustal strength for the deformation of intraplate lithosphere. Tectonophysics 336, 19–30. doi:10.1016/S0040-1951(01)00091-9

Appendix

Paper appendix:

- Extended abstract for WRI-15 international symposium in Evora

Electronic appendix:

- Maps related to chapter 2
    - Petrological map of the GTS
    - Structural geological map of the ductile deformation of the GTS
    - Structural geological map of the brittle deformation of the GTS
    - Surface map
    - Surface interpretation map
- Groundwater analyses (Chapter 3)
- Input parameters and code for kinetic modelling (Chapter 3)
- Structural 3D model of the GTS (Chapter 4)
- Kilometre scale structural 3D model of the Juchlistock (Chapter 4)
- Combined structural 3D model (Chapter 5)

Abstract published in the Conference Proceedings (Schneeberger et al., 2017).

15th Water-Rock Interaction International Symposium, WRI-15

Hydrochemical and isotopic (δ^2H, δ^{18}O, ^{3}H) characterization of fracture water in crystalline rock (Grimsel, Switzerland)

Raphael Schneeberger*, Urs K. Mäder, H. Niklaus Waber

Institute of Geological Sciences, University of Bern, Baltzerstrasse 3, 3012 Bern, Switzerland

---

Abstract

Knowledge on water circulation through crystalline rock is of key interest for radioactive waste disposal, geothermal projects or groundwater supply. This study presents first results of long-term monitoring of fracture groundwater chemical and isotope compositions combined with structural data on fracture networks developed in the crystalline rocks at the Grimsel Test Site (GTS), Switzerland. Groundwater circulation in the two major lithologies, the Central Aar Granite (CaGr) and the Grimsel Granodiorite (GrGr) is mainly associated to NE-SW trending brittle deformation structures. Within the different lithologies groundwater chemical and water isotope (δ^{18}O, δ^2H) compositions remain constant over the 2 years monitoring period. This suggests the absence of seasonal variations at the sampling depth of 420–520 m below surface. Differences in chemical and isotope composition occur, however, between groundwater collected from the CaGr and GrGr and can be related to differences in infiltration area, flow paths, residence time and water-rock interaction in the two rock units. The δ^2H and δ^{18}O signatures indicate a meteoric origin from the same moisture sources under present-day climatic conditions and the absence of measurable ^{3}H suggests residence times > 65 yrs for groundwater from both units.

Peer-review under responsibility of the organizing committee of WRI-15.

Keywords: fracture water; crystalline rocks; disposal of radioactive waste;

---

1. Introduction

In crystalline rocks, groundwater circulation is essentially limited to brittle fractures that locally increase the rock permeability and enable advective water flow. Groundwater mineralisation in crystalline rock depends on the water pathway, the interaction with the host rock, the residence time, and mixing of groundwater from different fracture networks. The Grimsel Test Site (GTS) underground rock laboratory (Fig. 1) located in the Grimsel area, Central Swiss Alps, and operated by the Swiss National Cooperative for the Disposal of Radioactive Waste (Nagra) offers a unique possibility for studying the evolution of crystalline groundwater in combination with deformation structures developed in the rocks. The bedrock in the rock laboratory and surroundings is made of three different rock types: (i) Grimsel Granodiorite (GrGr), (ii) Central Aar granite (CAGr) and (iii) metabasic dykes[1]. The GrGr and the CAGr form a calc-alkaline differentiation series of Permian age[2] whereas the metabasic dykes are younger and are of various magmatic origins. During Alpine Orogeny, the bedrock was subjected to greenshist metamorphism and ductile as well as brittle deformation[1]. This brittle deformation resulted in ubiquitous brittle fractures and fault zones (Fig. 1) with enhanced permeability. Fault zones mainly strike NE-SW and dip steeply towards S, reaching today's topography, and so crosscut the entire rock mass above the rock laboratory. These zones constitute the major flow paths for infiltrating meteoric water. The brittle

---

* Corresponding author. Tel.: +41 31 631 52 79
E-mail address: raphael.schneeberger@geo.unibe.ch

fault zones are thin (< 1dm) and form fault gouges with nearly no neo-formation of clay minerals[3]. The GTS underground laboratory is located some 420-520 m below the surface offers the unique possibility to collect fracture groundwater from such fault zones from instrumented intervals in numerous boreholes besides detailed mapping of the water-conducting structures.

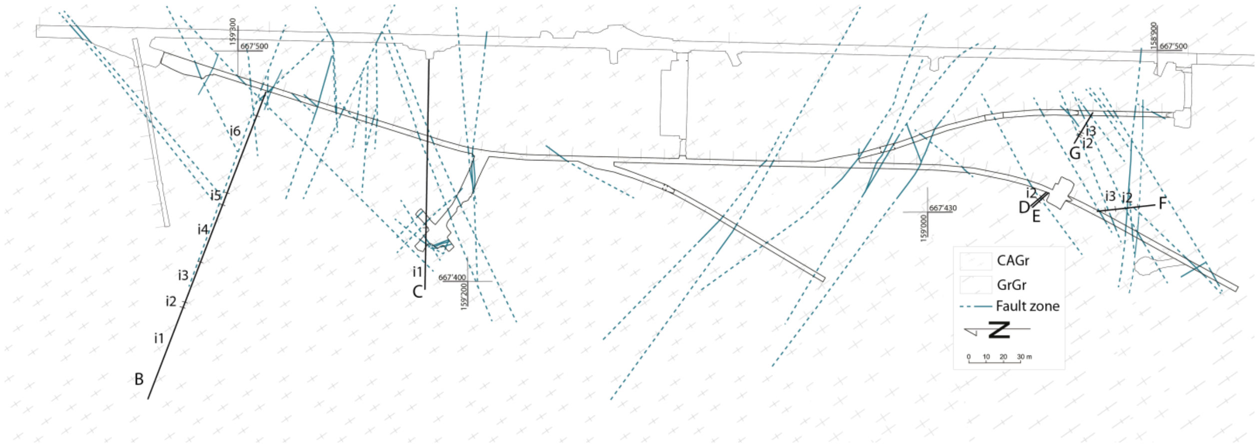

Fig. 1. Situation plan of the GTS underground rock laboratory with mapped traces of brittle fault zone (solid lines) and interpreted traces (dashed lines). Boreholes (n= 6) and packed of intervals (n= 13) are shown by black solid lines.

2. Fracture water chemical composition and evolution

Fracture water within the underground rock laboratory has been sampled in the 1980s[1] and in the 1990s[4]. In this study, fracture water was sampled five times (April 2014, August 2014, October 2014, January 2015 and August 2015) from 15 intervals in 7 boreholes (Fig. 1). Sampled boreholes are located either within the CAGr (A, B, C) or within the GrGr (D, E, F, G).

Regardless of the bedrock and with very little variation, the large majority of the fracture waters are of a general Na-Ca-TIC-F-(SO_4) chemical type and of low total mineralization (TDS: 51.9 – 71.4 mg/L). Within the individual rock units, the chemical and isotope composition of fracture water at a specific location remained constant over the 2 years sampling period and – where available – also compared to the early surveys in the 80ies[1] and 90ies[4] of the last century.

Although similar in the general aspects, the chemical and isotopic composition of fracture water collected from the CAGr and GrGr differ systematically in several parameters. Differences include temperature, which is on average higher (13.7 ± 0.9°C) in the GrGr compared to that of water collected from the CAGr (12.5 ± 0.6°C). This difference can be associated with the higher overburden in the GrGr (ca. 500m) compared to that in the CAGr (450m) part of the rock laboratory based on a geothermal gradient of 25°C/km[5], which would suggest a temperature difference of 1.2 °C for the different depths below surface. Furthermore, fracture water in the GrGr part is more alkaline (pH = 8.85 – 9.78) than that in the CAGr part (pH = 8.13 – 9.43). Related to the differences in pH the partial pressure of CO_2 is below that in the atmosphere and lower in the GrGr part ($P[CO_2] = 10^{-5.26}$ bar) compared to that in the CAGr part ($P[CO_2] = 10^{-4.91}$ bar). Fracture water in the GrGr part has higher concentrations of Na, K, Li, and Cl, but lower Ca and TIC concentrations compared to fracture water in the CAGr part (Fig. 2a). Higher Cl concentrations in the waters from the GrGr may be associated with greater interaction with pore water in the low-permeability rock matrix (known to be more saline) because no easily soluble Cl-bearing minerals occur in the fractures. The more intense diffusive exchange with such porewater, which is of moderately mineralised Na-Cl type (Cl ≈ 330–440 mg/kg_{H2O}[6]) in the GrGr, might also indicate a somewhat longer residence time for the GrGr fracture waters. Mg concentrations are close to detection limit and do not show variation, indicating minor dissolution of Mg-bearing minerals.

The mineralogical composition of the GrGr and the CaGr is very similar except for modal abundance of mafic minerals (mainly biotite), which is higher in the GrGr[1]. This allows using ion-ion ratios to deduce the evolution and reaction progress of fracture groundwater within the two lithologies. Ratios of

Na/Ca and Sr/Ca are higher in fracture water of the GrGr compared to those of fracture water in the CAGr, whereas the Na/Cl ratio is considerably lower (Fig. 2b). These ratios indicate an increased dissolution of plagioclase (albite composition), a larger addition of Na and Cl from the matrix porewater, and a more advanced precipitation of calcite in fracture water of the GrGr. The latter explains the lower TIC concentrations and the higher concentrations of Sr, which comes from feldspar dissolution, in these waters whereas Ca concentrations are controlled by calcite equilibrium. In both types of fracture groundwater, the increase in pH is explained by the effect of feldspar dissolution under concurrent precipitation of kaolinite and calcite. Such an evolution is consistent with calculated mineral saturations indices for the fracture waters: All analysed fracture waters are saturated with respect to quartz (CAGr, SI = -0.01 ± 0.05; GrGr, SI = -0.11 ± 0.09) and calcite (CAGr, SI = -0.51 ± 0.82; GrGr, SI = -0.07 ± 0.19). Kaolinite saturation index varies strongly (CAGr, SI = 0.35 ± 0.96; GrGr, SI = -0.29 ± 0.94) but most waters are close to saturation. Mg phases as well as fluorite, K-feldspar, and plagioclase are undersaturated.

It is concluded that the general reactions of fracture water in the CAGr and GrGr are similar, but the reaction progress and the exchange with porewater from the rock matrix is different. This implies longer circulation times of fracture water in the GrGr compared to that in the CaGr what is consistent with their isotope composition (see below).

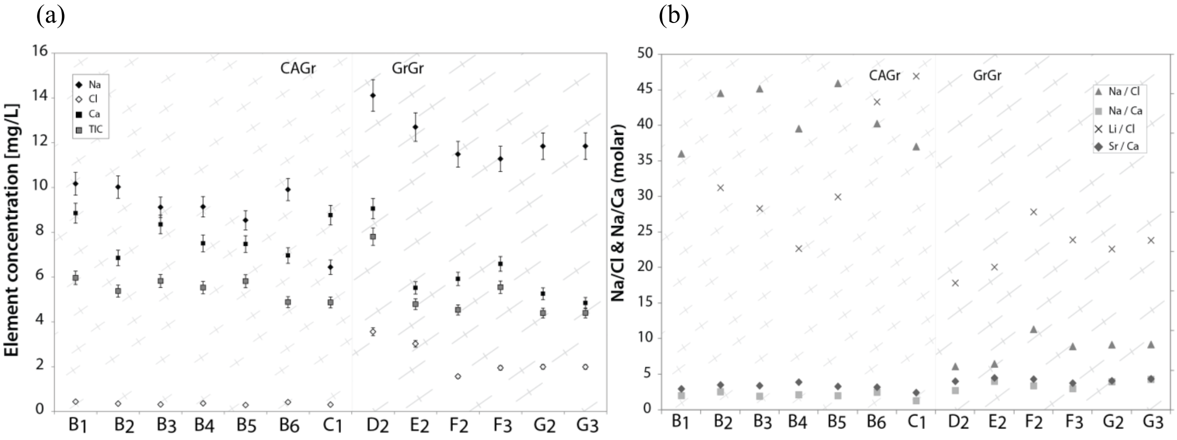

Fig. 2. (a) Concentrations of Na, Cl, Ca, and TIC in fracture water collected from various borehole intervals (x-axis) in the CAGr and GrGr (b) Molar ion ratios in fracture water collected from various borehole intervals (x-axis).

3. Groundwater origin and residence time

Fracture waters collected from within the CAGr and GrGr in the GTS underground rock laboratory show $\delta^{18}O$ and $\delta^{2}H$ values that plot on the Local Meteoric Water Line (LMWL)[7] defined by the precipitation on the Grimsel pass (Fig. 3a). The deuterium excess (d) of all samples is very similar and follows the trend given by the annual means of the local precipitation. Fracture water is therefore of meteoric origin in both rock units, infiltrated under present-day climatic conditions and stems from the same moisture sources. No systematic variation was observed between the different sampling campaigns and seasonal variations got erased by homogenization through mixing during infiltration and circulation in the rock mass down the depth of the GTS underground rock laboratory.

Conversion of the $\delta^{18}O$ values into infiltration altitude based on surface water isotope data[7] yields in higher infiltration altitudes of about 110m for the fracture water collected in the GrGr (Fig. 3b), which is in good agreement with present-day topography. As the dip of the water-conducting structures in the CAGr and GrGr is similar, this could indicate longer flow paths and longer residence times of fracture water in the GrGr as suggested by the chemical differences and assuming similar flow rates in both units.

So far the absolute residence time of the fracture waters could not be constrained. In 2016, all sampled waters have ^{3}H activities below a detection limit of 0.6 TU. Given the tritium concentration in surface waters in the area (7.0 ± 1.1 TU, 2016), the ^{3}H input at Grimsel[8] and using a piston flow model – as a first approximation – the fracture waters must have infiltrated before the bomb peak in 1950s and thus have residence times of more than 65 years.

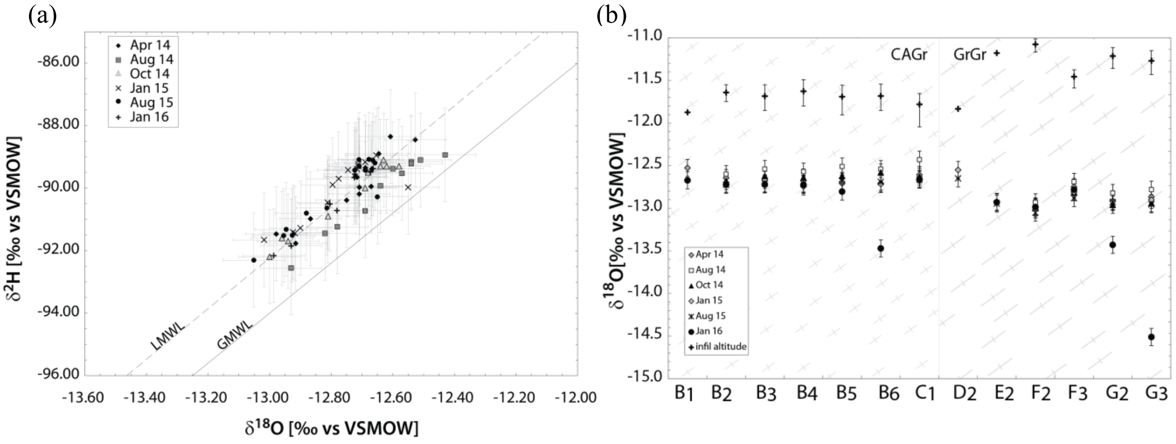

Fig. 3. (a) δ^{18}O versus δ^{2}H of fracture water in the GTS underground laboratory compared to Grimsel Local Meteoric Water Line (LMWL, data from [7]). (b) δ^{18}O values of fracture water and infiltration altitude derived from these as function of sampling intervals (x-axes) and rock type.

4. Conclusions

Sampling over 2 years enabled the definition of a baseline of fracture water chemical and isotope composition at the GTS underground rock laboratory. Chemical and isotope compositions remain constant within specific water-conducting zones encountered by packed-off borehole interval, but vary between intervals in the two main lithologies of the Grimsel Granodiorite (GrGr) and Central Aar Granite (CAGr). Fracture water flow is related to fault zones that were established by brittle deformation of the rocks and that are encountered in the rock laboratory as well as at the surface.

The isotopic composition and deuterium excess indicate a meteoric origin under present-day climatic conditions and from similar moisture source for the fracture water in both rock units. In both lithologies the major water-rock interactions are identical, but fracture water in the GrGr is chemically more evolved. Consistent with differences in chemical compositions, temperature and isotope signatures, longer flow paths related to the larger overburden and higher residence times are proposed for the GrGr fractures waters assuming similar flow rates in the water-conducting zones of both units. Based on measured ^{3}H activities the minimum residence time is more than 65 years for all fracture waters.

References

1 Keusen HR, Ganguin J, Schuler P, Buletti M. Felslabor Grimsel: Geologie, Nagra Technical report 87-14, 1989, Baden, Switzerland.

2 Schaltegger, U 1994. Unravelling the pre-Mesozoic history of Aar and Gotthard massifs (Central Alps) by isotopic dating: a review. Schweiz. Min.-Petr. Mitt. 1994; **74**: 41-51.

3 Wehrens P. Structural evolution in the Aar Massif (Haslital transect): Implications for mid-crustal deformation. Doctoral thesis, University of Bern, 2015, Bern, Switzerland.

4 Keppler A. Hydrogeologische, hydrochemische und isotopenhydrologische Untersuchungen an den Oberflächen- und Kluftwässern im Grimselgebiet, Schweiz, 1994, Doctoral thesis, Ludwig-Maximilians-Universität München, München, Germany.

5 Vernon AJ, Van der Beek P, Sinclar H, Rahn M. Increase in late Neogene denudation of the European Alps confirmed by analysis of fission-track thermochronology database. Earth and Planetary Science Letters, 2008; **270**; 316-329

6 Eichinger F., Gimmi T. Möeri A, Rüedi J. (subm.). Profiles of chloride in matrix porewater as natural tracer for matrix diffusion in crystalline rocks. Applied Geochemistry, submitted.

7 Schotterer U, Bürki H.-U., Leuenberger M. Physics Institute, Climate and Environmental Physics, University of Bern, Switzerland. Written comm. 2016.

8 Waber HN, Schneeberger R, Mäder UK, Wanner C. Constraints on evolution and residence time of geothermal water in granitic rocks at Grimsel (Switzerland). Procedia Earth and Planetary Science, this volume.

Erklärung

gemäss Art. 28 Abs. 2 RSL 05

Name/Vorname: Schneeberger Raphael

Matrikelnummer: 08-130-957

Studiengang: Earth Sciences

Bachelor ☐ Master ☐ Dissertation ☑

Titel der Arbeit: Interplay in 3D between faults and water flow paths in crystalline bedrock (Grimsel, Switzerland)

LeiterIn der Arbeit: Prof. Dr. Marco Herwegh,
PD Dr. Urs K. Mäder

Ich erkläre hiermit, dass ich diese Arbeit selbständig verfasst und keine anderen als die angegebenen Quellen benutzt habe. Alle Stellen, die wörtlich oder sinngemäss aus Quellen entnommen wurden, habe ich als solche gekennzeichnet. Mir ist bekannt, dass andernfalls der Senat gemäss Artikel 36 Absatz 1 Buchstabe r des Gesetzes vom 5. September 1996 über die Universität zum Entzug des auf Grund dieser Arbeit verliehenen Titels berechtigt ist. Ich gewähre hiermit Einsicht in diese Arbeit.

Bern, 25.07.2017

Ort/Datum

Unterschrift

Curriculum Vitae

Raphael Benedict Schneeberger

Geburtsdatum: 22.06.1989

Geburtsort: Neuchâtel, NE

Heimatort: Basel-Stadt, BS

Ausbildung

2014 – 2017	**Institut für Geologie, Universität Bern** Doktorand Dissertationstitel: Interplay in 3D between faults and water flow paths in crystalline bedrock (Grimsel, Switzerland) Betreuung: Prof. Dr. M. Herwegh, PD Dr. U.K. Mäder, PD Dr. A. Berger, & PD Dr. H.N. Waber
2011-2013	**Institut für Geologie, Universität Bern** Master of Sciences in Earth Sciences Masterarbeitstitel: Shear zone pattern and 3D geometry in the Gelmersee-Gruebensee transect (Grimsel, Switzerland) Betreuung: Prof. Dr. M. Herwegh, PD Dr. U.K. Mäder
2008-2011	**Institut für Geologie, Universität Bern** Bachelor of Sciences in Earth Sciences Bachelorarbeitstitel: Die Pseudo(sub)fossilien vom Lai Ova Spin, Schweizer Nationalpark, Graubünden Betreuung: Prof. Dr. C. Schlüchter
2004-2007	**Lycée Denis-de-Rougemont, Neuchâtel** Maturaabschluss